**Topology Optimization Considering Additive Manufacturing Process Constraints**

By

Shuzhi Xu

**A thesis submitted in partial fulfillment of the requirements for the degree of Doctor of Philosophy**

**Department of Mechanical Engineering**

**University of Alberta**

# Abstract

Additive Manufacturing (AM) is a transformative method in industrial manufacturing, facilitating the creation of lighter, stronger, and smarter parts and systems. Both plastic and metal AM technologies are extensively employed in various fields, including medical, automotive, and aeronautical industries.

As AM provides new design opportunities, topology optimization is ideal for AM since it can be deployed to design high-performance structures and fully exploit the fabrication freedom provided by AM. However, there are still some challenges of printing topologically designed parts in AM, such as multi-material design, porous infill design, residual stress, and residual distortion, which impede its widespread use in industrial applications. These challenges can be controlled by better understanding the influence of the process or material properties used in the AM process. Nevertheless, relying exclusively on experimental efforts is expensive and time-consuming. Therefore, it is very important to consider the AM issues (such as the AM material properties, AM process model and so forth) into topology optimization.

This research proposes a coupled topology optimization and AM process constraints system to deal with the challenges and utilize the opportunities of the AM process. Based on this system, the issues of topology optimization for AM are solved from two perspectives: improvement and prevention.

The main objective in the perspective of 'improvement' is to utilize the advantages offered by AM technologies for designing high-performance parts using topology optimization algorithms. This perspective comprises two crucial contributions: one involving topology optimization methods for designing stress-based multi-material structures, and the other focusing on multi-scale porous infill structure design. In the stress-based design fabricated

with multiple materials, a novel optimization algorithm that constrains the maximum stress is introduced. This new interpolation avoids the numerical issues of the extended SIMP interpolation for multi-phase stress measures. Additionally, a stress scaling method is proposed to impose the material-dependent yield stress limits. The STM based P-norm stress correction has been adopted to close the gap between the maximum local stress and the P-norm global approximation. Results of the numerical examples demonstrated that the proposed method can efficiently solve the stress constrained multi-material topology optimization problems with different material combinations. For multi-scale porous infill structure design, an innovative two-scale concurrent optimization algorithm is presented. The introduction of solid interface layers addresses the connectivity issue and thus improves the robustness of the multiscale structures. The effect of adding the interface layers has been validated through experiments and the design without interior interface layers has demonstrated an evidently degraded stiffness and strength performance. Due to the generality, the proposed methodology can reliably create optimized porous infill structures suitable for fabrication through Stereolithography (SLA) or Laser Powder Bed Fusion (LPBF).

The perspective of 'prevention' is dedicated to tackling issues related to AM process defects from a preventative standpoint, specifically within the LPBF metal AM process context. These efforts primarily concentrate on mitigating defects in parts resulting from the LPBF fabrication process, such as the residual stress and distortion. Firstly, an accelerated LPBF process simulation solver is proposed based on inherent strain theory. The results are validated with a commercial software Simufact Additive 2022®, and show an average of less 5% error. Building upon this solver, a series of design methods are proposed, including a topology optimization method with constraints related to residual stress for self-supporting LPBF-fabricated parts, laser printing path optimization to

minimize residual deformation in LPBF parts, support structure design that takes into account various LPBF processing constraints, and a large-scale concurrent optimization method accelerated by the PETSc framework is proposed. One featured optimization model is implemented on multiple computational cores and shows a computational advantage of almost 4.6 times over a reference case. It indicates that it is possible to reduce the residual distortion of a part by designing the part geometry, support structure, and printing path. Last but not least, the optimized structure obtained from the concurrent printing path and structure optimization has demonstrated the best structural performance (both the least residual warpage and the best stiffness).

# Preface

This thesis is an original work by Shuzhi Xu, and the research is performed under the supervision of Dr. Yongsheng Ma and Dr. Xinming Li. The contents of the chapters are partially from the published/submitted papers listed as follows:

Chapter 4:

**Xu, S.**, Liu, J., Zou, B., Li, Q., & Ma, Y. (2021). Stress constrained multi-material topology optimization with the ordered SIMP method. *Computer Methods in Applied Mechanics and Engineering*, *373*, 113453.

**Xu, S.**, Liu, J., Huang, J., Zou, B., & Ma, Y. (2021). Multi-scale topology optimization with shell and interface layers for additive manufacturing. *Additive Manufacturing*, *37*, 101698.

Chapter 5:

**Xu, S.**, Liu, J., Li, X., & Ma, Y. (2023). Large-scale concurrent island scanning pattern and topology optimization method for laser powder bed fusion parts. *Finite Elements in Analysis and Design*, *225*, 104018.

Chapter 6:

**Xu, S.**, Liu, J., & Ma, Y. (2022). Residual stress constrained self-support topology optimization for metal additive manufacturing. *Computer Methods in Applied Mechanics and Engineering*, *389*, 114380.

**Xu, S.**, Huang, J., Liu, J., Ma, Y., & Liu, J. (2022). An Island Scanning Path-Patten Optimization for Metal Additive Manufacturing Based on Inherent Strain Method. *Computer-Aided Design and Applications*, *19(4)*:812-824.

**Xu, S.**, Liu, J., Li, X., & Ma, Y. (2023). Support Structure Topology Optimization Considering the Residual Distortion for Laser Powder Bed Fusion Metal Additive Manufacturing. *Structural and Multidisciplinary Optimization*, Under review.

Chapter 7:

**Xu, S.**, Liu, J., Li, X., & Ma, Y. (2023). Large-scale concurrent island scanning pattern and topology optimization method for laser powder bed fusion parts. *Finite Elements in Analysis and Design*, *225*, 104018.

# Acknowledgements

# Table of content

x

# List of tables

# List of figures

xvi

xvii

# List of abbreviations

| Abbreviation | Full name |
|:---:|:---:|
| AM | Additive Manufacturing |
| CAD | Computer-Aided Design |
| CPU | Central Processing Unit |
| CFD | Computational Fluid Dynamics |
| DED | Directed Energy Deposition |
| DSP | Double Smoothing and Projection |
| DfAM | Design for Additive Manufacturing |
| DMO | Discrete Material Optimization |
| EBHM | Energy Based Homogenization Method |
| FDM | Fused Deposition Modeling |
| FEM | Finite Element Method |
| HPC | High Performance Computing |
| ISM | Inherent Strain Method |
| KS | Kresselmeier-Steinhauser |

| | |
|---|---|
| **LPBF** | Laser Powder Bed Fusion |
| **MMTO** | Multiple Material Topology Optimization |
| **MBB** | Messerschmidt-Bölkow-Blohm |
| **MMA** | Method of Moving Asymptote |
| **MMC** | Moving Morphable Component |
| **MPI** | Massage Passing Interface |
| **PETSc** | Portable and Extensible Toolkit for Scientific computation |
| **PDEs** | Partial Differential Equations |
| **PCG** | Preconditioned Conjugate Gradients |
| **RAM** | Random Access Memory |
| **RHS** | Right Hand Side |
| **SLM** | Selective Laser Melting |
| **SMMTO** | Stress based Multiple Material Topology Optimization |
| **SIMP** | Solid Isotropic Material with Penalization |
| **TMTO** | Triple Material Topology Optimizatio |
| **VTS** | Variable Thickness Sheet |

| WAAM | Wire Arc Additive Manufacturing |
| --- | --- |

# List of Symbols

| Chapter 3 | |
|:---:|:---:|
| $\Omega$ | Target domain |
| $\Omega_d$ | Design domain |
| $\Omega_p$ | Passive domain |
| $\Omega_s$ | Structure domain |
| $\boldsymbol{\mu}$ | Elemental design variable |
| $\boldsymbol{\rho}$ | Elemental physical density |
| $\mathbf{u}$ | Nodal response information |
| $g_0(\boldsymbol{\rho}, \mathbf{u})$ | The objective functions |
| $g_r(\boldsymbol{\rho}, \mathbf{u})$ | The robust objective functions |
| $R(\boldsymbol{\rho}, \mathbf{u})$ | The governing equations |
| $g_i(\boldsymbol{\rho}, \mathbf{u})$ | the equality constraint functions. |
| $g_j(\boldsymbol{\rho}, \mathbf{u})$ | the inequality constraint functions. |
| $N_{eq}$ | the number of equality constraint functions |
| $N_{Noneq}$ | the number of inequality constraint functions |

| | |
|---|---|
| $E_{min}$ | the young's modulus for void material |
| $E_0$ | the young's modulus for solid material |
| $p$ | The penalization factor |
| K | K RAMP penalization parameters |
| $r_{min}$ | the filter radius |
| $H_{ei}$ | The weighting factor between the element e and element i |
| $\Delta(e, i)$ | the center-to-center distance between the element e and element i |
| $N_e$ | the set of elements i for which $\Delta(e, i)$ to element e is smaller than $r_{min}$ |
| **K** | the stiffness matrices for the projected structures |
| $*_{ero}$ | Erosion state |
| $\xi$ | The design variable operated by AM filter |
| $\mathbf{k}_0$ | the stiffness matrix of a solid element with unit Young's modulus/conductivity |
| $\omega$ | the weighting factor to balance the intermediate design and erosion design |
| $\beta$ | a parameter governing the curvature of the projection approximation |
| $\eta$ | the threshold value for the projection |

| | |
|---|---|
| $\psi$ | the response value |
| $\psi_Y$ | the maximum value limit |
| $\psi_{PN}$ | the global P-norm measured value |
| P | the aggregation parameter |
| Nel | the number of elements |
| e | the element number index |
| $c^I$ | the correction parameter at the $I^{th}$ iteration |
| $\alpha^I$ | The modification factor to restrict the variation between $c^I$ and $c^{I-1}$ |
| k | the iteration index for the MMA |
| **x** | the design variable |
| $L_i^{(k)}$ | The moving asymptote lower limit |
| $U_i^{(k)}$ | The moving asymptote up limit |
| **A** | the system coefficient matrix |
| **u** | the vector of all state variables |
| **b** | the forcing vector |
| $g_0$ | a given arbitrary function |

| | |
|---|---|
| L | the Lagrangian function |
| $\boldsymbol{\lambda}$ | the vector of adjoint variables |
| $\epsilon_s$ | the parameter that controls the accuracy of the P-Q approximation |
| **Chapter 4** | |
| $\eta^E$ | the SIMP elastic modulus interpolation function |
| $\eta^S$ | the SIMP like stress state interpolation function |
| $\overline{\eta^E}$ | the ordered SIMP elastic modulus interpolation function |
| $\overline{\eta^S}$ | the ordered SIMP like stress state interpolation function |
| $E_i$ | the elastic modulus of the $i^{th}$ material |
| $S_i$ | the stress factor of the $i^{th}$ material |
| $P^E_i$ | the penalty value of $\overline{\eta^E}(*)$ |
| $P^S_i$ | the penalty value of $\overline{\eta^S}(*)$ |
| $\sigma_{Y,i}$ | the yield stress of the $i^{th}$ material (except the maximum yield stress) |
| $\sigma_Y$ | the maximum yield stress among the candidate materials |
| $\boldsymbol{\sigma}_0$ | the stress vector evaluated with solid material |
| $\overline{\boldsymbol{\sigma}}$ | the relaxed stress measure with penalization |

| | |
|---|---|
| **V** | the stress coefficient matrix |
| $\widehat{\sigma}_{PN}$ | the aggregated maximum von-mises stress value |
| $\widehat{*}$ | The smoothing operation |
| $\overline{*}$ | The projection operation |
| $\nabla *$ | The spatial gradient operation |
| $\|*\|$ | The Euclidean norm operation |
| $*_n$ | The normalization operation |
| $\delta(*)$ | The element stiffness matrix assembly operation |
| $*^{\mathrm{T}}$ | Transpose operation |
| $\max(*)$ | Operation of querying maximum value |
| $G_v$ | Total material volume fraction |
| $\xi$ | The $\xi^{th}$ microstructure for infill |
| $N_\xi$ | The total number of microstructures for infill |
| $\zeta$ | The $\zeta^{th}$ microstructure (including the solid phase) |
| $N_\zeta$ | The total number of representative microstructures (including the solid phase) |

| | |
|---|---|
| $\mathbf{K}$ | Global stiffness matrix |
| $\mathbf{K}_0$ | Stiffness matrix of the solid |
| $V_{ele}$ | The solid element volume in macroscale |
| $V_0$ | The total material volume in macroscale when all elements are solid |
| $N_E$ | The total number of elements in macroscale |
| $J$ | The structural compliance |
| $\boldsymbol{\rho}^{VTS}$ | Density variable in VTS method |
| $\rho_{min}$ | The lower bound of density variables in preprocessing |
| $n$ | The normalization term |
| $T_{in}$ | The width of interior interface |
| $R_1$ | The radius of the first smoothing filter |
| $\Omega$ | The design domain |
| $\psi_E$ | The macroscale elemental property indicator |
| $\psi_\zeta$ | The property indicator of the $\zeta$th representative microstructure |
| $\vartheta_{E,\zeta}$ | The elemental logic operator |
| $\varrho_\zeta$ | The characteristic density for the $\zeta$th representative microstructure |

| | |
|---|---|
| $T_{ex}$ | The thickness of the exterior shell layer |
| $N_e$ | The total number of elements within a representative microstructure unit |
| $G^M$ | The volume constraint function in macroscale |
| $g^m_{\xi}$ | The volume constraint function for the $\xi$th infilled microstructure |
| $V_d$ | The total material volume fraction limit in macroscale |
| $v_{d,\xi}$ | The material volume fraction limit of the $\xi$th infilled microstructure |
| $\boldsymbol{\mu}^M$ | The design variable vector in macroscale |
| $\boldsymbol{\varphi}$ | The projected smoothed density field in macroscale |
| $\mu^M_{min}$ | The lower bound of density variables in macroscale |
| $\boldsymbol{\mu}^m$ | The design variable vector in microscale |
| $\boldsymbol{\varphi}_m$ | The projected smoothed density field in microscale |
| $\mu^m_{min}$ | The lower bound of density variables in microscale |
| $\mathbf{KE}_E$ | The element stiffness matrix for the element $E$ in macroscale |
| $\mathbf{Ke}_1$ | The stiffness matrix for the element made by the shell layer material |
| $\mathbf{Ke}_{\zeta}(\zeta \neq 1)$ | The homogenized stiffness matrix for the element made by the $\zeta^{th}$ microstructure |

| | |
|---|---|
| $\boldsymbol{\rho}^{M}$ | The physical density in macroscale |
| $\mathbf{D}_{\zeta}^{H}$ | The effective properties of the $\zeta^{th}$ microstructure |
| $\mathbf{k}_{e}$ | The stiffness matrix for the eth element in microscale |
| $\mathbf{u}_{e}^{A(ij)}$ | The microscale elemental displacement corresponding to the unit test strain fields |
| $\Omega_{0}$ | The volume of the solid homogeneous medium |
| $C$ | The structural compliance |
| $Q_{E}$ | The elemental strain energy in macroscale |
| $v_{ele}$ | The solid element volume in microscale |
| $r$ | The length control parameter for PDE filter |
| $\alpha$ | The normalization factor for the gradient boundary |
| **Chapter 5-7** | |
| $\epsilon_{p}^{ihs}$ | The plastic strain |
| $\epsilon_{t}^{ihs}$ | The thermal strain |
| $\epsilon_{o}^{ihs}$ | The other strains that are not classified as elastic strain |
| $\epsilon^{ihs}$ | The inherent strain |

| | |
|---|---|
| $\boldsymbol{\epsilon}^{ihs0}$ | The original inherent strain |
| $\mathbf{R}(*)$ | the xy-plane rotation matrix |
| $\theta$ | the scanning orientation angle |
| $T$ | The surface traction |
| $V$ | The volume of a linear elastic solid |
| $S$ | The surface of a linear elastic solid |
| $V_0$ | A sub-volume |
| $S_0$ | A sub-surface |
| $\mathbf{U}$ | the part-scale distortion |
| $\Delta \mathbf{U}_n$ | the layer-wise distortion |
| $m$ | The number of printing layers |
| $\Omega_n$ | Each layer domain |
| $\Omega_{Ihs}$ | the layer to be printed and to apply the inherent strain |
| $\Omega_A$ | the already printed layers |
| $\Omega_I$ | the inactivated layers |
| $\boldsymbol{\delta}^n / \boldsymbol{\vartheta}^n$ | The layer wise flag field variables |

| | |
|---|---|
| $\eta_e^\beta$ | the inherent strain load coefficient interpolation function |
| $\mathbf{B}$ | the strain-displacement matrix |
| $\mathbf{L}_e$ | gathering the nodal displacements of the eth element ($\mathbf{u}_e$) from the global displacement vector ($\mathbf{U}$) satisfying $\mathbf{u}_e = \mathbf{L}_e\mathbf{U}$ |
| $\mathbf{U}_{res}$ | the final stage part-scale distortion |
| $\mathbf{H}_{DOF}^n$ | a flag array that indicates the activated nodes in each printed layer |
| $\mathbf{K}_{cutoff}$ | the assembled stiffness matrix corresponding to elements that are removed in the final separation step |
| $\mathbf{K}_{remain}$ | the assembled stiffness matrix for the remained elements |

# Chapter 1. Introduction

Additive Manufacturing (AM), also known as 3D printing, rapid prototyping, and rapid manufacturing [1], is a class of advanced manufacturing. In the last four decades, AM technology has revolutionized the manufacturing industry. Along with the technological advancements in AM, topology optimization methods [2] have also made significant progress. Today, products designed through topology optimization and manufactured using AM technology have gained widespread recognition among the public.

## 1.1. Research motivation

Topology optimization for AM is a design methodology aiming at optimizing the structural configuration of a component to minimize material usage while maintaining its performance. It considers the specific requirements of AM, such as manufacturing constraints and build direction, and utilizes multi-objective optimization techniques to obtain trade-off solutions by balancing various design goals. This approach enables the generation of highly optimized and lightweight component designs for AM, utilizing the advantages of materials and manufacturing processes.

However, because of the expanded design space, the gained topological design has often been criticized for being too organic, which poses challenges during the construction and postediting of the associated CAD model. It is difficult to guarantee that a topologically optimized design to be manufacturable and aesthetically acceptable (deviates from what conventionally a mechanical part would look like) [3]. Generally, engineers will perform an 'interpretation' step in which the organic shape is simplified into standard geometries and rebuilt from typical CAD primitives. Unfortunately, sizable optimality is often lost in this step. To address these issues, significant research has been carried out on manufacturability-oriented topology optimization, but not all of them are mature enough

for industrial applications [4].

Despite the numerous advantages associated with AM, this manufacturing method does possess certain limitations that need to be considered when developing suitable topology optimization algorithms. For some AM techniques, such as LPBF, DED, WAAM, and other metal fabrication methods, inherent defects may be presented in the manufactured components due to their unique material forming processes [5][6][7]. These defects can ultimately impact the geometry and performance of the resulting products. Traditionally, topology optimization algorithms assume an ideal manufacturing scenario [8], which often leads to discrepancies between components successfully manufactured through AM and the originally designed parts. Eliminating these discrepancies can significantly enhance the practical application of topology optimization in engineering. In summary, currently, many components designed and optimized using topology optimization algorithms often neglect real-world manufacturing processes. This can potentially lead to a disconnect between product design and practical manufacturing considerations. Therefore, it becomes crucial to consider actual AM process requirements into the topology optimization algorithms.

## 1.2. Research gaps

As highlighted a decade ago by Brackett et al. [3], the lack of topology optimization solutions compatible with AM was a significant impediment (like the low mesh resolution limit, less manufacturing constraint consideration, difficulty in post-optimization topology handling, and so forth), and there were also some opportunities for topology optimization for AM (lattice infilled structure design, multiple material design, and processing parameter considered optimization). Over the years, efforts have been made to meet some of these challenges [9][10][11][12]. Based on the aforementioned discussions, new issues

have been arisen which are still under investigations and could be listed as follows:

1. There is still a lack of a robust and efficient topology optimization framework for AM. Much of the existing work is only applicable to simple structural designs with specific boundary conditions and cannot be applicable to real practices. In addition, too many tunable parameters exist in the algorithms, making the work difficult to reproduce [15];

2. New rules and restrictions emerge due to the diverse and intricate AM processes, which requires further explorations. For example, in multiple material structure design, the stress constrained problem has not been fully solved [16]. While in multi-scale lattice infilled topology optimization, the problem of microstructural connectivity is still being explored [17]. In addition, as in the design for fiber reinforced composites, the obtained structure is difficult to match with the actual processing technology [18];

3. There is still a lack of efficient and robust topology optimization algorithms for metal AM. Topology optimization combined with metal AM processes is time-consuming and unstable since metal AM processes involve multiple complex physical coupling phenomena. Meanwhile, balancing accuracy and efficiency properly remains a huge challenge for metal AM solvers [9][19];

4. Most algorithms are only suitable for coarse or low-resolution meshes, which greatly limits the improvement of structural performance and real-world applications. Although there are several open-source computing frameworks for large-scale topology optimization problems [20][21][22][23][24][25], it is still difficult to integrate them with metal AM oriented topology optimization [26].

## 1.3. Research objectives

The thesis, titled 'Topology Optimization Considering Additive Manufacturing Process

Constraints,' aims to establish a foundational framework for design and optimization in AM. This framework assists structural designers take full advantage of AM by offering insights into material properties, residual stresses/deformations, and structural topology optimization. The work can be categorized into two distinct aspects based on research objectives: 'improvement' and 'avoidance.'

Firstly, regarding the aspect of 'improvement', it refers to the endeavor to enhance the performance of the manufactured structure by utilizing the distinctive characteristics of the AM process. For instance, in the case of conventional fabrication methods such as FDM, the resulting material exhibits significant anisotropy [13]. Taking this factor into account at the component design phase, the reliability of the part can be significantly improved.

Moreover, in the context of 'prevention', the aim is to design a manufacturable part while considering process constraints and ensuring structural performance. For example, in metal AM, the presence of residual stresses can lead to processing failures [14]. The generation of these residual stresses is highly influenced by the geometry of the part. By employing topology optimization techniques to modify the part's geometry, the generation of residual stresses can be significantly reduced, thereby enhancing the manufacturability of the component.

## 1.4. Research contributions

At the beginning of this chapter, an overview of the current state of integration between topology optimization and AM is provided. The main contributions of this work are demonstrated in Figure 1.
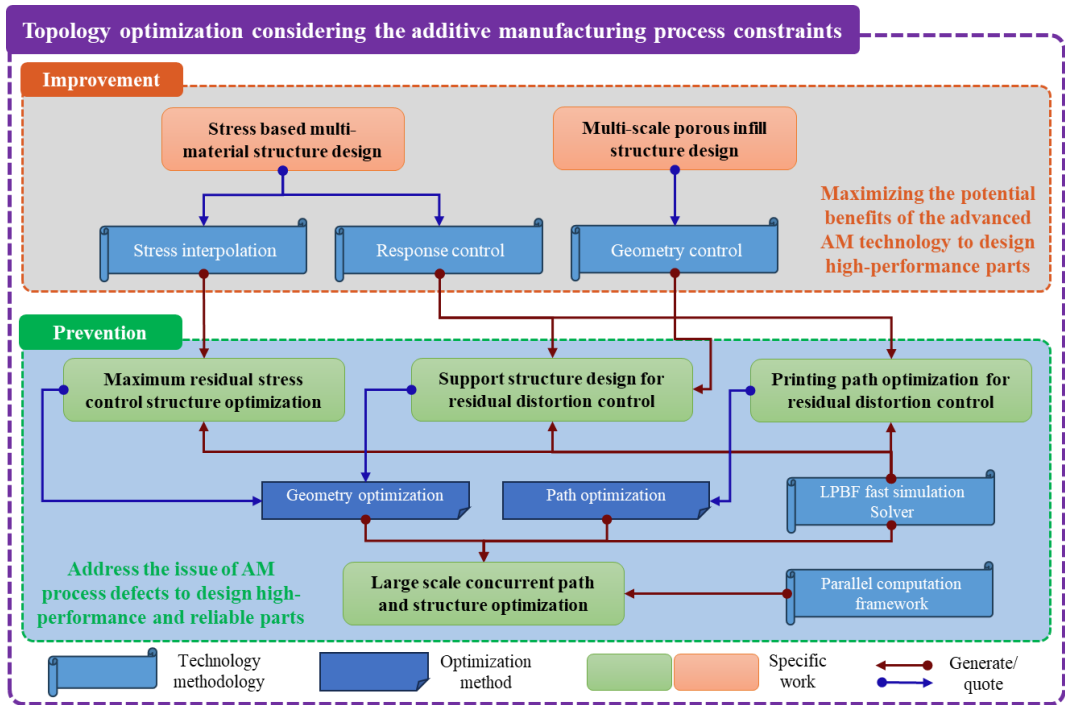
Figure 1. Main contributions and logical relationship between them

The main contributions can be summarized into two parts: topology optimization for parts design in advanced AM technology and topology optimization considering the AM process constraints.

The primary objective related to topology optimization for advanced AM parts is to leverage the advantages of AM technology to design high-performance components using topology optimization algorithms from the 'improvement' view, encompassing two key contributions: topology optimization methods for stress-based multi-material structures design and multi-scale porous infill structures design. In terms of stress-based structures fabricated by multi-material, a maximum stress constrained optimization algorithm is proposed, which involves the development of a novel stress scaling ordered SIMP interpolation. Multi-scale porous infill structures design, an innovative two-scale concurrent optimization algorithm is introduced. This algorithm incorporates the shell

extraction algorithm and the energy-based homogenization method, while also considering structural connectivity. Using this approach, it is possible to create a reliable and optimized porous infill structure fabricated through SLA or LPBF.

In the next part, several studies (Papers 2 to 6) have been conducted to address the issue of AM process defects from the 'prevention' view, particularly in the context of the LPBF metal AM process. These works primarily focus on mitigating part defects induced by the LPBF fabrication process, such as residual stress and distortion. Firstly, a fast LPBF process simulation solver is developed based on the inherent strain method (ISM). Building upon this solver, a series of works have been proposed, including a topology optimization method with residual stress constraints for self-support LPBF fabricated parts, laser printing path optimization to reduce residual deformation in LPBF parts, support structure design considering various LPBF processing constraints, and large-scale concurrent optimization method (based on the PETSc framework) of laser printing path and structure geometry for LPBF metal AM.

It is noted that this thesis incorporates both existing technical methods and novel approaches. The integration of these methods offers a robust and dependable solution to address the challenges at hand. In the subsequent chapters, each of these technical methods will be individually introduced, according to their relevance to the research objectives.

## 1.5. Structure of the thesis

The thesis is organized into seven chapters, as depicted in Figure 2. First, Chapter 2 presents the literature review closely related to the research topic. In this chapter, a brief overview of topology optimization methods and some typical applications of topology optimization are provided. Subsequently, the works regarding topology optimization for AM has been introduced, specifically addressing the material, geometry, support, and

fabrication process aspects. These perspectives are summarized and reviewed in conjunction with topology optimization algorithms. It is worth noting that, in terms of the fabrication process aspect, the thesis primarily focuses on metal AM, and therefore, only introduces LPBF as a typical metal processing method along with relevant topology optimization works.
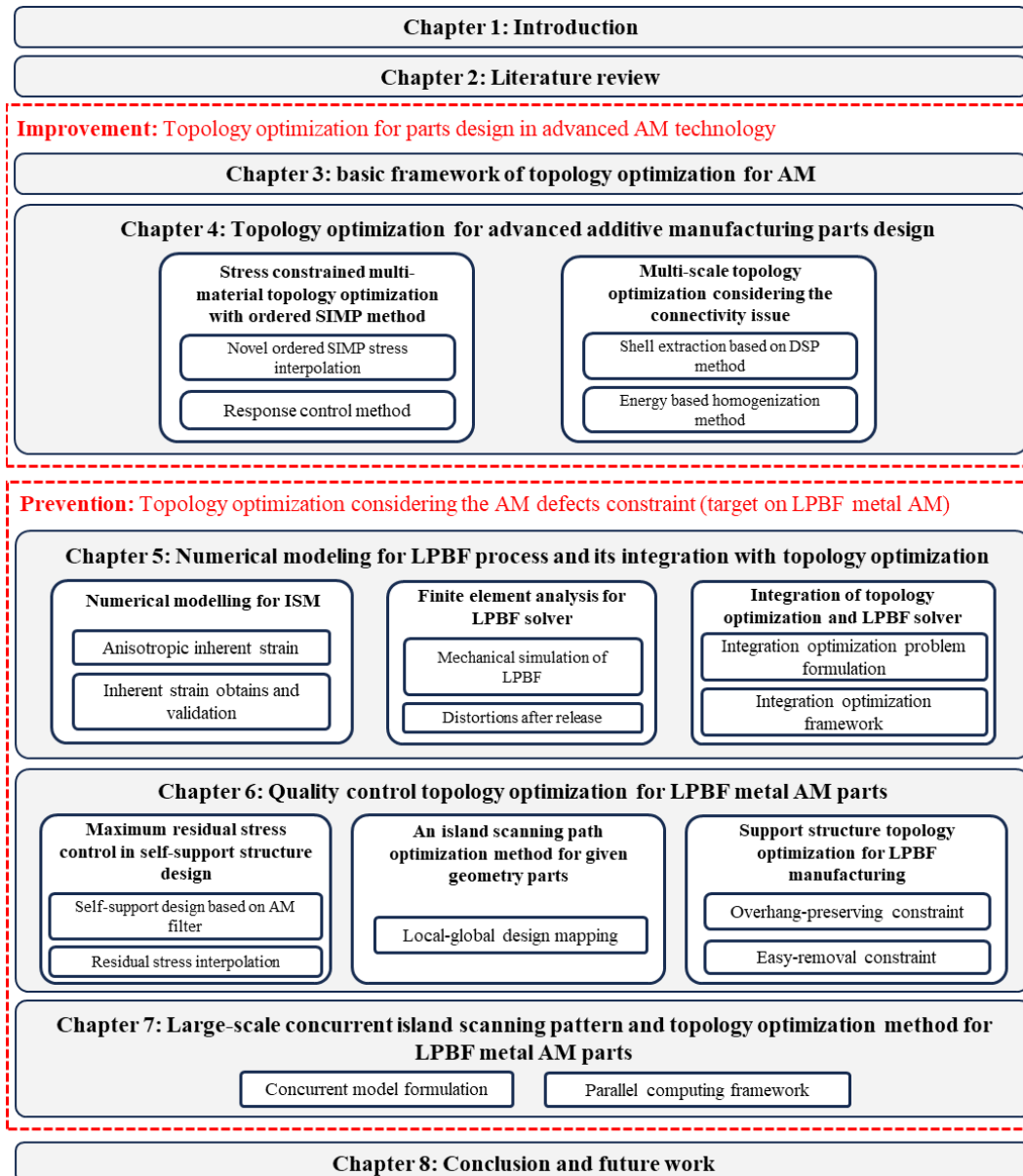


Figure 2. Structure of thesis.

Chapter 3 presents the basic framework concerning topology optimization for AM. A system comprises topology optimization, post-processing, performance simulation, and mechanical testing, serving as an integrated solution for achieving high-performance products, expediting product enhancements, and curbing design expenses. Chapter 4 delves into topology optimization for advanced AM parts. This chapter is divided into two main aspects. The first (Section 4.1), focuses on introducing topology optimization methods for stress constrained design in the context of multi-material FDM. The second (Section 4.2) covers the design of porous infill structures using topology optimization techniques.

The works about topology optimization for the AM process constraint is covered in Chapters 5 to 7. Chapter 5 introduces a rapid solver for LPBF process simulation and its integration with topology optimization algorithm. Chapter 6 mainly discusses several approaches to address defect control issues in the LPBF manufacturing process, which includes three aspects, including the residual stress control design method for LPBF metal manufacturing (Section 6.1), the LPBF laser printing path optimization (Section 6.2), and the support structure design for LPBF parts (Section 6.3). Chapter 7 proposes a concurrent optimization framework for printing path/structure for the large-scale part design.

Finally, Chapter 8 provides a summary of the works conducted in this thesis and offers an analysis and outlook on the limitations and future directions of the research.

# Chapter 2. Literature Review

## 2.1. Brief introduction to topology optimization methods and their applications

Compared with traditional structural optimization methods, topology optimization enables the creation, merging and splitting of the interior solids and voids during the structural evolution via three optimization methods (Figure 3), and therefore a much larger design space can be explored, and the superior structural performance can be expected.
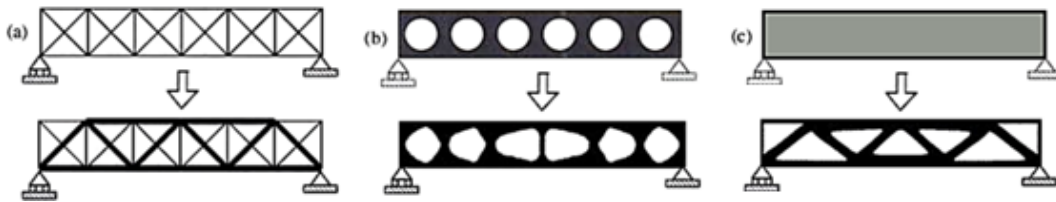


Figure 3. Three different structure optimization methods: (a) size optimization, (b) shape optimization, and (c) topology optimization [27].

Topology optimization gives answers to the fundamental engineering question: how to place material within a prescribed design domain to obtain the best structural performance? The concept was initiated for mechanical design problems but has spread to a wide range of other physical disciplines, including fluids [28], acoustics [29], electromagnetics [30], optics [31] and combinations thereof [32].

A number of prior developments within homogenization theory and numerical optimization methods provided the foundation for the seminal paper on numerical topology optimization by Bendsøe and Kikuchi [33]. Since the original 'homogenization approach to topology optimization', the concept has developed in a number of different directions Figure 4, including the density-based approach [34][35][36], the level-set method [37][38][39][40], the topology derivative method [41], the phase field method [42], the evolutionary approaches [43], the geometry expression [44], and some others.
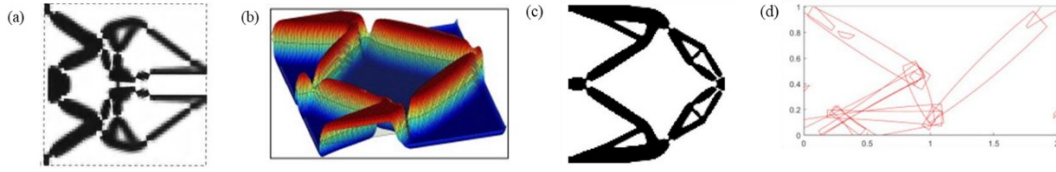
Figure 4. Four different topology optimization methods: (a) density-based method [27]; (b) level-set method [39]; (c) BESO method [43]; (d) MMC method [44].

For a comparative and critical review of topology optimization approaches, some excellent papers can be found in [45][46][47][48][49], among which the density-based approach uses simple element or nodal-based design variables without complex topological derivatives, and thus they could better combine with various numerical analyses or optimization approaches. Therefore, all the research mentioned in this research is based on the density-based approach.

### 2.1.1. Multi-material topology optimization

The utilization of multi-material structures has garnered significant attention thanks to the rapid advancements in manufacturing technologies. Multi-material structures have been found to possess superior structural properties compared to single-material structures [50]. Therefore, one of works in this research aims to incorporate the multi-material model into algorithms as a means of enhancing the performance of manufacturable structures.

To solve the MMTO problems, a typical extension was to include one more density variable in the SIMP interpolation model to distinguish the different solid material phases [50]. Alternatively, a peak function interpolation scheme was developed with the SIMP method to deal with the MMTO [51] which has the advantage of not increasing the amount of design variables. The multi-material extension of phase field and level-set methods [52][53] and its integration with other disciplines [54] have also been successfully conducted. Generally, more phase field or level-set functions are involved to realize the

multi-phase interpolation [55][56].

Recently, the ordered SIMP interpolation method was proposed by Zuo and Saitou [57]. This method employs a continuous function to interpolate the elastic properties of the multi-phase materials with respect to a single density variable.

## 2.1.2. Multi-scale topology optimization

To enhance the macroscale structural performance, research attention has been drawn to the field of multi-scale topology optimization, i.e., to concurrently optimize both macro- and micro-structural details through the homogenization method [58][59]. Different categories of microstructures will co-exist inside the design domain [60][61][62][63][64][65][66][67]. However, this method has several limitations. First is the prohibitive computational cost, since both topology optimization and homogenization need to be conducted on a large number of local microstructural unit cells for each iteration; second is the manufacturable difficulty, due to the dis-connectivity issue between adjacent microstructures and the computing intensive post-processing of the numerous lattice microstructures. Hence, to simplify the situation, we have seen many optimization works only dealing with an identical lattice microstructure to periodically infill the entire structural interior [68][69][70][71][72]. In this approach, all elements in macroscale will be characterized with the same effective properties. Thus, the computational cost is greatly saved, and the dis-connectivity issue can be easily addressed. This method, however, is incapable of fully utilizing the design space, leading to severely compromised structural performance.

Efforts have been made to address the research issues mentioned above. To deal with the connectivity issue, a heuristic treatment was used to predefine the connecting passive space between adjacent microstructures [64][73]. The shape interpolation method was developed

to build interpolation functions of the mechanical properties of a series of graded microstructures having similar shape and topological features [74][75]. Du et al. [76] introduced a connectivity functional into multi-scale topology optimization model to ensure all the microstructures being well connected. In addition, a novel projection scheme was presented by Groen and Sigmund [77] and used in homogenization based topology optimization to efficiently obtain high-resolution macro topologies with connectable microstructures. Based on the MMC method, Deng et al. [78] devised an effective linkage scheme to guarantee smooth transitions between neighboring material microstructures.

To save the computational cost, Zhao et al. [79] proposed an efficient decoupled sensitivity analysis method for concurrent topology optimization of frequency response problems to reduce the computational burden. Kato et al. [80] introduced a decoupling multiscale analysis strategy and applied it to three-dimensional structure optimization undergoing large deformation. A trial-and-error criterion was presented by Sivapuram et al. [81] to divide the geometrical domain into subdomains and have each subdomain composed of a unique microstructure. Principal stress distribution [82] or VTS method [83] were also employed to classify the subdomains. Xia and Breitkopf [67] constructed an approximate constitutive model with a reduced database to approximate the local material properties, which effectively circumvented the massive computational burden related to the local material optimization.

In conclusion, multi-scale design has the potential to expand the design space and improve structural performance compared to single design. Therefore, this research proposes solutions to the multi-scale design problem based on AM.

### 2.1.3. Stress constrained topology optimization

Stress-related topology optimization is challenging given the numerous underlying

numerical and optimization issues. Since the pioneering work by Bendsoe and Duysinx, considerable research efforts have been dedicated to this subject. Notably, mainstream topology optimization methods such as SIMP and BESO have effectively addressed stress-related problems.

Le et al. [84] summarized three main challenges of stress constrained topology optimization: the singularity problem [85][86], the local nature of stress [87], and the highly nonlinear behavior of stress distribution [88]. The singularity problem only arises with the density-based method. It refers to the fact that some elements with low densities still present high stress values, making the optimization algorithm incapable of eliminating materials entirely at the local spot. For this problem, relaxation techniques (such as the ε-relaxed method, q-p approach and so forth) have been proposed [87][89][90][91][92][93], and some of the technical details will be introduced in the following chapter. Regarding the second problem, the local property of the stress evaluation leads to a large number of local stress constraints included in the optimization formulation that induces the enormous computational burden.

One common strategy to solve this dilemma is to build a global evaluation to quantify the peak stresses through adopting aggregation functions, such as the p-norm function and the K-S function [87][94][95]. Then, a large number of local constraints are transformed into one global stress constraint that simplifies the solution of the optimization problem. Moreover, clustering technology also works well to reduce the number of local stress constraints [84][96][97]. As for the third challenge, the stress constraints are highly nonlinear and sensitive to local material changes, which brings up difficulties in deriving a smooth convergence. For this reason, density filter is adopted instead of sensitivity filter for stabilization consideration [84], and a conservative move limit setting of the optimizer

13

is also useful [98].

Furthermore, stress constrained topology optimization methods have been developed to address different kinds of failure criteria other than the von-Mises stress [99][100][101], to consider geometrical nonlinearity [102], and to consider the thermal stress [103]. Here, the yield stress constraint issue in AM fabricated parts will be targeted, and the solutions will be proposed from different perspectives (the mechanical performance and manufacturing performance).

## 2.2. Additive manufacturing

AM is a technology that fabricates solid components by gradually adding material based on three-dimensional design data. In contrast to subtractive manufacturing, which involves material removal, AM follows a bottom-up approach of material accumulation. This technology is based on the principles of discrete/layered fabrication, utilizing powder or filament materials, and employing high-energy beams such as lasers or electron beams for metal melting/solidification. The material is stacked and fused to create the desired component layer by layer. This enables the production of sophisticated structures that were previously unattainable due to constraints imposed by traditional manufacturing methods such as machining and casting.

AM can reduce the manufacturing cost of enterprises and improve production efficiency by reducing mold costs, materials, assembly, and research period [104]. Based on the type of processed material and the manufacturing method, AM can be categorized into metal forming, non-metal forming, and biomaterial forming [105]. Moreover, depending on the state of the raw material, AM systems can be classified into three major categories: liquid-based AM, solid-based AM, and powder-based AM systems [106].

AM technologies utilize various energy sources, including lasers, electron beams, and

ultraviolet light. The employed materials encompass resins, plastics, metals, ceramics, waxes, among others [106]. Due to the diverse range of forming methods, materials, and heat sources involved, AM encompasses multiple process techniques [107]. Widely used AM techniques range from FDM and SLA for plastic printing to LPBF and EBM for metal printing. Figure 5 illustrates the schematic diagrams of FDM and LPBF.



(a)         (b)
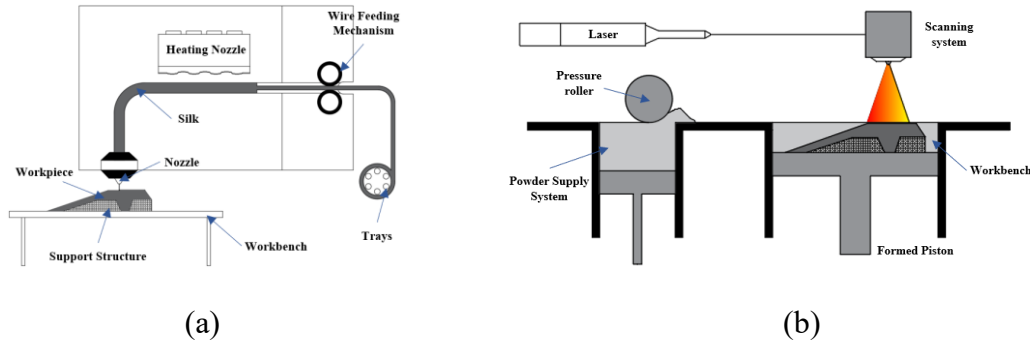
Figure 5. Schematic diagrams of (a) FDM and (b) LPBF.

It can be concluded that AM processes rely on layer-by-layer material deposition or solidification, which removes the geometric complexity restriction to a large extent. Besides, in AM, manufacturing efficiency and fabrication cost are not sensitive to geometric complexity. Therefore, AM can easily create freeform design from topology optimization, and many of the manufacturability related issues (for conventional manufacturing method) are eliminated.

### 2.2.1. Laser powder bed fusion

This system typically comprises several essential components, including a fabrication platform, a laser system, and a powder delivery platform. During LPBF manufacturing, a high-power laser selectively scans over metal powder to facilitate the formation of successive solidified metal layers that are integrated with the pre-existing layers. This process will be repeated until the final product, in its desired configuration, is obtained.

Figure 6 provides several representative parts made by LPBF.



Figure 6. Several sophisticated parts made by LPBF.

LPBF boasts a plethora of advantages. Foremost, it offers exceptional design freedom, empowering the creation of intricate geometries that traditional manufacturing methods would struggle to achieve. Additionally, LPBF yields parts with outstanding mechanical properties due to the thorough melting and solidification of metal, resulting in a dense and robust final product. Moreover, LPBF excels in material efficiency, adding material only where necessary, unlike subtractive manufacturing methods. Lastly, LPBF proves to be highly suitable for rapid prototyping, facilitating swift iteration and efficient design validation.

Despite its numerous benefits, LPBF does come with certain limitations, including elevated equipment costs, restricted build size, challenges related to specific materials, and the presence of printing-induced defects. The primary focus of this research centers on addressing the issues concerning its printing defects.

## 2.2.2. LPBF manufacturing process simulation

For addressing this challenge, process parameter optimization is necessary, but relying exclusively on experimental efforts to investigate melt-pool behaviors is expensive and time-consuming. Therefore, LPBF process modeling has been used to investigate the LPBF process. It can be significantly helpful not only in optimizing process parameters

but also in predicting the residual stresses and deformation.
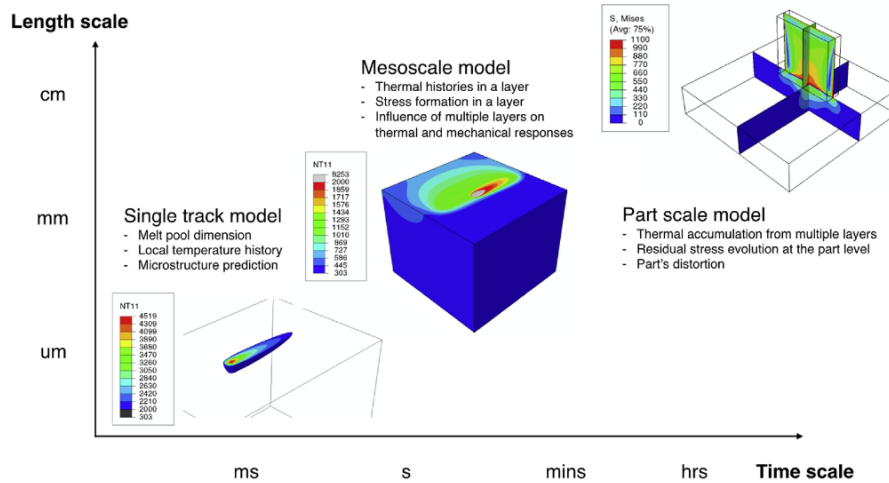


Figure 7. Multiscale computational framework for estimating thermal and mechanical responses in LPBF AM of metal powder [107].

Overall, as shown in Figure 7, according to different time and space discrete standards, LPBF simulation mainly involves models of three scales: single track model (particle scale), mesoscopic scale model, and part scale model.

### 2.2.2.1. Particle-level modeling

The modeling of LPBF is a complex task, as it involves various physical phenomena. These include photon absorption [108], heat transfer, hydrodynamics [109], dynamics of particles [110], phase change dynamics [111], solid mechanics [112], and so forth. Therefore, several researchers have employed particle-level models to investigate heat flow and mass flow within melt pools [113][114][115][116]. These models incorporate various details, including CFD models, randomly distributed particles, and the simulation of laser-ray transmission through particles, in order to accurately simulate the behavior of melt pools.

Korner et al. [117][118] initially investigated a 2D randomly packed powder bed to

17

examinate the stochastic effects of particles, the influence of relative density, wetting, and capillary phenomena in LPBF. Khairallah et al. [119] developed a comprehensive multi-physics code for simulating the 3D LPBF process. Their approach involved the coupling of thermal analysis and hydrodynamics to investigate the Plateau-Rayleigh instability phenomenon. Xia et al. [120] investigated the porosity evolution during LPBF by considering a randomly packed powder bed, thermodynamics, phase transition, and interfacial force. Recently, Panwisawas et al. [112] established a model including almost all interfacial phenomena and derived the temperature distribution of single-track molten zones. Furthermore, a CFD model was built to investigate the influence of the shield gas on the microstructures of the LPBF parts [121]. For calculating the absorption of a laser beam by powders, Boley et al. [122] used ray-trace simulations. The relationships between absorption and powder content (material, size, distribution, and geometry) have been investigated.

Additionally, the substantial computational requirements associated with these methods hinder their direct applicability to thermo-mechanical simulation models for calculating residual stresses and deformations. Moreover, the intricate characteristics of particle-level models have restricted their usage in multi-layer simulations, and the computational cost for such simulations is exceptionally high [116][117][118].

## 2.2.2.2. Meso-level modeling

Efficient and accurate prediction of melt pool dimensions, such as melt pool width and depth, in meso-level models often relies on effective approximations and assumptions. These models can be validated by comparing their results against particle-level modeling or experimental data. To simplify the modeling process, volumetric heat source models are commonly employed instead of laser-ray tracing methods using randomly distributed

particles. Additionally, key considerations for effective modeling include heat source models, model dimensions, material addition techniques, thermal-mechanical coupling techniques, and boundary conditions, as summarized in a valuable study [123]. Heat source models play a fundamental role in predicting microstructures in LPBF since they provide the thermal history that directly influences microstructure formation [124][125].

A one-way coupled thermo-mechanical model was developed to examine the residual stresses [126]. In addition to residual stresses, other properties have been incorporated into thermo-mechanical modeling. Li et al. [127] accounted for the shrinkage of the powder layer following melting in a model, aiming at predicting the temperature and residual stress fields in LPBF. Importantly, studies have shown that scanning strategies influence the residual stresses in the LPBF parts [128][129]. Therefore, many researchers have paid attention to studying scanning strategies for the sake of reducing residual stresses [130][131][132][133].

Advanced computing techniques have employed in the LPBF process modeling. Denlinger et al. [134] proposed a three-dimensional non-linear thermo-elastic-plastic finite element model for LPBF, where adaptive mesh was employed. The model has been validated by comparing with the experimental deformations. Neiva et al. [135] developed a parallel finite element framework for metal additive manufacturing at the part scale. The adaptive mesh was also incorporated into the framework where a maximum of 19 times speedup was achieved.

### 2.2.2.3. Part-level modeling

Even though comprehending the physics within melt pools is crucial, it is worth noting that the dimensions of the models employed in the aforementioned studies are relatively small compared to the actual size of an AM part. To achieve a comprehensive

understanding, part-level simulations should encompass the deposition process across multiple layers. However, applying the aforementioned methods to handle part-level simulations can become challenging and impractical. Therefore, the development of fast computation methods for part-level analysis remains critical, particularly for topology optimization, given its iterative nature.

Mercelis et al. [136] proposed an analytical model to investigate residual stresses in LPBF, demonstrating a favorable qualitative coherence with experimental data. To accelerate simulations, researchers have explored the use of larger heat sources, known as the equivalent heat flux domain method. Alternatively, an equivalent mechanical method has been introduced, wherein an entire layer of material with predefined inherent strains is added at each iteration. This method eliminates the need for heat transfer simulations, enabling further acceleration of the simulation process. Additionally, various techniques and methods, such as the birth and death method and the adaptive mesh technique, have been employed in pursuit of faster simulations or less memory usage.

For the equivalent heat flux domain method, the technique of birth and death is suitable for describing AM's material adding procedure, in which new elements are activated at the desired time. Matsumoto et al. [137][138] calculated the distribution of temperature and stress in one single layer in LPBF. Robert et al. [139] proposed a multi-layer simulation model of LPBF using the element birth and death method. Zhao et al. [141] investigated the thermal behavior of a single-pass multi-layer rapid prototyping by FEM and experiments. Kolossov et al. [142] developed a thermal model of selective laser sintering, which was comparable with experimental results. Zhang et al. [143] investigated the influence of the different dimensions of the activated domains in a domain-by-domain activation method. Computational efficiency may be improved by using the adaptive-mesh

technique, in which mesh is automatically adjusted during the simulation process. Keller et al. [144] built a part-level simulation for LPBF by implementing the heat flux on a slice of a part at once instead of the actual-scan process, which could decrease the calculation time. In Seidel et al.'s work [145], four heat-input models for calculation temperature distribution in the LPBF process have been explained separately. Chiumenti et al. [146] employed the element birth-and-death technique to simulate the temperature distributions in LPBF. Three different sizes of the domain for activating are used, and they are hatch-by-hatch, layer-by-layer, and reduced hatch-by-hatch. Thermal couples were embedded in the printed part when the printing was stopped halfway in order to validate the temperature distribution. The temperatures from simulated results and experiments have a good agreement. However, the residual stress distribution should be further validated.

Similar to the equivalent heat flux domain method, researchers used an equivalent mechanical layer method – inherent strain method (ISM) to achieve the part level simulation of LPBF, in which a whole layer of material with some specified inherent strains are added at each time. ISM can accelerate part-level modeling because only elastic modeling is needed to estimate the deformation and residual stresses given the initial inherent strain.
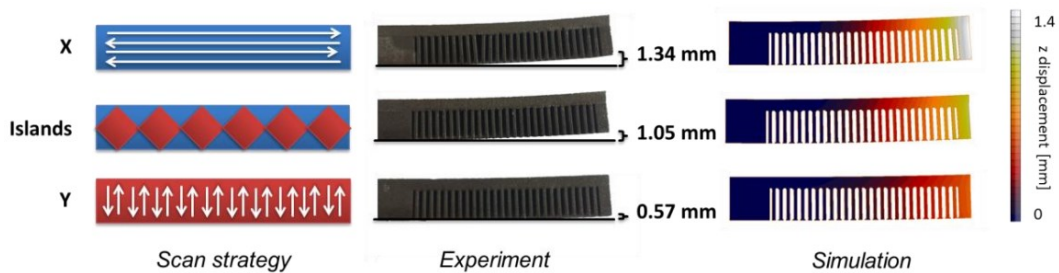


Figure 8. Results of experimental investigation and simulation of thermal distortion for a cantilever specimen [148].

Their similar ideology is that mechanical results of a mesoscale analysis are imported into

a macro-scale part due to the comparable mechanical history in melt pools. Li et al. [147] built a multiscale model with the idea of the initial residual stress, in order to rapidly predict the part deformation in LPBF, which included microscale, mesoscale, and macroscale simulations. Keller et al. [148] used the concept of inherent strain to build a fast simulation model for predicting deformation and residual stresses of AM parts. A part-level simulation proved a similar trend of deformation as the experiments did. Comparison of the deformation of a cantilever specimen between the results of simulation and those of experiments (Figure 8). Most recently, Siewert et al. [149] did a comprehensive validation for the inherent strain method, in which both the residual stresses and deformation are validated by experiments. They found that even though the inherent strain method has some simplifications, reliable predictions of residual stresses and deformations can still be achieved.

## 2.3. Topology optimization for additive manufacturing

Although AM significantly expands the design space, it is not a completely free-form manufacturing technique [150]. At the design stage, several basic issues arise, including material, geometry, support, and manufacturing process issues [151]. This research will take all of these previously identified issues into full consideration and incorporate them as basic manufacturing constraints in the proposed algorithm. A brief overview of the relevant literature concerning these problems is provided in this section.

### 2.3.1. Material issues

AM-induced material anisotropy is widely known [152][153]. Although efforts have been made to reduce the anisotropy [154], it generally cannot be totally avoided, and therefore should be carefully addressed. A systematic study of this topic can be found in [155], while we briefly revisit the problems and present some updated perspectives. AM-induced

anisotropy manifests itself in two ways: (1) anisotropic constitutive properties related to stress and strain, and (2) directional strengths. In [156], the latter was addressed by replacing conventional von Mises stress criterion [157] with the Tsai-Wu stress criterion.

Regarding the anisotropic constitutive properties, it can be either build direction or raster direction dependent where the former is more evident for most AM processes. Therefore, optimizing the build direction has attracted the early attention, and effective improvement of mechanical performance [158][159][160] has been observed. In addition, concurrent build direction and topology optimization problem is trivial to solve, for example, through continuous orientation optimization [161][162]. A major challenge lies in multi-build direction AM, where the part is printed in multiple directions [163][164][165][166], and material properties in each building area would be different. Even though multi-material topology optimization [55][56] can readily solve this problem, how to customize the algorithm to facilitate the AM process planning remains a tough problem.

Investigation on the raster direction optimization is less focused since the raster direction-dependent material anisotropy is mainly for the filament extrusion-based process. Smith and Hoglund [167] explored the raster direction optimization and realized the optimized printing paths into real parts. However, a limitation is that the raster directions are treated as discrete orientation variables without considering the tool path continuity. Liu and Yu [168] performed the concurrent raster direction and topology optimization by building continuous contour-offset tool paths. In the same work, continuous tool path design for fixed geometry problems was also addressed, and the limitations of treating the raster directions as discrete variables were revealed, i.e., the sharp path turnings reduce both the printing efficiency and quality. Recently, Dapogny et al. [169] performed an even more thorough study on the tool path-integrated topology optimization where a couple of tool

23

path patterns were comparatively evaluated, and the full sensitivity result is given other than the simplified version in [170]. In this research, the material antistrophic feature in different AM methods will be further explored, and several new AM oriented algorithms will be proposed.

**2.3.2. Geometry issues**

**2.3.2.1. Feature length scale control**

The length scale control has been a long-lasting issue in topology optimization [171], because constraining sizes of the structural members in topology designs is meaningful to improve the design manufacturability [172]. Under the density-based topology optimization framework, the early method was developed by constraining monotonic density variations, where minimum length scale requirements on both the component and void phases had been addressed [173]. Then, density filtering plus Heaviside projection emerged as a popular approach [174] in achieving the minimum component length scale control, and in a following work [175], the length scale control of both the component and void phases had been realized through a modified double Heaviside projection. Morphology based density filters were developed by Sigmund [176], and through flexible combinations of these filters, both single-phase and double-phase minimum length scale control effects have been realized. Later, a robust topology optimization algorithm [177][178][179] was developed based on these morphology-based filters, wherein the worst case scenario was optimized by simultaneously evaluating multiple design realizations. Zhou et al. [180] developed the explicit constraint formulations for the minimum length scale control of both material and void phases to reduce the computational cost of the robust formulation. Other than the minimum length scale control, Guest et al. [181] realized the maximum component length scale control by restricting any circular

areas that have the diameters of the maximum length scale target not fully filled. Zhang et al. [182] developed a structural skeleton-based approach to simultaneously constrain the maximum and minimum component length scales. The method proposed in [175] was further developed to concurrently constrain the maximum and minimum length scales of both phases. Very recently, an interesting idea was explored in [183] to relieve the stress concentrations through length scale control.

### 2.3.2.2. Non-enclosed voids

Another important constraint is enclosed voids, since the existence of enclosed voids implies that there is no way to get the unmelted powders and inner supports out of these voids after the part is completed [184][185][186][187][188][189][190] by the AM techniques, e.g., SLM, SLA, laser and electron-beam powder bed fusion, binder jetting, etc. Establishing void connectivity is an approach to resolving enclosed voids. Succinctly expressed, imposing the connectivity of voids is akin to treating the outside of the structure as a 'void' and ensuring all internal voids are connected to it. Imposing a constraint on enclosed voids can be done through the Virtual Temperature Method (VTM) described by Liu et al. [192] and Li et al. [193]. The VTM is inspired by heat transfer concepts and treats all enclosed cavities as heat sources, while the solid parts around the cavities are treated as insulators. They applied the enclosed void constraint in the optimization of torsional cantilevers. They also optimized and printed the cantilever without the constraint, resulting in the retention of internal support structures and powder as revealed in the sectioned cantilever. However, with the inclusion of the enclosed void constraint, the optimized structure ensured that the internal void was connected to the 'outer void' guaranteeing the removal of internal support structures and powder. Moreover, the elimination of enclosed voids in a structure is also required in casting, cutting, and some other manufacturing

25

processes. Xia et al. [194] proposed a novel level-set method to forcibly reduce the appearance of inner voids. Gersborg and Andreasen [195] implicitly involved a connectivity constraint by using a Heaviside design parameterization. Currently, the enclosed void issue could be successfully solved by aforementioned works.

### 2.3.3. Support issues

For many AM processes, supports are needed to ensure the successful fabrication of the large overhang areas. Printing the support will greatly increase the manufacturing time and requires extra post-processing to remove the support. The support material may be inaccessible, and extra weight will be added to the final AM part in an undesirable manner. Although using dissolvable materials for support structures can somewhat solve the problem [196], it is still a challenging issue in many cases, especially for those manufacturing processes that can only handle single material, such as metal AM. Therefore, it is important to design slimmed support or structure that without support requirement [151].

### 2.3.3.1. Support structure design

Currently, several structural patterns have been adopted to realize the support slimming, including the sloping wall structure [197], tree-like structure [198][199], bridge-like scaffold [200], and repetitive cellular structures [201][202], which form lightweight support subjected to the well-defined part geometry and build direction. In contrast to these fixed geometry support patterns, methods that deal with the support structure as the target structure for optimization where the performance of the part is maintained are also found [203][204][205]. Hu et al. [206] developed a shape optimization-based support slimming method, which slimmed the support by varying the part shape. Optimization of the build direction would also effectively reduce the support material consumption [207]. An

orientation optimization framework that considers multiple factors in optimization was investigated in [208][209], where the optimizer is constructed by a training and learning approach. For topology optimization, work was conducted by [210], which transformed the part design into a multi-objective topology optimization problem. A balanced objective function was proposed by concurrently considering the support material volume and structural compliance.

## 2.3.3.2. Optimal build orientation

The build orientation in AM has a significant influence on both the final printed components and the corresponding support structures [211][212][213]. The spatial orientation of a part plays a crucial role in determining the resulting overhang areas located above the substrate. Consequently, the fabrication process necessitates varying volumes of support structures to accommodate these distinct overhang areas.

Zhang et al. [214] developed a perceptual model to identify the optimal printing directions that effectively preserve crucial visual features. Similarly, Hu et al. [215] proposed a method to enhance self-support ability by optimizing both the orientation of an original model and the model itself. Additionally, Zhang et al. [216] presented a multi-part orientation optimization approach utilizing a genetic algorithm, which strives to achieve minimal total build time and cost on a global scale.
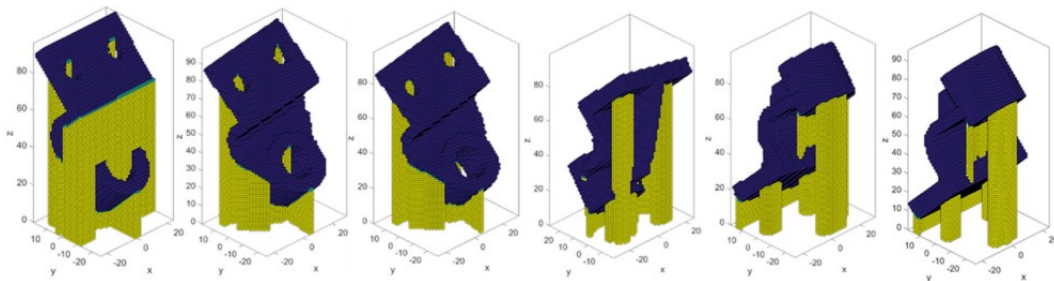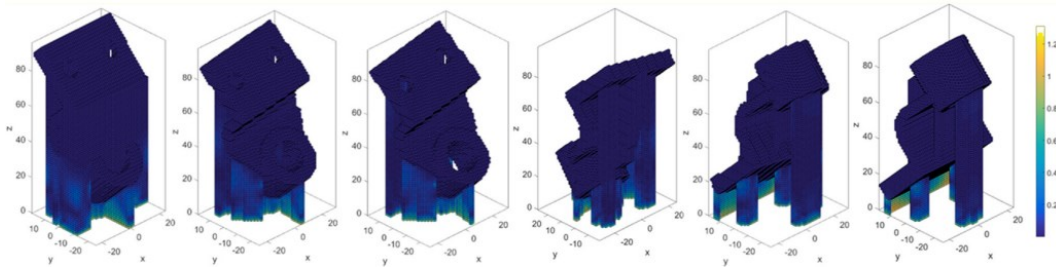
Figure 9. Top line: Optimal results for bear bracket with different weight factors. Bot line: Normalized residual stress results for bear bracket with different weight factors. [218].

Furthermore, the optimization of support structures holds significance as it serves to minimize both material consumption and printing time [217]. Cheng and To [218] proposed a method to minimize the residual stress and support volume by optimizing the build orientation as shown in Figure 9. More information on the build orientation optimization is referred to [212], which provided a comprehensive review of the optimal build direction in AM and how the orientation influences part quality, surface quality, support structure, build time, manufacturing cost, and mechanical properties.

### 2.3.3.3. Self-support structure design

A more appealing topic is developing the overhang-free topology optimization, i.e., the complete removal of support structures. Here, the overhang-free indicates that all overhang angles are larger than the minimum self-supporting angle (usually choosing as 45°). A variety of solutions have been developed to design self-support and topologically optimized structures [219][220][221][222]. The AM filter proposed by Langelaar [223][224] and the front propagation-based overhang filter proposed by van de Ven et al. [225] are used to achieve self-supporting structures. Gaynor et al. used an overhang projection scheme to design a structure with the minimum allowable self-supporting angle [226][227]. Qian [228] proposed a constraint by a Heaviside projection based integral of

density gradient to control the undercut or the overhang angle for the optimized structure. Wu et al. used rhombic structures to design self-support infill structure [229], and Liu et al. developed an overhang constraint based on the AM filter to design infill structures without the use of support material [230]. Leary et al. developed a post-processing method by adding extra structure members to a topology optimized design such that the final structure is self-supporting [231].

### 2.3.4. Manufacturing process issues

Since LPBF has better manufacturing accuracy which makes it suitable for the fine-scale structures from topology optimization. Hence, LPBF is majorly focused on the current study. With LPBF, a high-power beam (either laser beam or electron beam) selectively melts and fuses the metal powders to form the 3D geometric object. However, during the manufacturing process of LPBF, metal powders are rapidly heated and cooled down, leading to sharp thermal gradients and thus residual stresses. Consequently, severe defects such as cracks and distortion may reduce the manufacturing process stability and the part quality [232][233]. Therefore, it is important to consider the manufacturing process during topology optimization.

### 2.3.4.1. Part geometry

Currently, topology optimization addressing residual stress-induced defects is less focused due to the lack of efficient solvers to simulate the manufacturing process. For the few works addressing the residual stress or distortion constraint, Wildman et al. [234] proposed a SIMP-based topology optimization method to minimize the mean compliance and the part distortion, wherein a thermo-elastic element-birth model is adopted to simulate the AM process. Allaire and Lukas [235] developed a layer-by-layer thermo-elastic model for the process simulation and incorporated it with LSTO to constrain the structural thermal

residual stress. Reasonable results have been achieved using the above approaches. However, when extended to practical 3D problems, the above methods will involve computationally intensive transient thermo-mechanical analysis with a very fine mesh (related to the laser spot size) and a large number of load steps (related to the manufacturing time), which make the iterative finite element analysis for topology optimization computationally unaffordable. Hence, ISM, as a simplified AM process simulation solver, has been highly concentrated in topology optimization recently. Yasin et al. [236] investigated the minimization of process-induced warpage in a protector cover using topology optimization. Their results demonstrated a significant reduction in warpage for the printed product, indicating the effectiveness of their approach. Miki and Yamada [237] developed an analytical solution that accounts for distortion in the topology optimization process. They utilized a two-dimensional design model to validate their methodology, providing further insights into incorporating deformation considerations. Takezawa et al. [238][239] further explored the integration of ISM into a homogenization-based topology optimization model, enabling the design of variable density lattice structures that effectively limit process-induced deformation.

### 2.3.4.2. Support geometry

It was observed that the support structures for LPBF parts could dissipate the heat and thus could prevent severe defects by the thermal effect of laser irradiation. Therefore, a reasonable support material distribution is of great help to improve the fabrication quality of parts. From the viewpoint of design for AM, it is an excellent solution to consider the LPBF process characteristics during topology optimization of the support structure.

Cheng et al. [218][240] proposed a multi-scale lattice optimization method to design support structures for LPBF part, which could restrict the maximum residual stress below

the yield strength. Zhou et al. [citation here] presented a topology optimization approach to design support structures with the efficient thermal conduction capability for LPBF. Zhang et al. [26] proposed a support structure design method using parallel computing topology optimization based on the ISM, as illustrated in Figure 10. Their findings indicated that the deflection of printed cantilevers could be reduced by more than 60% compared to the support structures provided by the conventional design. Pellens et al. [241] adopted an adapted stiffness tensor formulation based on a surrogate model to control the residual distortions of LPBF printed parts by adding extra lattice type support structures.

Several studies have specifically focused on incorporating in-process residual stresses and/or deformations into topology optimization, considering both the support structure and the entire part geometry. In the context of designing process-tailored self-supported structures, Xu et al. [242] proposed an ISM-based residual stress-constrained self-support topology optimization approach. Misiun et al. [243] addressed recoater collision and part deformation constraints in their optimization approach for the cantilever geometry. By considering these constraints, they aimed to optimize the design while mitigating issues related to recoater collision and part deformation.
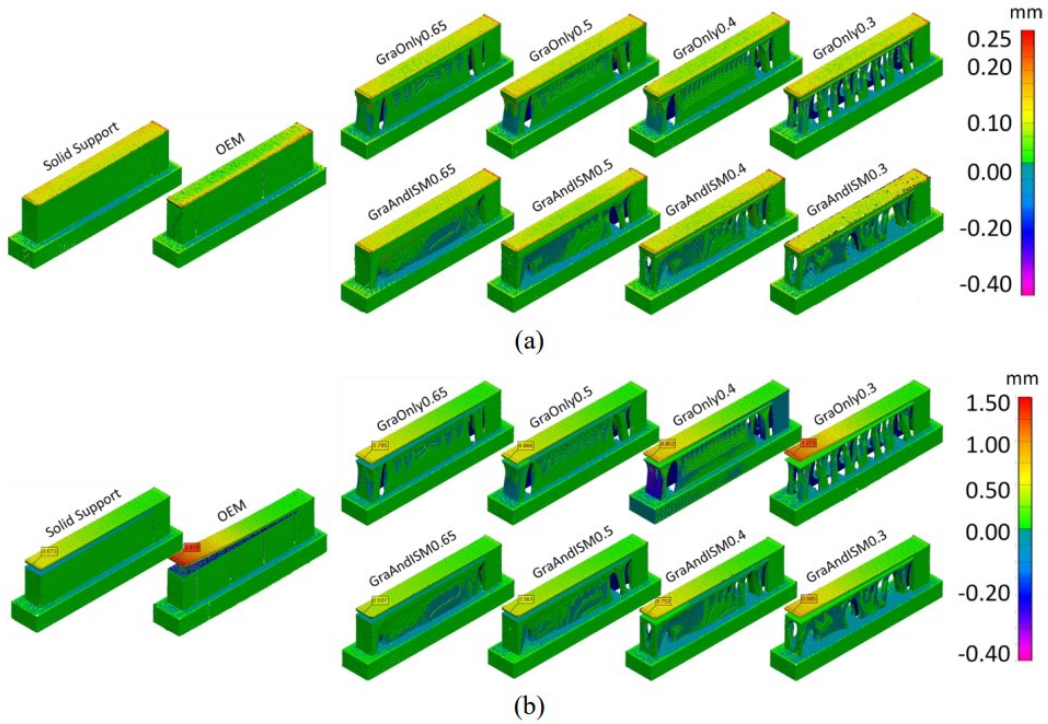
Figure 10. Support topology optimization results designed by Zhang et al. [26] considering the LPBF process to reduce part deflection. The Coordinate Measuring Machine results of the printed cantilevers for the distortion in the z-direction, (a) before cutting, (b) after cutting.

### 2.3.4.3. Laser scanning path

In addition to the consideration of process-induced residual stresses in topology optimization using ISM or its variants, researchers have also explored the impact of laser scanning patterns. The thermal stress distribution around the molten pool is found anisotropic, and a larger thermal stress component is produced along the laser scanning direction [244][245][246][247][248][249]. Based on this characteristic, Chen et al. [250] and Xu et al. [251] investigated the optimization of hatching orientation and the utilization of an island scanning strategy, respectively. They combined these approaches with ISM for the residual stress prediction to mitigate both in-situ and ex-situ deformations.

More recently, to account for the synergistic effect of these two optimizations (part

geometry and processing parameters), Takizawa et al. [252] developed a method to simultaneously optimize the hatching orientation and lattice density distribution to reduce the residual warpage of the metal AM component after cutting-off from the platen. This simultaneous optimization further reduced the residual warpage in comparison with single-factor optimization.

# Chapter 3. Basic topology optimization framework for AM

## 3.1. Topology optimization model formulation

Generally, the Topology optimization problem involves the division of a domain $\Omega$ into two distinct regions: the 'design domain' $(\Omega_d)$, subject to modifications throughout the optimization process, and the 'passive domain' $(\Omega_p)$, which remains unchanged. The inclusion of the passive domain ensures the compliance of specific regions in the final design with geometrical or process specifications, thereby preserving their solid or void characteristics. The primary objective of topology optimization is to determine the optimal distribution of one or more materials, given their limited availability, within the design domain $\Omega_d$. In essence, the aim is to identify the domain $\Omega_s \subseteq \Omega_d$ occupied by the solid material. This objective can be formulated as a non-linear programming problem:

$$
\begin{cases}
\underset{\boldsymbol{\rho}(\boldsymbol{\mu}), \mathbf{u}(\boldsymbol{\mu})}{\text{minimize}} : g_0(\boldsymbol{\rho}, \mathbf{u}) \\
\text{subject to:} \begin{cases}
R(\boldsymbol{\rho}, \mathbf{u}) = 0 \\
g_i(\boldsymbol{\rho}, \mathbf{u}) = 0 \quad i \in N_{eq} \\
g_j(\boldsymbol{\rho}, \mathbf{u}) \leq 0 \quad j \in N_{Noneq} \\
\boldsymbol{\rho}(\boldsymbol{\mu}) \in [0,1] \\
\mathbf{u}(\boldsymbol{\mu}) \in U
\end{cases}
\end{cases}
\tag{3.1}
$$

In this problem, the optimization variables are represented by $\boldsymbol{\mu}$, and we consider two fields within the domain $\Omega$ for $\boldsymbol{\mu} \in \Omega$: (1) The control field $\boldsymbol{\rho} = \boldsymbol{\rho}(\boldsymbol{\mu})$ is utilized to define the structure, specifically the domain $\Omega_s$. In structural applications, $\boldsymbol{\rho}$ is commonly interpreted as a 'relative density'. It should be noted that this relative density might not necessarily correspond to the physical density of the solid material, as the latter may depend on $\boldsymbol{\rho}$ itself when considering factors such as inertial forces and self-weight. (2) The field of state variables $\mathbf{u} = \mathbf{u}(\boldsymbol{\mu})$ represents the variables that satisfy the governing and coupling equations associated with different systems. These equations dictate the behavior and interrelationship of the state variables within the given system. For example,

34

**u** can represent the temperature, displacements, or the velocity field for a thermal, mechanical, or fluid system, respectively. For multi-physics applications, we clearly have the state variables from each physics, satisfying the corresponding governing and coupling equations.

The two fields mentioned above are generally coupled through a generally nonlinear relationship $R(\boldsymbol{\rho}, \mathbf{u}) = 0$, which arises from the set of PDEs governing the equilibrium of the system. This set of equations is typically discretized and solved using FEM or other numerical methods. The objective $g_0(\boldsymbol{\rho}, \mathbf{u})$ is the index used to measure the performance of the current design, and the equality/inequality constraints $g_i(\boldsymbol{\rho}, \mathbf{u}) = 0$ and $g_j(\boldsymbol{\rho}, \mathbf{u}) \leq 0$ prescribe behavioural requirements on the design.

### 3.1.1. Material interpolation

The parameterization of $R(\boldsymbol{\rho}, \mathbf{u})$ makes Eq. (3.1) to be an integer optimization problem. In each point within the design domain $\Omega_d$, two possibilities arise: either there exists material ($\rho(\mu) = 1$), or there is an absence of material ($\rho(\mu) = 0$). Earlier research works conducted by Beckers et al. [253][254], as well as more recent contributions [255][256][257], have successfully solved basic instances of Eq. (3.1) through the integer programming. However, this approach becomes impractical as the count of design variables increases and considered nonlinear constraints. Consequently, Eq. (3.1) has been transformed into a continuous optimization problem. This is achieved by allowing the relative density to assume any value within the range of $\rho(\mu) \in [0,1]$ for $\mu \in \Omega$, and utilizing this range to interpolate the material properties that govern the physical response. As an illustrative method, the SIMP method [258][259] employs interpolation for Young's modulus as expressed by

$$E_e(\rho(\mu)) = E_{min} + (E_0 - E_{min})\rho(\mu)^p \tag{3.2}$$

where $E_0$ is the value on the solid $(\rho(\mu) = 1)$, and $E_{min} \ll E_0$ that of the material mimicking void $(\rho(\mu) = 0)$. The penalization factor $p > 1$ promotes discrete solutions to the optimization problem, as intermediate values $\rho \in (0, 1)$ become uneconomical when $p$ is raised, due to the linear increase of the mass, and the sublinear increase of the stiffness.

The SIMP-interpolated elasticity tensor can find practical application as the effective tensor for an isotropic porous material. In fact, Bendsøe and Sigmund [260] demonstrated that, when the Poisson ratio $(\nu)$ equals 0.3, the bulk and shear moduli associated with a SIMP interpolation with $p \geq 3$ fall within the Hashin-Strickman bounds [261], both in 2D and 3D scenarios. The SIMP method stands out as the most widely adopted interpolation technique for compliance minimization. Furthermore, SIMP-like stress interpolations, rooted in physical principles from a homogenization perspective, have been devised by Duysinx and Bendsøe [262] and by Lipton [263].



(a)                                                              (b)
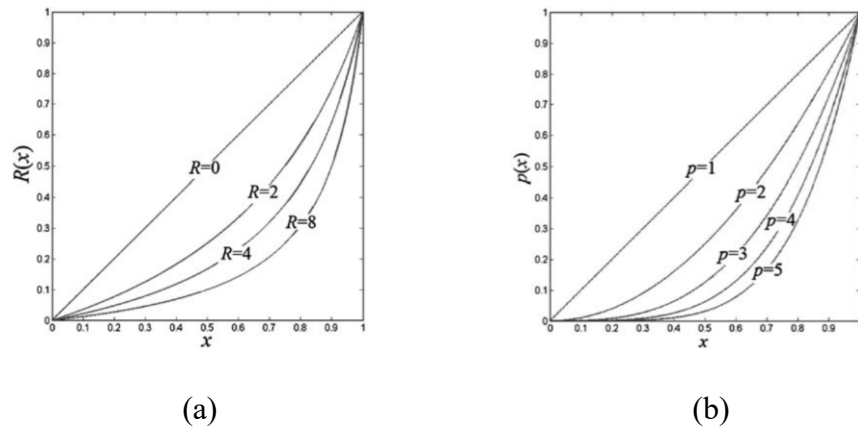
Figure 11. SIMP and RAMP interpolation functions: (a) Curves of RAMP [266] and (b) Curves of SIMP [260].

However, there are alternative approaches that might demonstrate superior performance in specific applications [264][265]. Among these, it is worth noting the Rational Approximation of Material Properties (RAMP) [266], which was designed to retain the concave characteristics of the problem while providing a non-zero derivative at/near

$\rho(\mu) = 0$:

$$E_e(\rho(\mu)) = E_{min} + \frac{(E_0 - E_{min})\rho(\mu)}{1 + K(1 - \rho(\mu))} \tag{3.3}$$

where K are RAMP penalization parameters. This interpolation strategy yields remarkable results in design-dependent problems. The interpolation curves for RAMP and SIMP are shown in Figure 11. Interpolation methods based on other available bounds for effective properties of mixtures, such as the Reuss-Voigt bounds, have been proposed in [267][268]. Using the SIMP relaxation, the problem described in Eq. (3.1) transforms into a continuous optimization problem, amenable to gradient-based optimization techniques. These methods will be introduced in the subsequent chapter.

### 3.1.2. Problem regularization

Without the incorporation of any regularization, the fundamental topology optimization problem remains unsolvable even within the continuous framework, as evidenced by Lurie [269]. Also, the mesh dependency of the discretized solutions is also an important issue. The optimized design obtained from without regularization qualitatively changes when refining the mesh, which first acknowledged by KenoTung, Olhoff and Cheng [270][271].

A survey on numerical instabilities appearing in topology optimization can be found in Sigmund and Peterson [272], whereas Diaz and Sigmund [273] explained another spurious effect: the formation of checkerboard patterns in the optimized design. This originates from the use of low order finite elements and can be cured by choosing higher orders for the discretization of the state and control fields (**u** and $\boldsymbol{\rho}$), as discussed by Jog and Haber [274]. Alternative approaches, using node-based discretization of the $\boldsymbol{\rho}$ field also fall in the framework of Jog and Haber, as they cure the phenomenon only for some choices of the discretization orders [275][276]. To avoid mesh-dependency of solutions, first methods

were based on explicitly constraining the oscillations of the density field [277][278], thus avoiding designs with infinitely many, infinitely small holes [277]. The existence of solutions to the topology optimization problem with total variation regularization was proven by Ambrosio et al. [279] and Petersson [280], as well as their mesh-independency by Sigmund and Petersson [281].

Nowadays, the most used regularization approach, not requiring additional constraints or penalization terms, is based on domain filters. First introduced by Sigmund in the context of compliance minimization problems [282], sensitivity filtering of the objective function. This has proven to avoid checkerboards and mesh-dependency in several applications, and Sigmund and Maute [283] have interpreted the sensitivity filtered minimum compliance problem, as the minimization of a non-local elasticity problem. Another method, commonly named 'density filter' [282][284] relies on introducing an additional field which has the form:

$$\tilde{\mu}_e = \frac{1}{\sum_{i \in N_e} H_{ei}} \sum_{i \in N_e} H_{ei} \, \mu_i \tag{3.4}$$

where $N_e$ is the set of elements i for which the center-to-center distance $\Delta(e, i)$ to element e is smaller than the filter radius $r_{min}$, and $H_{ei}$ is a weighting factor defined as:

$$H_{ei} = \max{(0, r_{min} - \Delta(e, i))} \tag{3.5}$$

such that $\mu \in [0, 1]$ becomes the field interpolating the material properties, whereas $\mu$ is just the auxiliary variable updated by the optimizer. The existence of solutions to the compliance minimization problem, regularized by the density filtering was proven by Bourdin [285]. A similar regularization effect given by Eq. (3.4) can be obtained by applying a PDE-based smoothing [286][287] such that the regularized field $\rho(\mu)$ is the solution to the Helmholtz problem, equipped with Neumann-like boundary conditions.

Linear filtering methods naturally promote grayscales (i.e., transition regions between solid and voids), which is a drawback from the manufacturing point of view. Such grayscales can be eliminated in a post-processing phase, by projecting the design to a discrete 0/1 material distribution. The most popular method is to adopt the density projection. This consists of applying a smooth approximation of the Heaviside function to the filtered field $\tilde{\mu}_e$, to obtain a more discrete density field $\bar{\mu}_e$. Projection was first applied to topology optimization by Guest et al. [288], referring to an idea first introduced in [289], obtaining the relative density as:

$$\bar{\tilde{\mu}}_e = 1 - e^{-\beta\tilde{\mu}_e} + \tilde{\mu}_e e^{-\beta} \tag{3.6}$$

where $\beta$ is a parameter governing the curvature of the approximation at $\rho = 0$. When Eq. (3.6) is applied on top of density filtering, and $\beta$ is large enough, the minimum length scale $r_{min}$ is implicitly imposed on the solid regions. However, this kind of implementation sometimes does not work well in some problems. A more general expression, called tanh-projection, is thus introduced [290]:

$$\bar{\tilde{\mu}}_e = \frac{\tanh(\beta\eta) + \tanh\left(\beta(\tilde{\mu}_e - \eta)\right)}{\tanh(\beta\eta) + \tanh\left(\beta(1 - \eta)\right)} \tag{3.7}$$

where a threshold $\eta \in [0, 1]$ defines the saddle point of the Heaviside approximation.

### 3.1.3. Aggregation method for maximum inequality constraints

Another noteworthy aspect is that, in many optimization problems, there are various types of maximum constraints, such as maximum stress, maximum displacement, maximum volume fraction, and so forth. Ideally, when utilizing Finite Element Method (FEM), each design unit should be subject to its corresponding stress constraint, leading to a substantial number of constraints. As a result, the computation of sensitivities, whether through direct or adjoint methods, becomes prohibitively expensive. This significant number of

constraints can be reformulated in the context of a single maximum constraint, as demonstrated by:

$$\psi_{max} = \max(\forall \psi_e) \leq \psi_Y \tag{3.8}$$

where $\psi_Y$ is the maximum value limit. However, the maximum function $\max(*)$ is not differentiable. A preferred approach is to use clustering functions to build a single global function that effectively quantifies the maximum value, for example, the P-norm function:

$$\psi_{PN} = \left( \sum_{e=1}^{Nel} (\psi_e)^P \right)^{\frac{1}{P}} \leq \psi_Y \tag{3.9}$$

where $\psi_{PN}$ is the global P-norm measure, $P$ is the aggregation parameter, and $Nel$ is the total number of elements. Note that the P-norm approaches the maximum value $\psi_{max}$ when $P \to \infty$. However, a large $P$ value tends to make the stress constrained problem ill-conditioned. Relatively small $P$ value is preferred in practice given the convergence stability which, however, leads to the gap between the exact and approximated maximum values. Consequently, the maximum value constrained optimization result is conservative. Therefore, to better approximate the maximum value without overly increasing the $P$ value, the global P-norm value measure is iteratively corrected through:

$$\overline{\psi}_{PN} = c \cdot \psi_{PN} \leq \psi_Y \tag{3.10}$$

where $c$ is the correction parameter at the $I^{th}$ iteration $(I > 1)$ that reflects the ratio of the real maximum value to the P-norm measured value from the current iteration. Note that the change of $c$ would be jumping if only taking the history-independent ratio to make the correction, causing oscillations and instabilities of the convergence. To address this issue, a parameter $\alpha^I$ $(\alpha^I \in (0,1])$ is added to restrict the variation between $c^I$ and $c^{I-1}$, as demonstrated by:

$$c^I = \alpha^I \cdot \frac{\max(\forall \psi_e)}{\psi_{PN}^I} + (1 - \alpha^I) \cdot c^{I-1} \tag{3.11}$$

In this work, $\alpha^I = 0.5$ is adopted for all iterations and $c^0 = 1$ is used. Note that the set of local value constraints in Eq. (3.8) is equivalent to a constraint on the maximum local value by:

$$\widehat{\psi}_{PN} = \frac{\overline{\psi}_{PN}}{\psi_Y} \leq 1 \tag{3.12}$$

where

$$\widehat{\psi}_{PN} = c \cdot \left( \sum_{e=1}^{Nel} \left( \frac{\psi_e}{\psi_Y} \right)^P \right)^{\frac{1}{P}} \leq 1 \tag{3.13}$$

## 3.2. Optimization model solution

By observing Eq. (3.1), it can be seen that the topology optimization problem is essentially a mathematical programming problem. Therefore, some well-established solution methods are used in mathematical programming to solve topology optimization problems. It is necessary to introduce a famous and widely used optimization algorithm –Give full name here (MMA) [291]. The objective and constraint functions may usually be implicit functions, so MMA uses the information of the current $k^{th}$ iteration ($k = 0, 1, 2, ...$) to rebuild explicit functions for approximating original functions, which is expressed in Eq. (3.14). The information includes sublimit of the variable $x_i$, which are $L_i^{(k)}$ and $U_i^{(k)}$, point position $x(k)$, function values $f_i(x(k))$, and gradients $\frac{\partial g_j^{(k)}}{\partial x_i}$ at $x = x(k)$. In addition, $k$ is the iteration number, and when it is equal to zero, it means that one uses the initial point to build explicit functions. The value of $k$ depends on how many iterations are needed to yield the optimal solution. $L_i^{(k)}$ and $U_i^{(k)}$ are known as moving asymptotes, which are normally changed between iterations.

41

Write something here to mention the following equation.

$$g_j^{(k)}(\mathbf{x}) = r_j^{(k)} + \sum_{i=1}^{n} \left( \frac{p_{ij}^{(k)}}{U_i^{(k)} - x_i} + \frac{q_{ij}^{(k)}}{x_i - L_i^{(k)}} \right), \quad j \in I \tag{3.14}$$

where

$$p_{ij}^{(k)} = \begin{cases} \left(U_i^{(k)} - x_i^{(k)}\right)^2 \dfrac{\partial g_j^{(k)}}{\partial x_i}, & \text{if } \dfrac{\partial g_j^{(k)}}{\partial x_i} > 0 \\[2em] 0, & \text{if } \dfrac{\partial g_j^{(k)}}{\partial x_i} \le 0 \end{cases} \tag{3.15}$$

$$q_{ij}^{(k)} = \begin{cases} 0, & \text{if } \dfrac{\partial g_j^{(k)}}{\partial x_i} \ge 0 \\[2em] -\left(x_i^{(k)} - L_i^{(k)}\right)^2 \dfrac{\partial g_j^{(k)}}{\partial x_i}, & \text{if } \dfrac{\partial g_j^{(k)}}{\partial x_i} < 0 \end{cases} \tag{3.16}$$

$$r_j^{(k)} = g_j^{(k)}(\mathbf{x}) - \sum_{i=1}^{n} \left( \frac{p_{ij}^{(k)}}{U_i^{(k)} - x_i} + \frac{q_{ij}^{(k)}}{x_i - L_i^{(k)}} \right), \quad j \in I \tag{3.17}$$

The whole MMA optimization process is illustrated in Figure 12.
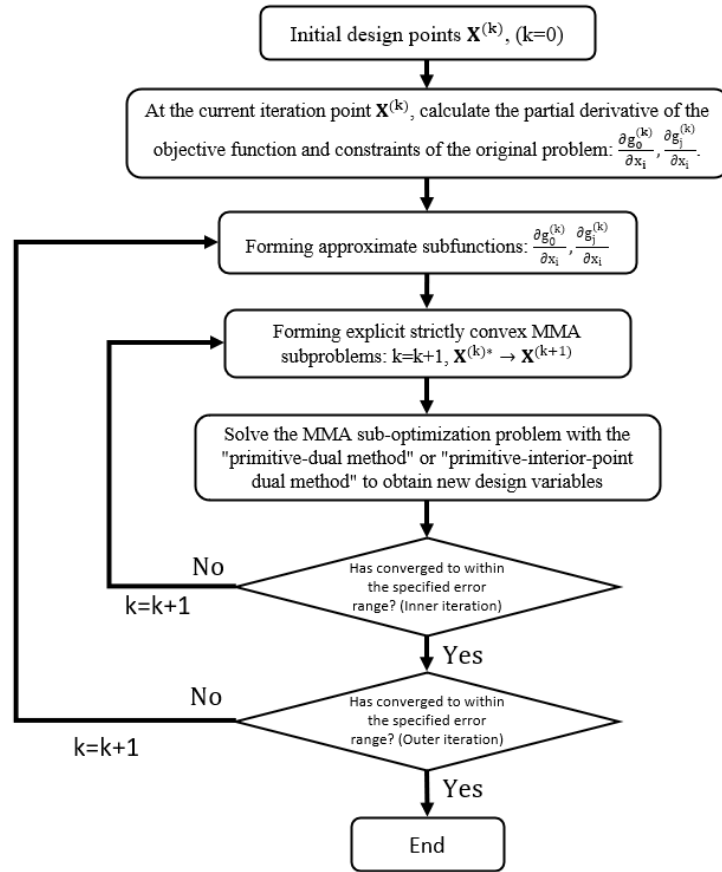
Figure 12. MMA optimization process.

## 3.3. Adjoint sensitivity analysis

Since the MMA approach will be employed to address the optimization problem, which necessitates access to first-order sensitivity information for both the constraints and objective function. It is important to note that sensitivity analysis does not have to be a complex and custom process for each problem type. In general, the adjoint method is commonly used for conducting sensitivity analysis. The derivation process is rather straightforward, achieved by representing the system of equations, whether they are uncoupled, weakly coupled, or strongly coupled, as a common residual:

$$\mathbf{R} = \mathbf{Au} - \mathbf{b} = 0 \tag{3.18}$$

where **A** is the system coefficient matrix, **u** is the vector of all state variables and **b** is the forcing vector. To find the derivatives of a given functional $g_0$, the Lagrangian L is defined as:

$$L = g_0 + \boldsymbol{\lambda}^T \mathbf{R} \tag{3.19}$$

where $\boldsymbol{\lambda}$ is the vector of adjoint variables. The total derivative with respect to a design variable $\rho_e$ is then taken of the Lagrangian:

$$\frac{dL}{d\rho_e} = \frac{dg_0}{d\rho_e} + \boldsymbol{\lambda}^T \frac{d\mathbf{R}}{d\rho_e} \tag{3.20}$$

where the total derivative is given by:

$$\frac{dg_0}{d\rho_e} = \frac{\partial g_0}{\partial \rho_e} + \frac{\partial g_0}{\partial \mathbf{u}} \frac{\partial \mathbf{u}}{\partial \rho_e} \tag{3.21}$$

due to the implicit dependence of $g_0$ on the state field. Expanding the total derivative of the Lagrangian gives:

$$\frac{dL}{d\rho_e} = \frac{\partial g_0}{\partial \rho_e} + \frac{\partial g_0}{\partial \mathbf{u}} \frac{\partial \mathbf{u}}{\partial \rho_e} + \boldsymbol{\lambda}^T \left( \frac{\partial \mathbf{R}}{\partial \rho_e} + \frac{\partial \mathbf{R}}{\partial \mathbf{u}} \frac{\partial \mathbf{u}}{\partial \rho_e} \right) \tag{3.22}$$

which can be rewritten to:

$$\frac{dL}{d\rho_e} = \frac{\partial g_0}{\partial \rho_e} + \boldsymbol{\lambda}^T \frac{\partial \mathbf{R}}{\partial \rho_e} + \left( \frac{\partial g_0}{\partial \mathbf{u}} + \boldsymbol{\lambda}^T \frac{\partial \mathbf{R}}{\partial \mathbf{u}} \right) \frac{\partial \mathbf{u}}{\partial \rho_e} \tag{3.23}$$

by collecting the terms multiplied by the derivative of the state field. The adjoint problem is then defined as what is inside the brackets:

$$\frac{\partial g_0}{\partial \mathbf{u}} = -\boldsymbol{\lambda}^T \frac{\partial \mathbf{R}}{\partial \mathbf{u}} \tag{3.24}$$

When $\boldsymbol{\lambda}$ is the solution to the adjoint problem, the terms inside the brackets become zero, and it is avoided to compute the design sensitivities of the state field:

$$\frac{dL}{d\rho_e} = \frac{\partial g_0}{\partial \rho_e} + \boldsymbol{\lambda}^T \frac{\partial \mathbf{R}}{\partial \rho_e} \tag{3.25}$$

44

Since the state solution will be updated after a design change to make the residual equal to zero, the total derivative of the residual with respect to the design variable is equal to zero. Thus, the total derivative of the Lagrangian will be equal to that of the functional and Eq. (3.21) gives:

$$\frac{dL}{d\rho_e} = \frac{dg_0}{d\rho_e} \qquad (3.26)$$

Thus, final sensitivities of the given functional can be calculated by

$$\frac{dg_0}{d\rho_e} = \frac{\partial g_0}{\partial \rho_e} + \boldsymbol{\lambda}^T \frac{\partial \mathbf{R}}{\partial \rho_e} \qquad (3.27)$$

The above result is valid for almost all the systems of equations.

As discussed above, through step-by-step iterations, the optimal solution may be found; however, this process may need many repetitions. This inherently iterative character of the topology optimization process should require fast simulation at each iteration; otherwise, the total computational time could be unacceptable. Therefore, if the AM process is taken into consideration during topology optimization, the computational time of the AM-process simulation should be fast enough.

### 3.4. Solutions to some important additive manufacturing issues

### 3.4.1. Minimum length size control

It is desirable that a topologically optimized design can be fabricated reliably by a certain manufacturing process. To fulfill the requirement for manufacturing, one recent trend is to directly consider the manufacturing characteristics in the optimization process, i.e. to achieve the minimum length scale on the optimized design and thus ensure prototype manufacturability. In AM, if this condition is not satisfied, holes or disconnected parts may appear in the prototype. Another example is the design of compliant mechanisms, for

which achieving minimum length scale is crucial to avoid the tiny-hinges at structural joints.

To prevent this phenomenon, the simplified robust formulation is used to ensure a minimum length scale of the structure, which is to consider both the erosion projection ($\eta_{ero} > 0.5$) and the intermediate projection ($\eta = 0.5$) by a robust formulation. In the case of compliance minimization, the density field associated with erosion projection uses the least number of materials and has a higher compliance value compared with the intermediate projection. Therefore, including both the intermediate and eroded projections into the objective function indeed takes the effect of the minimum length scale control. In addition to the base region $\boldsymbol{\mu}$, the filtered field $\widetilde{\boldsymbol{\mu}}$ is further projected to the so-called eroded fields of the base region $\overline{\widetilde{\boldsymbol{\mu}}}_{ero}$:

$$\overline{\widetilde{\boldsymbol{\mu}}}_{ero} = \frac{\tanh(\beta\eta_{ero}) + \tanh\big(\beta(\widetilde{\boldsymbol{\mu}} - \eta_{ero})\big)}{\tanh(\beta\eta_{ero}) + \tanh\big(\beta(1 - \eta_{ero})\big)} \tag{3.28}$$

where $\eta_{ero}$ is the erosion threshold. Then, both the erosion projection field $\overline{\widetilde{\boldsymbol{\mu}}}_{ero}$ and intermediate projection field $\overline{\widetilde{\boldsymbol{\mu}}}$ will be projected by the AM filter introduced in subsection 3.2.2. Based on the SIMP scheme, the elastic module of the $e^{th}$ element for these two fields is interpolated by

$$\begin{aligned} E_e(\rho(\overline{\widetilde{\mu}}_e)) &= E_{min} + (E_0 - E_{min})\rho(\overline{\widetilde{\mu}}_e)^{\,p} \\ E_{ero,e}(\rho(\overline{\widetilde{\mu}}_{ero,e})) &= E_{min} + (E_0 - E_{min})\rho(\overline{\widetilde{\mu}}_{ero,e})^{\,p} \end{aligned} \tag{3.29}$$

Specifically, the simplified robust formulation is expressed as:

$$g_r = \omega g(\mathbf{K}, \mathbf{u}) + (1 - \omega)g(\mathbf{K}_{ero}, \mathbf{u}_{ero}) \tag{3.30}$$

where $\omega$ is a weighting factor, and the superscript ero in the second term indicates the density field obtained from the erosion projection. T denotes the transpose operator, $\mathbf{u}$ and $\mathbf{u}_{ero}$ are the response fields, $\mathbf{K}$ and $\mathbf{K}_{ero}$ are the stiffness matrices for the intermediate

and erosion projected structures. The stiffness matrices $\mathbf{K}$ and $\mathbf{K}_{ero}$ are assembled from element stiffness matrices defined by $\mathbf{k}_e = E_e(\rho(\bar{\bar{\mu}}_e))\,\mathbf{k}_0$ and $\mathbf{k}_{ero,e} = E_{ero,e}(\rho(\bar{\bar{\mu}}_{ero,e}))\,\mathbf{k}_0$, where $\mathbf{k}_0$ is the stiffness matrix of a solid element with unit Young's modulus/conductivity. In the context of the compliance minimization problem, the density field associated with erosion projection uses the least amount of material and has a higher compliance value compared with the intermediate projection. Therefore, considering the intermediate projection case into the objective function indeed ensures a length scale. Then, the formulation of the optimization problem could be modified as:

$$
\begin{aligned}
&\underset{\mathbf{u}(\boldsymbol{\mu}),\,\mathbf{u}_{ero}(\boldsymbol{\mu}),\,\boldsymbol{\rho}(\boldsymbol{\mu})}{\text{minimize}} : g_r(\boldsymbol{\rho}(\boldsymbol{\mu}),\mathbf{u},\mathbf{u}_{ero}) \\
&\text{subject to:}
\begin{cases}
R(\boldsymbol{\rho}(\boldsymbol{\mu}),\mathbf{u},\mathbf{u}_{ero}) = 0 & \\
g_i(\boldsymbol{\rho}(\boldsymbol{\mu}),\mathbf{u}) = 0 & i \in E \\
g_j(\boldsymbol{\rho}(\boldsymbol{\mu}),\mathbf{u}) \le 0 & j \in I \\
\boldsymbol{\rho}(\boldsymbol{\mu}) \in [0,1] & \\
\mathbf{u}_{ero}(\boldsymbol{\mu}),\mathbf{u}(\boldsymbol{\mu}) \in U &
\end{cases}
\end{aligned}
\tag{3.31}
$$

The erosion version density field only acts on the objective function, while for other considered constraints, only the intermediate version density field is considered. Under this formulation, the computation cost has not increased dramatically.

The combined objective function involves a weighting factor $\omega$ is an approximate approach to ensure length scale. According to our experience, a fixed small $\omega$ value may lead to a worse design, while a large $\omega$ value may lead to a structure violating the length scale. A continuation is thus applied in our test where $\omega$ is gradually decreased from 0.8 to 0.3, by a decrement of 0.1 every 50 iterations.

### 3.4.2. Self-support design by AM filter

As described in the previous chapter, addressing the issue of support structures has consistently been a focal point when designing for AM. To minimize the material usage via reducing the need for support structures, it is crucial to carefully regulate the inclination

angles of overhangs during the fabrication process. A practical approach towards achieving this goal involves the utilization of the AM filter to ensure that the final structure is self-supported.
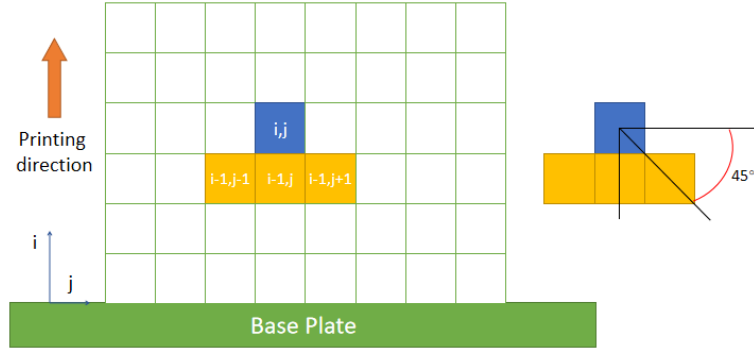


Figure 13. Schematic diagram of AM filter for 2D case.

Figure 13 shows the 2D schematic diagram for method in the AM filter, and the model is defined on a regular mesh. The elements that locate in a lower layer along the building direction with indices $(i-1,j-1)$ $(i,j-1)$ and $(i+1,j-1)$ are defined as the support region of the element $(i,j)$. If the support region has no material, the AM filter will remove the material in element $(i,j)$. Otherwise, it will appear the material in the element $(i,j)$. Finally, it could achieve the self-supporting structure with $45°$ overhang angle. The mathematical form of the AM filter is defined as follows:

$$\xi_{i,j} = \begin{cases} \min\left(\tilde{\bar{\mu}}_{i,j}, \max\left(\tilde{\bar{\mu}}_{i-1,j-1}, \tilde{\bar{\mu}}_{i,j-1}, \tilde{\bar{\mu}}_{i+1,j-1}\right)\right) & (i,j) \in \Omega_u \\ \tilde{\bar{\mu}}_{i,j} & (i,j) \in \Omega_b \end{cases} \tag{3.32}$$

where $\tilde{\bar{\mu}}$ is the projected field. The corresponding differentiable form is written by

$$\xi_{i,j} = \text{smin}\left(\tilde{\bar{\mu}}_{i,j}, \text{smax}\left(\tilde{\bar{\mu}}_{i-1,j-1}, \tilde{\bar{\mu}}_{i,j-1}, \tilde{\bar{x}}_{i+1,j-1}\right)\right) \quad (i,j) \in \Omega_u \tag{3.33}$$

where smin is defined as:

$$\text{smin}(a,b) = \frac{1}{2}\left(a + b - \sqrt{((a-b)^2 + \epsilon_s)} + \epsilon_s^2\right) \quad (i,j) \in \Omega_u \tag{3.34}$$

48

Moreover, smax is the softmax function used to calculate the maximum value of the elements in the supporting region instead of the P-Q max function in the origianl AM filter [223][224]:

$$\text{smax}(a, b, c) = \sqrt[Q]{(a^P + b^P + c^P)} \quad (i, j) \in \Omega_u \tag{3.35}$$

where $\epsilon_s = 1e - 4$ is the parameter that controls the accuracy of the approximation, $P = 40$, $Q = P + \frac{\log(3)}{\log(\frac{1}{2})}$ are used as suggested in [223][224].

**3.5. Post-processing: Converting optimized results into actual production objects.**

During topology optimization, optimization algorithms decide the distribution of solid and void material. Since the design domain has been discretized into finite elements, the boundary between material and non-material may become toothed. Thus, such a result of topology optimization with rough surfaces could not be manufactured or simulated easily. The result needs to be expressed in a more practicable CAD model.

The final elemental design variables are projected on nodes and then filtered with a radius of the element length. A threshold value that preserves the same material volume is determined for the level-set function constructed from nodal numbers. With the threshold value, smoothed representation of the topology is obtained from the contour cut of the level-set function. The structure is then reconstructed in Autodesk CAD. During this process, some detailed features could be adjusted artificially, which makes the structure more reasonable. After that, a 3D specimen model corresponding to the design in Autodesk CAD is generated by extruding the smoothed 2D representation normal to the sketch plane, and meanwhile, the detailed geometry feature will be constructed by Autodesk Inventor. Figure 14 shows the procedure of generating the part model.
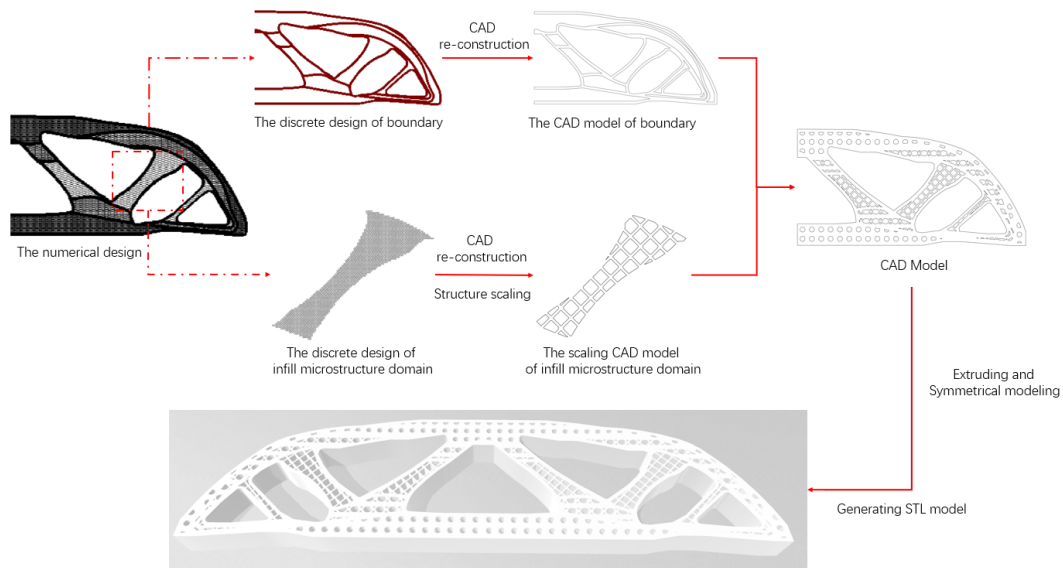
Figure 14. STL model generation procedure.

After obtaining the structure reconstructed by post-processing, the performance of the results needs to be further validated. Similarly, two methods can deal with this issue. One is to import the results into well-established commercial software to verify their structural properties, namely, numerical validation. The other method is to fabricate this structure by 3D printers, and then some mechanical tests are used to investigate its structural performance (i.e., experimental validation). Certainly, the later method is the most effective way. However, for some specific problems, the cost of conducting experiments can be very high, and it is a time-consuming process. This work therefore adopts both the numerical and experimental validations. The detailed implementation could refer to the following chapter.

### 3.6. Summery

This chapter introduces a comprehensive system involving design, optimization, simulation, and experimentation. The system comprises topology optimization, post-processing, performance simulation, and mechanical testing, serving as an integrated

solution for achieving high-performance products, expediting product enhancements, and curbing design expenses. Topology optimization emerges as a key technique for fortifying structures while minimizing the material usage, and we delve into its underlying mathematical model to enhance comprehension. Furthermore, the post-processing stage aids in bridging the gap between numerical outcomes and tangible products. Performance simulation, facilitated through FEM, empowers designers to refine their creations and gain insights into design performance prior to physical experimentation. Subsequently, experiments were conducted to validate the simulations and ascertain the efficacy of topology optimization in structural design. Notably, the structural failures predicted by simulations closely align with experimental findings.

# Chapter 4. Topology optimization for advanced AM parts design

With the emergence of various AM technologies, the field of structural design has reached new heights. From the perspective of structural optimization, the introduction of these new technologies has expanded the feasible design space while reducing constraints. This implies that we can design components with superior structural performance while ensuring manufacturability. Therefore, the effective utilization of these emerging AM technologies to design high-performance components has become a prominent research focus in the academic community. In this chapter, I will delve into the aforementioned subject matter. Taking 'improvement' as a starting point, a series of structural design methods utilizing the design freedom provided by topology optimization will be proposed. These methods will specifically target multi-material structure AM and porous infill structure AM, with the goal of maximizing the enhancement of structural performance in the designed components.

## 4.1. Stress constrained multi-material topology optimization

In this subsection, I will introduce the topology optimization method for stress-based structures design in multi-material FDM. So far, both the stress-related problem and MMTO have been extensively studied. However, there are few works addressing the SMMTO. In this subsection, a novel solution of the SMMTO problem is therefore proposed based on the ordered SIMP method. Description of the multi-material elastic model is achieved with the ordered SIMP interpolation. A novel order SIMP-like interpolation function has been proposed to realize the relaxed stress measure interpolation. At the same time, the stress measure is properly scaled to reflect the different yield limits.

### 4.1.1. Ordered SIMP interpolation for stress-based problem

Recalling the method proposed by Le et al. [84], the standard SIMP interpolation was

adopted to interpolate the elastic modulus and a SIMP-like relaxed stress definition was introduced to build the stress constraint. The specific interpolations could be expressed as follows. $\eta^E$ is used to interpolate elastic modulus $E_0$ of the solid material:

$$E = \eta^E(\mu) \cdot E_0 \tag{4.1}$$

Similarly, $\eta^S$ is introduced to interpolate the stress state $\boldsymbol{\sigma}_0 \equiv \mathbf{D}_0\mathbf{B}\mathbf{u}$, where $\mathbf{D}_0$ is the elasticity tensor of the solid material, $\mathbf{B}$ is the strain-displacement matrix, and $\mathbf{u}$ is the global displacement vector corresponding to the solid element.

$$\boldsymbol{\sigma} = \eta^S(\mu) \cdot \boldsymbol{\sigma}_0 \tag{4.2}$$

Note that $\eta^E(\mu) < \eta^S(\mu) < 1$ for $0 < \mu < 1$. In the standard SIMP interpolation, $\eta^E$ and $\eta^S$ could be expressed in a unified form:

$$\eta^x = \mu^{P_x} \tag{4.3}$$

wherein the superscript $x$ indicates the stiffness interpolation ($x = E$) or stress interpolation ($x = S$) and $P_x$ represents the interpolation penalty factor for stiffness or stress. With the standard SIMP interpolation, the discrete topology optimization problem, i.e. where $\mu \in \{0, 1\}$, is transformed to a continuous optimization problem, i.e. where $\mu \in [0, 1]$, that finalizes at a discrete design through the appropriate stiffness penalization. Note that this interpolation scheme makes no attempt to accurately represent the material behavior for intermediate density values and the ultimate goal is to achieve a white and black design through the artificial interpolation. This method has been approved as reasonable among a wide variety of studies [84][96][97].

In the present work, MMTO is focused and therefore, both the stiffness and stress interpolations need to be altered. For the elasticity tensor, the ordered SIMP like interpolation is adopted. The pseudo homogenous materials are sorted in the ascending

order of the material density $\rho_i^T$ (as depicted in Figure 15) and each material density corresponds to one type of solid material. Then, the material densities are normalized as:

$$\rho_i = \frac{\rho_i^T}{\rho_{max}}, \qquad (i = 1,2,3, \dots, \text{Mat}) \tag{4.4}$$

where $\rho_{max}$ is the maximum density among the involved materials and Mat is the total number of material phases. The ordered SIMP interpolation of the elastic modulus for the multi-material scheme is formulated as:

$$E_e = \overline{\eta^E}(\mu_e) \cdot E_{max} \tag{4.5}$$

where $\mu_e$ is the element density for the $e^{th}$ element; $E_{max}$ is the Young's modulus of the material with the highest stiffness. $\overline{\eta^E}(\mu_e)$ is the extended power function with respect to the elemental density as shown in Figure 15, and $\overline{\eta^E}(*)$ for $\mu_e \in [\rho_i, \ \rho_{i+1}]$ is given as:

$$\overline{\eta^E} = \left(\frac{\mu_e - \rho_i}{\rho_{i+1} - \rho_i}\right)^{P^E_i} \cdot \left(\frac{E_{i+1} - E_i}{E_{max}}\right) + \frac{E_i}{E_{max}} \tag{4.6}$$

where $E_i$ is the elastic modulus of the $i^{th}$ material and $P^E_i$ is the penalty value of $\overline{\eta^E}(*)$ for $\mu_e \in [\rho_i, \rho_{i+1}]$.
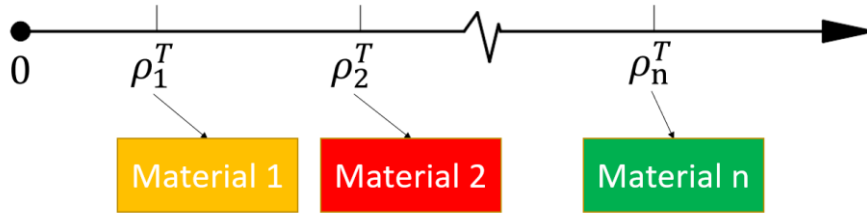


Figure 15. Illustration of the density-based material sorting.

For the $i^{th}$ material phase, the local stress constraint could be expressed as:

$$\langle \eta_i^S(\mu_e) \cdot \boldsymbol{\sigma}_0 \rangle \le \sigma_{Y,i}, \qquad (i = 1,2,3, \dots, \text{Mat}; e = 1,2,3, \dots, \text{Nel}) \tag{4.7}$$

where $\sigma_{Y,i}$ is the yield stress of the $i^{th}$ material and $\eta_i^S$ is the stress interpolation term of the $i^{th}$ material. $\langle * \rangle$ is the von Mises stress calculation operator. $\boldsymbol{\sigma}_0$ is the stress vector

54

evaluated with $E_{max}$. The bounds of $\eta_i^S$ is shown in Eq. (4.7):

$$\eta_i^S(\rho_i) = \frac{E_i}{E_{max}}, \qquad \eta_i^S(0) = 0, \tag{4.8}$$

which is consistent to the description in [84]. $\eta_i^S(0) = 0$ indicates the stress in void regions being zero and $\eta_i^S(\rho_i) = \frac{E_i}{E_{max}}$ guarantees the stress level being evaluated with the proper properties. For the sake of simplicity, in the remaining content of this subsection, we take a SMMTO problem with three material phases (i.e., material 1, material 2 and void, respectively) for example to demonstrate the relaxed and scaled stress evaluation. Then, we have the local stress constraints of the two solid material phases as:

$$\begin{cases} \langle \eta_1^S(\mu_e) \cdot \boldsymbol{\sigma}_0 \rangle \le \sigma_{Y,1} \\ \langle \eta_2^S(\mu_e) \cdot \boldsymbol{\sigma}_0 \rangle \le \sigma_{Y,2} \end{cases} \tag{4.9}$$

wherein $\rho_1 < \rho_2$, $E_1 < E_2$, $\sigma_{Y,1} \le \sigma_{Y,2}$. The above equation can be trivially adapted into:

$$\begin{cases} \langle \frac{\sigma_{Y,2}}{\sigma_{Y,1}} \cdot \eta_1^S(\mu_e) \cdot \boldsymbol{\sigma}_0 \rangle \le \sigma_{Y,2} \\ \langle \eta_2^S(\mu_e) \cdot \boldsymbol{\sigma}_0 \rangle \le \sigma_{Y,2} \end{cases} \tag{4.10}$$

Then, a new interpolation function ($\overline{\eta^S}$) for stress is constructed and a unified expression of Eq. (4.9) could be derived as:

$$\langle \overline{\eta^S}(\mu_e) \cdot \boldsymbol{\sigma}_0 \rangle \le \sigma_{Y,2} \tag{4.11}$$

where $\overline{\eta^S}$ needs to satisfy the following conditions: when $\mu_e = 0$ (void), $\overline{\eta^S}(\rho_1) = 0$; when $\mu_e = \rho_1$ (material 1), $\overline{\eta^S}(\rho_1) = \frac{\sigma_{Y,2}}{\sigma_{Y,1}} \cdot \eta_1^S(\rho_1) = \frac{\sigma_{Y,2}}{\sigma_{Y,1}} \cdot \frac{E_1}{E_2}$; when $\mu_e = \rho_2$ (material 2), $\overline{\eta^S}(\rho_2) = \eta_2^S(\rho_2) = 1$. Therefore, similar to the elastic interpolation, an ordered SIMP-like interpolation for stress is developed that transforms the above discrete definitions into a continuous function:

$$\overline{\eta^S} = \left( \frac{\mu_e - \rho_i}{\rho_{i+1} - \rho_i} \right)^{P_i^S} \cdot (S_{i+1} - S_i) + S_i \tag{4.12}$$

55

where $S_i$ is defined as the normalized and scaled stress factor for the $i^{th}$ material:

$$S_i = \frac{\sigma_Y}{\sigma_{Y,i}} \cdot \frac{E_i}{E_{max}}, \qquad \sigma_Y = \max(\sigma_{Y,i}) \qquad (4.13)$$

where $\sigma_{Y,i}$ is the yield stress corresponding to the $i^{th}$ material, and $\frac{\sigma_Y}{\sigma_{Y,i}}$ is the stress scaling coefficient for the $i^{th}$ material. We assume that $\overline{\eta^E}$ and $\overline{\eta^S}$ are monotonically increasing functions and $\overline{\eta^E}(\mu) < \overline{\eta^S}(\mu) < 1$ for $0 < \mu < 1$. Similar to [84], we define $\mu < \overline{\eta^S}(\mu)$ so that intermediate densities could be further penalized by the stress interpolation. Figure 16 shows a graph describing the ordered SIMP-like interpolation functions for the normalized elastic moduli and stress factor given the three-material scenario (material 1, material 2, and material 3).
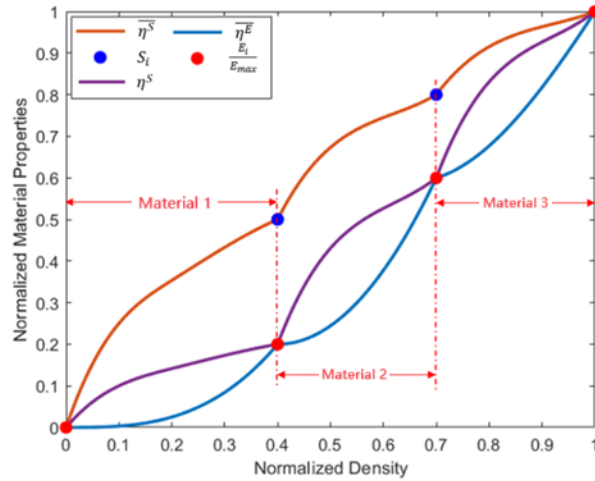


Figure 16. Ordered SIMP-like interpolations.

One more point to mention is that the interpolations of the normalized elastic moduli and stress factorare not physically precise. We are not particularly concerned with the fact that these ordered materials exist for intermediate density values. The ultimate goal is to have clear-cut $\mu_e = \rho_i$ ($i = 1,2,\dots,\text{Mat}$) designs.

**4.1.2. The maximum relaxed von-Mises stress measure**

The relaxed stress measure with penalization could be written as:

$$\overline{\boldsymbol{\sigma}}_e = \overline{\eta^S}_e \cdot \boldsymbol{\sigma}_0 \tag{4.14}$$

Then, the von Mises effective stress of the element centroid could be expressed as:

$$\sigma_{Vm,e} = \left(\overline{\boldsymbol{\sigma}}_e{}^T \mathbf{V} \overline{\boldsymbol{\sigma}}_e\right)^{\frac{1}{2}} \tag{4.15}$$

with $\mathbf{V}$ being the stress coefficient matrix:

$$\mathbf{V} = \begin{bmatrix} 1 & -\dfrac{1}{2} & 0 \\ -\dfrac{1}{2} & 1 & 0 \\ 0 & 0 & 3 \end{bmatrix} \tag{4.16}$$

Then, adopted the P-norm aggregation method introduced in subsection 3.1.2, the equivalent maximum relaxed von-Mises stress could be expressed as:

$$\hat{\sigma}_{PN} = c \cdot \left(\sum_{e=1}^{Nel} \left(\frac{\sigma_{Vm,e}}{\sigma_Y}\right)^P\right)^{\frac{1}{P}} \leq 1 \tag{4.17}$$

Where $\sigma_Y$ is the yield stress for the strongest material.

**4.1.3. Optimization problem formulation**

For the optimization problem, the objective function is to minimize structure weight subject to the maximum von Mises stress constraint. The optimization problem can be mathematically formulated as follows:

$$\begin{cases} \text{find: } \boldsymbol{\mu} \\ \text{minimize: } M(\boldsymbol{\mu}) = \displaystyle\sum_{e=1}^{Nel} (\tilde{\mu}_e \cdot m_0) \\ \text{subject to: } \begin{cases} \mathbf{KU} = \mathbf{F} \\ \hat{\sigma}_{PN} \leq 1 \\ \mu_{min} \leq \forall \tilde{\mu}_e \leq 1 \end{cases} \end{cases} \tag{4.18}$$

Where $\boldsymbol{\mu}$ is the design variable, $m_0$ is the unit mass of the $e^{th}$ element in case of being

filled with the heaviest material. M denotes the design domain mass containing the solid material. $\mathbf{K}$, $\mathbf{U}$, and $\mathbf{F}$ are the global stiffness matrix, displacement vector, and force vector, respectively. $\hat{\sigma}_{PN}$ is the aggregated maximum von-mises stress value obtained from Eq. (4.17). In this research, local stresses are evaluated at the element centroids. $\mu_{min}$ is set as $1e - 9$, which could be used to avoid matrix singularity.

### 4.1.4. Numerical examples

Table 1. The properties of 3 involved materials.

| Fictitious material name | Density $\rho$ | Elastic modulus E | Color |
|:---:|:---:|:---:|:---:|
| Material 1 | 1.00 | 100 | <span style="color:green">■■■</span> |
| Material 2 | 0.70 | 60 | <span style="color:red">■■■</span> |
| Material 3 | 0.40 | 20 | <span style="color:cyan">■■■</span> |

Three fictitious isotropic materials are investigated (see Table 1), and 3 different combinations of the three materials are considered in this subsection (see Table 2), and note that, the materials keep their density and elastic properties unchanged in different combinations, but their yield stress limits may vary across the combinations for the purpose of a robustness test of the proposed algorithm.

Table 2. The properties of the 3 involved cases.

| Case name | Material name | Density points | Elastic points | Stress points | Yield stress $\bar{\sigma}$ |
|:---:|:---:|:---:|:---:|:---:|:---:|
| SMTO | Material 1 | 1.00 | 1.00 | 1.00 | 1.750 |
| TMTO1 | Material 1 | 1.00 | 1.00 | 1.00 | 1.750 |
|  | Material 2 | 0.70 | 0.60 | 0.76 | 1.375 |

58

| | | | | | |
|---|---|---|---|---|---|
| | Material 3 | 0.40 | 0.20 | 0.50 | 0.700 |
| TMTO2 | Material 1 | 1.00 | 1.00 | 1.00 | 2.000 |
| | Material 2 | 0.70 | 0.60 | 0.76 | 1.570 |
| | Material 3 | 0.40 | 0.20 | 0.50 | 0.800 |

The interpolation curves of the normalized elastic modulus and the normalized and scaled stress modulus with respect to the density variable are shown in Figure 17.
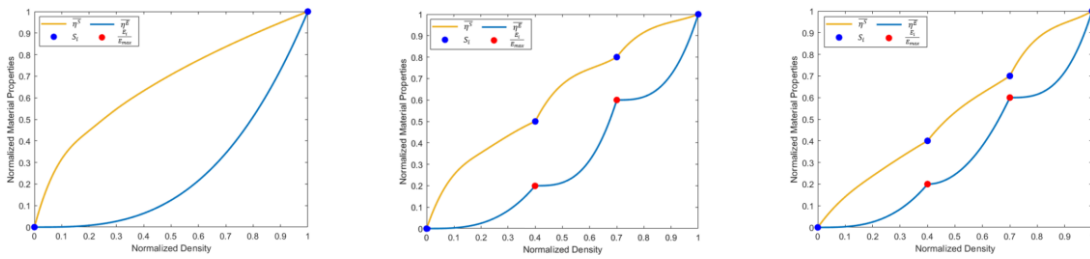


Figure 17. Interpolation curves of the normalized elastic modulus and the normalized and scaled stress modulus in different cases: (left) SMTO, (middle) TMTO1, and (right) TMTO2.

### 4.1.4.1. The L-bracket structure

The L-bracket structure is optimized. The initial design domain and boundary conditions are shown in Figure 18 with the characteristic dimensions. The design domain is discretized by 25584 square elements with uniform size of 0.005 by 0.005. The top edge of the L-bracket is clamped and a vertical load $F = 1$ is exerted to the right-side upper corner. Note that the load is distributed over 6 nodes to avoid stress concentration.
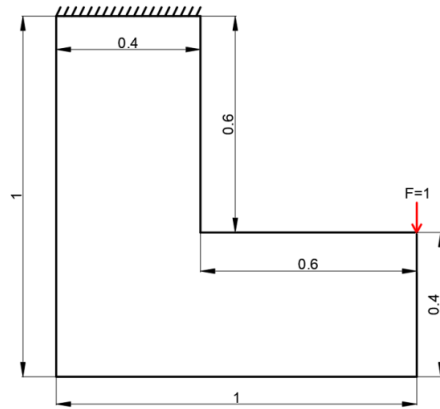
Figure 18. Design domain of L-shape beam.

Firstly, in order to investigate the influence of different maximum stress values, we compare the results obtained with SMTO, TMTO1, and TMTO2. The interpolation curves of the normalized elastic modulus and the normalized and scaled stress modulus with respect to the normalized density for these cases are shown in Figure 17. The other parameters hold the same values as those used in previous cases.
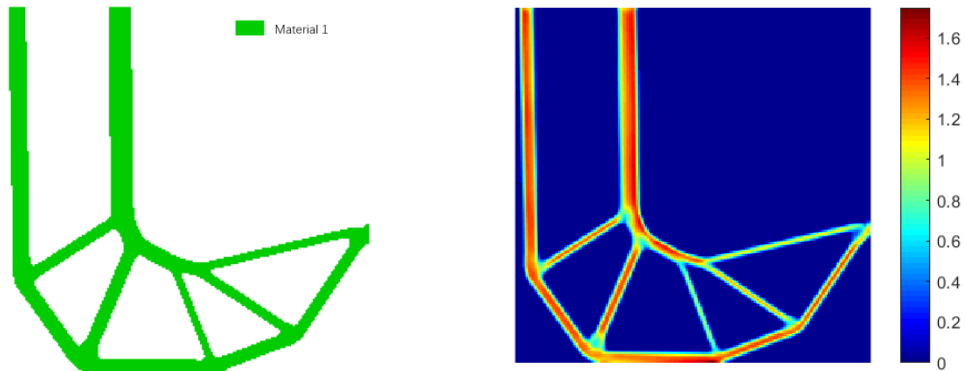


(a)
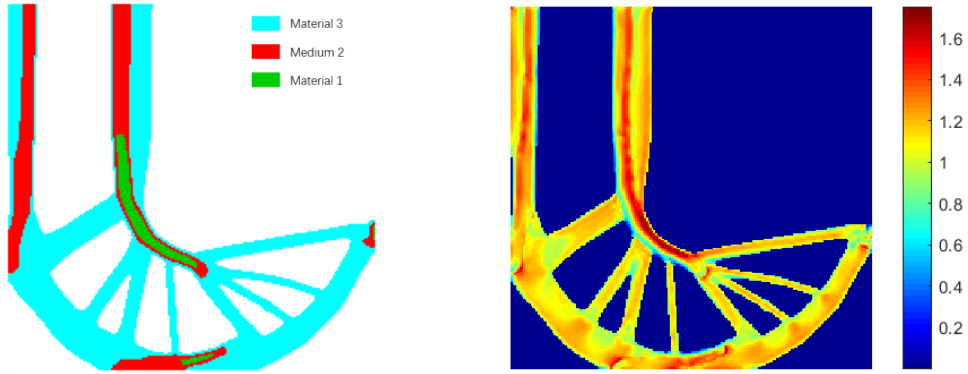
(b)
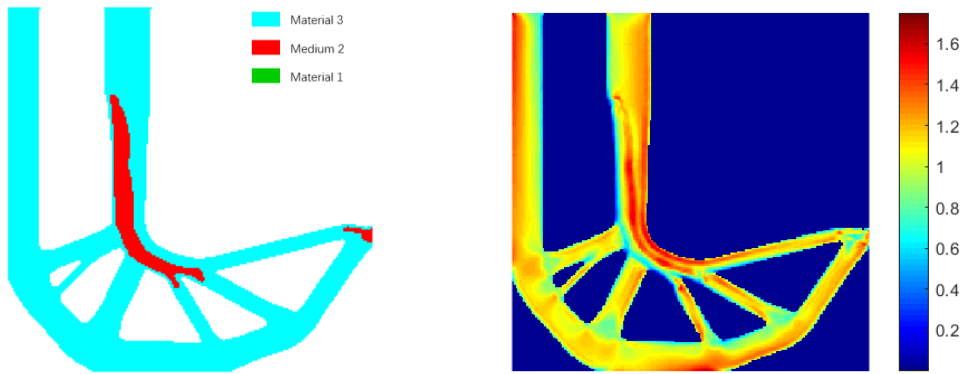


(c)

Figure 19. The optimized results, (a) SMTO2: the optimized topology (left) and scaled stress distribution (right); (b) TMTO1: the optimized topology (left) and scaled stress distribution (right); (c) TMTO2: the optimized topology (left) and scaled stress distribution (right).



(a)

61
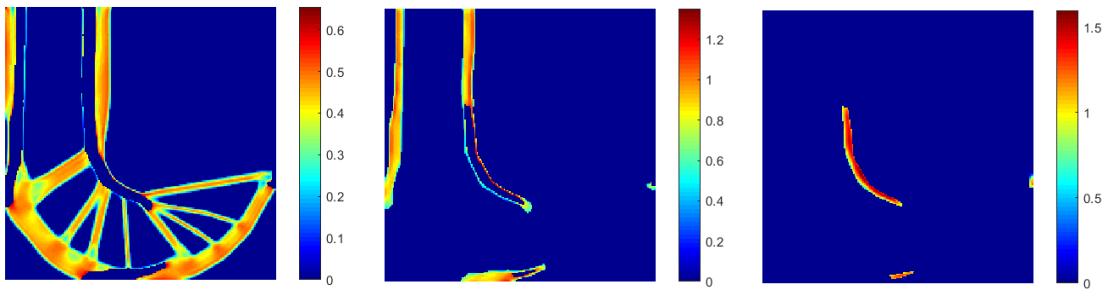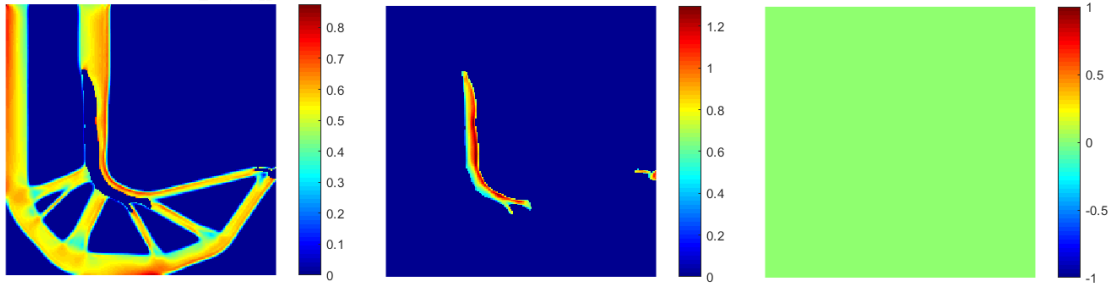
(b)

Figure 20. The real von Mises stress distribution, (a) TMTO1: material 3 (left), material 2 (middle), and material 1 (right); (b) TMTO2: material 3 (left), material 2 (middle), and material 1 (right).
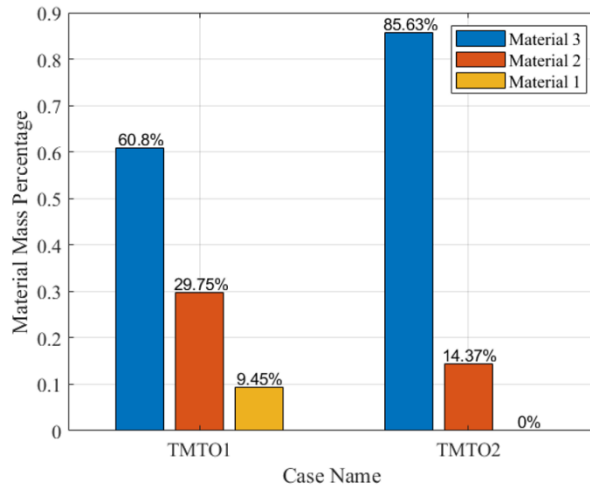


Figure 21. The three material mass percentages in each domain.

Figure 19 shows the optimized designs from SMTO, TMTO1, and TMTO2, respectively. The real von Mises distributions for different materials are shown in Figure 20, and the material mass percentage in each case could be found in Figure 21. The stress evaluation and the convergence history could be observed in Figure 22 and Figure 23.
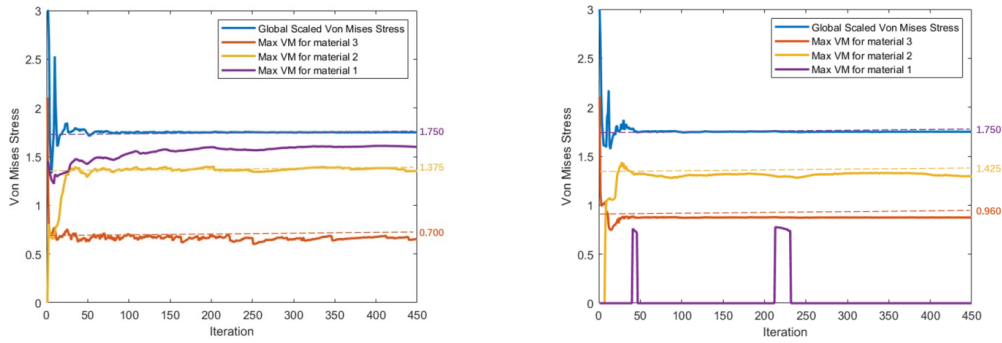
Figure 22. The real stress evaluation histories for the TMTO1 (left) and the TMTO2 (right).

For TMTO1, the optimization terminates after the maximum iteration, the final mass ratio is 0.2308, and the maximum von Mises stress in material 1, 2, and 3 are 1.5996, 1.3526 and 0.6547, respectively. In the optimization result, material 2 occupies the critical load bearing areas owing to its high strength-to-density ratio and material 3 occupies the majority of other areas for being lightweight.

For TMTO2, the optimization also stops at the maximum iteration. The final mass ratio is only 0.2073, and the maximum von Mises stress in material 2 and 3 are 1.2967 and 0.8749, respectively. Note that the optimization result from TMTO2 is majorly occupied by material 3 (85.63%), the lightest material phase simultaneously with the highest strength-to-density ratio. Material 2 takes 14.37% of the total mass, majorly distributing around the reentrant corner to relieve the local stress concentration. Material 1 does not appear in the final design due to the highest density and the smallest strength-to-density ratio.
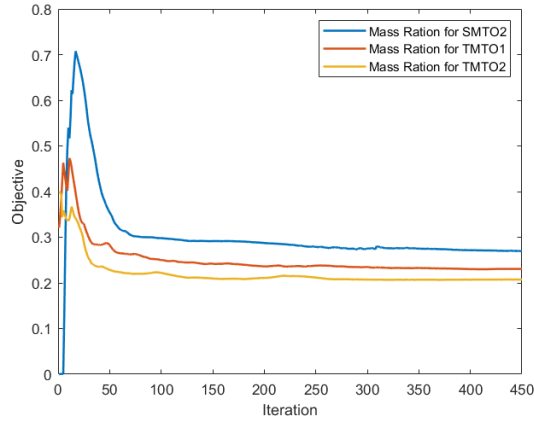
Figure 23. The iteration histories of objective values obtained with SMTO, TMTO1, and TMTO2.

## 4.1.4.2. The influence of $\overline{\eta^E}$ and $\overline{\eta^S}$ interpolation strategy

In this subsection, we investigate the effect of different interpolation strategies on the TMTO1 optimization result. The curves of the different interpolation strategies (with varying $P_i^E$ and $P_i^S$) are plotted in Figure 24. Other parameters hold the same values as those used in previous cases. From strategy 1 to strategy 4, the curvatures of the stress and elastic modulus interpolation curves keep reducing.



(a)                                                                 (b)

<center>(c)</center>



<center>(d)</center>
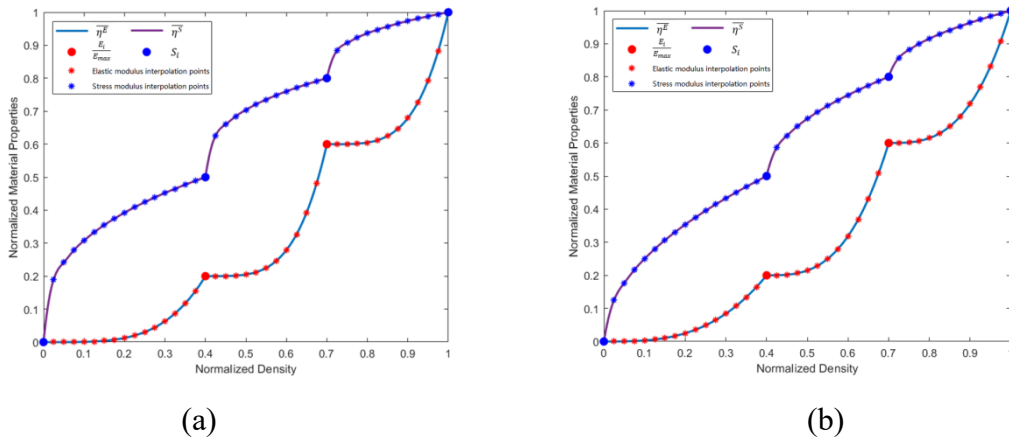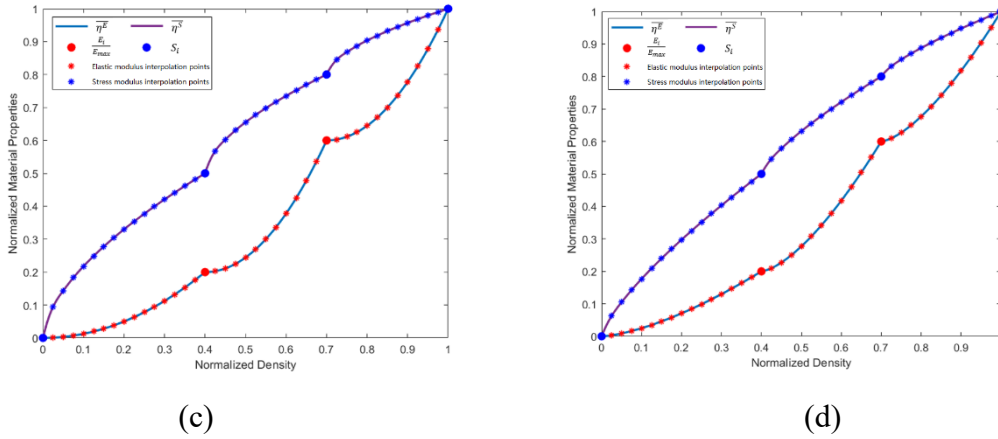
Figure 24. Illustrations of the different interpolation strategies, (a) strategy 1 ($P_1^E = 4, P_2^E = 4, P_3^E = 4$; $P_1^S = 0.35, P_2^S = 0.35, P_3^S = 0.35$); (b) strategy 2 ($P_1^E = 3, P_2^E = 3, P_3^E = 3$; $P_1^S = 0.5, P_2^S = 0.5, P_3^S = 0.5$); (c) strategy 3 ($P_1^E = 2, P_2^E = 2, P_3^E = 2$; $P_1^S = 0.6, P_2^S = 0.6, P_3^S = 0.6$); (d) strategy 4 ($P_1^E = 1.5, P_2^E = 1.5, P_3^E = 1.5$; $P_1^S = 0.75, P_2^S = 0.75, P_3^S = 0.75$).

The optimized results and material mass percentages are shown in Figure 25 and Figure 260. The final mass ratios are 0.2918, 0.2308, 0.2050, and 0.1933, respectively.



<center>(a)        (b)        (c)        (d)</center>
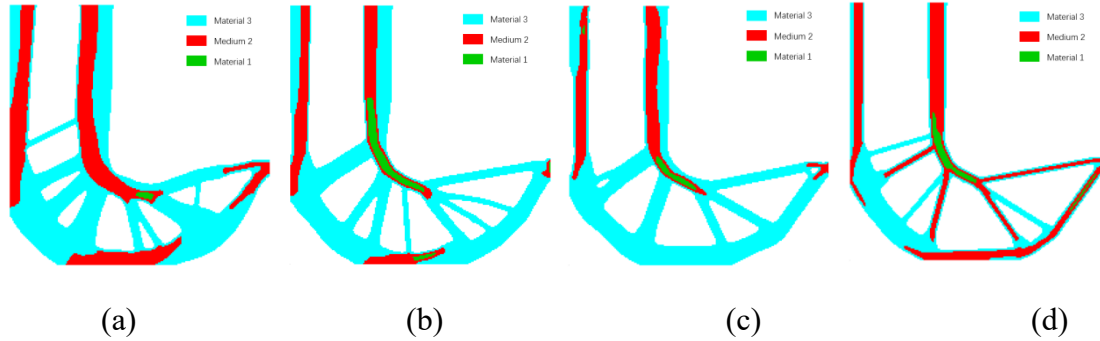
Figure 25. The optimized topological designs obtained with different interpolation strategies: (a) strategy 1; (b) strategy 2; (c) strategy 3; (d) strategy 4.

<center>65</center>
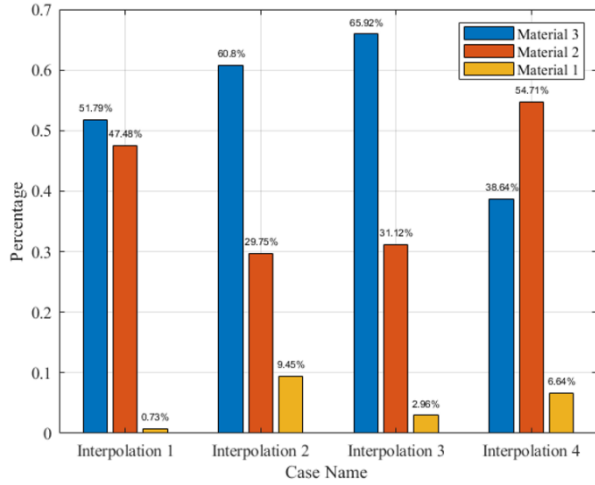
Figure 26. The three material mass percentages in each interpolation strategy.

The conditions of stress constraint violation (defined as $\max(\max(\sigma_{Vm} - \bar{\sigma}), 0)$) during the structure evolution process are plotted in Figure 27. It is clearly demonstrated that only interpolation strategy 1 and strategy 2 (with higher $P_i^E$ and lower $P_i^S$) have the capability of accurately constraining the local stress level of all material phases. Hence, deriving a well-suited setting of $P_i^x$ is extremely important. The experience of the authors shows that:1) a combination of $P_i^E$ larger than 3 and $P_i^S$ smaller than 0.5 could always stratify the stress constraint and get acceptable results; 2) for the $i^{th}$ material who's final maximum stress is far from the limit value, a proper lower $P_i^E$ and higher $P_i^S$ could be adopted to further achieve the lighter-weight effect.



(a)

66
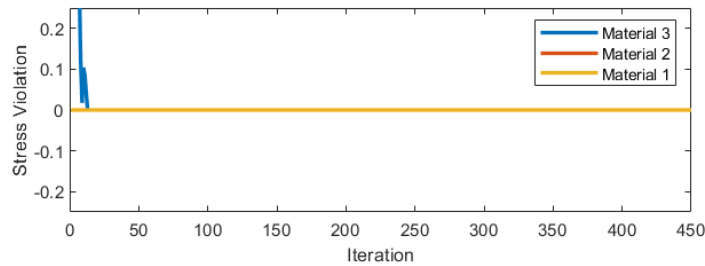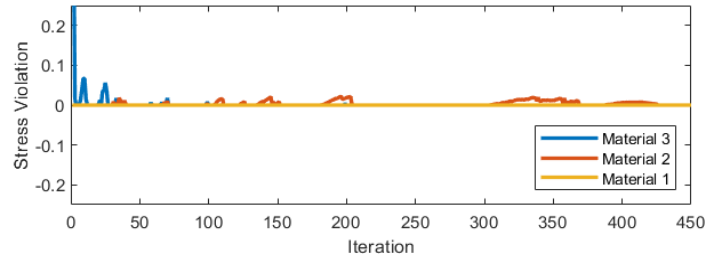
(b)
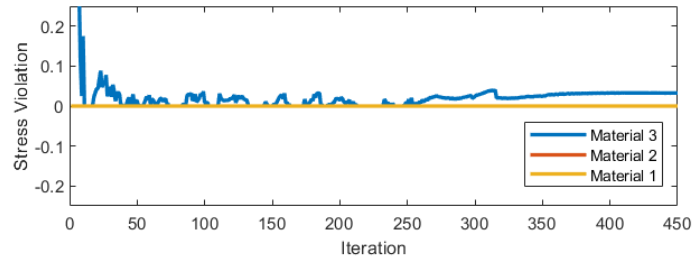


(c)
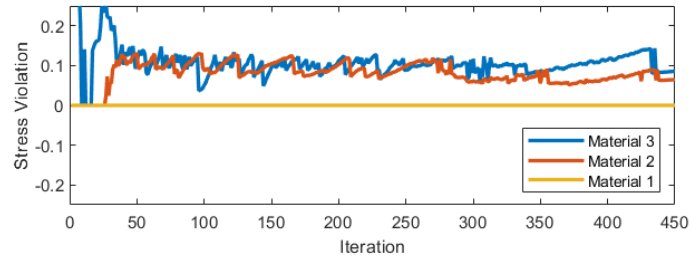


(d)

Figure 27. Variation of the real maximum von Mises stress with the yield stress of different materials under different interpolation strategy: (a) strategy 1; (b) strategy 2; (c) strategy 3; (d) strategy 4.

### 4.1.4.3. The Double L-bracket structure

The proposed method is applied to the double L-bracket design with multiple load cases and stress constraints. The initial design domain and boundary conditions of the double L-bracket benchmark are illustrated in Figure 28 (a) with the characteristic dimensions.

67

(a)                                          (b)
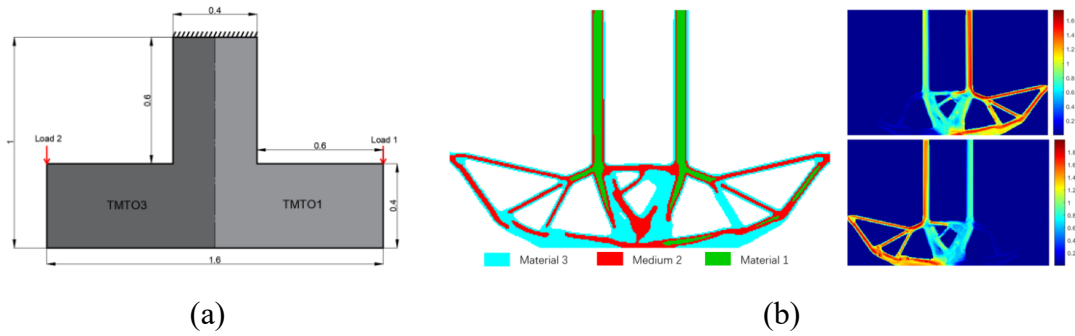
Figure 28. Design domain of double L-bracket beam and its results.

In this case, TMTO2 and TMTO1 are separately applied to the left and right sub-regions. Correspondingly, the optimization results are shown in Figure 28 (b). The structural topology of Figure 28 (b) is asymmetric due to the different stress criteria. The final mass ratio (0.2365) with TMTO2 is less than the result with TMTO1 (0.2460). This is reasonable given the fact that the stress criteria in the left sub-region are relaxed. The real von Mises stress distribution for different materials is given in Figure 29, the maximum von Mises stress in each material is less than its corresponding yield stress, and the objective value and the real stress evaluation histories are plotted in Figure 30. The real stress evaluation histories are demonstrated in Figure 30: (a) for TMTO1 and (b) for TMTO2. The corresponding material mass percentages in each sub-domain are provided in Figure 29 left.



(a)
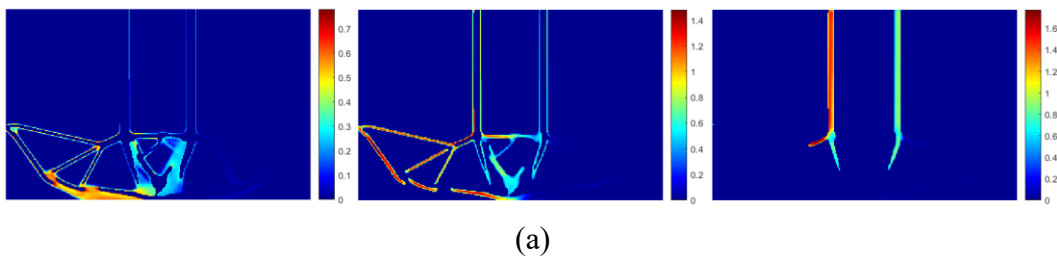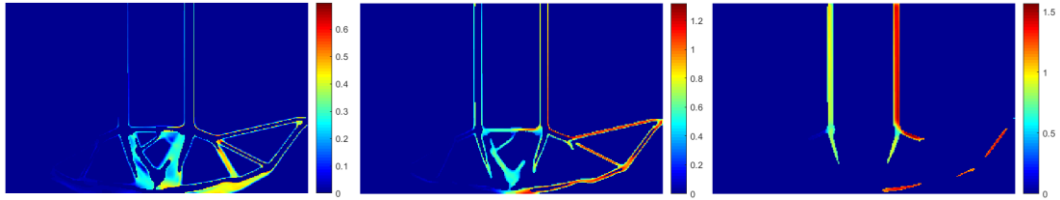
(b)

Figure 29. The real von Mises stress distribution for material 3 (left), material 2 (middle), and material 1 (right) under the TMTO2 in left domain (a) and TMTO1 in right domain (b).
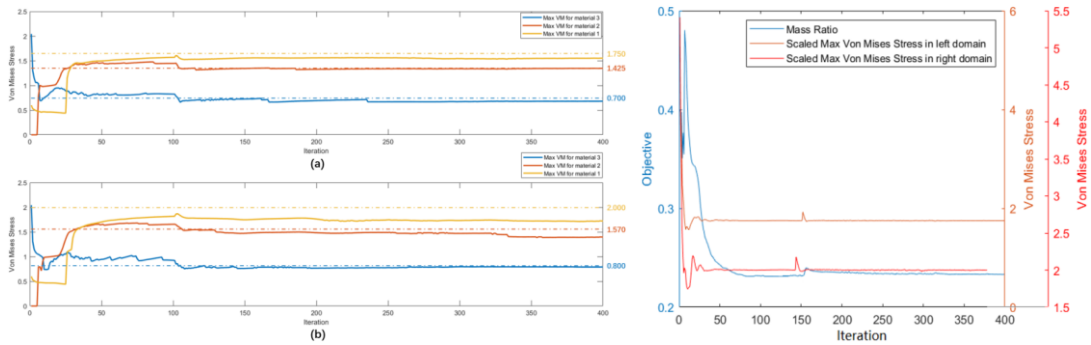


Figure 30. The objective value and real stress evaluation history.

**4.1.4.4. The initial design condition independence**



(a)

69

(b)



(c)



(d)
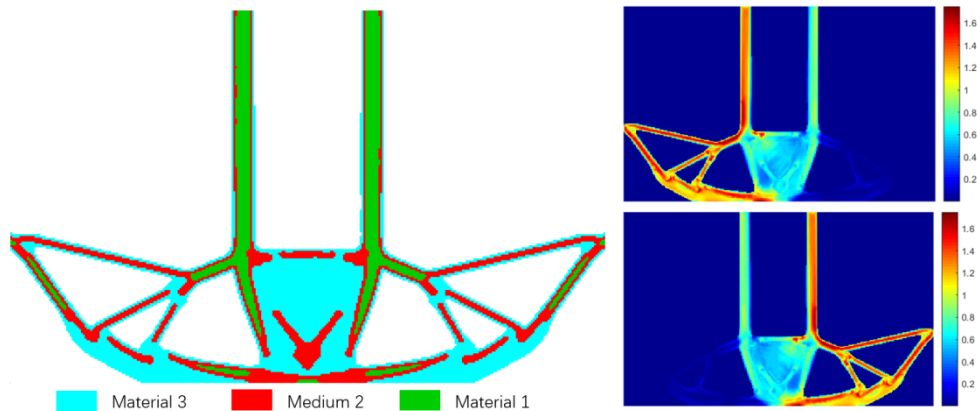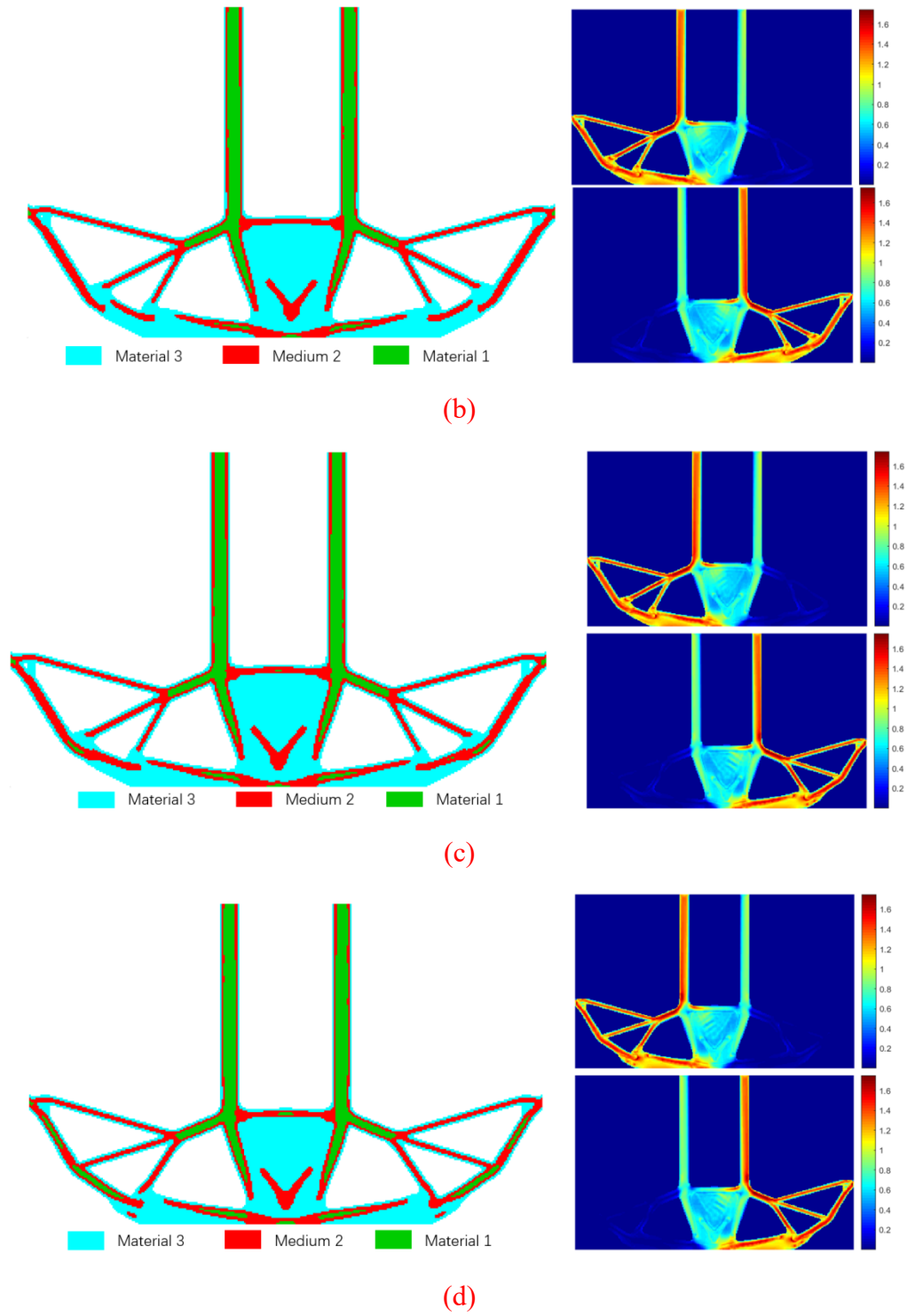
Figure 31. The optimized double L-bracket result of the TMTO1 with different initial design guesses: (a) μ = 0.4; (b) μ = 0.5; (c) μ = 0.6; (d) μ = 0.7.

In the end, the influence of different initial design guesses under the scheme of TMTO1 is investigated. The same optimization parameters of former subsection are adopted and the optimizations with different initial densities of 0.4, 0.5, 0.6, and 0.7 are performed. The optimization results are shown in Figure 31. Their optimized mass ratios are 0.2487, 0.2411, 0.2440, and 0.2466, respectively. The final topological structures and material distributions are analogous for the results with the initial guess of $\mu = 0.4$. The results indicate that the optimization result would be perturbed by the initial element densities, but the perturbation is random since the influence is non-monotonic.

**4.1.5. Conclusion for this work**

This paper proposed a stress-constrained multi-material topology optimization algorithm with the ordered SIMP interpolation. Innovatively, an ordered SIMP-like relaxed stress interpolation function is developed to realize the multi-phase stress interpolation subject to a single set of density variables. This new interpolation avoids the numerical issues of the extended SIMP interpolation for multi-phase stress measures. Additionally, a stress scaling method is proposed to impose the material-dependent yield stress limits. The STM based P-norm stress correction has been adopted to close the gap between the maximum local stress and the P-norm global approximation. Results of the numerical examples demonstrated that the proposed method can efficiently solve the stress constrained multi-material topology optimization problems with different material combinations.

**4.2. Multi-scale porous infill structure topology optimization**

Even though widely studied, there is still a large room for further investigations on multi-scale topology optimization. A new multi-scale topology optimization method for porous infill structure is developed in this research (Figure 32), which balances the design requirements on structural mechanical performance, computational efficiency, and

manufacturability.
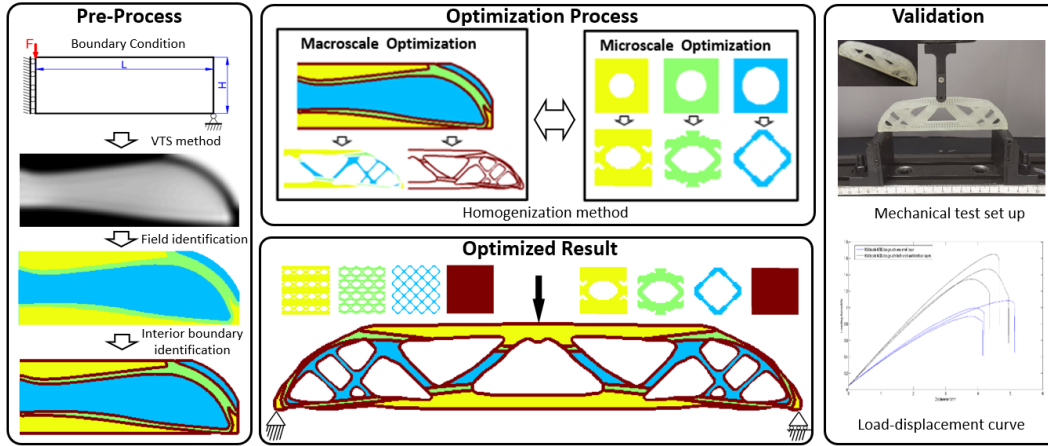


Figure 32. The methodology of the proposed work.

Specifically, multiple patches of microstructures will be involved, and each patch consists of a unique periodic microstructure. Hence, the number of microstructures is restricted to reduce the computational burden of repetitive homogenization of the microstructures. A solid interface layer will be built between adjacent patches of lattice microstructures to ensure connectivity. Additionally, a solid shell layer is added to the structural boundary to avoid the rough surfaces of the cut lattice microstructures. In summary of the proposed method, the macro structure, multiple microstructures, interface, and shell layers will all be optimized to simultaneously enhance the structural aesthetical, mechanical, and manufacturability properties. Figure 32 schematically illustrates the idea of this proposed method. It is worth noticing that the interface layer is similar to the coating structure mentioned in [292][293][294], while being different in functionality.

### 4.2.1. Explicit shell extraction based on DSP method.

The topological density variables could explicitly represent the boundary shell through a series of filtering, projection, and gradient norm approach. In the following subsection, the

numerical details of this approach will be introduced.
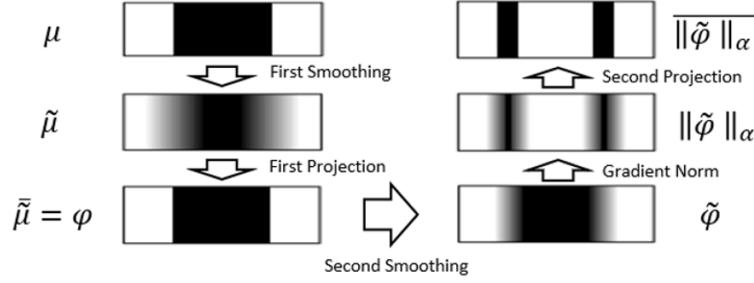


Figure 33. Illustration of the procedures of boundary shell identification.

Figure 33 shows the procedures of modeling the boundary shell contents. Firstly, the density design field $\boldsymbol{\mu}$ is smoothed by PDE filter with $r_{min1}$ to have $\widetilde{\boldsymbol{\mu}}$ so that checkerboard patterns can be avoided. This process could be achieved by solving the following PDE equation [295]:

$$-r^2 \nabla^2 \widetilde{\boldsymbol{\mu}} + \widetilde{\boldsymbol{\mu}} = \boldsymbol{\mu}, \tag{4.19}$$

where $r$ is the length control parameter, and its relationship with the filter radius $R_1$ is:

$$r = \frac{r_{min1}}{2\sqrt{3}}. \tag{4.20}$$

The smoothed density field $\widetilde{\boldsymbol{\mu}}$ is projected with Heaviside function with the sharpness factor $\beta_1$ and threshold factor $\eta_1$ to obtain a clear phase $\overline{\widetilde{\boldsymbol{\mu}}} = \boldsymbol{\varphi}$. In this study, the following continuous Heaviside function is used:

$$\boldsymbol{\varphi} = \overline{\widetilde{\boldsymbol{\mu}}} = \frac{\tanh(\beta_1 \alpha_1) + \tanh\big(\beta_1(\boldsymbol{\mu} - \alpha_1)\big)}{\tanh(\beta_1 \alpha_1) + \tanh\big(\beta_1(1 - \alpha_1)\big)}. \tag{4.21}$$

Then, the PDE filter (with radius $r_{min2}$) is applied again, resulting in the density field $\widetilde{\boldsymbol{\varphi}}$ with a fuzzy boundary. The boundary layer for fiber content modeling can be tracked with the Euclidean norm of the spatial gradient $\|\nabla \widetilde{\boldsymbol{\varphi}}\|$. $\|\nabla \widetilde{\boldsymbol{\varphi}}\|$ is normalized with the normalization factor $\alpha$ which should be chosen as the inverse of the maximum possible value of $\|\nabla \widetilde{\boldsymbol{\varphi}}\|$. It is intuitive that the maximum value of $\|\nabla \widetilde{\boldsymbol{\varphi}}\|$ will appear at the place

that the first projected field $\boldsymbol{\varphi}$ has a step edge, and it is a fixed value which can be pre-defined before optimization. To obtain normalization factor, a simplified 1D (only having x-direction) case is considered. In this case, the field $\boldsymbol{\varphi}$ could be expressed by:

$$\boldsymbol{\varphi} = H(x), \tag{4.22}$$

where $H(x)$ represents the continuous Heaviside function. Solving the following 1D Helmholtz PDE with boundary conditions at infinity:

$$\begin{cases} -\dfrac{r_{min2}{}^2}{12} \nabla^2 \widetilde{\boldsymbol{\varphi}} + \widetilde{\boldsymbol{\varphi}} = \boldsymbol{\varphi} \\ \widetilde{\boldsymbol{\varphi}}(x \pm \infty) = 0 \end{cases}. \tag{4.23}$$

Then, the second smoothed field $\widetilde{\boldsymbol{\varphi}}$ can be theoretically solved as:

$$\widetilde{\boldsymbol{\varphi}} = H(x) + \frac{e^{x\frac{2\sqrt{3}}{r_{min2}}}}{2}\left(1 - H(x)\right) - \frac{e^{-x\frac{2\sqrt{3}}{r_{min2}}}}{2}H(x), \tag{4.24}$$

the spatial gradient could be expressed by the following equation:

$$\|\nabla\widetilde{\boldsymbol{\varphi}}\| = \frac{dH(x)}{dx}\left(1 - \frac{e^{x\frac{2\sqrt{3}}{r_{min2}}}}{2} - \frac{e^{-x\frac{2\sqrt{3}}{r_{min2}}}}{2}\right) + \frac{\sqrt{3}e^{x\frac{2\sqrt{3}}{r_{min2}}}}{r_{min2}}\left(1 - H(x)\right) + \frac{\sqrt{3}e^{-x\frac{2\sqrt{3}}{r_{min2}}}}{r_{min2}}H(x). \tag{4.25}$$

The maximum gradient norm could be calculated by:

$$\|\nabla\widetilde{\boldsymbol{\varphi}}\|_{max} = \lim_{x \to 0}\|\nabla\widetilde{\boldsymbol{\varphi}}\| = \frac{\sqrt{3}}{r_{min2}}. \tag{4.26}$$

So, the normalization factor $\alpha$ is obtained as:

$$\alpha = \frac{1}{\|\nabla\widetilde{\boldsymbol{\varphi}}\|_{max}} = \frac{r_{min2}}{\sqrt{3}}. \tag{4.27}$$

The normalized gradient norm $\|\nabla\widetilde{\boldsymbol{\varphi}}\|_{\alpha} = \alpha \cdot \|\nabla\widetilde{\boldsymbol{\varphi}}\|$ is subsequently projected using $\beta_2$ and $\eta_2$ to define clearly the boundary layer $\overline{\|\nabla\widetilde{\boldsymbol{\varphi}}\|_{\alpha}}$ with controlled thickness.

## 4.2.2. Energy based homogenization method

Homogenization theory has been widely used in evaluating effective properties of a heterogeneous materials. From the macroscopic perspective, the whole structure can be treated as a homogenous material, and displacements are continuous and change slowly over the whole design domain. From the microscopic perspective, the displacements will vary over single cell. According to the asymptotic homogenization [297][298], the displacement can be represented in the following expression:

$$u^{\varepsilon}(x) = u_0(x, y) + \varepsilon u_0(x, y) + \varepsilon^2 u_0(x, y) \dots \tag{4.28}$$

The above component functions are dependent on the aspect ratio $\varepsilon$ of the global variable x and the local variable y. When only the first order terms of the asymptotic expansion in Eq. (4.28) are considered, the homogenized stiffness tensor $K_{ijkl}^H$ is given by averaging the integral over the base cell:

$$K_{ijkl}^H = \frac{1}{|Y|} \int_Y K_{ijpq} \left( \varepsilon_{pq}^{0(kl)} - \varepsilon_{pq}^{*(kl)} \right) dY \tag{4.29}$$

Where Y indicates the whole domain of the unit cell, $\varepsilon_{pq}^{0(kl)}$ denotes the three (2-D) or six (3-D) linearly unit test strain fields, and $\varepsilon_{pq}^{*(kl)}$ is the Y-periodic solution of

$$\int_Y K_{ijpq} \varepsilon_{pq}^{*(kl)} \frac{\partial u_i}{\partial x_j} dY = \int_Y K_{ijpq} \varepsilon_{pq}^{0(kl)} \frac{\partial u_i}{\partial x_j} dY \tag{4.30}$$

Where $u_i$ is the domain admissible displacement in the base cell field. Recalling that the homogenized stiffness tensor could be rewritten in an equivalent form in terms of the microscale element mutual energies, the effective properties of the periodic lattice can be evaluated with the energy-based homogenization method [299]:

75

$$D^{H}_{\zeta(ijkl)} = \frac{1}{\Omega_0} \cdot \sum_{e=1}^{N_e} \left[ \left( \mathbf{u}_e^{A(ij)} \right)^{T} \mathbf{k}_e \mathbf{u}_e^{A(ij)} \right] \tag{4.31}$$

where $\mathbf{u}_e^{A(ij)}$ are the microscale element displacement solutions corresponding to the unit test strain fields (the details could refer to [300]). $\mathbf{k}_e$ is the element stiffness matrix in microscale. $\Omega_0$ is the volume of the solid homogeneous medium. With the homogenized elastic tensor, the stiffness matrix of the $\zeta^{th}$ representative material microstructure could be derived through:

$$\mathbf{Ke}_{\zeta} = \delta(\mathbf{D}^{H}_{\zeta}) \tag{4.32}$$

where $\delta(*)$ is the element stiffness matrix assembly operator.

### 4.2.3. Method Statement and problem formulation

### 4.2.3.1. Method Statement

The whole procedure of the proposed method could be divided into two steps: the preprocess and the optimization process. The preprocessing is conducted to optimize the free material distribution, to recognize the interface and shell layers, and then to assemble them to create the initial guess for the following multi-scale optimization. To realize the free material optimization, the VTS method will be applied to generate the optimized element density field. The VTS method will create continuously varying element densities with many intermediate values. Then, a projection-based regularization mechanism will be introduced to discretize the density field into several clusters. Elements with the same or close densities will be projected to the same cluster, so that the design domain will be divided into sub-domains corresponding to the clusters. Note that each sub-domain is characterized by one microstructure and its representative density value (which is also the maximum volume fraction for the corresponding microstructure) is calculated by

averaging the element densities within the cluster. In the next stage, two well-established filtering and projection operators will be adopted to identify the interface layers between adjacent sub-domains with controllable layer thickness. In summary, the preprocessing derives the overall distribution of the multiple representative microstructures and identifies the interface layers between distinct microstructures, which provides the initial guess for the next-stage multi-scale topology optimization. The numerical implementation workflow for preprocess is illustrated in Figure 34.
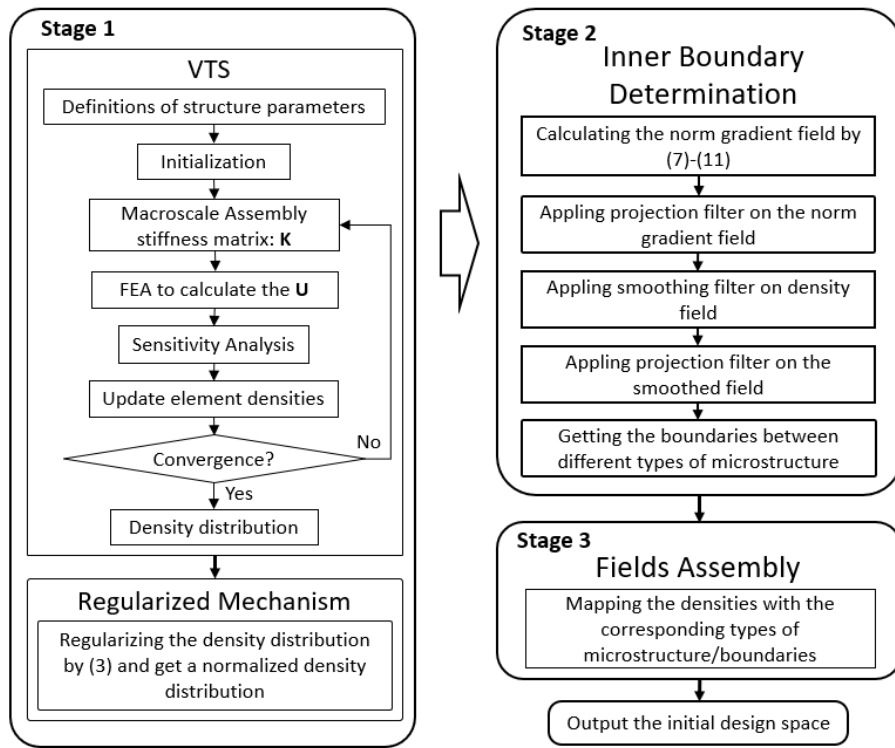


Figure 34. Flowchart of the preprocessing.

In the optimization process, the macroscale structural topology with a shell layer and the microscale structural details will be concurrently optimized subject to their corresponding volume constraints. At the macroscale, the DSP approach [56] will be applied to distinguish the interior porous infill and the exterior solid shell layer, and the macro-

structural topology will be optimized with the gradient-based optimizer. Meanwhile, at the microscale, the topologies of the representative microstructures will be simultaneously optimized based on the SIMP interpolation [61]. The energy-based homogenization method [21] will be adopted to bridge the macroscale and microscale computations. Finally, the optimized macrostructure and a few representative microstructures with well-established interface and shell layers will be derived as the optimization result. The numerical implementation workflow for optimization process is illustrated in Figure 35.
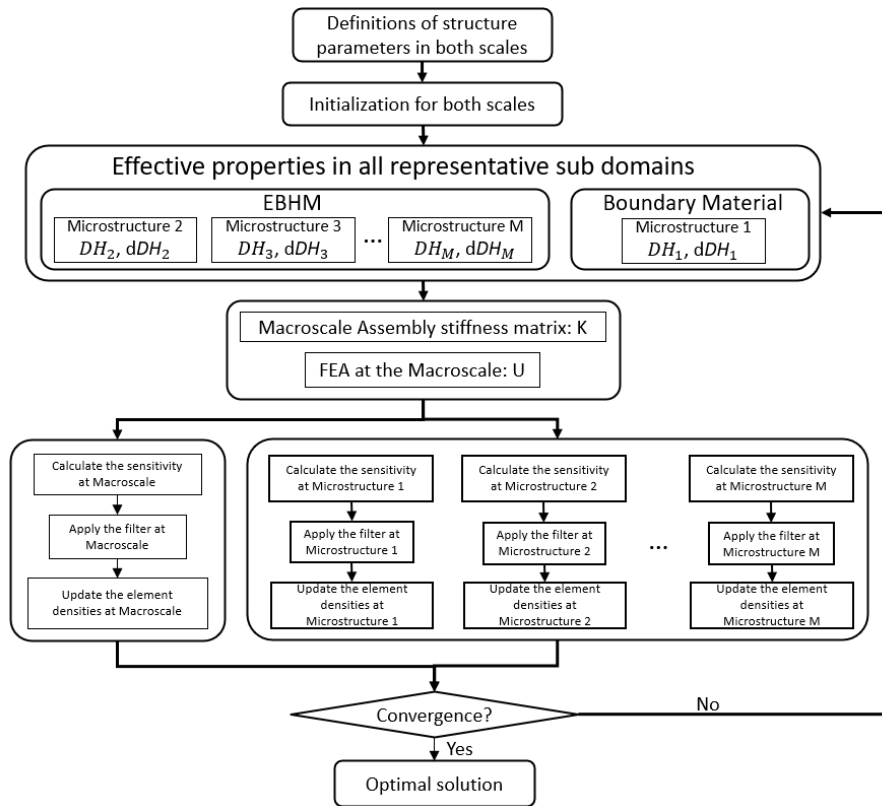


Figure 35. Flowchart of the multiscale optimization process.

### 4.2.3.2. Two-scale optimization problem formulation

In this work, a standard compliance minimization problem subject to volume constraints on both macro- and micro-scale is studied. The two-scale optimization problem is

formulated as:

$$\begin{cases} \text{Find: } \mu_E^M, \mu_{e,\xi}^m \left( E = 1,2, \dots, N_E; \ e = 1,2, \dots, N_e; \ \xi = 1,2, \dots, N_\xi \right) \\[2mm] \qquad \text{Min: } C = \mathbf{U^T K U} = \displaystyle\sum_{E=1}^{N_E} \mathbf{U_E^T K_E U_E} \\[2mm] \qquad \text{Subject to: } \begin{cases} \mathbf{KU = F} \\ G^M \leq V_d \\ g^m{}_\xi \leq v_{d,\xi} \\ 0 < \mu^M{}_{min} \leq \mu_E^M \leq 1, \\ 0 < \mu^m{}_{min} \leq \mu_{e,\xi}^m \leq 1, \end{cases} \end{cases} \qquad (4.33)$$

where $\mu_E^M$ is the macro design variable, also the macro elemental density. $\mu_{e,\xi}^m$ is the micro design variable for the microstructure $\xi$. $\mu_{min}^M$ and $\mu_{min}^m$ are two small number to avoid calculation singularity in two scale. $G^M$ is the macroscale volume fraction constrained by the maximum volume fraction $V_d$; $g^m{}_\xi$ is the volume fraction of the $\xi^{th}$ representative porous material region, which is subject to the maximum volume fraction of the corresponding representative microstructure ($v_{d,\xi}$) defined during the preprocess. The expression of $G^M$ and $g^m{}_\xi$ can be found in the later content. $N_e$ indicates the total number of elements within the $\xi^{th}$ microstructure.

### 4.2.3.2.1. Material Interpolation Strategy

The macroscale interpolation in this work is slightly different from [292]. The element stiffness matrix interpolation of element $E$ could be expressed as:

$$\mathbf{KE_E} = \sum_{\zeta=1}^{N_\zeta} \left( \mathbf{K_{E,\zeta}} \cdot \vartheta_{E,\zeta} \right)$$

$$\mathbf{K_{E,\zeta}} = (\varphi_E)^p \cdot \mathbf{Ke_\zeta} + \left( \overline{\|\nabla\widehat{\varphi_E}\|_\alpha} \right)^p \cdot \mathbf{Ke_1} - (\varphi_E)^p \cdot \left( \overline{\|\nabla\widehat{\varphi_E}\|_\alpha} \right)^p \cdot \mathbf{Ke_\zeta} \qquad (4.34)$$

$\mathbf{Ke_1}$ is the element stiffness matrix of the interface solid material, $\mathbf{Ke_\zeta}(\zeta \neq 1)$ is the homogenized element stiffness matrix (refer to the next subsection) of the $(\zeta - 1)^{th}$

infilled microstructure. p is employed to penalize the intermediate densities, so that to derive the black and white solution to distinguish the infill microstructure domain and void. While for the elemental density $\rho_E^M$ in macroscale, it could be expressed as:

$$\rho_E^M = \sum_{\zeta=1}^{N_\zeta} \left( \rho_{E,\zeta}^M \cdot \vartheta_{E,\zeta} \right)$$

$$\rho_{E,\zeta}^M = \varphi_E \cdot \varrho_\zeta + \left( \varrho_1 - \varphi_E \cdot \varrho_\zeta \right) \cdot \left( \overline{\|\nabla\widehat{\varphi_E}\|_\alpha} \right)$$

(4.35)

As the macroscale design region $\boldsymbol{\varphi}$ converges to a discrete $0/1$ solution, Eq. (4.34) and Eq. (4.35) will export a mixed physical field. Recalling that when the element E belongs to subdomain $\Omega_\zeta$, and the term $\overline{\|\nabla\widehat{\varphi_E}\|_\alpha}$ approaches zero, i.e. far away from the interface while within the non-void field of $\Omega_\zeta$ ($\varphi_E = 1$), Eq. (4.34) and Eq. (4.35) reduce to:

$$\mathbf{KE}_E = \mathbf{Ke}_\zeta \ , \zeta \neq 1,$$

$$\rho_E^M = \varrho_\zeta \ , \zeta \neq 1;$$

(4.36)

At the other extreme where the $\overline{\|\nabla\widehat{\varphi_E}\|_\alpha}$ approaches 1, i.e. at the interface region $\Omega_1$ ($\varphi_E = 0$), the Eq. (4.34) and Eq. (4.35) reduce to:

$$\mathbf{KE}_E = \mathbf{Ke}_1,$$

$$\rho_E^M = \varrho_1;$$

(4.37)

Note that, in the microscale, the SIMP interposition strategy is adopted to define the physical density and stiffness.

### 4.2.3.2.2. Objective function

The structural compliance is equal to the sum of element strain energies, which could be expressed as:

$$C = \sum_{E=1}^{N_E} Q_E$$

(4.38)

where $Q_E$ is the strain energy of the element E:

$$Q_E = U_E{}^T KE_E U_E \tag{4.39}$$

Substituting the element stiffness matrix interpolation Eq. (4.34) into Eq. (4.39) will yield:

$$Q_E = \sum_{\zeta=1}^{N_\zeta}\left\{\left[U_E{}^T(\varphi_E)^p Ke_\zeta U_E\right]\cdot\vartheta_{E,\zeta}\right\} + \sum_{\zeta=1}^{N_\zeta}\left\{\left[U_E{}^T\left(\overline{\|\nabla\widehat{\varphi_E}\|_\alpha}\right)^p Ke_1 U_E\right]\cdot\vartheta_{E,\zeta}\right\}$$
$$-\sum_{\zeta=1}^{N_\zeta}\left\{\left[U_E{}^T(\varphi_E)^p\left(\overline{\|\nabla\widehat{\varphi_E}\|_\alpha}\right)^p Ke_\zeta U_E\right]\cdot\vartheta_{E,\zeta}\right\} \tag{4.40}$$

For brevity, the following notation is introduced:

$$Q_E = \varepsilon_E^S \cdot Q2_E + \varepsilon_E^G \cdot Q1_E - \varepsilon_E^{SG} \cdot Q2_E \tag{4.41}$$

where $\varepsilon_E^S$, $\varepsilon_E^G$, and $\varepsilon_E^{SG}$ have the expressions of:

$$\begin{cases} \varepsilon_E^S = (\varphi_E)^p \\ \varepsilon_E^G = \left(\overline{\|\nabla\widehat{\varphi_E}\|_\alpha}\right)^p \\ \varepsilon_E^{SG} = (\varphi_E)^p \cdot \left(\overline{\|\nabla\widehat{\varphi_E}\|_\alpha}\right)^p \end{cases} \tag{4.42}$$

$Q1_E$ and $Q2_E$ could be treated as the corresponding element strain energy and defined as:

$$\begin{cases} Q1_E = \sum_{\zeta=1}^{N_\zeta}\left(U_E{}^T Ke_1 U_E\right)\cdot\vartheta_{E,\zeta} \\ Q2_E = \sum_{\zeta=1}^{N_\zeta}\left(U_E{}^T Ke_\zeta U_E\right)\cdot\vartheta_{E,\zeta} \end{cases} \tag{4.43}$$

### 4.2.3.2.3. Constraints for Microscale and Macroscale Volumes

In this paper, the volume constraints are separately built on the macro- and micro-scale structures. In macroscale, the global volume constraint function could be written as:

$$G^M = \frac{\sum_{E=1}^{N_E} G_E}{V_0} \tag{4.44}$$

where $G_E$ is the volume of the element $E$:

$$G_E = V_{ele}\cdot\rho_E^M = V_{ele}\cdot\sum_{\zeta=1}^{N_\zeta}\left(\left(\varphi_E\cdot\varrho_\zeta + \left(\varrho_1 - \varphi_E\cdot\varrho_\zeta\right)\cdot\left(\overline{\|\nabla\widehat{\varphi_E}\|_\alpha}\right)\right)\cdot\vartheta_{E,\zeta}\right) \tag{4.45}$$

81

In microscale, it arrives:

$$g^m{}_\xi = \frac{\sum_{e=1}^{N_e} g_{e,\xi}}{\Omega_0} \qquad (4.46)$$

where $g_{e,\xi}$ indicates the local volume of element $e$ in the $\xi^{th}$ representative microstructure, giving:

$$g_{e,\xi} = v_{ele} \cdot \varphi_{e,\xi} \qquad (4.47)$$

$v_{ele}$ is the solid element volume in microscale.

### 4.2.4. Numerical examples

An MBB structure will be optimized in this subsection. Note that, only three microstructures with the volume fraction of 80%, 60% and 30% are used to compose the macrostructure. Unless otherwise specified, the boundary in all cases is made of solid materials and the material type is the same with those microstructures.
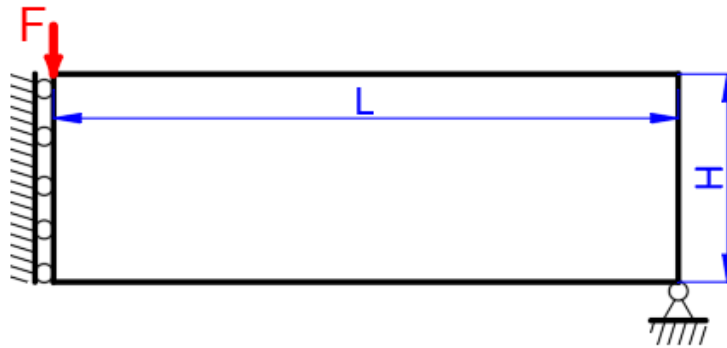


Figure 36. The MBB beam.

The first numerical example is the MBB benchmark example, whose structural sizes are defined with $L = 30$ and $H = 10$. Because of the symmetry condition, only one half of the structure will be optimized, which is shown in Figure 36. The MBB structure is loaded with a concentrated vertical force ($F = 1$) at the up-left corner; the bottom-right corner is supported on a roller; and the asymmetrical boundary condition is applied to the left edge.

82

A mesh with $300 \times 100$ square elements of size $0.1 \times 0.1$ is employed to discretize the design space in macroscale, and all the micro base cells are discretized with $30 \times 30$ square elements. The objective function is to minimize the macrostructure compliance under a volume constraint of 42%.

### 4.2.4.1. The MBB Beam Structure Optimization

The interface has the thickness of $T = 4$. The topologies of the macrostructure, the exterior boundary, and three representative microstructures are concurrently optimized subject to the overall microstructure and interior boundary distribution. Figure 37 gives the optimized topologies of the macrostructure and boundary, respectively.



(a)



(b)
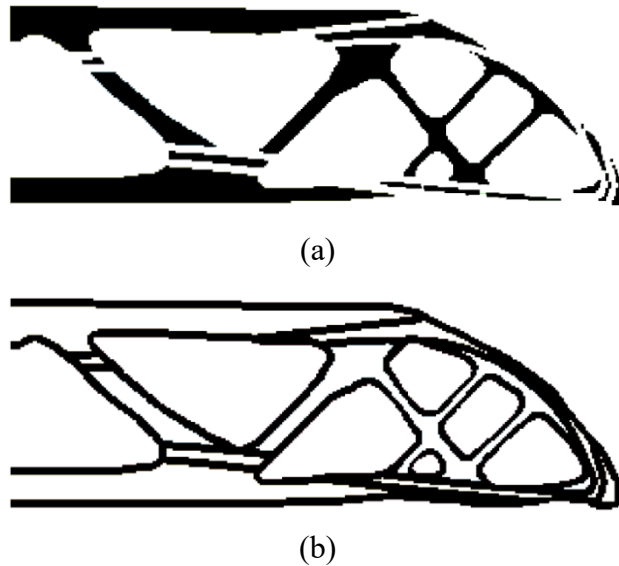
Figure 37. The optimized topology of the MBB beam: (a) microstructure area and (b) interface and shell layers.

Figure 38 gives the final multiscale design of the MBB beam. The different sub domains are plotted by yellow, green, and blue, separately. The interface and shell layers are plotted in red. Each sub domain is periodically configured by the corresponding representative microstructure shown at the bottom of Figure 38.
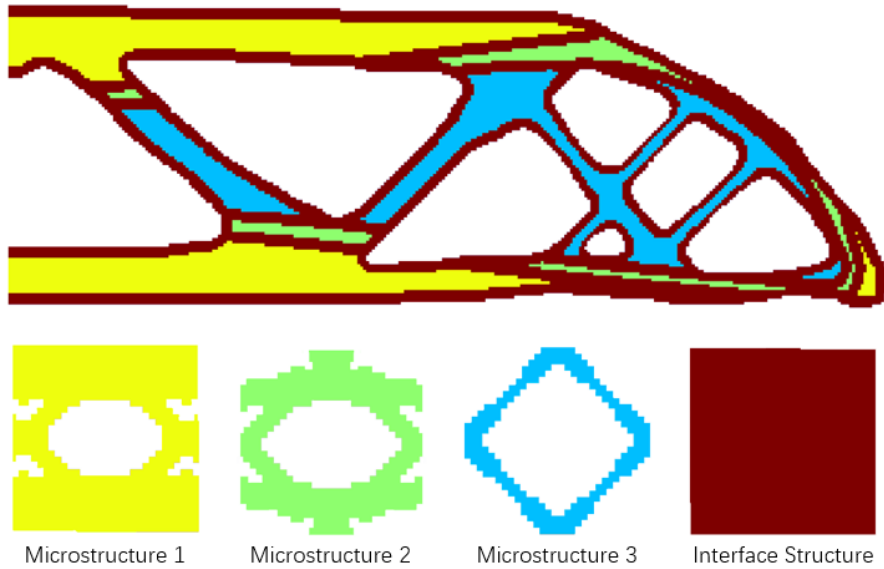
Figure 38. The multiscale design of the MBB beam.

The optimized maro-structural topology matches well with the widely accepted design results for the MBB beam [82][83]. Figure 39 shows the geometric details of the three microstructures, the $4 \times 4$ repetitions of the microstructures, as well as the corresponding homogenized elastic tensors. It is obvious that the microstructures do not match well if directly connected, while the interface layer addresses the connectivity issue that greatly enhances structural stability.
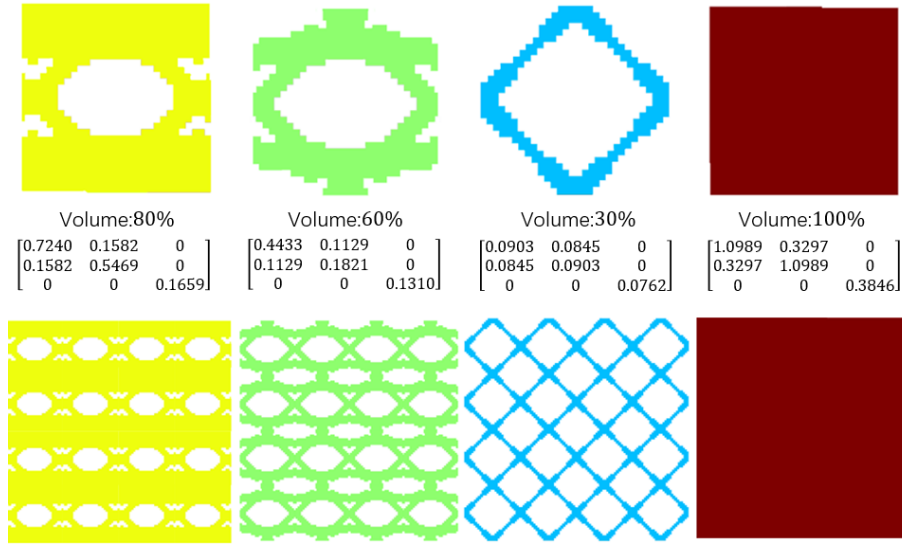
Figure 39. The optimized results of the three material microstructures.

The convergence history is plotted in Figure 40. Moreover, the intermediate results of the macrostructure and the intermediate distributions of the interface and shell layers are plotted in Figure 40, as well. To better perform a visual result, in the post-processing, we discretize the structures by following rules: $\varphi_E \geq 0.95$ indicates the clearly-identified material domain, and $\overline{\|\nabla\widehat{\varphi_E}\|_\alpha} \geq 0.5$ represents the clearly-formed boundary layer. The structural compliance and the two-scale material distributions do not change much from the 250th step, therefore, the optimization process stopped at the 300th step. The objective value of the final MBB beam design is 231.9582.
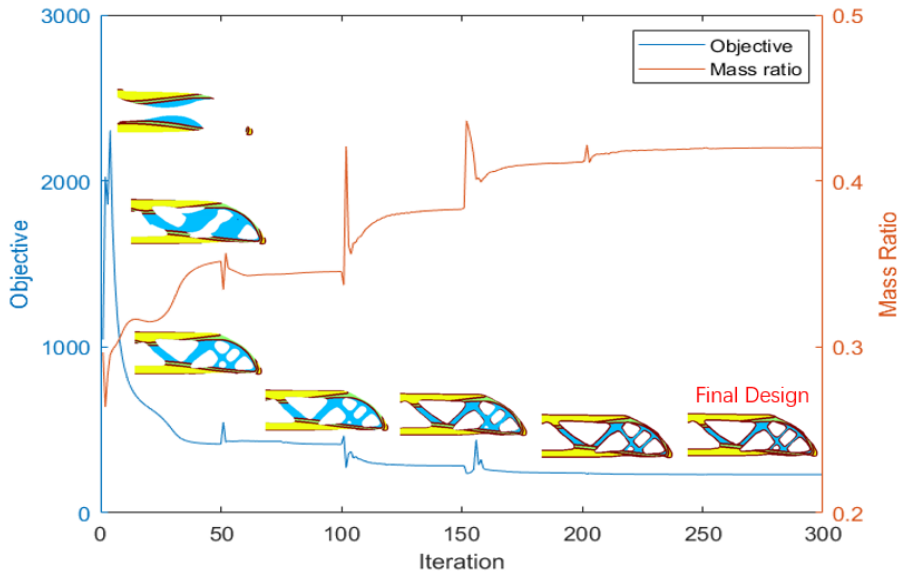
Figure 40. The convergence history and the macro-structure evolution.

The evolution histories of the three microstructures are given in Figure 41.
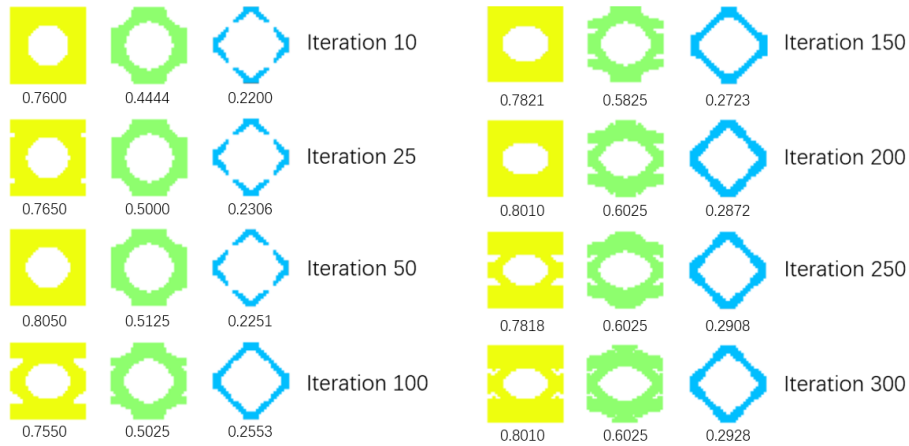


Figure 41. The evolutions for three representative microstructures.

### 4.2.4.2. The Interface Thickness Control

In general, if the thickness of the shell layer is extremely thin, the sloping interfaces and shells will be one-node connected that does not physically make sense. Therefore, the boundary features should at least have the width of two elements. In this work, to ensure

the consistency of the thicknesses of the interior and exterior boundaries, the following equation could arrive by recalling Eq. (4.20) and Eq. (4.27):

$$T_{ex} = \frac{\ln(2)}{\sqrt{3}} \cdot R_3 \approx 2 \cdot R_1 = T_{in}$$
$$R_3 \approx 5 \cdot R_1$$

(4.44)

Figure 42 shows the optimized macro topology results and the boundary distributions using three different boundary thicknesses of approximately $T = 2$, $T = 4$ and $T = 6$, respectively. The resolutions of the three cases are all $300 \times 100$.



Microstructure 1    Microstructure 2    Microstructure 3    Interface Structure

■ Minimum Length Control: $T = 2$

(a)



Microstructure 1    Microstructure 2    Microstructure 3    Interface Structure

■ Minimum Length Control: $T = 4$

(b)
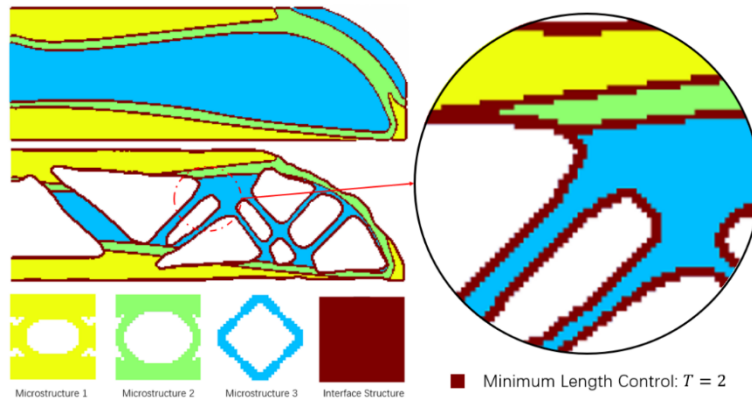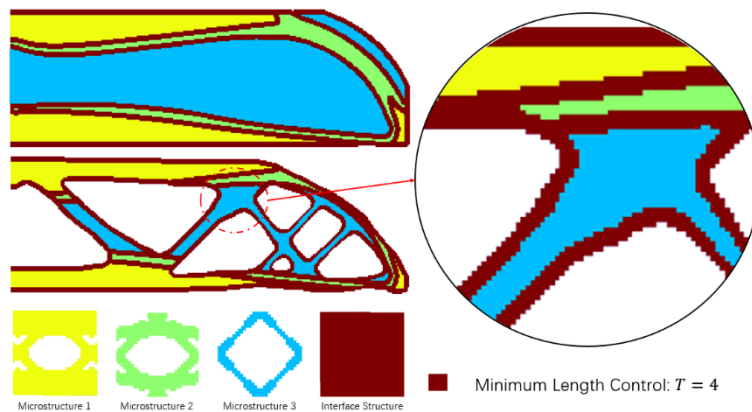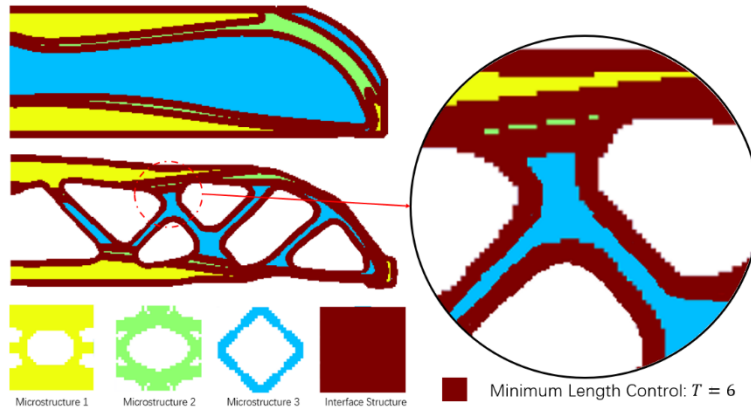
Figure 42. Optimization results with different thicknesses of the interface and shell layers: (a) $T = 2$ ($R_3 = 5, R_1 = 1,\ C = 265.6539$); (b) $T = 4$ ($R_3 = 10, R_1 = 2, C = 231.9582$); (c) $T = 6$ ($R_3 = 15, R_1 = 3,\ C = 210.1825$).

It could be shown that the thicknesses of the interface and shell layers are identical within each scheme, but the optimized structural topologies are evidently distinctive given the different boundary thicknesses. The boundary thickness can be accurately controlled by the corresponding filter radius. To maintain the structural physical meaning, $R_2$ should be greater than or equal to $R_3$, and $R_2 = 2 \cdot R_3$ is adopted in this work. Therefore, the increase of the boundary thickness T will cause the increase of $R_2$. Recalling that the smoothing filter with $R_2$ and projection filter with $\beta_3$ and $\sigma_3$ have the length control effect, small geometric features will be eliminated with an increasing boundary thickness T. Hence, the derived structural topology will be altered as well.

## 4.2.5. Mechanical Testing
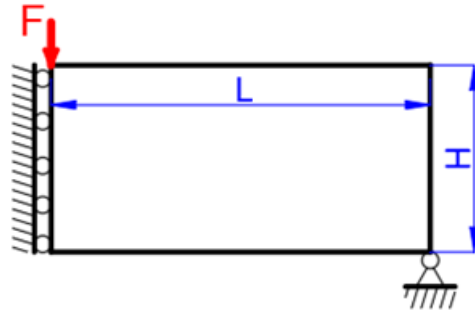


Figure 43. The short MBB beam.

To perform experimental validation of the effect of the interface layers, a short MBB beam (Figure 43) will be optimized and manufactured for mechanical testing. Its structural sizes are defined with $L = 20$ and $H = 10$. All the parameters except the structural sizes hold the same values as those used in the previous cases. Two optimized designs with the same mass ratio ($V_d = 0.4$) have been obtained. The first contains both interior and exterior interfaces under the same boundary thickness of $T = 4$. The optimized macro- and micro-scale results are illustrated in Figure 44, and the final compliance was found to be 109.5102.
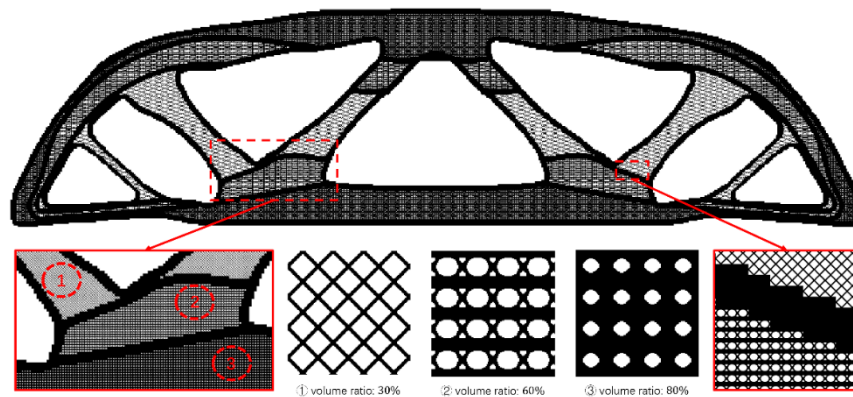


Figure 44. The optimized short MBB beam with both interior and exterior interfaces $(T = 4)$.

The second is a structure which only contains exterior interface (shell layer) with the thickness of $T = 2$. The optimized macro- and micro-scale results are illustrated in Figure 45. The final compliance was found to be $137.3501$.
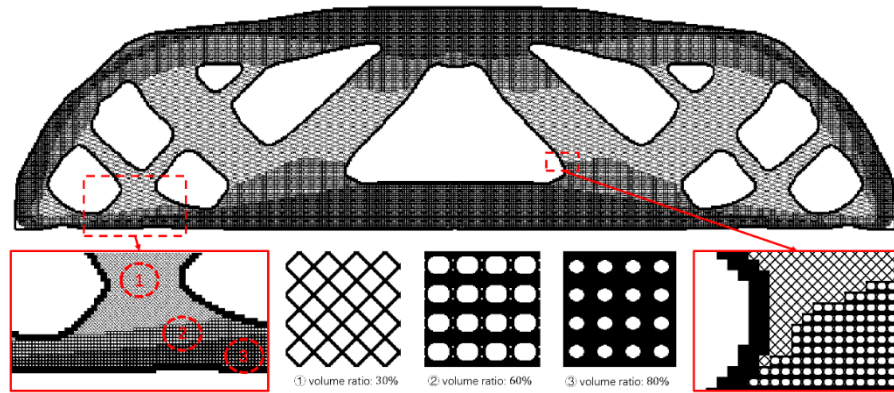


Figure 45. The optimized short MBB beam with only the exterior interface (T = 2).

Before generating 3D specimens for fabrication and test, post-processing is required for the numerical 2D designs in Figure 44 and Figure 45. Theoretically, in homogenization theory, the microstructure unit cells are assumed to be infinitely small compared with the macroscale structures. However, due to the limits of the 3D printer's resolution, the size of the microstructure needs to be appropriately configured. Then the structure is smoothed and reconstructed in CAD software.

Figure 46 presents the reconstructed CAD models and the manufactured samples for testing, which makes some appropriate simplification compared with the numerical results in Figure 44 and Figure 45. The size of the microstructure is configured to be $4 \times 4$ mm. The samples are printed with Formlab Form 3 which has the overall size of 140mm × 35.5mm × 12.5mm.
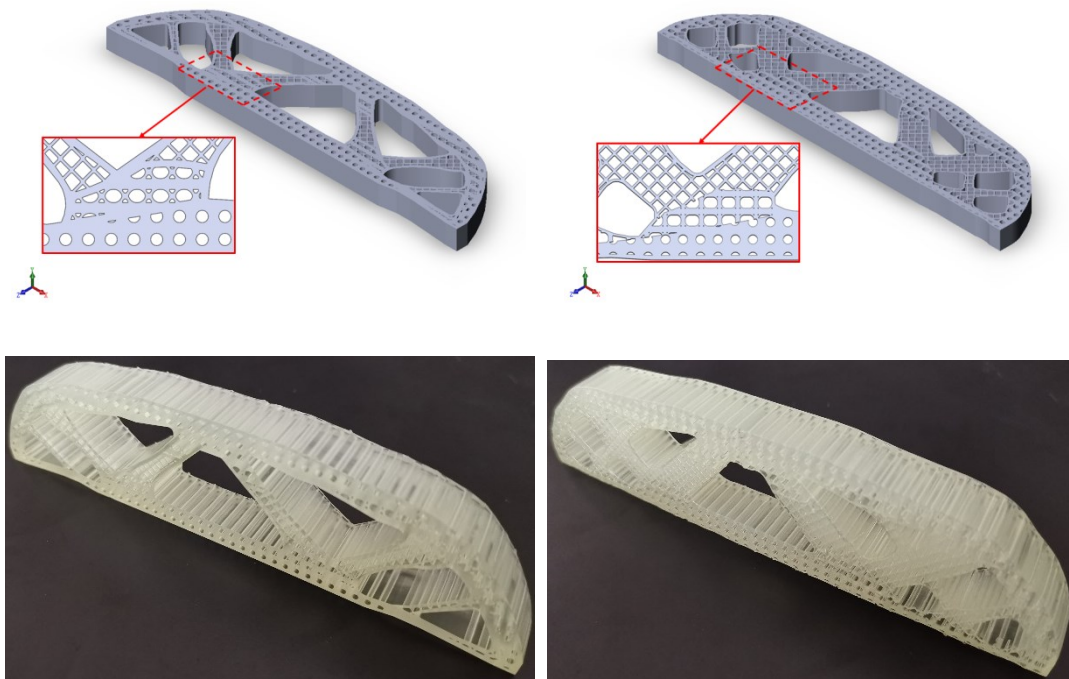
Figure 46. The reconstructed CAD models and manufactured samples of the multi-scale designs

Three samples have been printed for each design. The experiments are performed with a universal mechanical testing machine with the loading speed of 5mm/min. The testing setup is shown in Figure 47 and the testing result is demonstrated in Figure 48. The testing data show that the average structural compliance of the designs with only the shell layer is around 1.5 times of the average structural compliance of the designs with both shell and interface layers, while the rate of the numerical results is only 1.25. It clearly indicates that the poor connectivity between microstructures severely degrades the structural mechanical performance, and it is necessary to fix the connectivity issue, e.g., by adding a solid interface layer.
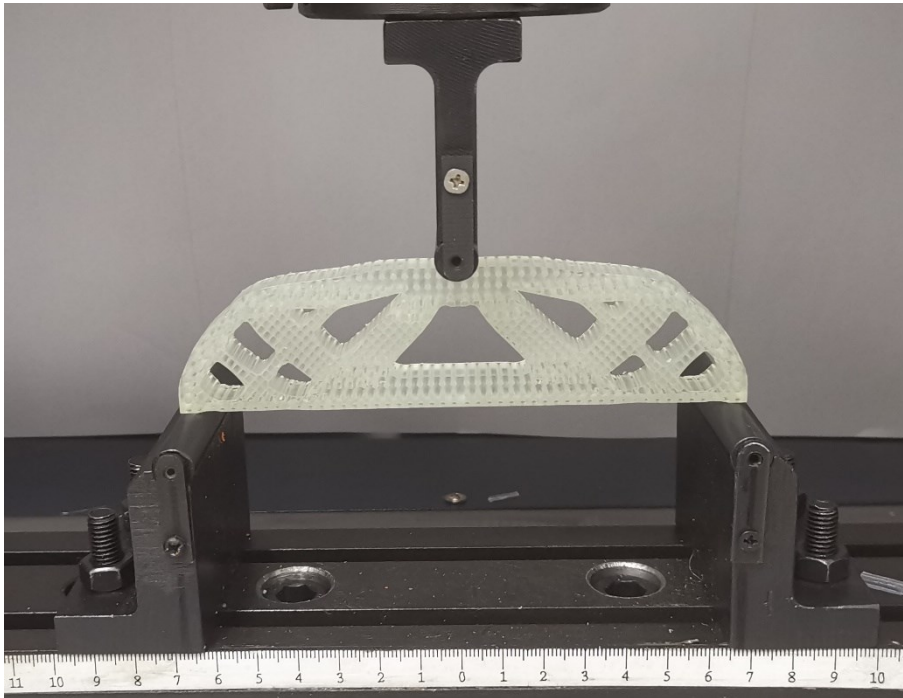
Figure 47. Mechanical testing setup
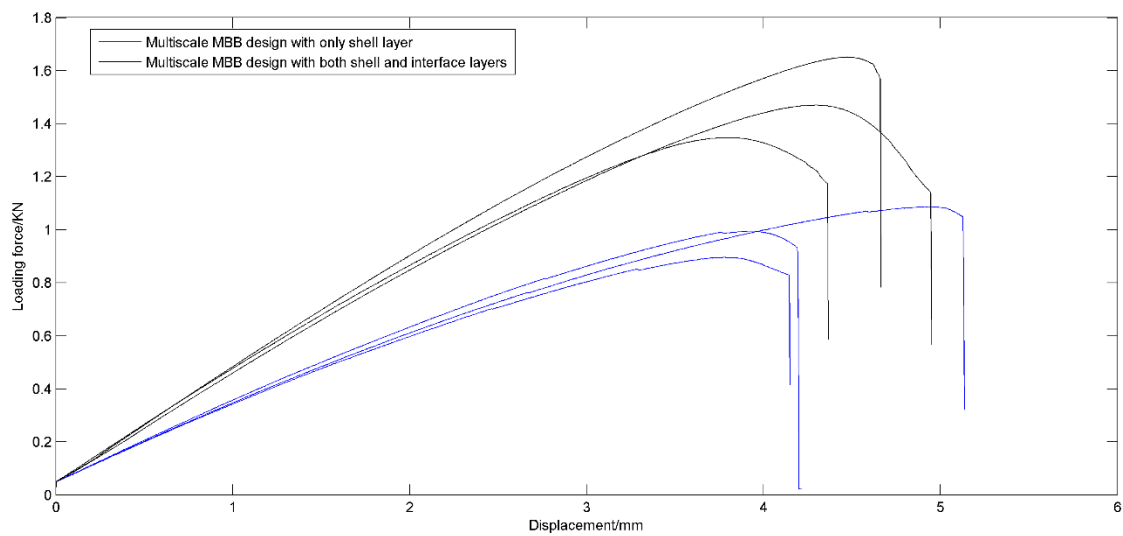


Figure 48. Mechanical testing result

### 4.2.6. Conclusion for this work

The current study presents a novel approach that effectively optimizes both the

macrostructure and multiple microstructures, while also considering the interior and exterior solid interfaces. Through various numerical examples, we have demonstrated the effectiveness of this method and validated its capability to achieve flexible control over interface thickness. In summary, the incorporation of solid interface layers successfully addresses the connectivity challenge, enhancing the overall robustness of the multiscale structures. Experimental validation confirms the positive impact of adding interface layers, as the designs lacking interior interface layers exhibit noticeably reduced stiffness and strength performance.

## 4.3. Summary

In this chapter, a series of topology optimization methods are proposed to address the challenges in the design of multi-material structures, and multi-scale porous infill structures. The pursuit of lightweight design is combined with the utilization of the distinctive AM process to maximize the structural performance of the designed components.

The research in this chapter primarily focuses on the perspective of 'improvement' and introduces various innovative equivalent material models and geometric control methods. These methods are utilized to describe the process characteristics of novel AM technologies and translate them into implicit/explicit constraints integrated with topology optimization algorithms. In comparison to traditional topology optimization algorithms, the proposed algorithms pay greater attention to the practical aspects of AM processes. Through numerical analysis and experimental validation, the feasibility and effectiveness of these methods have been demonstrated.

In the subsequent chapters, building upon the works presented in this chapter, further consideration will be given to the process defects in AM, with a specific emphasis on LPBF

metal AM. By means of geometric design approaches, efforts will be made to minimize residual deformations and residual stresses caused by the LPBF process while ensuring the performance of the components.

## Chapter 5. Numerical modeling for LPBF process and its integration with topology optimization

As LPBF provides new design opportunities, topology optimization is ideal for LPBF because it can be used to design high-performance structures and can fully exploit the fabrication freedom provided by AM. Moreover, topology optimization can reversely help to mitigate the limitations of the AM process by considering manufacturing issues in the structural-design stage. The mechanical response and thermal response induced by the LPBF process must be simulated before fabrication.

However, as reviewed in Chapter 2, numerical modeling of LPBF is a difficult and complex task. According to the different type of results that are sought, it often needs to be analyzed on different scales. It is unfeasible to include all relevant factors in a single simulation, as there is always a trade-off between accuracy and computational efficiency. In the context of topology optimization, an iterative algorithm is employed, where new solutions are derived based on the current and previous iterations. This process can require many iterations to reach a satisfactory solution, resulting in the need for hundreds of simulations. Thus, it is important to employ numerical techniques that can reduce computational time without sacrificing accuracy.

The present study employs a numerical model to calculate the mechanical response at the part scale level for topology optimization. This chapter introduces an in-house fast process simulation solver that serves predicting deformation and residual stresses in LPBF to model the mechanical response. The procedure of the implementation of proposed fast solver is shown in Figure 49.
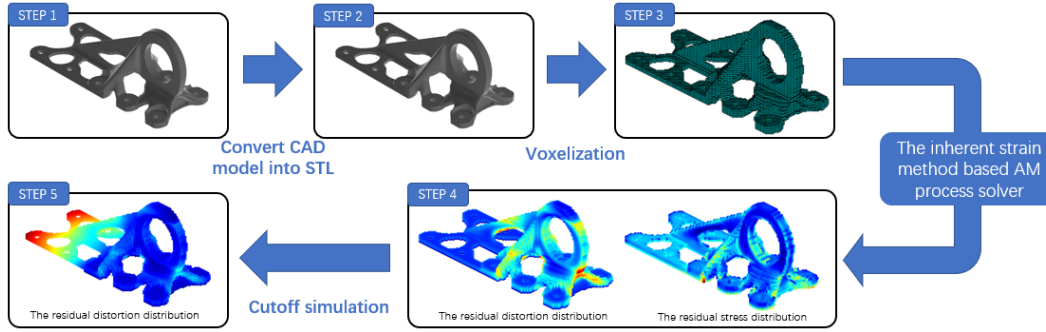
Figure 49. The procedure of the LPBF solver proposed in this research.

The ISM-based LPBF process modeling will be introduced first. Then, the finite element solver for this method will be introduced, along with its corresponding result verification. Finally, it introduces the combination of the solver and the topology optimization framework.

## 5.1. Numerical modelling of LPBF process in part level by ISM

In this subsection, the finite modelling of LPBF process will be introduced. Firstly, the simplified process simulation model for metal LPBF manufacturing process is discussed. The layer-by-layer building process is simulated based on ISM, which enables for a fast prediction of the residual stresses and distortions of the LPBF fabricated components.

### 5.1.1. Anisotropic inherent strain

The presence of incompatible strains, such as thermal strains and plastic strains, has been identified as a major contributor to distortions and residual stresses in welding-like manufacturing processes. These inherent strains arise due to an uneven distribution of temperature during the heating process and are considered to be process-dependent in nature. In particular, three primary sources of inherent strains have been identified: plastic strain ($\epsilon_p^{ihs}$), thermal strain ($\epsilon_t^{ihs}$), and other strains that are not classified as elastic strain ($\epsilon_o^{ihs}$). The inherent strain could thus be written as:

$$\epsilon^{ihs} = \epsilon_p^{ihs} + \epsilon_t^{ihs} + \epsilon_o^{ihs} \tag{5.1}$$

The unique elliptical shape of the melt pool in the x-y plane during laser scanning has been observed to result in anisotropic residual stress. The inherent strain should be therefore modeled as anisotropic with respect to the laser scanning direction. The present assumes that a constant strain is generated with each layer addition, and that the strain components within the x-y plane are dependent on the scanning orientation. The original inherent strain ($\epsilon^{ihs0}$) is defined as the principal strain based on the local coordinate system and is typically obtained through experimental calibration or high-fidelity numerical simulation techniques. By rotating the direction of the original inherent strain $\epsilon^{ihs0}$, the anisotropic inherent strain $\epsilon^{ihs}$ in each scanned island (Figure 50) for an arbitrary scanning orientation $\theta$ within the global coordinate system could be expressed as:

$$\epsilon^{ihs}(\theta) = \mathbf{R}(\theta)\epsilon^{ihs0}\mathbf{R}(\theta)^T \tag{5.2}$$



(a)                                                                (b)
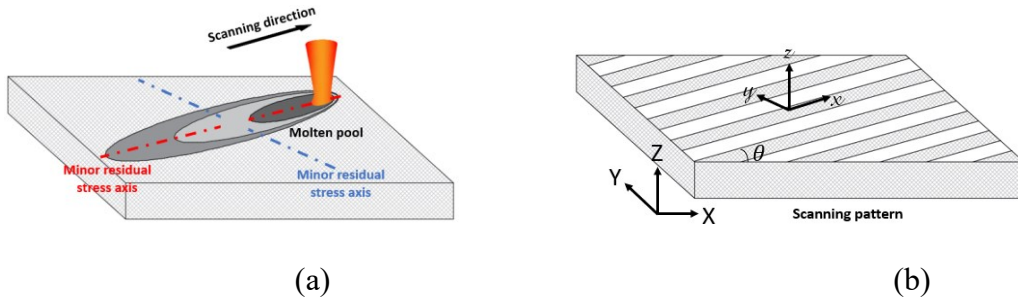
Figure 50. Outline of the anisotropic residual stress of the molten pool (a) and the relationship between the global coordinate system and the local coordinate system of the hatching line (b).

where $\mathbf{R}(\theta)$ is the xy-plane rotation matrix, which could be expressed as a function of the scanning orientation angle $\theta$:

$$\mathbf{R}(\theta) = \begin{bmatrix} \cos(\theta) & -\sin(\theta) & 0 \\ \sin(\theta) & \cos(\theta) & 0 \\ 0 & 0 & 1 \end{bmatrix} \tag{5.3}$$

97

### 5.1.2. Inherent strain obtains and validation

The accuracy of part-scale simulation results depends on the accuracy of the inherent strain. Two methods can be used to calibrate the derived inherent strains: (a) the reduced-order method and (b) the empirical method. The reduced-order method uses a hierarchical procedure to predetermine inherent strains through high-fidelity finite element models. A coupled thermo-mechanical analysis is carried out, considering the actual scanning strategy sequence with a moving heat source representing the power input. This allows for the accurate computation of both thermal and elastic-plastic deformations, enabling the identification of corresponding inherent strains. On the other hand, the empirical method obtains the characteristic inherent strains of each single layer through experimental tests and iterative fitting. The equivalent inherent strain is then calculated based on the layer thickness used in the simulation.

An iterative calibration process based on the empirical results is employed in this work. The whole process is shown in Figure 51. The residual stresses are proportional to the inherent strains applied to the structure. Therefore, an indirect measurement of this residual stress state enables to calculate the inherent strain field through inverse analysis.

In our specific case, the utilization of the twin-cantilever beam geometry is proposed due to its ability to enable a straightforward indirect assessment of residual stresses. This assessment is based on the beam's bending deformation following the cutting phase. According to our hypothesis, only two inherent strain components need to be determined, necessitating a minimum of two experiments. To capitalize on the orthogonal nature of hatches, two scanning strategies are employed for the same twin-cantilever beam: longitudinal and transversal hatching. This approach yields two distinct residual stress states and, consequently, two different final bending deformations. Additionally, a

scanning strategy with an orientation of $45°$ is implemented to validate the model. The connection between inherent strains and distortion is established through an optimization loop, wherein the objective function is defined as the discrepancy between the numerical results and the experimental measurements.
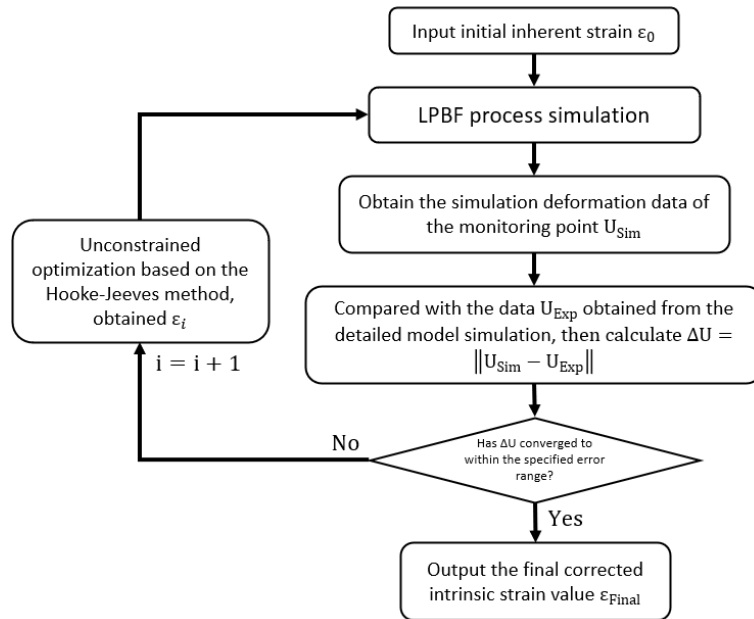


Figure 51. The flowchart for the inherent strain calibration process

The optimization problem is addressed through the Hooke-Jeeves direct penalty method. Consequently, the resulting inherent strain tensor at the layer level is acquired, serving as a reference dataset for comparable scanning strategies. It is important to emphasize that the obtained inherent strain tensor relies on the specific process parameters employed during the fabrication of the twin-cantilever beam. Furthermore, a straightforward validation of the calibrated outcomes is performed by employing the acquired inherent strain tensor in a $45°$ scanning strategy and subsequently comparing the numerical results with the experimental data.

### 5.1.3. Mechanical simulation based on ISM.
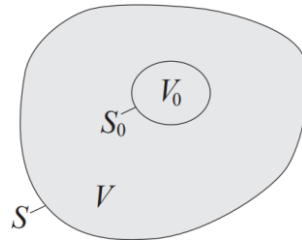


Figure 52. A linear elastic solid with volume V and surface S. A sub-volume $V_0$ and surface $S_0$ undergoes a permanent (inelastic) deformation. The material inside $V_0$ is called an inclusion and the material outside is called the matrix.

In LPBF, the material is gradually melted and added to a solidified part that is defined as a matrix. The newly deposited materials can be regarded as an inclusion in the matrix. The problem is to solve the stress, strain, and displacement both in the matrix and the inclusion, whose procedure is similar to that of the classic Eshelby's inclusion problem (Figure 52) [301]. The known and constant permanent strain (inherent strain) arising within the domain of the inclusion due to some inelastic process, while remaining absent throughout other regions. The corresponding elastic strain and the total strain are, on the other hand, unknown, and need to be determined everywhere.

Figure 53 shows the process. First, the inclusion is removed from the matrix, during which it will change shape to a zero-stress state because of the interior inherent strain. Then, one should apply surface traction $\mathbf{T}$ on the surface $S_0$ of the inclusion, changing it back to its original shape. Lastly, putting the inclusion back to the matrix and adding a traction $\mathbf{F} = -\mathbf{T}$ on the boundary between the inclusion and the matrix to resume the original inclusion. Therefore, the stress, strain, and displacement in this two-body system can be solved by elastic analysis based on the superposition principle of linear elasticity. In the LPBF process, when more materials are added, the above process will be repeated until the part is completely manufactured.

100
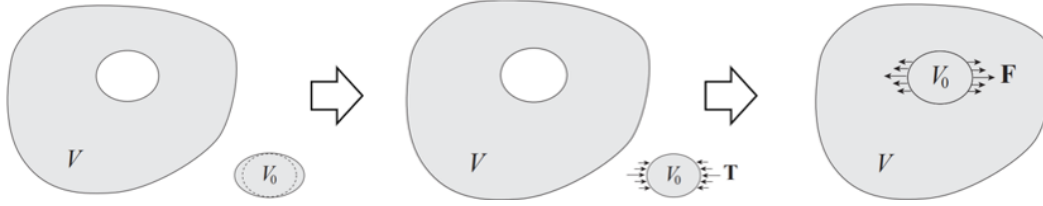
Figure 53. Virtual experiment for explaining the inherent strain method.

## 5.2. Finite element analysis of LPBF process

### 5.2.1. Mechanical simulation of LPBF by finite element method
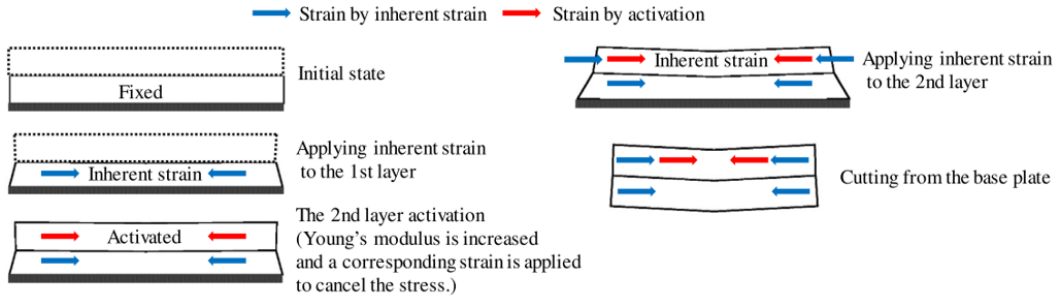


Figure 54. Outline of the sequential layer-by-layer process of the AM inherent strain method representing a warping deformation.

Considering the linear elastic problem discretized using the FEM, the equilibrium equation at the nth step is as follows:

$$\mathbf{K}_n \mathbf{U}_n = \mathbf{F}_n \tag{5.4}$$

where $\mathbf{K}$, $\mathbf{U}$, and $\mathbf{F}$ are the stiffness matrix, the displacement vector, and the force vector. The increment on both sides is represented as follows:

$$\Delta(\mathbf{K}_n \mathbf{U}_n) = \Delta \mathbf{F}_n \tag{5.5}$$

$$\mathbf{K}_{n+1} \mathbf{U}_{n+1} - \mathbf{K}_n \mathbf{U}_n = \Delta \mathbf{F}_n \tag{5.6}$$

$\Delta \mathbf{F}_n$ can be divided as $\Delta \mathbf{F}_n^{act} + \Delta \mathbf{F}_n^{ihs}$, $\Delta \mathbf{F}_n^{act}$ represents the strain to cancel the stress state indicated by red arrow (the so-called traction $\mathbf{F} = -\mathbf{T}$ mentioned in last subsection):

101

$$\Delta \mathbf{F}_n^{act} = \Delta \mathbf{K}_n \mathbf{U}_n = (\mathbf{K}_{n+1} - \mathbf{K}_n)\mathbf{U}_n \qquad (5.7)$$

and $\Delta \mathbf{F}_n^{ihs}$ represents the inherent strain applied in the $n^{th}$ step indicated by blue arrow (Figure 54):

$$\Delta \mathbf{F}_n^{ihs} = \Delta \mathbf{K}_n \mathbf{U}_{ihs} \qquad (5.8)$$

Then substitute the expressions $\Delta \mathbf{F}_n^{act}$ and $\Delta \mathbf{F}_n^{ihs}$ into Eq. (5.6):

$$\mathbf{K}_{n+1}\mathbf{U}_{n+1} - \mathbf{K}_n\mathbf{U}_n = (\mathbf{K}_{n+1} - \mathbf{K}_n)\mathbf{U}_n + \Delta \mathbf{K}_n \mathbf{U}_{ihs} \qquad (5.9)$$

Then the $n^{th}$ independent equation could be arrived:

$$\mathbf{K}_{n+1}\Delta \mathbf{U}_n = \Delta \mathbf{K}_n \mathbf{U}_{ihs} \qquad (5.10)$$

After activating the inherent strains of all layers, the part-scale distortion $\mathbf{U}$ is calculated by summing up the layer-wise distortion $\Delta \mathbf{U}_n$ as:

$$\mathbf{U} = \sum_{n=1}^{m} \Delta \mathbf{U}_n \qquad (5.11)$$

Consequently, according to Eq. (5.10), all layer printing steps during the building stage can be treated as independent linear problems, which can be solved in parallel. In this work, as shown in Figure 55, the number of layers in domain $\Omega$ is divided into $m$ lumped layers more than an actual material layer thickness in terms of computational effort and each layer domain is represented by $\Omega_n$. The generation of the structure is represented by changing Young's modulus from a small value (like 1E-9) to a great value using a static mesh. Therefore, the entire mesh will participate in the analysis of each printing step simulation.
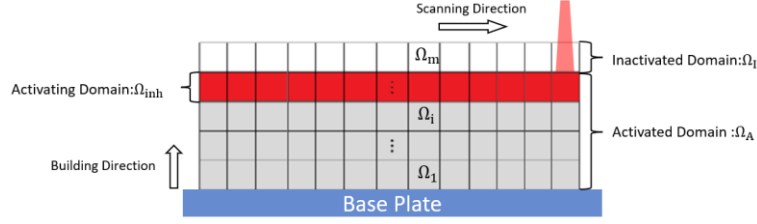
Figure 55. Domains and boundary during the building process.

The domain $\Omega$ is composed of three subdomains in each separate time step, where represented by $\Omega_{\text{Ihs}}$, $\Omega_A$, and $\Omega_I$. $\Omega_{\text{Ihs}}$ is the layer to be printed and to apply the inherent strain, $\Omega_A$ is the already printed layers, and $\Omega_I$ is the inactivated layers. The inherent strain $\boldsymbol{\varepsilon}_*$ at the domain $\Omega_{\text{ihs}}$ contributes to the distortion in the rest part of the substrate. Within the inactivated domain $\Omega_I$, the material with a small elastic modulus is occupied by the inactivated domain, which is activated sequentially along the building direction by m steps. Two layer wise flag field variables ($\boldsymbol{\delta}^n$ and $\boldsymbol{\vartheta}^n$) are thus provided to better indicates this activation process:

$$\begin{cases} \delta_e^n = 1 & \text{when} \quad \Omega_n \in \Omega_{\text{Inh}} \\ \delta_e^n = 0 & \text{otherwise} \end{cases} \quad \text{and} \quad \begin{cases} \vartheta_e^n = 1 & \text{when} \quad \Omega_n \in \Omega_A \cup \Omega_{\text{Inh}} \\ \vartheta_e^n = 0 & \text{otherwise} \end{cases} \tag{5.12}$$

In each step, the right-hand-side of Eq. (5.10) is equivalent to the nodal force applied to each activating domain ($\Omega_{\text{Inh}}$) through the following expression:

$$\Delta \mathbf{K}_n \mathbf{U}_n^{\text{ihs}} = \sum_{e=1}^{\text{Nel}} \left( \delta_e^n \mathbf{L}_e^T \eta_e^\beta \int \mathbf{B}^T \mathbf{D}_0 \boldsymbol{\epsilon}^{\text{ihs}}(\theta) \, d\Omega_e \right) \tag{5.13}$$

where $\boldsymbol{\epsilon}^{\text{ihs}}$ is the inherent strain for solids, $\eta_e^\beta$ is the inherent strain load coefficient interpolation function [242], $\mathbf{B}$ is the strain-displacement matrix, and $\mathbf{D}_0$ is the constitutive matrix for the solid material. The matrix $\mathbf{L}_e$ gathers the nodal displacements of the $e^{\text{th}}$ element ($\mathbf{u}_e$) from the global displacement vector ($\mathbf{U}$) satisfying $\mathbf{u}_e = \mathbf{L}_e \mathbf{U}$. The global stiffness matrix $\mathbf{K}_n$ when printing the $n^{\text{th}}$ layer is constructed by summing up

element stiffness matrices in the $\Omega_A$, which could be explicitly expressed as:

$$\mathbf{K}_n = \sum_{e=1}^{Nel} \vartheta_e^n \mathbf{L}_e^T \eta_e^E \int \mathbf{B}^T \mathbf{D}_0 \, \mathbf{B} \, d\Omega_e \, \mathbf{L}_e \tag{5.14}$$

where $\eta_e^E$ is the elastic modulus interpolation function. It is noted that to avoid the influence of non-activated elements during the previous printing stage, the final stage part-scale distortion $\mathbf{U}_{res}$ expression in this work should be modified as:

$$\mathbf{U}_{res} = \sum_{n=1}^{m} (\Delta \mathbf{U}_n \cdot \mathbf{H}_{DOF}^n) \tag{5.15}$$

where $\mathbf{H}_{DOF}^n$ is a flag array that indicates the activated nodes in each printed layer. In practice, the metal powders are deposited on a large build tray. Therefore, the boundary condition is to clamp the bottom surface of the build tray. However, the thick build tray forms a strong constraint to the bottom of the metal builds. In order to save computational cost, the build plate can be neglected, and the boundary condition can be changed to fix the metal components at the bottom surface.

**5.2.2. Distortions after release from the base plate**

For the part deformation, once it is separated from the baseplate, a new stress-free state is solved from the following equation:

$$\mathbf{K}_{remain} \mathbf{U}_{cut} = \mathbf{K}_{cutoff} \sum_{n=cut+1}^{m} \Delta \mathbf{U}_n \tag{5.16}$$

where $\mathbf{K}_{cutoff}$ is the assembled stiffness matrix corresponding to elements that are removed in the final separation step, and $\mathbf{K}_{remain}$ is the assembled stiffness matrix for the remained elements, as shown in Figure 55. It should be noted that the right-hand side of Eq. (5.16) indicates the effective mechanical load for these removed elements, which only

104

depends on the newly deposited powder (above the cutting layer). Then the final displacement state is the superposition of the fields $\mathbf{U}_{cut}$ and $\mathbf{U}_{res}$:

$$\mathbf{U}_{final} = \mathbf{U}_{cut} + \mathbf{U}_{res} \tag{5.17}$$
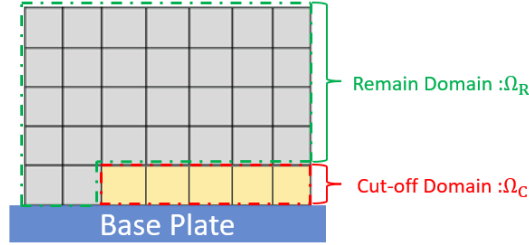


Figure 56. Domains and boundary during the cut-off process.

For the cut-off simulation, the remain domain $\Omega_R$ and cut-off domain $\Omega_C$ are shown in Figure 56, and Eq. (5.16) is modified as:

$$\mathbf{K}_{remain}\mathbf{U}_{cut} = \mathbf{K}_{cutoff} \sum_{n=cut+1}^{m} (\Delta\mathbf{U}_n \cdot \mathbf{H}_{DOF}^n) \tag{5.18}$$

The detailed expression of the global stiffness matrix for remain structure $\mathbf{K}_{remain}$ is:

$$\mathbf{K}_{remain} = \sum_{e\in\Omega_R} \mathbf{L}_e^T \eta_e^E \int \mathbf{B}^T \mathbf{D}_0 \, \mathbf{B} \, d\Omega_e \, \mathbf{L}_e \tag{5.19}$$

and the detailed expression of the global stiffness matrix for the removed structure $\mathbf{K}_{cutoff}$ is:

$$\mathbf{K}_{cutoff} = \sum_{e\in\Omega_C} \mathbf{L}_e^T \eta_e^E \int \mathbf{B}^T \mathbf{D}_0 \, \mathbf{B} \, d\Omega_e \, \mathbf{L}_e \tag{5.20}$$

### 5.2.3. Numerical Verification

Figure 57displays the comparison of the results obtained from commercial software MSC Simufact Additive® and our method using the same inherent strain value. The inherent strain model is only valid in the elastic domain, so the strains are overestimated above the limit of elasticity. To compare our results with the simulation of Simufact Additive®, we

first apply a maximum threshold to the Von Mises criterion obtained with our model. This maximum threshold is chosen equal to the maximum value of the Von Mises criterion obtained with Simufact Additive®, which uses an elastic model.
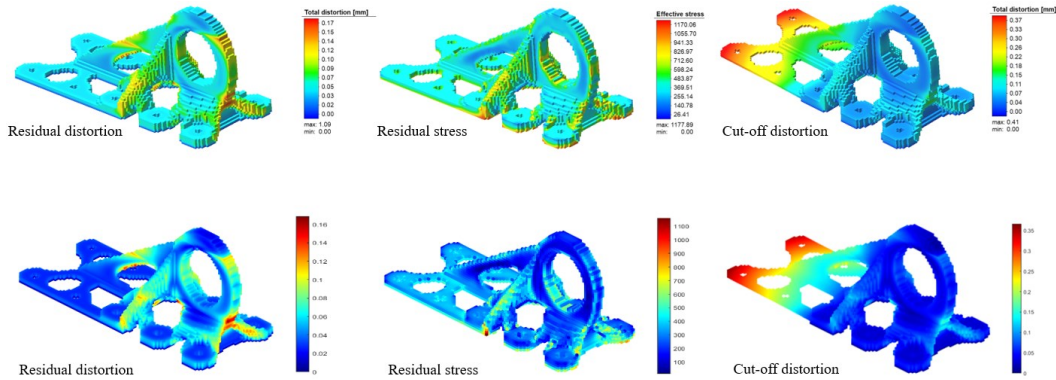


Figure 57. The comparison of the results obtained from proposed works and commercial software.

Figure 57 comparatively displays the results obtained from commercial software MSC Simufact Additive® and our method using the same inherent strain input and the same scanning strategy. Our numerical result shows qualitative good agreement with the one from Simufact Additive 2022®, and the detail comparison data is shown in Table 3.

|  | Simufact Additive® | Proposed Solver | Error |
|---|---|---|---|
| Residual distortion | 0.1732 mm | 0.1702 mm | 1.732 % |
| Residual stress | 1177.89 MPa | 1172.42 MPa | 0.464 % |
| Cut-off distortion | 0.41 mm | 0.39 mm | 4.878 % |
| Voxel Mesh | 156323 | 154323 | - |

Table 3. The detail comparison between the proposed solver and Simufact Additive®.

## 5.3. Integration of topology optimization and LPBF fast simulation solver

As mentioned in chapter 2, limited by the high-power input during LPBF, the fabricated structures often face the problem of residual stress accumulation induced by the high temperature gradients near the molten pool. Generally, residual stresses result in significant plastic deformation, leading to warping and distortion of the object. Parts can exhibit much larger deformation after removal from the building platform due to stress relief. Residual stresses and warpage severely degrade the mechanical performance, dimensional accuracy, and fatigue life of the fabricated part. Hence, reducing the residual stresses and warpage is a top priority for promoting the practical applications of LPBF technology. One straightforward approach is to reduce the temperature differences between heated and cooled down states by preheating the substrate. Adopting residual stress-relief methods (such as heat treatment and shot peening), can also reduce the residual stress level. An alternative approach to address prone-to-warp features in AM is to use DfAM that optimizes both structural geometry and process parameters. Altering the structural geometry can modify the heat conduction paths, thereby changing the thermal history and residual stress distribution significantly. LPBF oriented topology optimization is a promising solution to this issue.

### 5.3.1. The optimization problem formulation and solution

$$\begin{cases} \underset{\rho(\mu),\, u(\mu)}{\text{minimize}} : g_0(\rho, u) \\ \text{subject to:} \begin{cases} \mathbf{R}(\rho, u) = 0 \\ g_i(\rho, u) = 0 \quad i \in E \\ g_j(\rho, u) \leq 0 \quad j \in I \\ \rho(\mu) \in [0,1] \\ u(\mu) \in U \end{cases} \end{cases} \tag{5.21}$$

Where the response field $\mathbf{u}$ contains two parts: the physical filed response $\mathbf{u}_{\text{phy}}$ and the LPBF simulation field $\mathbf{u}_{\text{final}}$, and the residual state equations system could be expressed as:

$$R_{phy}(\boldsymbol{\rho}, \mathbf{u}_{phy}) = 0$$

$$\sum_{n=1}^{m} \left( \mathbf{K}_n \Delta \mathbf{U}_n - \Delta \mathbf{K}_n \mathbf{U}_n^{ihs} \right) \mathbf{H}_{DOF}^n = 0 \tag{5.22}$$

$$\mathbf{K}_{remain} \mathbf{U}_{cut} - \mathbf{K}_{cutoff} \sum_{n=cut+1}^{m} \Delta \mathbf{U}_n \, \mathbf{H}_{DOF}^n = 0$$

By help of the adjoint method, the objective functional is augmented by the product of adjoint fields and the residuals, and two adjoint variables $\boldsymbol{\lambda}^1$ and $\boldsymbol{\lambda}$ are proposed:

$$L = g_0 + \sum_{n=1}^{m} \boldsymbol{\lambda}_n^{1\,T} \left( \mathbf{K}_n \Delta \mathbf{U}_n - \Delta \mathbf{K}_n \mathbf{U}_n^{ihs} \right) \mathbf{H}_{DOF}^n + \boldsymbol{\lambda}^T \left( \mathbf{K}_{remain} \mathbf{U}_{cut} - \mathbf{K}_{cutoff} \sum_{n=cut+1}^{m} \Delta \mathbf{U}_n \, \mathbf{H}_{DOF}^n \right) \tag{5.23}$$

The gradient of the Lagrangian function is calculated by:

$$\frac{dL}{d\rho_e} = \frac{\partial g_0}{\partial \rho_e} + \frac{\partial g_0}{\partial \mathbf{U}_{res}} \sum_{n=1}^{m} \frac{\partial \Delta \mathbf{U}_n}{\partial \rho_e} \mathbf{H}_{DOF}^n + \frac{\partial g_0}{\partial \mathbf{U}_{cut}} \frac{\partial \mathbf{U}_{cut}}{\partial \rho_e} - \sum_{n=1}^{m} \boldsymbol{\lambda}_n^1 \left( \mathbf{K}_n \frac{\partial \Delta \mathbf{U}_n}{\partial \rho_e} + \frac{\partial \mathbf{K}_n}{\partial \rho_e} \Delta \mathbf{U}_n - \frac{\partial \Delta \mathbf{K}_n \mathbf{U}_n^{ihs}}{\partial \rho_e} \right) \mathbf{H}_{DOF}^n$$
$$- \boldsymbol{\lambda}^T \left( \frac{\partial \mathbf{K}_{remain}}{\partial \rho_e} \mathbf{U}_{cut} + \mathbf{K}_{remain} \frac{\partial \mathbf{U}_{cut}}{\partial \rho_e} - \mathbf{K}_{cutoff} \sum_{n=cut+1}^{m} \frac{\partial \Delta \mathbf{U}_n}{\partial \rho_e} \mathbf{H}_{DOF}^n - \frac{\partial \mathbf{K}_{cutoff}}{\partial \rho_e} \sum_{i=cut+1}^{m} \Delta \mathbf{U}_n \, \mathbf{H}_{DOF}^n \right) \tag{5.24}$$

Collecting the $\dfrac{\partial \Delta \mathbf{U}_n}{\partial \rho_e}$ and $\dfrac{\partial \mathbf{U}_{cut}}{\partial \rho_e}$ terms:

$$\frac{dL}{d\rho_e} = \frac{\partial g_0}{\partial \rho_e} + \sum_{n=1}^{cut} \left( \frac{\partial g_0}{\partial \mathbf{U}_{res}} + \mathbf{K}_n \boldsymbol{\lambda}_n^1 \right) \frac{\partial \Delta \mathbf{U}_n}{\partial \rho_e} \mathbf{H}_{DOF}^n + \left( \frac{\partial g_0}{\partial \mathbf{U}_{cut}} + \mathbf{K}_{remain} \boldsymbol{\lambda} \right) \frac{\partial \mathbf{U}_{cut}}{\partial \rho_e} + \sum_{n=1}^{m} \left( \boldsymbol{\lambda}_n^{1\,T} \frac{\partial \mathbf{K}_n}{\partial \rho_e} \Delta \mathbf{U}_n - \boldsymbol{\lambda}_n^{1\,T} \frac{\partial \Delta \mathbf{K}_n \mathbf{U}_n^{ihs}}{\partial \rho_e} \right)$$
$$+ \boldsymbol{\lambda}^T \frac{\partial \mathbf{K}_{remain}}{\partial \rho_e} \mathbf{U}_{cut} - \boldsymbol{\lambda}^T \frac{\partial \mathbf{K}_{cutoff}}{\partial \rho_e} \sum_{n=cut+1}^{m} \Delta \mathbf{U}_n \, \mathbf{H}_{DOF}^n + \sum_{n=cut+1}^{m} \left( \frac{\partial g_0}{\partial \mathbf{U}_{res}} - \boldsymbol{\lambda}^T \mathbf{K}_{cutoff} + \boldsymbol{\lambda}_n^{1\,T} \mathbf{K}_n \right) \frac{\partial \Delta \mathbf{U}_n}{\partial \rho_e} \mathbf{H}_{DOF}^n \tag{5.25}$$

Then solving the following adjoint equations to obtain the $\boldsymbol{\lambda}$ and $\boldsymbol{\lambda}_n^1$ ($n = 1 : m$):

$$\frac{\partial g_0}{\partial \mathbf{U}_{cut}} + \mathbf{K}_{remain} \boldsymbol{\lambda} = 0$$

$$\frac{\partial g_0}{\partial \mathbf{U}_{res}} + \mathbf{K}_n \boldsymbol{\lambda}_n^1 = 0 \quad n = 1 : cut \tag{5.26}$$

$$\frac{\partial g_0}{\partial \mathbf{U}_{res}} - \boldsymbol{\lambda}^T \mathbf{K}_{cutoff} + \boldsymbol{\lambda}_n^{1\,T} \mathbf{K}_n = 0 \quad n = cut + 1 : m$$

Then, recalling the derivation introduced in `former content`, the gradient of objective

function could be expressed as:

$$\frac{dg_0}{d\rho_e} = \frac{\partial g_0}{\partial \rho_e} + \sum_{n=1}^{m}\left(\boldsymbol{\lambda}_n^{1\,T}\frac{\partial \mathbf{K}_n}{\partial \rho_e}\Delta \mathbf{U}_n - \boldsymbol{\lambda}_n^{1\,T}\frac{\partial \Delta \mathbf{K}_n \mathbf{U}_n^{ihs}}{\partial \rho_e}\right)\mathbf{H}_{DOF}^n + \boldsymbol{\lambda}^T\frac{\partial \mathbf{K}_{remain}}{\partial \rho_e}\mathbf{U}_{cut} - \boldsymbol{\lambda}^T\frac{\partial \mathbf{K}_{cutoff}}{\partial \rho_e}\sum_{n=cut+1}^{m}\Delta \mathbf{U}_n\,\mathbf{H}_{DOF}^n (5.27)$$

## 5.3.2. Topology optimization for LPBF framework

In this subsection, the topology optimization for LPBF framework is introduced, and the flowchart for the LPBF oriented topology optimization is shown in Figure 58. It can be seen from Figure 58 that the LPBF process simulation is considered into the loop of topology optimization.
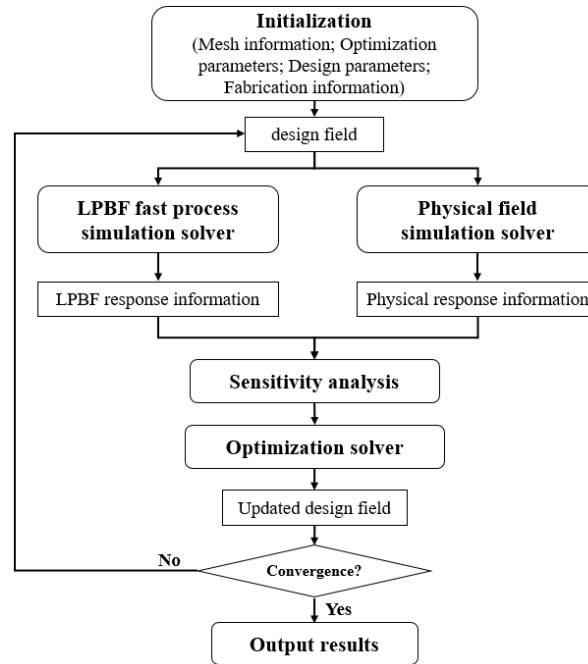


Figure 58. The flowchart for the topology optimization for LPBF framework.

Although topology optimization for addressing defects caused by residual stress/deformation has received some attention, effective solvers to simulate the manufacturing process (even though adopting the simplified ISM model) are still lacking. For the works addressing the residual stress or distortion constraint, when extended to

practical 3D problems, it will make the iterative finite element analysis for topology optimization computationally unaffordable. Therefore, the current mainstream-related work is still dominated by two-dimensional or three-dimensional coarse grid problems. In order to obtain optimized structures with detailed features to meet the industrial needs in AM field, a high-resolution design domain is required.

## 5.4. Summary

In this chapter, a fast LPBF process simulation solver based on ISM is proposed. This solver is capable of predicting the mechanical response resulting from the LPBF metal AM process, eliminating the need for complex multi-physics coupling calculations. By ensuring high accuracy while significantly reducing computational costs, this solver efficiently integrates with iterative topology optimization algorithms, enabling effective control over the manufacturing quality of the designed components.

In the subsequent chapter, building upon this solver, a series of topology optimization algorithms will be proposed to optimize the geometry of the workpiece and laser scanning path. This optimization aims to minimize defect responses and other issues associated with the LPBF process while ensuring the performance of the components.

## Chapter 6. Quality control topology optimization for LPBF metal AM

Recalling the content in chapter 2, each AM process introduces various process defects. In the previous chapter, I proposed a fast LPBF process simulation solver to accurately predict the mechanical defect response at the part scale. Additionally, I developed a mathematical model and algorithm framework that integrates this solver with topology optimization techniques. Therefore, in this chapter, I will focus on controlling the defect response in LPBF metal AM based on this framework.

Regarding the quality control of LPBF metal AM, this work primarily addresses residual stresses and residual distortion caused by the forming process. It is known that residual stresses or distortion in fabricated parts are influenced by factors such as the geometric shape of the parts themselves, laser scanning paths, and support structure geometry. Therefore, this chapter will consist of three works.

Firstly, controlling the maximum residual stress in the formed parts will be addressed by proposing a topology optimization algorithm that considers multiple manufacturing constraints. Secondly, an optimized scanning path algorithm will be introduced to control the maximum residual distortion of the formed parts by optimizing the printing direction for each laser scanning pattern. Finally, a support structure design perspective will be taken to reduce the residual distortion by optimizing the topology geometry of the support structures.

### 6.1. Maximum residual stress control in self-support structure design

Based on the fast LPBF process simulation solver and stress control method mentioned in former paragraph, a new algorithm coupled with the AM oriented topology optimization and the fast simulation solver are proposed to realize the residual stress control, which will be introduced in this subsection. This work proposes a topology optimization method to

design self-support structures for metal AM. Constraining the process-induced residual stresses is considered with this method to avoid part failures of cracking, delamination, or warpage. Specifically, the ISM-based FEM model mentioned in former subsections is adopted to simulate the mechanical behavior during the LPBF process. Then, the residual stress constrained self-support topology optimization problem is formulated. Finally, the proposed method is applied to a 2D benchmark example to demonstrate the effectiveness of residual stress and distortion control.

### 6.1.1. Optimization solution

### 6.1.1.1. Material state interpolation

Similar to thermal strain loading, inherent strain is also a type of design-dependent loading. The usual SIMP interpolation scheme presents numerical difficulties in the presence of design-dependent loading. Both the element stiffness and design-dependent load are insensitive to the varying density when the density is close to zero, and the penalizations are larger than 1, leading to non-trivialness of totally eliminating the grey elements. This phenomenon has been deeply investigated and explained in [242]. The RAMP interpolation scheme avoids the above issue and therefore is employed as:

$$\eta_e^E = \frac{\rho_e}{1 + R_E(1 - \rho_e)} \tag{6.1}$$

$$\eta_e^\beta = \frac{\rho_e}{1 + R_\beta(1 - \rho_e)} \tag{6.2}$$

After solving Eq. (5.13) to determine the displacements for each printing stage, the residual stress tensor for element e could be computed by:

$$\boldsymbol{\sigma}_e = \eta_e^S \sum_{n=1}^{m} \left[ \vartheta_e^n \mathbf{D}_0 \left( \mathbf{B} \Delta \mathbf{U}_e^n - \delta_e^n \boldsymbol{\epsilon}^{ihs} \right) \right] \tag{6.3}$$

Where $\eta_e^S$ ($\eta_e^S = \xi^{Ps}$) is a SIMP-like interpolation for the stress level to remove the stress

112

singularity phenomena, and $P_S$ is the relaxation parameter for stress and is usually set as 0.5. The von Mises failure criteria is adopted in this work, and the effective stress of the element centroid could be expressed as:

$$\sigma_{Vm,e} = \left(\overline{\boldsymbol{\sigma}}_e{}^T \mathbf{V} \overline{\boldsymbol{\sigma}}_e\right)^{\frac{1}{2}} \tag{6.4}$$

### 6.1.1.2. Model formulation

For the optimization problem, the objective function is to minimize the structural compliance subject to the maximum residual stress constraint and mass fraction constraint. The mathematical formulation of this optimization problem can be expressed as follows:

$$
\begin{cases}
\quad\text{find: } \boldsymbol{\mu} \\
\quad\text{minimize: } C = \mathbf{U}_c{}^T \mathbf{K}_c \mathbf{U}_c \\
\text{subject to: }
\begin{cases}
\mathbf{K}_n \Delta \mathbf{U}_n = \Delta \mathbf{K}_n \mathbf{U}_n^{ihs} \ (n = 1,2,\dots,m) \\
\dfrac{M}{\overline{M}} \le M_f \\
\widehat{\boldsymbol{\sigma}}_{PN} \le 1 \\
\mu_{min} \le \forall \mu_e \le 1
\end{cases}
\end{cases}
\tag{6.5}
$$

Where $\mathbf{U}_c$ is the nodal displacement field due to the external mechanical load, $\mathbf{K}_c$ is the structure global stiffness matrix, $M = \sum_{e=1}^{Nel}(\xi_e \cdot m_0)$ is the total mass of the structure, $m_0$ is the solid elemental mass, and $M_f$ is the mass fraction defined by users. $\mu_{min}$ is set as $1E - 9$, which could be used to avoid matrix singularity during the layer-by-layer AM analysis and static mechanical analysis. $\widehat{\boldsymbol{\sigma}}_{PN}$ indicates the maximum residual distortion through the aggregation method.

### 6.1.1.3. Sensitivity analysis

The MMA will be adopted to solve the optimization problem, which requires first-order sensitivity information of the constraints and the objective function. Special care should be taken to treat the residual stress constraint properly. The gradients of $\widehat{\boldsymbol{\sigma}}_{PN}$ are derived following the chain rule, as:

$$\frac{\partial \widehat{\sigma}_{PN}}{\partial \mu_j} = \frac{\partial \widehat{\sigma}_{PN}}{\partial \xi_j} \frac{\partial \xi_j}{\partial \bar{\bar{\mu}}_j} \frac{\partial \bar{\bar{\mu}}_j}{\partial \tilde{\mu}_j} \frac{\partial \tilde{\mu}_j}{\partial \mu_j} \tag{6.6}$$

Where $\xi_j$ is the physical density field after three layers of filters. $\frac{\partial \xi_j}{\partial \bar{\bar{\mu}}_j}$, $\frac{\partial \bar{\bar{\mu}}_j}{\partial \tilde{\mu}_j}$, and $\frac{\partial \tilde{\mu}_j}{\partial \mu_j}$ represent the standard modifications to the sensitivity due to AM filter, Heaviside projection filter, and PDE smoothing filter, respectively. The detailed expressions could be found in [224][296][295].

For the term $\frac{\partial \widehat{\sigma}_{PN}}{\partial \xi_j}$, we could have:

$$\frac{\partial \widehat{\sigma}_{PN}}{\partial \xi_j} = \sum_{e=1}^{Nel} \left[ \frac{\partial \widehat{\sigma}_{PN}}{\partial \sigma_{Vm,e}} \left( \frac{\partial \sigma_{Vm,e}}{\partial \boldsymbol{\sigma}_e} \right)^T \frac{\partial \boldsymbol{\sigma}_e}{\partial \xi_j} \right] \tag{6.7}$$

$\widehat{\sigma}_{PN}$ with respect to the element-wise von Mises stress, we arrive:

$$\frac{\partial \widehat{\sigma}_{PN}}{\partial \sigma_{Vm,e}} = c \cdot \frac{1}{P} \cdot \left[ \sum_{e=1}^{Nel} \left( \frac{\sigma_{Vm,e}}{\sigma_Y} \right)^P \right]^{\left( \frac{1}{P} - 1 \right)} \cdot P \cdot \left( \frac{\sigma_{Vm,e}}{\sigma_Y} \right)^{(P-1)} \cdot \frac{1}{\sigma_Y} \tag{6.8}$$

$\sigma_Y$ is the yield stress value. The derivative of the element-wise von Mises stress with respect to its stress components can be expressed as:

$$\frac{\partial \sigma_{Vm,e}}{\partial \boldsymbol{\sigma}_e} = \sigma_{Vm,e}^{-1} \cdot \boldsymbol{\sigma}_e^T \cdot \mathbf{V} \tag{6.9}$$

$$\frac{\partial \boldsymbol{\sigma}_e}{\partial \xi_j} = \frac{\partial \left[ \eta_e^S \sum_{n=1}^m \vartheta_e^n \mathbf{D}_0 \left( \mathbf{B} \Delta \mathbf{U}_e^n - \delta_e^n \boldsymbol{\epsilon}^{ihs} \right) \right]}{\partial \xi_j} \tag{6.10}$$

$$\frac{\partial \boldsymbol{\sigma}_e}{\partial \xi_j} = \sum_{n=1}^m \left( \vartheta_e^n \frac{\partial \eta_e^S}{\partial \xi_j} \mathbf{D}_0 \mathbf{B} \Delta \mathbf{U}_e^n + \vartheta_e^n \eta_e^S \mathbf{D}_0 \mathbf{B} \frac{\partial \Delta \mathbf{U}_e^n}{\partial \xi_j} - \delta_e^n \vartheta_e^n \frac{\partial \eta_e^S}{\partial \xi_j} \mathbf{D}_0 \boldsymbol{\epsilon}^{ihs} \right) \tag{6.11}$$

and,

$$\frac{\partial \widehat{\sigma}_{PN}}{\partial \xi_j} = \sum_{e=1}^{Nel} \left[ \frac{\partial \widehat{\sigma}_{PN}}{\partial \sigma_{Vm,e}} \left( \frac{\partial \sigma_{Vm,e}}{\partial \boldsymbol{\sigma}_e} \right)^T \sum_{n=1}^m \left( \vartheta_e^n \frac{\partial \eta_e^S}{\partial \xi_j} \mathbf{D}_0 \mathbf{B} \Delta \mathbf{U}_e^n + \vartheta_e^n \eta_e^S \mathbf{D}_0 \mathbf{B} \frac{\partial \Delta \mathbf{U}_e^n}{\partial \xi_j} - \delta_e^n \vartheta_e^n \frac{\partial \eta_e^S}{\partial \xi_j} \mathbf{D}_0 \boldsymbol{\epsilon}^{ihs} \right) \right] \tag{6.12}$$

Note that the $\frac{\partial \eta_e^S}{\partial \xi_j}$ term is nonzero only for $e = j$. Thus, the summation for some terms can be ignored, and the equation Eq. (6.12) can be reduced as:

$$\frac{\partial \widehat{\sigma}_{PN}}{\partial \xi_j} = \sum_{n=1}^{m} \left[ \frac{\partial \widehat{\sigma}_{PN}}{\partial \sigma_{Vm,j}} \left( \frac{\partial \sigma_{Vm,j}}{\partial \sigma_e} \right)^T \left( \vartheta_j^n \frac{\partial \eta_j^S}{\partial \xi_j} D_0 B \Delta U_e^n - \delta_j^n \vartheta_j^n \frac{\partial \eta_j^S}{\partial \xi_j} D_0 \epsilon^{ihs} \right) \right] + \\ \sum_{n=1}^{m} \left[ \sum_{e=1}^{Nel} \frac{\partial \widehat{\sigma}_{PN}}{\partial \sigma_{Vm,e}} \left( \frac{\partial \sigma_{Vm,e}}{\partial \sigma_e} \right)^T \left( \vartheta_e^n \eta_e^S D_0 B \frac{\partial \Delta U_e^n}{\partial \xi_j} \right) \right] \tag{6.13}$$

The adjoint method will be adopted to address the unknown term $\frac{\partial \Delta U_e^n}{\partial \xi_j}$ in Eq. (6.13). Specifically, for the $i^{th}$ layer in the additive manufacturing process, we have: $K_n \Delta U_n = \Delta K_n U_n^{ihs}$. Taking derivatives of both sides of the balance equation yields:

$$\frac{\partial K_n}{\partial \xi_j} \Delta U_n + K_n \frac{\partial \Delta U_n}{\partial \xi_j} = \frac{\partial \Delta K_n U_n^{ihs}}{\partial \xi_j} \tag{6.18}$$

Then, we could arrive at the following expression:

$$\frac{\partial \Delta U_e^n}{\partial \xi_j} = L_e (K_n)^{-1} \left( \frac{\partial \Delta K_n U_n^{ihs}}{\partial \xi_j} - \frac{\partial K_n}{\partial \xi_j} \Delta U_n \right) \tag{6.19}$$

Substituting the preceding relation into Eq. (6.17) and introducing the adjoint variable $\lambda_n$ yields:

$$\frac{\partial \widehat{\sigma}_{PN}}{\partial \xi_j} = \sum_{n=1}^{m} \left[ \frac{\partial \widehat{\sigma}_{PN}}{\partial \sigma_{Vm,e}} \left( \frac{\partial \sigma_{Vm,j}}{\partial \sigma_j} \right)^T \left( \vartheta_j^n \frac{\partial \eta_j^S}{\partial \xi_j} D_0 B \Delta U_e^n - \delta_j^n \vartheta_j^n \frac{\partial \eta_j^S}{\partial \xi_j} D_0 \epsilon^{ihs} \right) \right] + \sum_{n=1}^{m} \lambda_n^T \left( \frac{\partial \Delta K_n U_n^{ihs}}{\partial \xi_j} - \frac{\partial K_n}{\partial \xi_j} \Delta U_n \right) \tag{6.20}$$

where the solution of the adjoint problem determines the adjoint variable:

$$K_n \lambda_n = \sum_{e=1}^{Nel} \left[ \vartheta_e^n \eta_e^S \frac{\partial \widehat{\sigma}_{PN}}{\partial \sigma_{Vm,e}} \left( \frac{\partial \sigma_{Vm,e}}{\partial \sigma_e} \right)^T D_0 B L_e \right] \tag{6.21}$$

### 6.1.2. Numerical example

### 6.1.2.1. The MBB beam structure design

This section validates the proposed method with a classical 2-D benchmark case: the MBB

115

beam. The 'Rule 45 degree', indicating the maximum self-support overhang angle of 45 degrees, is adopted in this research. For all numerical examples, 4-node quadrilateral elements are adopted. The smoothing filter radius for topology variables is twice the typical finite element size. The material adopted in this research is Ti6Al4V, Young's modulus of 110 GPa, Poisson's ratio of 0.3, and yield strength of $\sigma_Y = 1160$ MPa. In this research, the inherent strain value is set as $\epsilon_x^{ihs} = \epsilon_y^{ihs} = -0.002$. The objective function is to minimize the structure compliance under a mass fraction constraint of 50%.
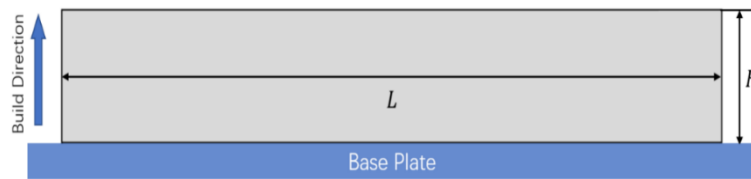


Figure 59. Illustration of the design domain for the MBB beam.

The MBB benchmark example, as shown in Figure 59, whose structural sizes are defined with L = 240mm and H = 40mm. The building direction is assumed bottom-up. The fixed design domain in Figure 60 is divided into m = 80 layers with a constant layer thickness of 0.5mm in the building direction.
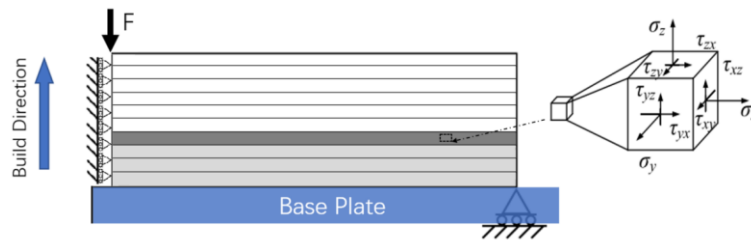


Figure 60. The boundary condition for the MBB beam.

Because of the symmetry condition, only one-half of the structure will be optimized; see Figure 59. The MBB structure is loaded with a concentrated vertical force (F = 800N) at the up-left corner, the bottom-right corner is supported on a roller, and the symmetry

boundary condition is applied to the left edge. A mesh with $240 \times 80$ first-order square elements of size $0.5\text{mm} \times 0.5\text{mm}$ is employed to discretize the design space.
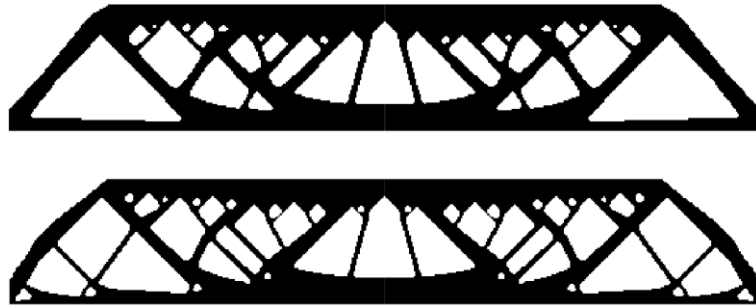


Figure 61. The MBB beam results: (top) with self-support but without residual stress constraint; (bellow) with self-support and residual stress constraints.

Figure 61 displays the topology-optimized solutions found when the build direction is 'bottom-up', and different sets of constraints are applied for these solutions. The final objective values of the results in Figure 61 are 1062.235 J and 1081.113 J, respectively.
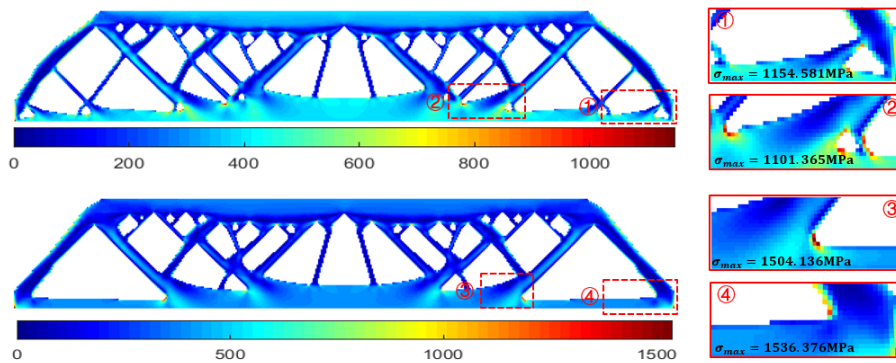


Figure 62. The residual stress distribution of the MBB results before cut-off from the platen.

Figure 62 presents the simulation results containing the total distortion and residual stress distribution for the two as-fabricated parts. The maximum stresses are observed at the lower corners for both results. For the design in Figure 61 (a), the maximum stress amplitude is 1536.376 MPa, which exceeds the allowable material stress limit. This will

cause delamination of the printed beam from the substrate. Then, for the design in Figure 61 (b), the maximum stress level is reduced to 1154.581 MPa (satisfy the stress constraint) through an optimized material distribution. Additionally, as observed from Figure 63, the residual stress-constrained design exhibits minor cut-off deformation (i.e., the maximum distortion is $u_{max}= 0.62$ mm) compared to non-constrained design, where $u_{max}= 0.87$ mm.
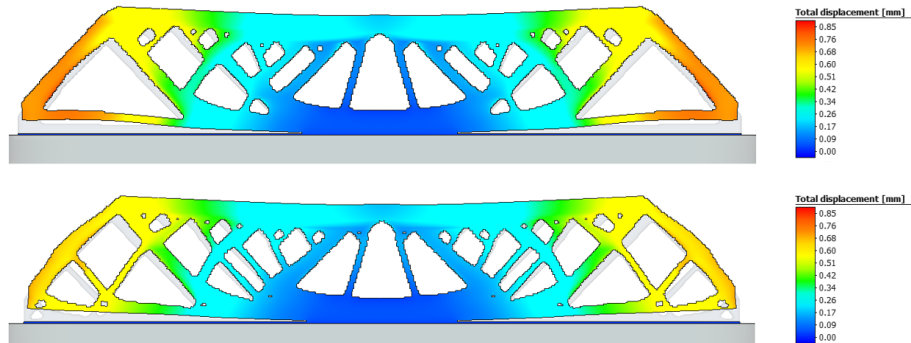


Figure 63. The residual distortion distribution of the MBB results after cut-off from the platen.

### 6.1.2.2. The minimum length control for the results

| Filter radius | Eroded version | Intermediate (final) version |
|---|---|---|
| $r_{min}$ = 0.67mm |  |  |
| $r_{min}$ = 1.33mm |  |  |

| | | |
|---|---|---|
| $r_{min}$ $= 2.00mm$ | | |
| $r_{min}$ $= 2.67mm$ | | |

Table 4. The obtained design with different length control parameters.

The first MBB benchmark example shown in Figure 61 is investigated again, but a finer mesh with $360 \times 120$ first order square elements of size $0.33mm \times 0.33mm$ is employed to discretize the design space. In this case, four different smoothed filter radii are adopted in this case, which are 0.667mm, 1.333mm, 2.000mm, and 2.667mm, respectively. The threshold value for the erosion projection is set as 0.65.
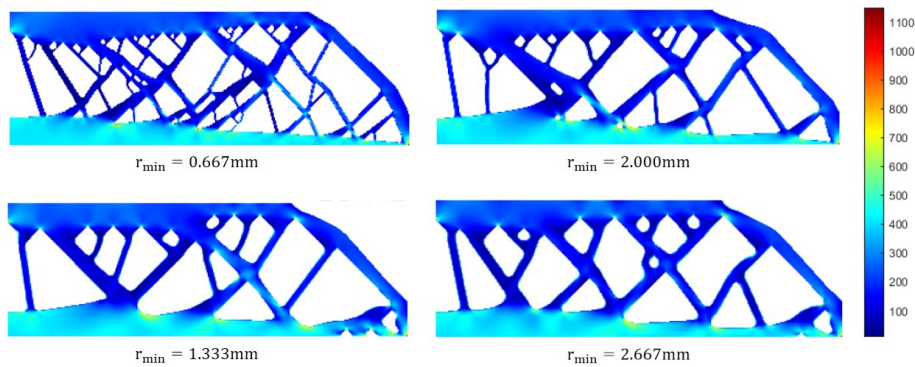


Figure 64. The residual stress distribution for the results with different length control parameters.

Table 4 lists the eroded and Intermediate designs with different length control sizes. Their residual stress distributions are plotted in Figure 64. As expected, the eroded design consists of solid features with small thicknesses and the intermediate design exhibits

119

features with larger thicknesses. In all the cases, the checkerboard pattern and the length control could be effectively avoided and achieved. As indicated by the optimization data concluded in Figure 65, as the density filter radius (length control size) increases, the overall stiffness of the structure gradually decreases under the premise that the maximum stress constraint remains unchanged.
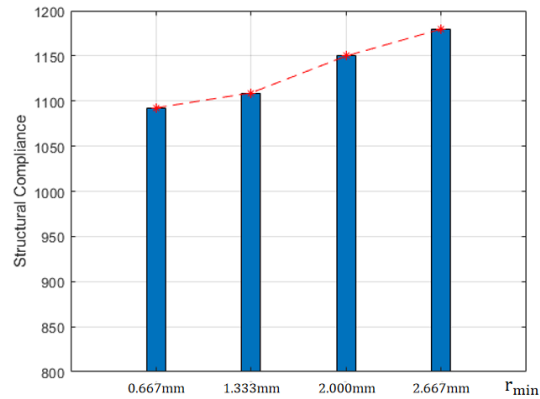


Figure 65. The mechanical performance of the results shown in 0.

### 6.1.3. Conclusion for this work

A topology optimization method to design self-support structures with residual stress constraint is proposed in this paper. A couple of conclusions can be drawn as follows: (1) A compliance-minimization problem considering the maximum volume fraction and residual stress constraints is formulated. Besides, to ensure the manufacturability of the structures, all overhang boundaries are designed with an inclination angle greater than the minimum allowable self-supporting angle (45 degrees); (2) To facilitate the formulation of the topology optimization problem involving the inherent strain load, the concept of ILC is introduced in this study as an inherent property of the material; (3) Using the RAMP interpolation and a corrected aggregation technique for elemental stresses, the proposed method is shown to effectively enforce the maximum residual stress and volume fraction

limits on benchmark numerical examples; (4) Effect of different RAMP parameters for the interpolation of ILC is discussed. To obtain an optimal result with a stable converging process, $R_\beta = R_E = 8$ is suggested; (5) An interesting finding is that even though no direct relationship exists between the maximum residual stress and maximum residual distortion; however, constraining the maximum residual stress always leads to a reduced maximum residual distortion; (6) The minimum length control for the proposed method is investigated by us. Under the same residual stress constraint, as the minimum length size increases, the obtained structural performance will become worse.

In our forthcoming work, the proposed method focused on large-scale 3D case under more mature parallel framework will be concentrated, which is challenging since the huge computation and RAM cost for the FEM solver limit us for solving larger industrial-level problems. Additionally, the adopted parallel based ISM will be further modified to make the performance of obtained complex structure more in line with the actual experimental results.

## 6.2. An island scanning optimization method for given geometry parts.

It is widely acknowledged that the residual stress distribution for a given part is closely related to the laser scanning path pattern and its support structure, as shown by both experiments and numerical tests [250][251][252]. In ISM, differently oriented inherent strains could be activated by different scanning paths in each layer, and thus affect the printing quality of part. The influence on thermal residual stress or distortion of different scanning orientations have been widely explored by many researchers. In this research, a systemic metal AM oriented island-type scanning pattern optimization method, which could reduce the maximum distortion during the manufacturing process, is proposed. A non-constraint optimization problem is formulated to find the optimal island scanning path

in each print layer. The stability-based aggregation method is adopted to explicitly describe the maximum distortion. Figure 66 shows the methodology of this work.
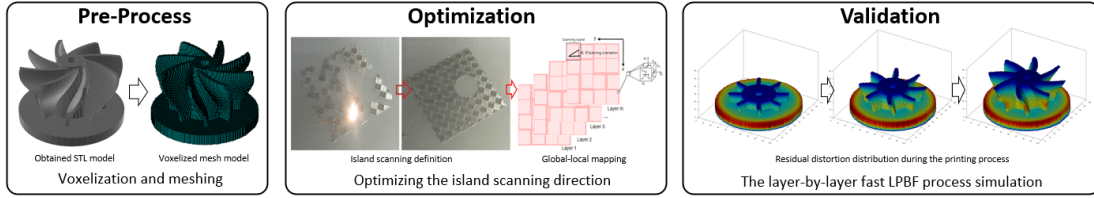


Figure 66. The methodology of the proposed work.

### 6.2.1. Non-constraint optimization problem formulation

### 6.2.1.1. Local-global mapping

Note that there is a mapping relationship between the island-wise orientation angle $\varrho$ and element-wise orientation angle $\boldsymbol{\theta}$:

$$\varrho = \mathbf{M}\boldsymbol{\theta} \tag{6.22}$$

where the $\mathbf{M}$ is $0-1$ mapping matrix with $\text{Nel} \times \text{Nd}$ dimensions, $\text{Nel}$ is the total number of finite elements in this model, and $\text{Nd}$ is the total number of design variables (the number of scanning island Figure 67).
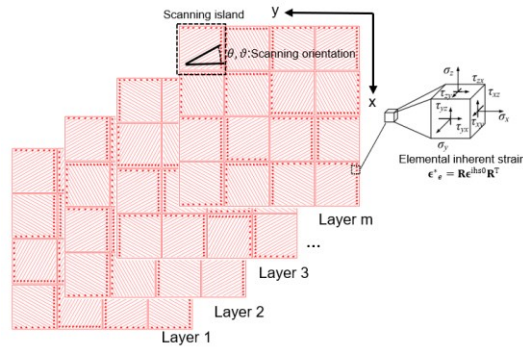


Figure 67. Illustration of rotated inherent strains in different print layers.

### 6.2.1.2. Optimization model formulation

For the optimization problem, the objective function is formulated to minimize the

maximum structural distortion under the inherent strain load. The mathematical

formulation of this optimization problem can be expressed as follows:

$$\begin{cases} \text{find: } \boldsymbol{\varrho} = \{\varrho_k\} \ (k = 1,2,3, \dots, Nd) \\ \text{minimize: } U_{max}(\boldsymbol{\varrho}) \\ \text{subject to: } \begin{cases} \mathbf{K}_n \Delta \mathbf{U}_n = \Delta \mathbf{K}_n \mathbf{U}_n^{ihs} \ (n = 1,2, \dots, m) \\ 0° \leq \forall \varrho \leq 180° \end{cases} \end{cases} \tag{6.23}$$

$U_{max}$ indicates the maximum residual distortion, which can be restated in terms of a single

differentiable global quantity through the aggregation method. The P-norm aggregation

function is adopted in this research, and the maximum displacement could be

approximately expressed as:

$$U_{max} \approx \overline{U}_{PN} = c \cdot U_{PN} = c \cdot \left( \sum_{i=1}^{Nod} \left( U_{res,i} \right)^P \right)^{\frac{1}{P}} \tag{6.24}$$

$\overline{U}_{PN}$ is the corrected global P-norm measure, which is the same with the aggregation

expression mentioned in subsection 3.1.2. $Nod$ is the node number involved in the mesh.

### 6.2.1.3. Sensitivity analysis

The MMA will be adopted to solve the optimization problem, which requires first order

sensitivity information of the objective function. The corresponding Lagrangian function

for the objective could be written as:

$$L = \overline{U}_{PN} + \sum_{n=1}^{m} \boldsymbol{\lambda}_n^T \left( \mathbf{K}_n \Delta \mathbf{U}_n - \Delta \mathbf{K}_n \mathbf{U}_n^{ihs} \right) \mathbf{H}_{DOF}^n \tag{6.25}$$

The gradient of the $L$ respect to the $\boldsymbol{\varrho}$ is:

$$\frac{\partial L}{\partial \boldsymbol{\varrho}} = \frac{\partial L}{\partial \boldsymbol{\theta}} \mathbf{M} \tag{6.26}$$

$$\frac{\partial L}{\partial \boldsymbol{\theta}} = \frac{\partial \overline{U}_{PN}}{\partial \mathbf{U}_{res}} \left( \sum_{n=1}^{m} \frac{\partial \Delta \mathbf{U}_n}{\partial \boldsymbol{\theta}} \mathbf{H}_{DOF}^n \right) + \sum_{n=1}^{m} \boldsymbol{\lambda}_n^T \left( \mathbf{K}_n \frac{\partial \Delta \mathbf{U}_n}{\partial \boldsymbol{\theta}} - \frac{\partial \Delta \mathbf{K}_n \mathbf{U}_n^{ihs}}{\partial \boldsymbol{\theta}} \right) \mathbf{H}_{DOF}^n \tag{6.27}$$

123

Collecting the $\frac{\partial \Delta \mathbf{U}_n}{\partial \boldsymbol{\theta}}$ term:

$$\frac{\partial L}{\partial \boldsymbol{\theta}} = \sum_{n=1}^{m} \left( \frac{\partial \overline{\mathbf{U}}_{PN}}{\partial \mathbf{U}_{res}} + \boldsymbol{\lambda}_n^T \mathbf{K}_n \right) \frac{\partial \Delta \mathbf{U}_n}{\partial \boldsymbol{\theta}} \mathbf{H}_{DOF}^n - \sum_{n=1}^{m} \boldsymbol{\lambda}_n^T \frac{\partial \Delta \mathbf{K}_n \mathbf{U}_n^{ihs}}{\partial \boldsymbol{\theta}} \mathbf{H}_{DOF}^n \tag{6.28}$$

Then solving the following adjoint equations to obtain the $\boldsymbol{\lambda}_n$ ($n = 1:m$):

$$\frac{\partial \overline{\mathbf{U}}_{PN}}{\partial \mathbf{U}_{res}} + \mathbf{K}_n \boldsymbol{\lambda}_n = 0 \tag{6.29}$$

where

$$\frac{\partial \overline{\mathbf{U}}_{PN}}{\partial \mathbf{U}_{res,i}} = c \cdot \frac{1}{P} \cdot \left[ \sum_{i=1}^{Nod} \left( \mathbf{U}_{res,i} \right)^P \right]^{\left( \frac{1}{P} - 1 \right)} \cdot P \cdot \left( \mathbf{U}_{res,i} \right)^{(P-1)} \tag{6.30}$$

$$\frac{\partial \Delta \mathbf{K}_n \mathbf{U}_n^{ihs}}{\partial \boldsymbol{\theta}} = \sum_{e=1}^{Nel} \left( \vartheta_e^n \mathbf{L}_e^T \int \mathbf{B}^T \mathbf{D}_0 \frac{\partial \boldsymbol{\epsilon}^{ihs}}{\partial \theta_e} d\Omega_e \right) \tag{6.31}$$

The final expression is:

$$\frac{\partial L}{\partial \boldsymbol{\varrho}} = - \left( \sum_{n=1}^{m} \boldsymbol{\lambda}_n^T \frac{\partial \Delta \mathbf{K}_n \mathbf{U}_n^{ihs}}{\partial \boldsymbol{\theta}} \mathbf{H}_{DOF}^n \right) \mathbf{M} \tag{6.32}$$

### 6.2.1.4. Numerical implementation

The flowchart of the proposed optimization approach is illustrated in Figure 68. In the first stage, the STL model of the printed part will be constructed by commercial software. In the next stage, a voxel-based methodology is employed to generate efficient structured hexahedral elements. Then, the initialization of design and optimization parameters will be conducted. After initialization, the ISM based layer-by-layer finite element model is constructed to simulate the structural physical behavior during the PBF process. The sensitivity analysis introduced in section 6.2.1.3 will be performed in the next stage. Subsequently, MMA optimizer will be adopted to update the design variables. The optimization will terminate when the objective value cannot be further improved. Namely,

the difference of the objective values within three successive iterations is less than 0.001, and the constraints are satisfied, or the maximum iterative number (400) is exceeded.
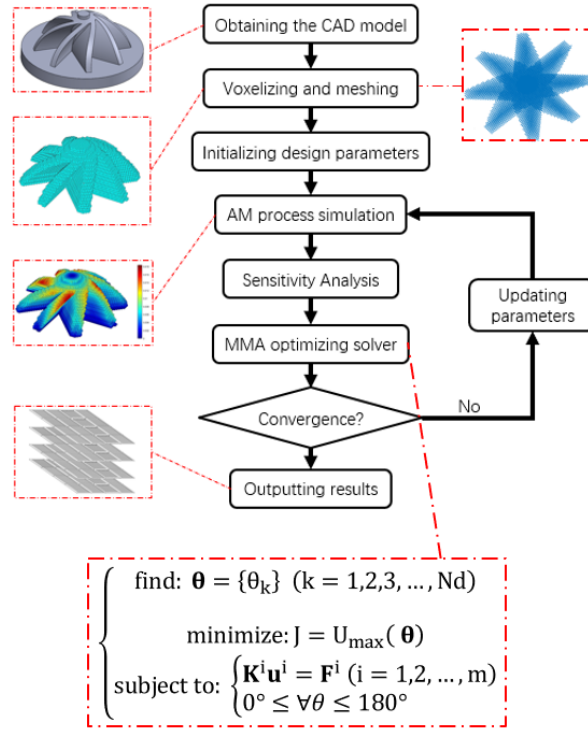


Figure 68. The process of the proposed method.

### 6.2.2. Numerical example

The numerical example is a fan blade with complex geometry used in mining machinery industry. For the outer section of the model, the length and width are 100 mm. The height of the entire component is 60 mm, indicating around 2160 thin layers in the large part. The whole model has been meshed by 6e5 first order Hexahedron elements of size $1 \times 1 \times 1$ mm, and its voxelized mesh model is shown in Figure 69 (a). The material properties are the same with the case shown in [Paper 3] section 3.

Firstly, this part is simulated by all scanning islands with the same scanning orientation 180°. Figure 69 (b) presents the simulation result containing the part-scale distortion

distribution for the as-fabricated part. Larger distortions are concentrated at the outer edges of some blades, and the maximum distortion is 3.15 mm.



(a)               (b)               (c)
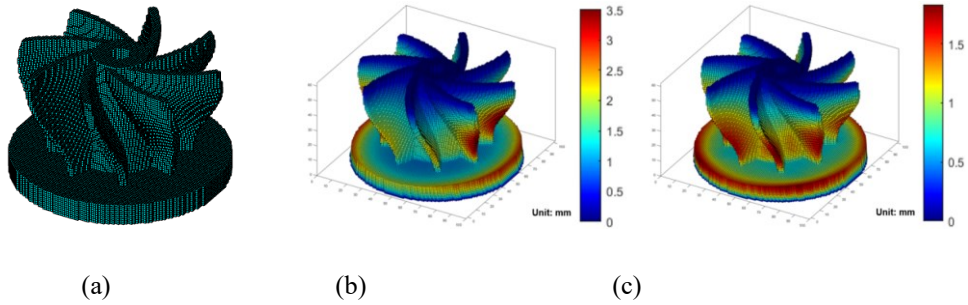
Figure 69. The voxelized model for the fan blade (a); The part-scale distortion distribution for the part with default scanning path (b); The part-scale distortion distribution for the part with optimized scanning path (c).

Figure 69 (c) presents the part-scale distortion distribution for the as-fabricated part with optimized scanning path and scanning paths for different layers are shown in Figure 70. Recalling that in our optimization problem formulation, the objective is to reduce the maximum part-scale distortion. Therefore, more even residual distortion distribution could be observed in the as-fabricated part, although the higher distortions are still distributed at outer edges of blades. Specifically, the part printed by optimized scanning path exhibits apparently smaller deformation (i.e., the maximum distortion is $u_{max} = 1.83$ mm ) compared to the part in Figure 69 (b), $u_{max} = 3.15$ mm.
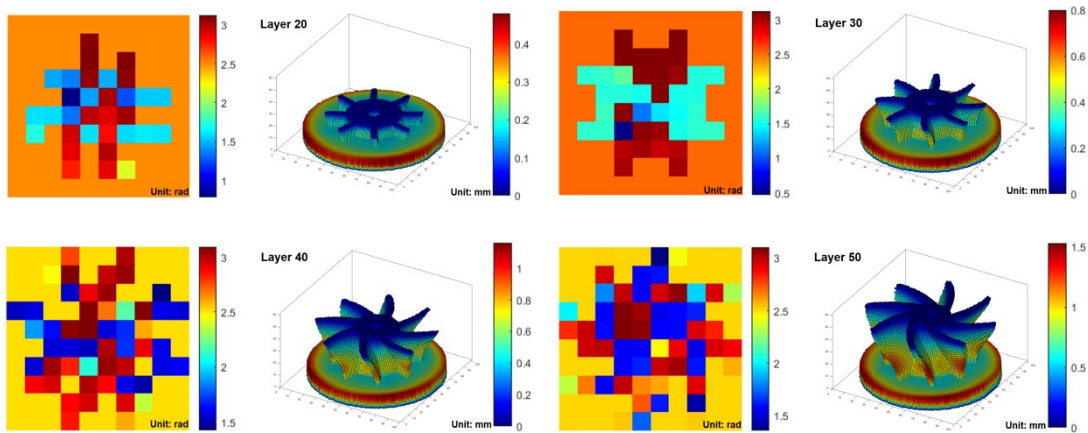
Figure 70. The distortions for the part and optimized scanning path: layer 20, layer 30, layer 40, and layer 50.

The convergence history curve for the optimization process is proposed in Figure 71. As the number of iterations increases, the objective value (blue line) is reduced and finally approached to a fixed value. Again, as we mentioned before, this optimization problem is non-constrained and the design variables are independent with each other, that is the reason why a smooth and sufficient convergence could be obtained within only 24 iterations. Additionally, the difference between the aggregated nodal maximum displacement value and real nodal maximum displacement is also plotted in Figure 71. The difference value is getting smaller and smaller with the number of iterations increasing, and it finally stabilized at 1e-8.
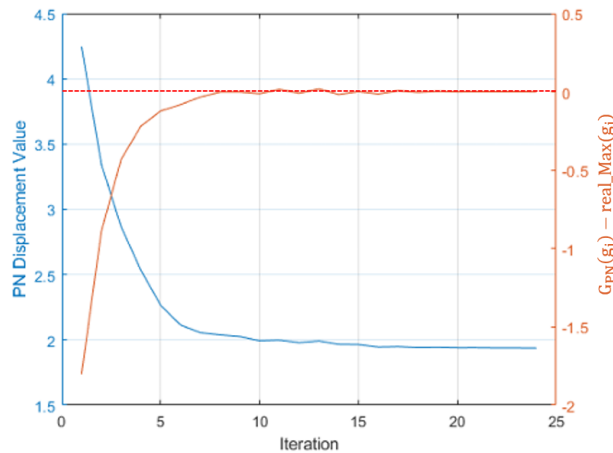


Figure 71. The convergence history plot.

### 6.2.3. Conclusion for this work

The proposed method could successfully reduce the distortion induced by the metal AM process through optimizing the laser scanning path. A typical AM oriented part is studied to examine the performance of this method. We compare the part-scale residual distortion distribution between the parts printed by different scanning path strategy. It is found that

the scanning path plays an important role for distortion minimization, and the part printed by the optimized scanning path exhibits better performances (smaller maximum distortion). Besides, a fast and stable convergence curve (Figure 71) also indicates the efficiency of the proposed method. Thus, this method is possible to ensure the manufacturability of AM builds.

## 6.3. Support structure topology optimization for LPBF metal AM

During the LPBF process, the support structures are manufactured in a consistent manner of the part and play a vital role in successfully printing out the component, since it gives support to the overhang features and transfer heats to the printing platform. However, the manufacturing cost is increased due to the additional printing time and metal powder consumption from introducing the extra support structure. Therefore, it is necessary to design cost-effective support structures that reduce both the manufacturing time and powder waste. In this subsection, a topology optimization method is proposed for the support structure design of LPBF metal parts to effectively prevent part failures caused by residual distortion.

A topology optimization model is constructed to design support structures for a given functional prototype by adopting a series of density filter [295], projection [296], and AM filter [223][224]. Figure 72 shows the procedures of filtering and projection.
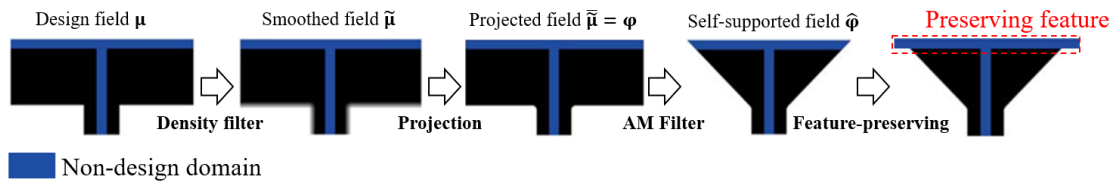


Figure 72. Workflow of topology optimization for AM support structures with three filters.

Firstly, the density design field $\boldsymbol{\mu}$ is smoothed by a PDE filter with $R_1$ to have $\tilde{\boldsymbol{\mu}}$ so that

checkerboard patterns can be avoided. Then, the smoothed density field $\tilde{\mu}$ is then projected with the sharpness factor $\beta_1$ and threshold factor $\alpha_1$ to obtain a clear phase $\bar{\tilde{\mu}} = \varphi$. The second AM filter removes overhang structures and ensures the self-support property, obtaining the phase $\hat{\varphi}$. The optimized result can be self-supported under a 45° overhang angle constraint, provided that a mesh with uniform square elements is used. Eventually, the non-design domain in $\hat{\varphi}$ is artificially set as 1 to maintain the prototype geometry.

## 6.3.1. AM constraint for support structure design

Multiple AM issues are considered, including the overhang issue, minimum length size control, and support structure easy removal. Among them, the application of minimum length control uses the same method as the work in subsection xx. Therefore, in this section, the minimum length control will not be described much, but the two newly introduced manufacturing constraints for the support structure design, the overhang constraint, and the support structure easy removal, will be introduced in detail.

### 6.3.1.1. Overhang constraint

The purpose of introducing the overhang constraint is to ensure that all overhang geometric features in the part to be supported can be effectively supported by the support structure.
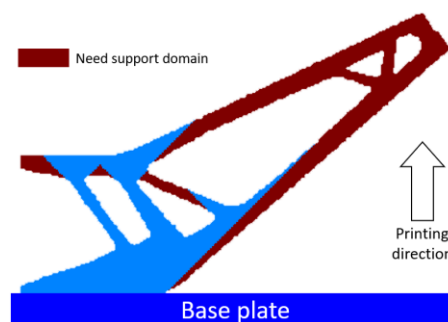


Figure 73. A given part needs a support domain (marked in deep red).

At the beginning of the optimization process, the AM filter will be ideally applied to the prototype without having any supports; the need-support region $\Omega_{sup}$ of the prototype will be obtained as shown in Figure 73 in deep red color. Then, a regional volume constraint is given as follows:

$$G_{sup} \leq \varepsilon_r \tag{6.33}$$

where $\varepsilon_r$ is a small value to ensure the convergence; and $G_{sup}$ is an indicator function to calculate the material volume of the non-supported overhang regions in $\Omega_{sup}$ as:

$$G_{sup} = \sum_{e \in \Omega_{sup}} (1 - \hat{\varphi}_e) \cdot V_0 \tag{6.34}$$

where $V_0$ is the volume fraction for the single element.

### 6.3.1.2. Easy removal constraint

To ensure that the support material can be removed easily. The simplest way is herein to ensure that the connection region between the support structure and its surroundings prototype geometry is porous. For a given prototype geometry Figure 74, a connection region $\Omega_{con}$ around the prototype and the baseplate with the thickness $t_{con}$ inside the design domain is defined first. Then, a local volume constraint proposed by Wu et al. [45] is applied in $\Omega_{con}$ to restrict the inside material volume fraction, hence resulting in a porous structural pattern in the $\Omega_{con}$.
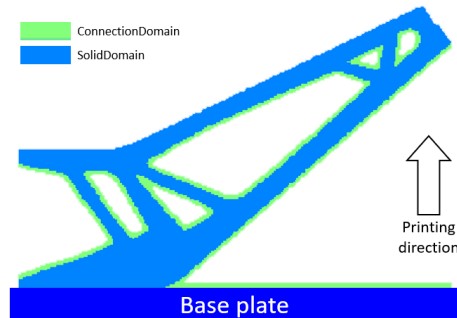


Figure 74. The connection domain (marked in green) of a given part.

130

For each element $e \in \Omega_{con}$, the local volume fraction $Vf_e$ in the neighborhood is calculated by:

$$Vf_e = \frac{\sum_{i \in \Omega_e} \widehat{\varphi}_i}{\#(\Omega_e)} \tag{6.35}$$

where $\Omega_e = \{i: \| x_e - x_i \| \leq R_2, \ e \in \Omega_{con}\}$ is the set of elements nearby the element $e$ within the distance $R_2$, and $\#(*)$ means 'the total number of'. Then the differentiable maximum local volume constraint could be formulated as follows:

$$G_{easy} = \left( \frac{1}{\#(\Omega_{con})} \sum_{e \in \Omega_{con}}^{\#(\Omega_{con})} (Vf_e)^P \right)^{\frac{1}{P}} \leq M_l \tag{6.36}$$

$G_{easy}$ is the global P-norm measure; $P$ is the aggregation parameter and $P = 16$; and $M_l$ is the local volume fraction.

### 6.3.2. Optimization Solution

### 6.3.2.1. Model formulation

For the optimization problem, the objective function is to minimize the structural gravity compliance and the maximum residual distortion subject to the volume fraction constraint, support constraints, and easy removal constraint. The scale of the structural gravity compliance value $C$ and measured maximum residual distortion value $\overline{U}_{PN}$ is significantly affected by the fixed design domain scale and boundary condition settings. Therefore, a normalized objective function is proposed with the following:

$$J = \gamma \cdot \overline{U}_{PN} + (1 - \gamma) \cdot C \tag{6.37}$$

$\gamma$ is the normalization factor which could make the values of $\overline{U}_{PN}$ and $C$ at the same order of magnitude. For $\overline{U}_{PN}$ is the approximation of $U_{max}$, which could be expressed as:

$$U_{max} \approx U_{PN} = \left( \sum_{i=1}^{Nod} \left( U_{m,i} \right)^P \right)^{\frac{1}{P}} \tag{6.38}$$

$U_{PN}$ is the global P-norm measure, $U_{m,i}$ is the printed distortion for the $i^{th}$ node, $P$ is the aggregation parameter, and $Nod$ is the total number of nodes. In conclusion, the mathematical formulation of this optimization problem can be expressed as follows:

$$\begin{cases} \text{find: } \boldsymbol{\mu} \\ \text{minimize: } J(\boldsymbol{\mu}) \\ \text{subject to: } \begin{cases} \mathbf{K_n \Delta U_n} = \Delta \mathbf{K_n U_n^{ihs}} \ (n = 1,2,\dots,m) \\ \mathbf{KU = T} \\ M \leq \overline{M} \\ G_{sup} \leq \varepsilon_r \\ G_{easy} \leq M_l \\ \mu_{min} \leq \forall \mu_e \leq 1 \end{cases} \end{cases} \tag{6.39}$$

where $m_0$ is the unit mass of the $e^{th}$ element in case of being filled with solid material. M denotes the design domain mass containing the solid material. $\mathbf{K}$, $\mathbf{U}$, and $\mathbf{T}$ are the global stiffness matrix, displacement vector, and gravity force vector, respectively. $\mu_{min}$ is set as $1e - 9$, which could be used to avoid matrix singularity.

### 6.3.2.2. Sensitivity analysis

The MMA will be adopted to solve the optimization problem, which requires first-order sensitivity information of the constraints and the objective function. Hence, details of the sensitivity analysis will be presented in this sub-section.

$$\frac{\partial Y}{\partial \mu} = \frac{\partial Y}{\partial \widehat{\varphi}} \cdot \frac{\partial \widehat{\varphi}}{\partial \varphi} \cdot \frac{\partial \varphi}{\partial \widetilde{\mu}} \cdot \frac{\partial \widetilde{\mu}}{\partial \mu} \tag{6.40}$$

where Y indicates the objective or constraint functions (J, M, $G_{sup}$, or $G_{easy}$); $\frac{\partial \widehat{\varphi}}{\partial \varphi}$, $\frac{\partial \varphi}{\partial \widetilde{\mu}}$, and $\frac{\partial \widetilde{\mu}}{\partial \mu}$ represent the standard modifications to the sensitivity due to AM filter, Heaviside projection filter, and PDE filter, respectively. The detailed expressions can be found in [223][224][296][295].

For the first objective, its Lagrange multiplier could be written as:

$$L_1 = C + \lambda_1^T(\mathbf{KU} - \mathbf{T}) \tag{6.41}$$

The gradient of the $L_1$ respect to the $\widehat{\varphi}_e$ is:

$$\frac{\partial L_1}{\partial \widehat{\varphi}_e} = \frac{\partial \mathbf{T}^T}{\partial \widehat{\varphi}_e}\mathbf{U} + (\mathbf{T}^T + \lambda_1^T\mathbf{K})\frac{\partial \mathbf{U}}{\partial \widehat{\varphi}_e} + \lambda_1^T\frac{\partial \mathbf{K}}{\partial \widehat{\varphi}_e}\mathbf{U} - \lambda_1^T\frac{\partial \mathbf{T}}{\partial \widehat{\varphi}_e} \tag{6.42}$$

collecting the $\frac{\partial \mathbf{U}}{\partial \widehat{\varphi}_e}$ term and solving the adjoint equation $\mathbf{T}^T + \lambda_1^T\mathbf{K}$, then we could arrive:

$$\frac{\partial L_1}{\partial \widehat{\varphi}_e} = 2\frac{\partial \mathbf{T}^T}{\partial \widehat{\varphi}_e}\mathbf{U} - \mathbf{U}^T\frac{\partial \mathbf{K}}{\partial \widehat{\varphi}_e}\mathbf{U} \tag{6.43}$$

The derivation of the terms $\frac{\partial \mathbf{T}^T}{\partial \widehat{\varphi}_e}$ and $\frac{\partial \mathbf{K}}{\partial \widehat{\varphi}_e}$ are the same with conventional design-dependent loading stiffness-based problems and thus omitted in this paper.

For the second objective, its Lagrange multiplier could be written as:

$$L_2 = \overline{\mathbf{U}}_{PN} + \sum_{n=1}^{m} \lambda_2^{nT}\left(\mathbf{K}_n\Delta\mathbf{U}_n \cdot \mathbf{H}_{DOF}^n - \Delta\mathbf{K}_n\mathbf{U}_n^{ihs} \cdot \mathbf{H}_{DOF}^n\right) \tag{6.44}$$

The gradient of the $L_2$ respect to the $\widehat{\varphi}_e$ is:

$$\frac{\partial L_2}{\partial \widehat{\varphi}_e} = \frac{\partial \overline{\mathbf{U}}_{PN}}{\partial \widehat{\varphi}_e} + \sum_{n=1}^{m}\left(\lambda_2^{nT}\left(\frac{\partial \mathbf{K}_n}{\partial \widehat{\varphi}_e}\Delta\mathbf{U}_n \cdot \mathbf{H}_{DOF}^n\right) + \lambda_2^{nT}\left(\mathbf{K}_n\frac{\partial \Delta\mathbf{U}_n}{\partial \widehat{\varphi}_e} \cdot \mathbf{H}_{DOF}^n\right) - \lambda_2^{nT}\left(\frac{\partial \Delta\mathbf{K}_n\mathbf{U}_n^{ihs}}{\partial \widehat{\varphi}_e} \cdot \mathbf{H}_{DOF}^n\right)\right) \tag{6.45}$$

For the $\frac{\partial \overline{\mathbf{U}}_{PN}}{\partial \widehat{\varphi}_e}$ term:

$$\frac{\partial \overline{\mathbf{U}}_{PN}}{\partial \widehat{\varphi}_e} = \frac{\partial \overline{\mathbf{U}}_{PN}}{\partial \mathbf{U}_{PN}}\frac{\partial \mathbf{U}_{PN}}{\partial \mathbf{U}_m}^T\frac{\partial \mathbf{U}_m}{\partial \widehat{\varphi}_e} = \frac{\partial \overline{\mathbf{U}}_{PN}}{\partial \mathbf{U}_{PN}}\left(\left[\sum_{i=1}^{Nod}(U_{m,i})^P\right]^{\left(\frac{1}{P}-1\right)}(U_m)^{(P-1)}\right)^T\frac{\partial \mathbf{U}_m}{\partial \widehat{\varphi}_e} \tag{6.46}$$

For the term $\frac{\partial \mathbf{U}_m}{\partial \widehat{\varphi}_e}$, we could arrive:

$$\frac{\partial \mathbf{U}_m}{\partial \widehat{\varphi}_e} = \sum_{n=1}^{m}\left(\frac{\partial \Delta\mathbf{U}_n}{\partial \widehat{\varphi}_e} \cdot \mathbf{H}_{DOF}^n\right) \tag{6.47}$$

Then collecting the $\frac{\partial \Delta U_n}{\partial \widehat{\varphi}_e}$ term:

$$\frac{\partial L_2}{\partial \widehat{\varphi}_e} = \sum_{n=1}^{m} \left( \frac{\partial \overline{U}_{PN}}{\partial U_{PN}} \frac{\partial U_{PN}}{\partial U_m}^T + \lambda_2^{nT} K_n \right) \left( \frac{\partial \Delta U_n}{\partial \widehat{\varphi}_e} \cdot H_{DOF}^n \right) + \sum_{n=1}^{m} \left( \lambda_2^{nT} \left( \frac{\partial K_n}{\partial \widehat{\varphi}_e} \Delta U_n \cdot H_{DOF}^n \right) - \lambda_2^{nT} \left( \frac{\partial \Delta K_n U_n^{ihs}}{\partial \widehat{\varphi}_e} \cdot H_{DOF}^n \right) \right) \tag{6.48}$$

Solving the following adjoint equation for each layer to obtain the $\lambda_2^n$:

$$\frac{\partial \overline{U}_{PN}}{\partial U_{PN}} \frac{\partial U_{PN}}{\partial U_m}^T + \lambda_2^{nT} K_n = 0, \tag{6.49}$$

then we could arrive:

$$\frac{\partial L_2}{\partial \widehat{\varphi}_e} = \sum_{n=1}^{m} \left( \lambda_2^{nT} \left( \frac{\partial K_n}{\partial \widehat{\varphi}_e} \Delta U_n \cdot H_{DOF}^n \right) - \lambda_2^{nT} \left( \frac{\partial \Delta K_n U_n^{ihs}}{\partial \widehat{\varphi}_e} \cdot H_{DOF}^n \right) \right) \tag{6.50}$$

and for the term $\frac{\partial \Delta K_n U_n^{ihs}}{\partial \widehat{\varphi}_e}$:

$$\frac{\partial \Delta K_n U_n^{ihs}}{\partial \widehat{\varphi}_e} = \sum_{e=1}^{Nel} \delta_e^n L_e^T \frac{\partial \eta_e^\beta}{\partial \widehat{\varphi}_e} \int B^T D_0 \varepsilon_0 \, d\Omega_e \tag{6.51}$$

and

$$\frac{\partial K_n}{\partial \widehat{\varphi}_e} = \sum_{e=1}^{Nel} \vartheta_e^n L_e^T \frac{\partial \eta_e^E}{\partial \widehat{\varphi}_e} \int B^T D_0 \, B \, d\Omega_e \, L_e \tag{6.52}$$

The gradient of the mass constraint function (M) respect to the $\widehat{\varphi}_e$ is:

$$\frac{\partial M}{\partial \widehat{\varphi}_e} = \sum_{i=1}^{Nel} \left( \frac{\partial (\widehat{\varphi}_i \cdot m_0)}{\partial \widehat{\varphi}_e} \right) \tag{6.53}$$

The gradient of the support constraint function $(G_{sup})$ respect to the $\widehat{\varphi}_e$ is:

$$\frac{\partial G_{sup}}{\partial \widehat{\varphi}_e} = - \sum_{i \in \Omega_{NS}} \left( \frac{\partial (\widehat{\varphi}_i \cdot V_0)}{\partial \widehat{\varphi}_e} \right) \tag{6.54}$$

The gradient of the easy removal constraint function $(G_{easy})$ respect to the $\widehat{\varphi}_e$ is:

$$\frac{\partial G_{sup}}{\partial \widehat{\varphi}_e} = \frac{1}{\#(\Omega_{con})} \left[ \sum_{e \in \Omega_{con}}^{\#(\Omega_{con})} (Vf_e)^P \right]^{\left(\frac{1}{P}-1\right)} (Vf_e)^{(P-1)} \frac{\partial Vf_e}{\partial \widehat{\varphi}_e} \tag{6.55}$$

Where $\frac{\partial Vf_e}{\partial \widehat{\varphi}_e}$ is the gradient of the elemental local volume fraction $Vf_e$:

$$\frac{\partial Vf_e}{\partial \widehat{\varphi}_e} = \sum_{i \in \Omega_e} \frac{1}{\#(\Omega_e)} \frac{\partial \widehat{\varphi}_i}{\partial \widehat{\varphi}_e} \tag{6.56}$$

### 6.3.2.3. Numerical implementation
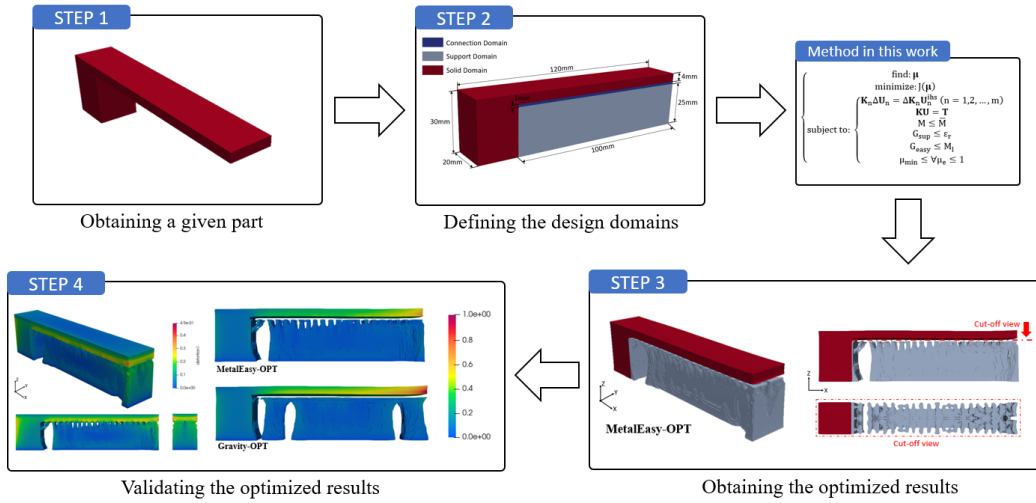


Figure 75. The flow chart of the proposed method.

The workflow of the topology optimization process is given in Figure 75, and the solution procedure is listed as follows:

Step 1: Obtaining the printed structure CAD model, and then voxelizing the model.

Step 2: Initializing the optimization parameters, the design domain, the non-design domain, the easy removal domain, and the metal additive manufacturing solver.

Step 3: Performing the proposed support structure topology optimization method considering the support constraint, mass constraint, minimum length control, and easy removal constraint.

Step 4: Post-processing and verification.

### 6.3.3. Numerical examples

The proposed method is validated in this section with several 2D and 3D benchmark examples. For the 2D numerical examples, four-node first-order quadrilateral elements are adopted; for 3D cases, eight-node first-order quadrilateral elements are adopted. Without any special statement, the density filter radius for topology variables is set as three element sizes (2D) or nine element sizes (3D). The material adopted in this work is Ti6Al4V, which has Young's modulus of 110 GPa, and Poisson's ratio of 0.3. The inherent strain value is set as $\epsilon_x^{ihs} = -0.02$ and $\epsilon_y^{ihs} = -0.02$, which is derived based on our experiment results.

For the MMA optimizer, the default move limit is 0.25. The optimization will terminate when the difference of the objective values within three successive iterations is less than 0.001 or the maximum iterative number is exceeded (300 in 2D cases or 150 in 3D cases).

### 6.3.3.1. Support structure design for a 2D wing structure
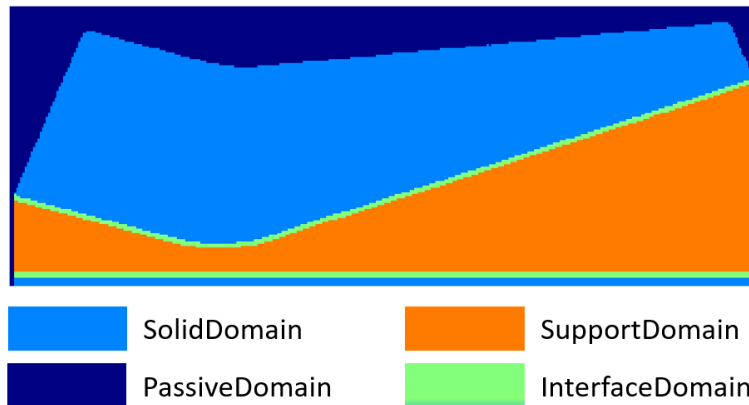


Figure 76. Fixed design domain and boundary conditions for the wing structure.

The first numerical example is to design the support structures for the wing structure shown in Figure 76, whose sizes are defined with $L = 350mm$ and $H = 130mm$, and the

build direction is still bottom-up. 130 printing layers with a thickness of 1mm are involved along the building direction. A mesh with $350 \times 130$ square elements of size $1 \times 1mm$ is employed to discretize the design space. The mass fraction constraint for the support structure has the upper limit of 40%, and the local volume fraction upper bound within $\Omega_{con}$ ($M_l$) is 60%. In this case, four different minimum length control sizes are considered, which are $R = 3.0$, $R = 3.5$, $R = 4.0$, and $R = 4.5$, respectively. For all the cases, the threshold value for the erosion projection is set as 0.65, and the weight coefficient $\gamma$ is 0.01.



(a)                                         (b)

(c)                                         (d)
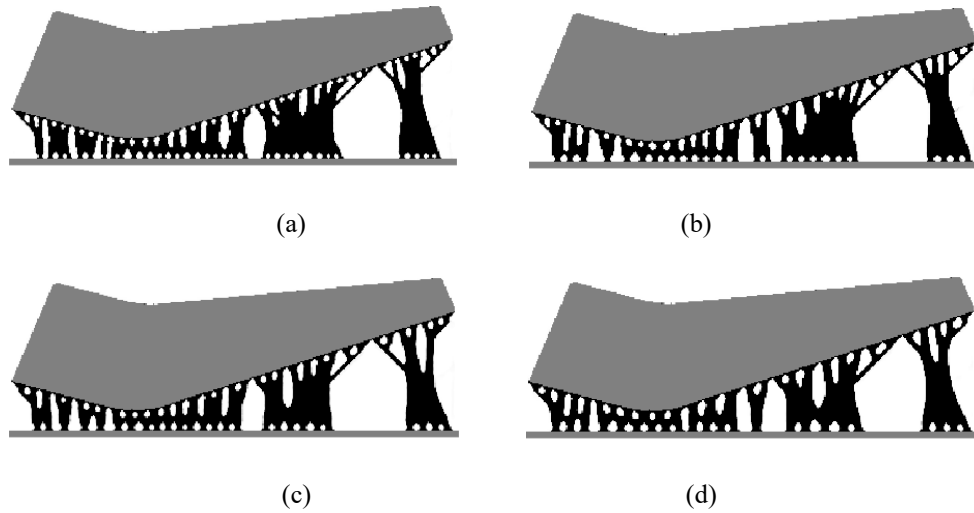
Figure 77. The optimal material distributions with different length scale control sizes: (a) $R = 3.0$; (b) $R = 3.5$; (c) $R = 4.0$; and (d) $R = 4.5$.

Figure 77 shows the structures designed from the four different length scale control sizes, and their residual distortion distributions are plotted in Figure 78. In all the cases, the one-node connection pattern/the minimum length control could be effectively avoided/achieved.
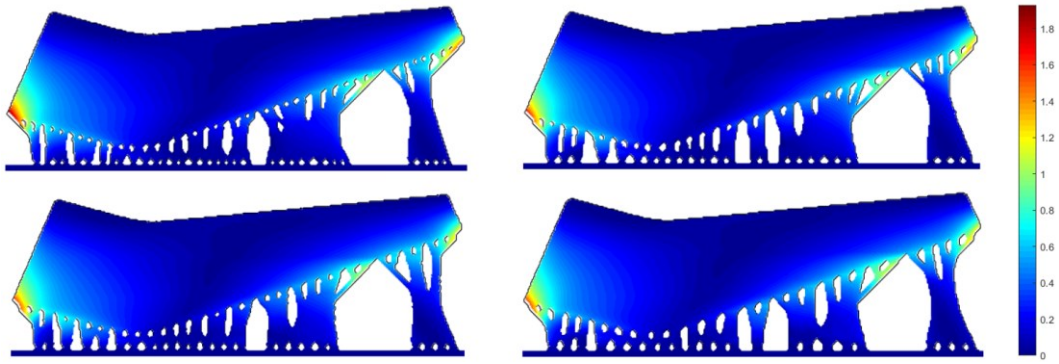
Figure 78. The residual distortion distributions with different length scale control sizes: (a) R = 3.0; (b) R = 3.5; (c) R = 4.0; and (d) R = 4.5.

Figure 79 summarizes the structural compliances and maximum residual distortions corresponding to the four optimization results. As indicated by the data, as the density filter radius increases, the structural compliance increases while the maximum residual distortion decreases.
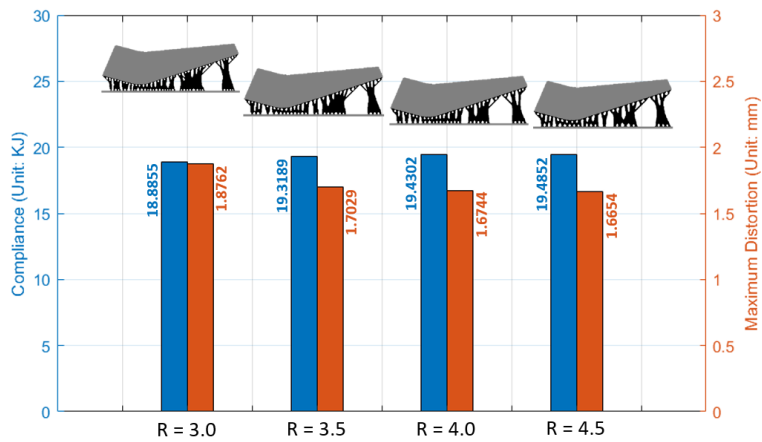


Figure 79. The summarized mechanical performance data.

**6.3.3.2. 3D support structure design for the teethed cantilever beam**
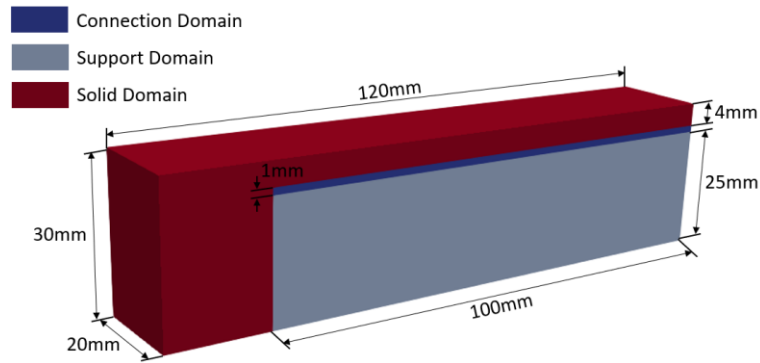


Figure 80. Fixed design domain and boundary conditions for the teeth cantilever.

The second numerical example is to design of the 3D support structures for the teeth cantilever beam, and its structural sizes are defined in Figure 80. The whole design domain is discretized with $360 \times 90 \times 60$ square elements. The build direction is bottom-up (along the positive z-axis), and the fixed design domain in Figure 80 is divided into $m = 30$ layers. Each printing layer is lumped with three elements along the building direction with a thickness of 1 mm. The objective function is to minimize the structural gravity compliance and the maximum residual distortion under a mass fraction of 40%, and the local volume constraint for the connection domain is 60%.
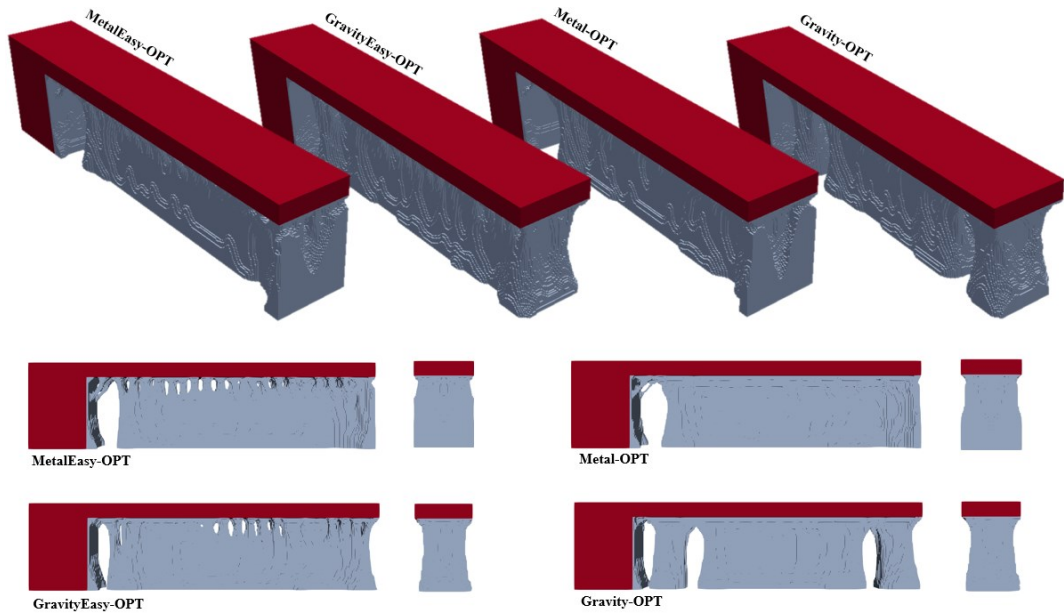
Figure 81. The results for the optimized support structures from Gravity-OPT, GravityEasy-OPT, Metal-OPT, and MetalEasy-OPT.
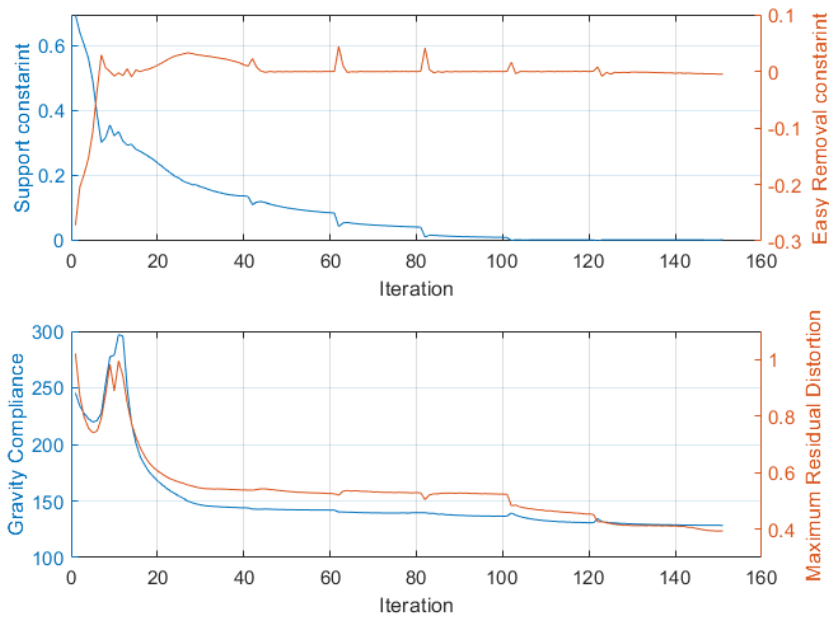


Figure 82. The convergence history for MetalEasy-OPT teeth cantilever beam case.

Similarly, four optimization cases are considered in this subsection (MetalEasy-OPT, GravityEasy-OPT, Metal-OPT, and Gravity-OPT), and their optimized results and

convergence history for MetalEasy-OPT are provided in Figure 81 and Figure 82, respectively. Figure 83 plots the part-scale residual distortion distributions for these results. Observing the results provided in Figure 81 and Figure 83, optimized support structures from Metal-based optimization are slightly different from Gravity-based results. The support structures tend to form stronger support near the free ends of the cantilevers, and this is where the occurrence of maximum deflection is observed during printing. Similar to the results obtained from the 2D Cantilever case, MetalEasy-OPT exhibits the lowest residual distortion, and the structures with easily removed features show better residual distortion reduction.
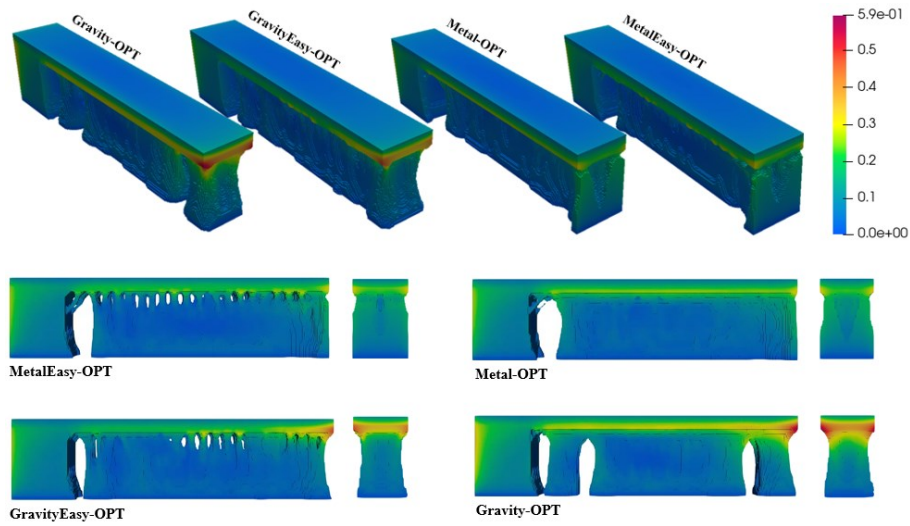


Figure 83. The residual distortion distribution for the optimized support structures from Gravity-OPT, GravityEasy-OPT, Metal-OPT, and MetalEasy-OPT.

Generally, the specimen will be partially cut with wire electric discharge machines. Figure 84 shows the top view of the required removal part for MetalEasy-OPT and Metal-OPT. The removal material in MetalEasy-OPT is obviously less than in Metal-OPT, which means that the support structure from MetalEasy-OPT could be quickly departed from the printed part. However, by this cutting, the residual stress is released, leading to large

deformation (residual warpage) of the specimens. Therefore, the residual warpage distortion after cutting for the four as-fabricated structures in Figure 81 is also provided in Figure 85.
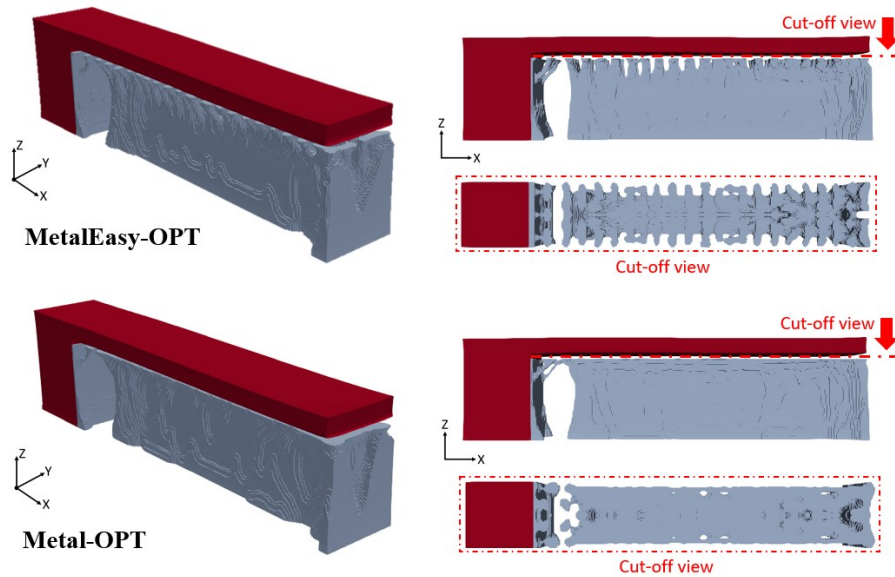


Figure 84. The removal material for the optimized support structure from MetalEasy-OPT and Metal-OPT.

Even though we have no specific control over residual warpage, the results obtained from metal-based optimization still exhibit better performance. Specifically, the largest maximum residual warpage (0.9973mm) is observed in the structure obtained from Gravity-OPT. The presence of easy-to-remove features also helps reduce residual warpage, as the GravityEasy-OPT result shows less residual warpage (0.8072mm) than the Gravity-OPT result. However, compared to the MetalEasy-OPT design and Metal-OPT design, their maximum residual warpages are very close (0.6123mm vs. 0.6178mm).
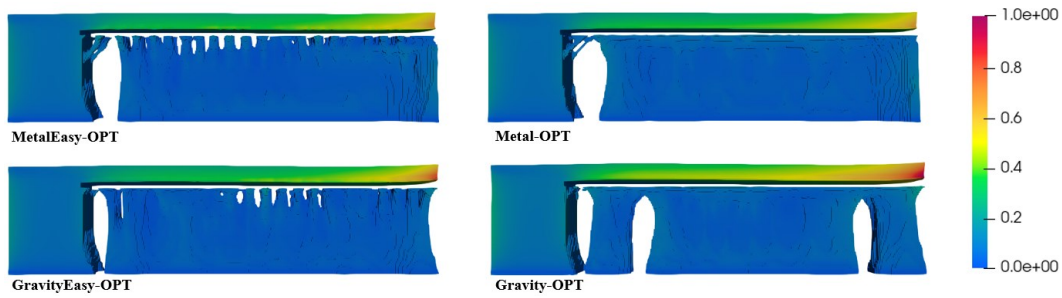
Figure 85. The residual warpage for the optimized support structures from Gravity-OPT, GravityEasy-OPT, Metal-OPT, and MetalEasy-OPT.

### 6.3.4. Conclusion

We have presented a topology optimization method to design manufacturable support structures considering the residual distortion induced in the LPBF AM process and various AM issues (easy removal support structure, self-support structure, and minimum length control). The formulation has been developed as a multi-objective topology optimization problem considering gravity compliance and residual distortion objective functions. A couple of conclusions can be drawn as follows: (1) introducing easy-to-remove features can effectively reduce the residual distortion during the printing stage and residual warpage after cutting, but these features will more or less sacrifice the structural stiffness; (2) the minimum length control of structures will affect structural performance. When the minimum length size is larger, the objective function representing the part residual distortion in AM decreases, and the structural gravity compliance increases; (3) even though we do not have specific control over the residual warpage, the results obtained by the metal-based optimization still show better residual warpage performance; (4) an interesting finding is that even though no direct relationship exists between the maximum residual distortion and maximum residual warpage; however, constraining the maximum residual distortion always leads to a reduced maximum residual warpage.

# Chapter 7. Large-scale concurrent island scanning pattern and topology optimization method for LPBF metal AM parts

In this subsection, a numerical method for concurrent scanning pattern and topology optimization has been proposed to design LPBF processed large-scale parts. The method developed in this work could effectively meet the emerging needs in metal LPBF AM-oriented design: the reduction in the part residual warpage and the high-resolution solution. Specifically, an ISM-based FEM model is presented to simulate the part-scale residual warpage induced by the LPBF process. Then, according to the fast simulation model, the scanning pattern and topology simultaneous optimization problem is formulated and accelerated by the PETSc parallel-computing framework. The proposed approach is applied to several 3D benchmark examples to demonstrate the effectiveness of stiffness improvement and residual warpage reduction.

## 7.1. Problem formulation and solution

DfAM optimizing the structural geometry and process parameters is an effective approach to eliminate the prone-to-warp features in LPBF manufacturing. Alternating the structural geometry changes the heat conduction paths and thus the thermal history and consequently, the residual stress distribution could vary significantly. It is reported that creating voids around the stress concentration spots can effectively reduce the maximum stress level. It is even more commonly known that the residual stress distribution is closely linked to the laser scanning path pattern from both experiments and numerical tests. Hence, conducting concurrent scanning pattern and structure optimization is concentrated in this subsection.

### 7.1.1. Concurrent optimization model formulation

For the optimization problem, the objective function is to minimize the structural compliance and the maximum residual warpage subject to the volume fraction constraint.

The scale of the structural compliance value $C$ and measured maximum residual distortion value $\overline{U}_{PN}$ is significantly affected by the fixed design domain scale and boundary condition settings. Therefore, we used a normalized objective function defined by:

$$J = \gamma \cdot \overline{U}_{PN} + (1 - \gamma) \cdot C \tag{7.1}$$

$\gamma$ is the normalization factor which could make the values of $\overline{U}_{PN}$ and $C$ at the same order of magnitude. In conclusion, the mathematical formulation of this optimization problem can be expressed as follows:

$$
\begin{cases}
\text{find: } \boldsymbol{\mu}, \boldsymbol{\theta} \\
\text{minimize: } J(\boldsymbol{\mu}, \boldsymbol{\theta}) \\
\text{subject to: }
\begin{cases}
\mathbf{K}_n \Delta \mathbf{U}_n = \Delta \mathbf{K}_n \mathbf{U}_n^{\text{ihs}} \ (n = 1, 2, \ldots, m) & (7.2.1) \\
\mathbf{K}_{\text{remain}} \mathbf{U}_{\text{cut}} = \mathbf{K}_{\text{cutoff}} \displaystyle\sum_{n=\text{cut}+1}^{m} \Delta \mathbf{U}_n & (7.2.2) \\
\mathbf{K}\mathbf{U} = \mathbf{F} & (7.2.3) \\
\dfrac{M}{\overline{M}} \leq M_f & (7.2.4) \\
\mu_{\min} \leq \forall \mu_e \leq 1 & (7.2.5)
\end{cases}
\end{cases}
\tag{7.2}
$$

where Eq. (7.2.1) to Eq. (7.2.2) are two control equations to obtain the residual distortion and residual warpage after cutting. Eq. (7.2.3) is the mechanical state control equation: $\mathbf{K}$, $\mathbf{U}$, and $\mathbf{F}$ are the global stiffness matrix, displacement vector, and force vector, respectively. Eq. (7.2.4) is the mass fraction constraint: $M = \sum_{e=1}^{\text{Nel}} (\widehat{\varphi}_e \cdot m_0)$ is the total mass of the structure, $m_0$ is the unit mass of the $e^{\text{th}}$ element in case of being filled with the solid material; $\overline{M}$ denotes the design domain mass containing the solid material; $M_f$ is the mass fraction. $\mu_{\min}$ is set as $1E - 9$, which could be used to avoid matrix singularity.

## 7.1.2. Sensitivity analysis

The gradient based optimization solver will be adopted to solve the optimization problem, which requires first order sensitivity information of the constraints and the objective function. Hence, details of the sensitivity analysis will be presented in this sub-section.

Special care should be taken to treat the objective function properly. Especially for the density design variable $\boldsymbol{\mu}$:

$$\frac{\partial J}{\partial \boldsymbol{\mu}} = \frac{\partial J}{\partial \widehat{\boldsymbol{\varphi}}} \cdot \frac{\partial \widehat{\boldsymbol{\varphi}}}{\partial \boldsymbol{\varphi}} \cdot \frac{\partial \boldsymbol{\varphi}}{\partial \widetilde{\boldsymbol{\mu}}} \cdot \frac{\partial \widetilde{\boldsymbol{\mu}}}{\partial \boldsymbol{\mu}} \tag{7.3}$$

where $\frac{\partial \widehat{\boldsymbol{\varphi}}}{\partial \boldsymbol{\varphi}}$, $\frac{\partial \boldsymbol{\varphi}}{\partial \widetilde{\boldsymbol{\mu}}}$, and $\frac{\partial \widetilde{\boldsymbol{\mu}}}{\partial \boldsymbol{\mu}}$ represent the standard modifications to the sensitivity due to AM filter, Heaviside projection filter, and smoothing filter, respectively. While for the scanning angle variables $\boldsymbol{\theta}$, it only affects the residual warpage, and thus only the sensitivity of the first objective term with respect to $\boldsymbol{\theta}$ needs to be considered.

### 7.1.2.1. Sensitivity analysis by adjoint method

For the first objective sensitivity analysis, only the information of $\frac{\partial C}{\partial \boldsymbol{\mu}}$ is considered. The corresponding Lagrange function could be written as:

$$L_1 = C + \boldsymbol{\lambda}_c^T(\mathbf{KU} - \mathbf{F}) \tag{7.4}$$

The gradient of the $L_1$ respect to the $\widehat{\boldsymbol{\varphi}}$ is:

$$\frac{\partial L_1}{\partial \widehat{\boldsymbol{\varphi}}} = \frac{\partial \mathbf{F}^T}{\partial \widehat{\boldsymbol{\varphi}}} \mathbf{U} + (\mathbf{F}^T + \boldsymbol{\lambda}_c^T \mathbf{K}) \frac{\partial \mathbf{U}}{\partial \widehat{\boldsymbol{\varphi}}} + \boldsymbol{\lambda}_c^T \frac{\partial \mathbf{K}}{\partial \widehat{\boldsymbol{\varphi}}} \mathbf{U} - \boldsymbol{\lambda}_c^T \frac{\partial \mathbf{F}}{\partial \widehat{\boldsymbol{\varphi}}} \tag{7.5}$$

collecting the $\frac{\partial \mathbf{U}}{\partial \widehat{\boldsymbol{\varphi}}}$ term and solving the adjoint equation $\mathbf{F}^T + \boldsymbol{\lambda}_c^T \mathbf{K}$, then we could arrive:

$$\frac{\partial L_1}{\partial \widehat{\boldsymbol{\varphi}}} = -\mathbf{U}^T \frac{\partial \mathbf{K}}{\partial \widehat{\boldsymbol{\varphi}}} \mathbf{U} \tag{7.6}$$

The derivation of the term $\frac{\partial \mathbf{K}}{\partial \widehat{\boldsymbol{\varphi}}}$ is the same with conventional stiffness-based problem, and thus omitted in this paper.

For the second objective term, its Lagrange function could be constructed as:

$$L_2 = \overline{\mathbf{U}}_{PN} + \sum_{n=1}^{m} \boldsymbol{\lambda}_n^{1^T}(\mathbf{K}_n \Delta \mathbf{U}_n - \Delta \mathbf{K}_n \mathbf{U}_n^{ihs}) \mathbf{H}_{DOF}^n + \boldsymbol{\lambda}^T \left( \mathbf{K}_{remain} \mathbf{U}_{cut} - \mathbf{K}_{cutoff} \sum_{n=cut+1}^{m} \Delta \mathbf{U}_n \mathbf{H}_{DOF}^n \right) \tag{7.7}$$

146

The gradient of the $L_2$ respect to the $\widehat{\boldsymbol{\varphi}}$ is:

$$\frac{\partial L_2}{\partial \widehat{\boldsymbol{\varphi}}} = \sum_{n=1}^{m} \frac{\partial \overline{U}_{PN}}{\partial U_{res}} \frac{\partial \Delta U_n}{\partial \widehat{\boldsymbol{\varphi}}} H_{DOF}^n + \frac{\partial \overline{U}_{PN}}{\partial U_{cut}} \frac{\partial U_{cut}}{\partial \widehat{\boldsymbol{\varphi}}} + \sum_{n=1}^{m} \lambda_n^1 \left( K_n \frac{\partial \Delta U_n}{\partial \widehat{\boldsymbol{\varphi}}} + \frac{\partial K_n}{\partial \widehat{\boldsymbol{\varphi}}} \Delta U_n - \frac{\partial \Delta K_n U_n^{ihs}}{\partial \widehat{\boldsymbol{\varphi}}} \right) H_{DOF}^n$$

$$+ \lambda^T \left( \frac{\partial K_{remain}}{\partial \widehat{\boldsymbol{\varphi}}} U_{cut} + K_{remain} \frac{\partial U_{cut}}{\partial \widehat{\boldsymbol{\varphi}}} - K_{cutoff} \sum_{n=cut+1}^{m} \frac{\partial \Delta U_n}{\partial \widehat{\boldsymbol{\varphi}}} H_{DOF}^n - \frac{\partial K_{cutoff}}{\partial \widehat{\boldsymbol{\varphi}}} \sum_{i=cut+1}^{m} \Delta U_n H_{DOF}^n \right) \tag{7.8}$$

Collecting the $\frac{\partial \Delta U_n}{\partial \widehat{\boldsymbol{\varphi}}}$ and $\frac{\partial U_{cut}}{\partial \widehat{\boldsymbol{\varphi}}}$ terms:

$$\frac{\partial L_2}{\partial \widehat{\boldsymbol{\varphi}}} = \sum_{n=1}^{cut} \left( \frac{\partial \overline{U}_{PN}}{\partial U_{res}} + K_n \lambda_n^1 \right) \frac{\partial \Delta U_n}{\partial \widehat{\boldsymbol{\varphi}}} H_{DOF}^n + \left( \frac{\partial \overline{U}_{PN}}{\partial U_{cut}} + K_{remain} \lambda \right) \frac{\partial U_{cut}}{\partial \widehat{\boldsymbol{\varphi}}} + \sum_{n=1}^{m} \left( \lambda_n^{1T} \frac{\partial K_n}{\partial \widehat{\boldsymbol{\varphi}}} \Delta U_n - \lambda_n^{1T} \frac{\partial \Delta K_n U_n^{ihs}}{\partial \widehat{\boldsymbol{\varphi}}} \right) H_{DOF}^n$$

$$+ \lambda^T \frac{\partial K_{remain}}{\partial \widehat{\boldsymbol{\varphi}}} U_{cut} - \lambda^T \frac{\partial K_{cutoff}}{\partial \widehat{\boldsymbol{\varphi}}} \sum_{n=cut+1}^{m} \Delta U_n H_{DOF}^n + \sum_{n=cut+1}^{m} \left( \frac{\partial \overline{U}_{PN}}{\partial U_{res}} - \lambda^T K_{cutoff} + \lambda_n^{1T} K_n \right) \frac{\partial \Delta U_n}{\partial \widehat{\boldsymbol{\varphi}}} H_{DOF}^n \tag{7.9}$$

Then solving the following adjoint equations to obtain the $\boldsymbol{\lambda}$ and $\boldsymbol{\lambda}_n^1$ ($n = 1:m$):

$$\frac{\partial \overline{U}_{PN}}{\partial U_{cut}} + K_{remain} \lambda = 0$$

$$\frac{\partial \overline{U}_{PN}}{\partial U_{res}} + K_n \lambda_n^1 = 0 \quad n = 1:cut \tag{7.10}$$

$$\frac{\partial \overline{U}_{PN}}{\partial U_{res}} - \lambda^T K_{cutoff} + \lambda_n^{1T} K_n = 0 \quad n = cut+1:m$$

Then we could arrive:

$$\frac{\partial L_2}{\partial \widehat{\boldsymbol{\varphi}}} = \sum_{n=1}^{m} \left( \lambda_n^{1T} \frac{\partial K_n}{\partial \widehat{\boldsymbol{\varphi}}} \Delta U_n - \lambda_n^{1T} \frac{\partial \Delta K_n U_n^{ihs}}{\partial \widehat{\boldsymbol{\varphi}}} \right) H_{DOF}^n + \lambda^T \frac{\partial K_{remain}}{\partial \widehat{\boldsymbol{\varphi}}} U_{cut} - \lambda^T \frac{\partial K_{cutoff}}{\partial \widehat{\boldsymbol{\varphi}}} \sum_{n=cut+1}^{m} \Delta U_n H_{DOF}^n \tag{7.11}$$

The gradient of the $L_2$ respect to the $\boldsymbol{\theta}$ is:

$$\frac{\partial L_2}{\partial \boldsymbol{\theta}} = \sum_{n=1}^{m} \frac{\partial \overline{U}_{PN}}{\partial U_{res}} \frac{\partial \Delta U_n}{\partial \boldsymbol{\theta}} H_{DOF}^n + \frac{\partial \overline{U}_{PN}}{\partial U_{cut}} \frac{\partial U_{cut}}{\partial \boldsymbol{\theta}} +$$

$$\sum_{n=1}^{m} \lambda_n^{2T} \left( K_n \frac{\partial \Delta U_n}{\partial \boldsymbol{\theta}} - \frac{\partial \Delta K_n U_n^{ihs}}{\partial \boldsymbol{\theta}} \right) H_{DOF}^n + \lambda^T \left( K_{remain} \frac{\partial U_{cut}}{\partial \boldsymbol{\theta}} - K_{cutoff} \sum_{n=cut+1}^{m} \frac{\partial \Delta U_n}{\partial \boldsymbol{\theta}} H_{DOF}^n \right) \tag{7.12}$$

Collecting the $\frac{\partial \Delta U_n}{\partial \boldsymbol{\theta}}$ and $\frac{\partial U_{cut}}{\partial \boldsymbol{\theta}}$ terms:

$$\frac{\partial L_2}{\partial \boldsymbol{\theta}} = \sum_{n=1}^{cut} \left( \frac{\partial \overline{U}_{PN}}{\partial U_{res}} + \lambda_n^{2^T} K_n \right) \frac{\partial \Delta U_n}{\partial \boldsymbol{\theta}} H_{DOF}^n + \left( \frac{\partial \overline{U}_{PN}}{\partial U_{cut}} + \lambda K_{remain} \right) \frac{\partial U_{cut}}{\partial \boldsymbol{\theta}} + \sum_{n=1}^{m} \lambda_n^2 \left( -\frac{\partial \Delta K_n U_n^{ihs}}{\partial \boldsymbol{\theta}} \right) H_{DOF}^n +$$
$$\sum_{n=cut+1}^{m} \left( \frac{\partial \overline{U}_{PN}}{\partial U_{res}} - \lambda K_{cutoff} + \lambda_n^2 K_n \right) \frac{\partial \Delta U_n}{\partial \boldsymbol{\theta}} H_{DOF}^n \tag{7.13}$$

Then solving the following adjoint equations to obtain the $\boldsymbol{\lambda}$ and $\boldsymbol{\lambda}_n^2$ $(n = 1: m)$:

$$\frac{\partial \overline{U}_{PN}}{\partial U_{cut}} + K_{remain} \lambda = 0$$
$$\frac{\partial \overline{U}_{PN}}{\partial U_{res}} + K_n \lambda_n^2 = 0 \quad n = 1: cut \tag{7.14}$$
$$\frac{\partial \overline{U}_{PN}}{\partial U_{cut}} - \lambda^T K_{cutoff} + \lambda_n^{1^T} K_n = 0 \quad n = cut + 1: m$$

The final expression for the term $\frac{\partial L_2}{\partial \boldsymbol{\theta}}$ is:

$$\frac{\partial L_2}{\partial \boldsymbol{\theta}} = \sum_{n=1}^{m} \lambda_n^{2^T} \left( -\frac{\partial \Delta K_n U_n^{ihs}}{\partial \boldsymbol{\theta}} \right) H_{DOF}^n \tag{7.15}$$

### 7.1.2.2. Constraint function sensitivity analysis

The analytical sensitivity analysis given by Eq. (7.11) and Eq. (7.15) is validated against forward finite difference sensitivities (FFDS). A square domain meshed by $4 \times 4 \times 4$ elements with $L = 1mm$, $H = 1mm$ and $W = 1mm$. All the bottom nodes are fixed, and the external strain is applied by a layer-by-layer process, as mentioned in Section 2. The domain in Figure 86 is divided into 4 layers, with a layer thickness of 0.25mm. The FFDS results are presented with a perturbation size of 0.001. The validation of Sensitivity analysis is conducted at one specified element, whose location is shown in Figure 86.
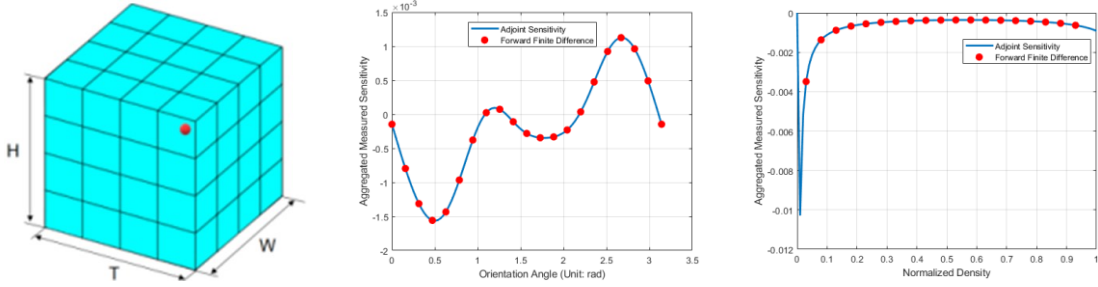
Figure 86. Verification of the analytical sensitivity through a comparison with the finite difference sensitivity for one specific element.

The sensitivity of the aggregated residual cut-off distortion measures $\frac{\partial L_2}{\partial \widehat{\varphi}}$ and $\frac{\partial L_2}{\partial \theta}$ with respect to the specific element are shown in Figure 86. The analytical sensitivity is shown in each plot by the solid lines, and the solid red dots represent the finite-difference sensitivities. Good agreements could be observed from the plots.

## 7.2. Numerical implementation

The workflow of the proposed optimization process is given in Figure 87 (a), and the detailed numerical implementation is introduced in this section. In this work, the scanning island pattern and structures are optimized simultaneously. A high-performance, parallel-computing platform of topology optimization for LPBF metal AM has been developed in this work. Within this framework, a parallel-computing ISM solver has been developed. It can be seen from Figure 87 that the parallel-computing ISM solver will be called in each optimization loop to obtain the nodal distortion information. With the sensitivity analysis and optimization model at hand, the MMA solver is employed to solve the topology optimization problem. A step-by-step description of the proposed work is outlined:

1. Initializing the LPBF fast simulation solver and optimization solver, then obtaining the initial scanning pattern of each layer and initial density field (The scanning orientations are uniformly set within each island, and the initial density field is set with a fixed value).

149

2. Adopting the LPBF fast simulation solver introduced in section 2 to obtain the part-scale distortion information.

3. Calculating density and path sensitivity according to Eq. (7.11) and Eq. (7.15) with the part-scale distortion information obtained from the last step.

4. Adopting the MMA solver and updating the density and scanning pattern.

5. Checking for convergence criteria: if not satisfied, return to step 2; if satisfied, the results will be post-processed to generate corresponding laser scan paths and structural visualizations.



(a)                                                    (b)
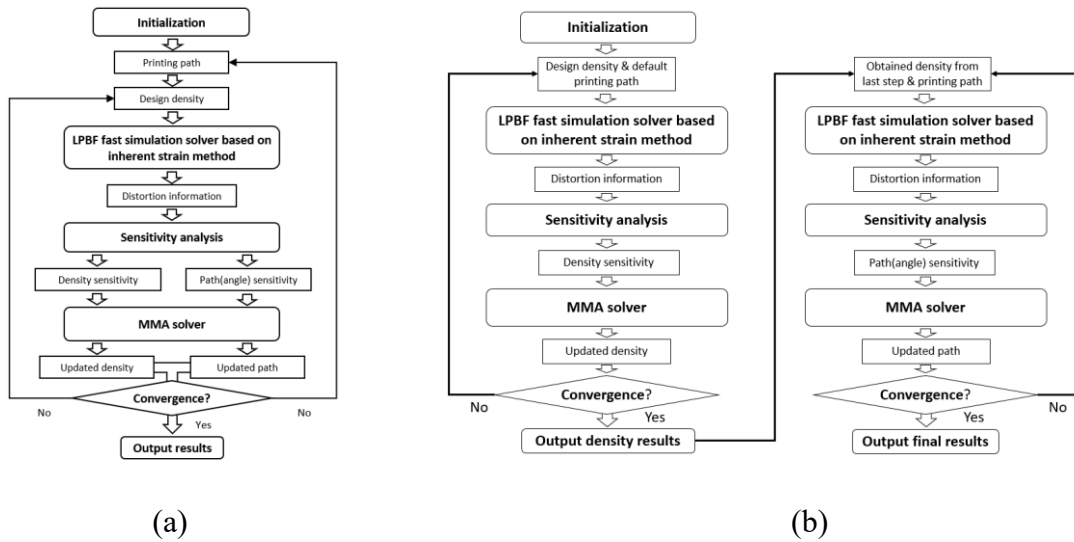
Figure 87. The flow chart of the proposed method.

Besides, the workflow of the sequential method is also given in Figure 87 (b). The sequential method includes two processes:

1. The first stage only seeks the material density distribution with uniform scanning orientation ($\theta = 0^\circ$). Then, there generates the initial guess of the design structure for the later scanning orientation optimization.

2. In the second stage, based on the optimized design structure from the first stage, the

scanning orientation optimization (the work introduced in subsection 6.2) is performed to reduce the residual warpage further.

## 7.3. Large scale optimization model implementation

The utilization of parallel processing in scientific computing is constantly increasing and has made a significant impact on the topology optimization community. This trend has been observed as more researchers are utilizing parallel computing to optimize complex systems in a shorter amount of time. Furthermore, the parallel processing approach has enabled researchers to overcome computational limitations that were previously encountered when working on large-scale optimization problems.
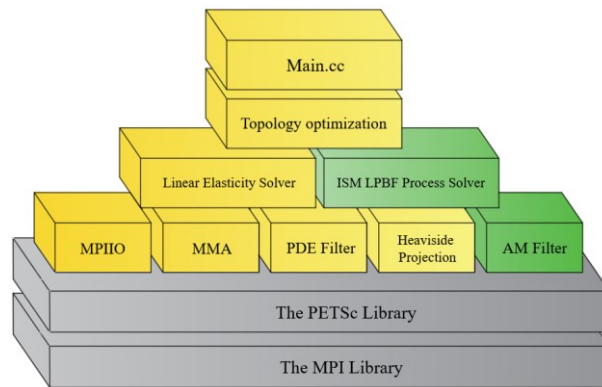


Figure 88. The framework of the topology optimization for metal AM solver based on PETSc.

The proposed framework is based on the flexible framework of parallel computing topology optimization proposed by Aage et al. [302]. Figure 88 depicts an overview of the topology optimization framework from the code scope. The base of the framework is the PETSc library and MPI library [303][304], which provides the basic sparse linear algebra routines within the field of parallel computing. It should be noted that PETSc supports different operating systems (Linux, macOS, Windows, and so on), so the proposed framework is also versatile to run on different systems.

The yellow blocks represent the existing C++ classes in the original framework of Aage et al. [302], while the green blocks are newly added classes. For the yellow blocks' detailed explanations, the reader is referred to the original paper [302]. As mentioned in the introduction, the major contributions of this work are the LPBF simulation solver and its integration with topology optimization.

## 7.4. Numerical examples

Four optimization cases are provided in this subsection as listed in Table 5. MetalStiff-PartPath-OPT, which is the simultaneous optimization of the scanning pattern and the structure material distribution using the optimization model proposed in this work (the weighting factor $\gamma$ is 0.01); StiffOnly-PartOnly-OPT, which is a conventional stiffness-based structure material distribution optimization (the weighting factor $\gamma$ is 1.00) with uniform scanning orientation ($\theta = 0°$). MetalStiff-PartOnly-OPT, which is a density distribution optimization with uniform scanning orientations ($\theta = 0°$) from the first stage of sequential method (the weighting factor $\gamma$ is 0.01); MetalOnly-PathOnly-OPT, which is a scanning orientation optimization based on the part geometry obtained from MetalStiff-PartOnly-OPT.

| Case name | Structural Compliance | Residual Warpage | Structure Optimization | Printing Path Optimization |
|---|---|---|---|---|
| MetalStiff-PartPath-OPT | √ | √ | √ | √ |
| StiffOnly-PartOnly-OPT | √ | × | √ | × |
| MetalStiff-PartOnly-OPT | √ | √ | √ | × |

| MetalOnly-PathOnly-OPT | × | √ | × | √ |

Table 5. The two optimization cases in subsection 7.4.

### 7.4.1. 3D MBB beam structure design



(a)                                          (b)
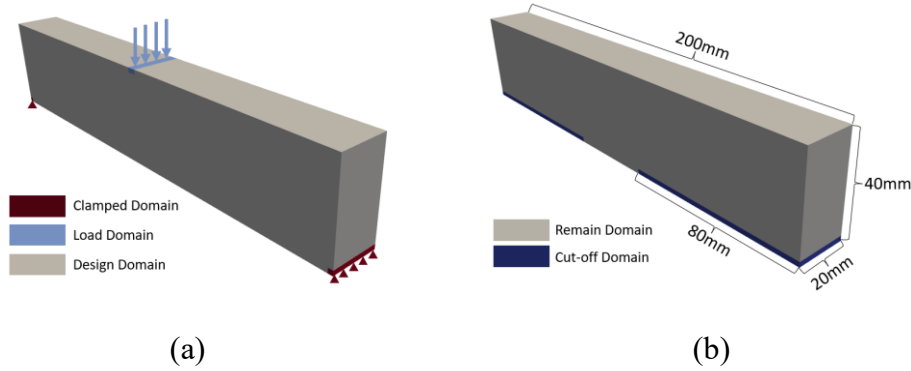
Figure 89. Fixed design domain and boundary conditions for the MBB beam.

The first numerical example is to design the classical MBB beam shown in Figure 89, whose structural sizes are defined with $L = 200$ mm, $H = 40$ mm, and $W = 20$ mm, and the build direction is bottom-up (along the positive z-axis). The blue surface is fully cramped, and the red surface is applied traction. A mesh with $600 \times 120 \times 60$ square elements is employed to discretize the design space. The fixed design domain in Figure 89 is divided into $m = 40$ layers (consisting of 39 printing layers and 1 base removal layer), with a layer thickness of $0.5$ mm and lumped with 3 elements along the building direction. For each layer, there are $40 \times 4$ islands with dimensions of 2.5mm×2.5mm, and the initial scanning pattern is the same as in subsection 2.4. The upper limit of the allowable volume is set to 35% of the fixed design domain.

### 7.4.1.1. Comparison between MetalStiff-PartPath-OPT and StiffOnly-PartOnly-OPT
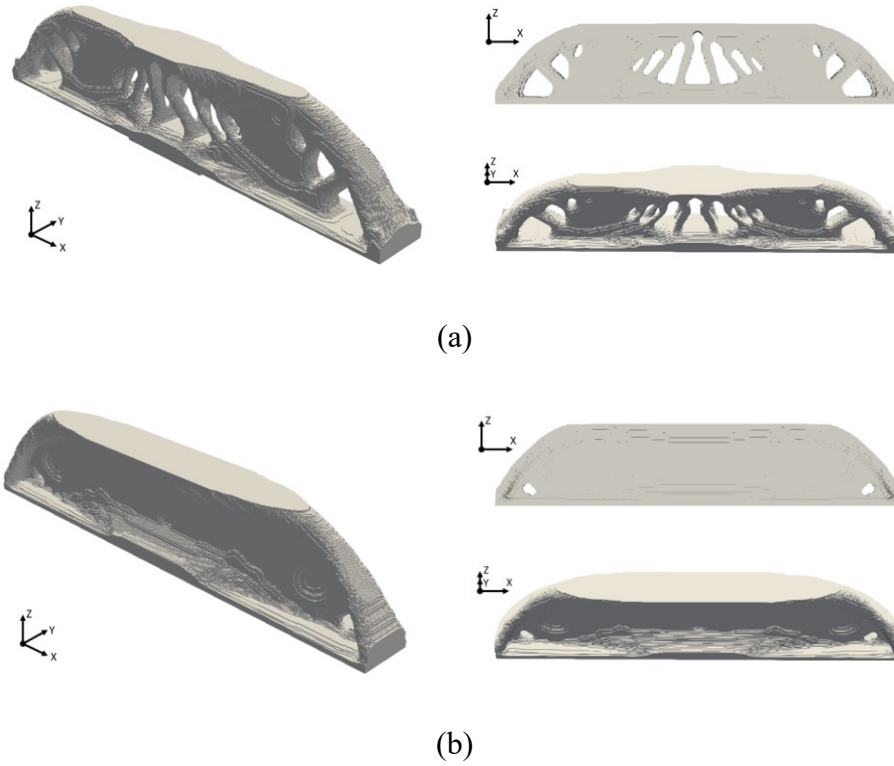
Figure 90. The as-constructed structures: (a) optimal design obtained from the proposed method; (b) conventional self-support stiffness-based design.

Firstly, two optimization cases are provided in this subsection: Case 1, which is the simultaneous optimization of the scanning pattern and the structure material distribution using the optimization model proposed in this work (the weighting factor $\gamma$ is 0.01); Case 2, which is a conventional stiffness-based structure material distribution optimization (the weighting factor $\gamma$ is 1.00) with uniform scanning orientation ($\theta = 0^{\circ}$). The detailed geometries constructed from the optimized results in Case 1 and 2 are presented in Figure 90, and the compliance value for the structure in Case 1 is 251.8277 KJ, while for the design in Case 2, the value is 227.1276 KJ.

Figure 91 presents the simulation results containing the total distortion distribution for the two as-constructed structures. Higher distortions are observed in the result of Case 2. For

the design in Case 1, the maximum distortion is 1.3202mm (Figure 91 (b)). However, for the design in Case 2, the maximum distortion is reduced to 0.4696mm through an optimized material distribution and scanning orientations (Figure 91 (a)). From the perspective of structure, compared with the stiffness-based design in Case 2, more void features appear in the proposed design, which means the complexity of the structural topology is increased accordingly. The results show that local nucleation of voids could reduce the local inherent strain loading sources while not decreasing the structural stiffness too much.



(a)                                                      (b)

(c)                                                      (d)
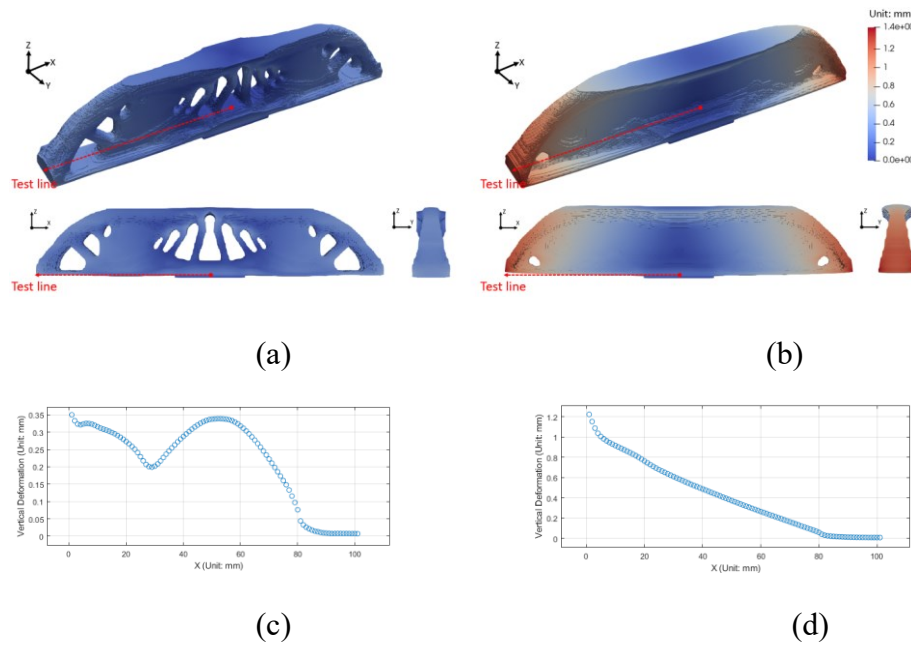
Figure 91. The residual warpage for the as-constructed structures: (a) optimal design obtained from the proposed method; (b) conventional self-support stiffness-based design. Plots of vertical deformation of the bottom surface of the as-constructed structures along the specified test line (c) optimal design obtained from the proposed method; (d) conventional self-support stiffness-based design.

The optimized layerwise island scanning path for design in Case 1 is presented in Figure 92. The scanning tracks within each island are determined by the optimized scanning

orientation ($\theta$), hatch spacing and the interaction between the scanning island and local geometry features.



(a)

(b)

(c)
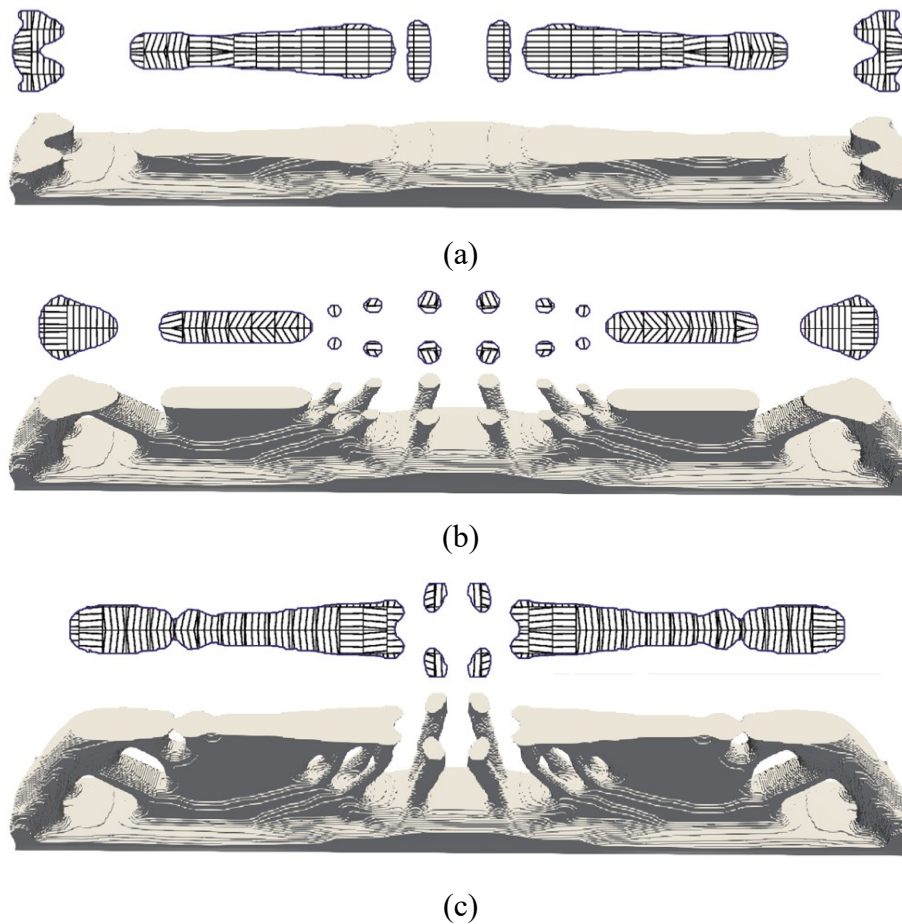
Figure 92. The corresponding part geometry and island scanning pattern for the design in 0 (a) with different printing heights along the z-axis: (a) $z = 5mm$; (b) $z = 10mm$; (c) $z = 15mm$.

The convergence history curves for the optimization process in Figure 90 (a) are proposed in Figure 93. As the number of iterations increases, the objective function for the part warpage after the LPBF process and structural compliance keep reducing and finally approaches a fixed value. It is also observed that several sudden oscillations happen after the update of Heaviside projection parameters for both the maximum residual distortion and structural compliance. This is due to the fact that the structural performance is sensitive

to material distribution changes (especially for the design-dependent loading problem).
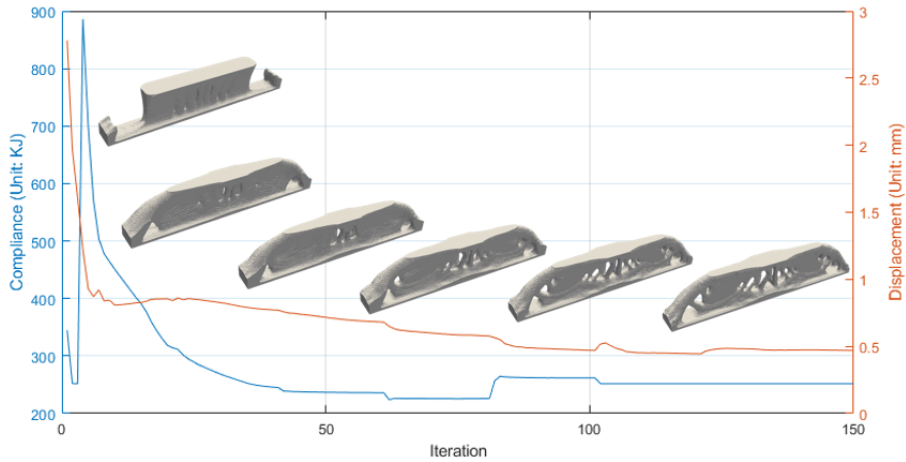


Figure 93. The convergence history of the objective values for the result in 0 (a).

### 7.4.1.2. Comparison between the concurrent method and sequential method

To further investigate the significance of the proposed concurrent method, the optimized structure proposed in Figure 90 (a) is compared with the structure designed by the method whose island scanning pattern and structure are optimized sequentially (sequential method).
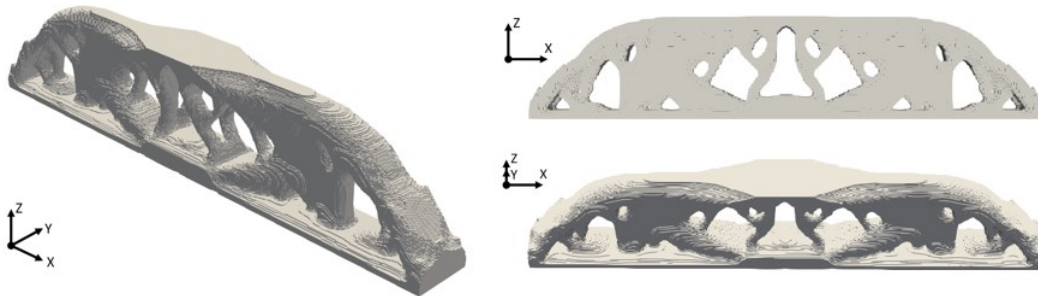


Figure 94. The as-constructed structure obtained from T-OPT.

Three optimization schemes (MetalStiff-PartPath-OPT, MetalStiff-PartOnly-OPT, and MetalOnly-PathOnly-OPT) are provided in this subsection. Figure 94 shows the optimized material distribution for the structure designed from the first stage of sequential method (MetalStiff-PartOnly-OPT). It shows that its topology is different with the one in

157

MetalStiff-PartPath-OPT.
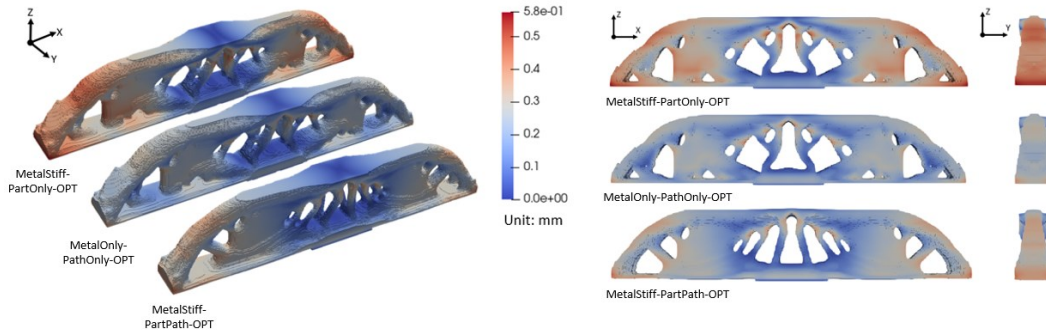


Figure 95. The residual distortion distribution for the optimization cases: MetalStiff-PartOnly-OPT, MetalOnly-PathOnly-OPT, and MetalStiff-PartPath-OPT.

Figure 95 and Figure 96 present the residual distortion distributions and the comparative magnitudes of the two objective terms from the three optimization schemes, respectively. The largest maximum residual warpage (0.5753mm) is exhibited in the structure obtained from MetalStiff-PartOnly-OPT design compared to the MetalOnly-PathOnly-OPT (0.4730mm) and MetalStiff-PartPath-OPT design (0.4696mm). In comparison between the MetalOnly-PathOnly-OPT design and MetalStiff-PartPath-OPT design, although their maximum residual warpages are very close, the structural stiffness of the MetalStiff-PartPath-OPT design is obviously better than that of the MetalOnly-PathOnly-OPT design (improvement around 6%: 251.8277KJ vs. 268.9869KJ).
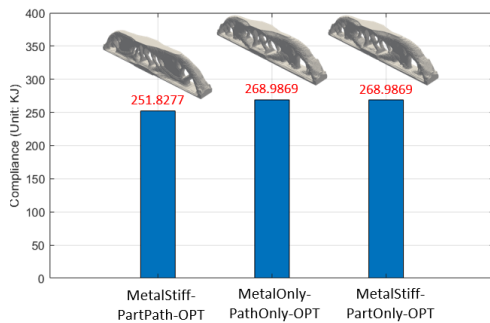


(a)
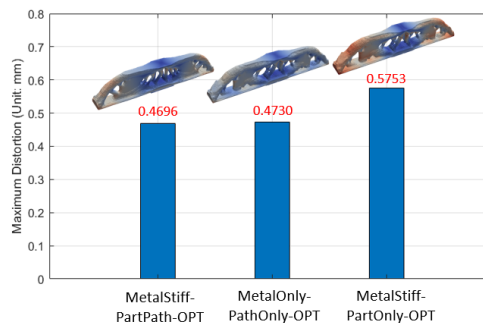


(b)

Figure 96. The plot of mechanical performances corresponding to the different optimization schemes: (a) structural compliance; (b) maximum residual warpage.

### 7.4.1.3. Investigation of different island scanning pattern

The influence of different island scanning patterns is investigated in this subsection. As shown in Figure 97, the structures designed from three different scanning pattern strategies (Pattern 1, Pattern 2, and Pattern 3) are provided here, and each scanning pattern parameter related to Figure 97 is set in Table 6.

| | Island Number for Each Layer | Island Dimension |
|---|---|---|
| Pattern 1 | 2 × 20 | 5.0mm × 5.0mm |
| Pattern 2 | 4 × 40 | 2.5mm × 2.5mm |
| Pattern 3 | 10 × 100 | 1.0mm × 1.0mm |

Table 6. The detail scanning pattern parameters for three cases.

As shown in Figure 97, The final topological structures and material distributions with these three patterns are slightly different. Within these three results, the result from pattern 2 has the highest structural complexity, while its designed island number for each layer is neither the highest nor lowest. This phenomenon indicates that the structural optimization result would be perturbed by the designed island number, but the perturbation is random since the complexity of the structural topology is non-monotonic.
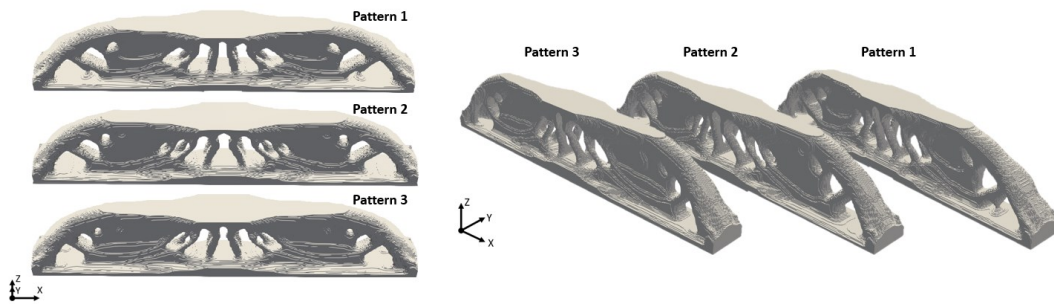
Figure 97. The as-constructed structures for different scanning patterns.

The total distortion distribution for the optimized shape solutions of these three cases are shown in Figure 98, and Figure 99 shows a plot of each structural compliance and residual warpage corresponding to the different scanning patterns. As indicated by the optimization data shown in Figure 98 and Figure 99, the pattern 3 approach presents a solution with better structural stiffness (250.8013KJ) than pattern 1 approach (256.8327KJ) and, meanwhile, achieves smaller residual warpage (maximum 0.4491mm vs. 0.5217mm).
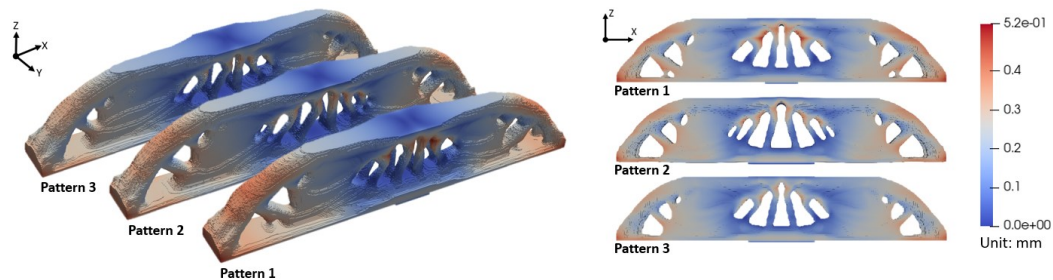


Figure 98. The residual distortion distribution for different scanning patterns.

Observing the optimized structural performance with varying scanning pattern shown in Figure 99, there exhibits a monotonically decreasing trend (from pattern 1 to pattern 3). It is reasonable since the density distribution and anisotropic residual stress loading owing to the scanning pattern are two independent phenomena. Within the case of a certain density design variable, the scanning pattern with more island number could greatly increase the scope of the design domain and thus makes the solver easier to put more

160

concentration on reducing residual warpage and improving structural stiffness simultaneously.
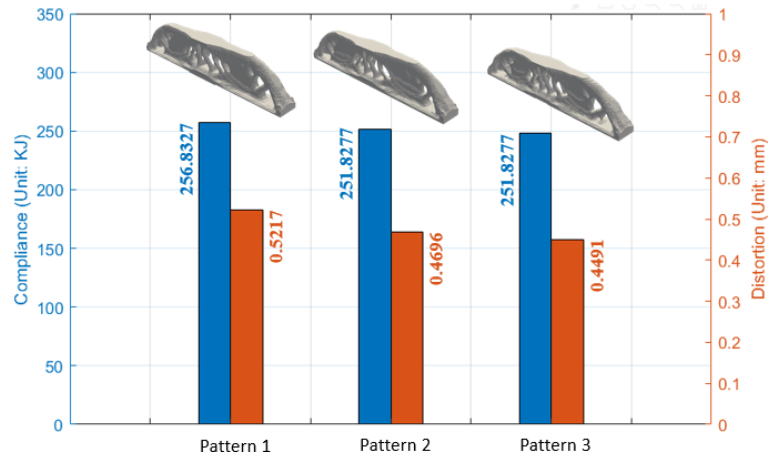


Figure 99. The plot of mechanical performance corresponding to the three different scanning patterns.

Finally, the optimized certain height layer-wise island scanning patterns ($z = 15$mm) for the designs obtained from three different scanning patterns are presented in Figure 100.



(a)



(b)



161
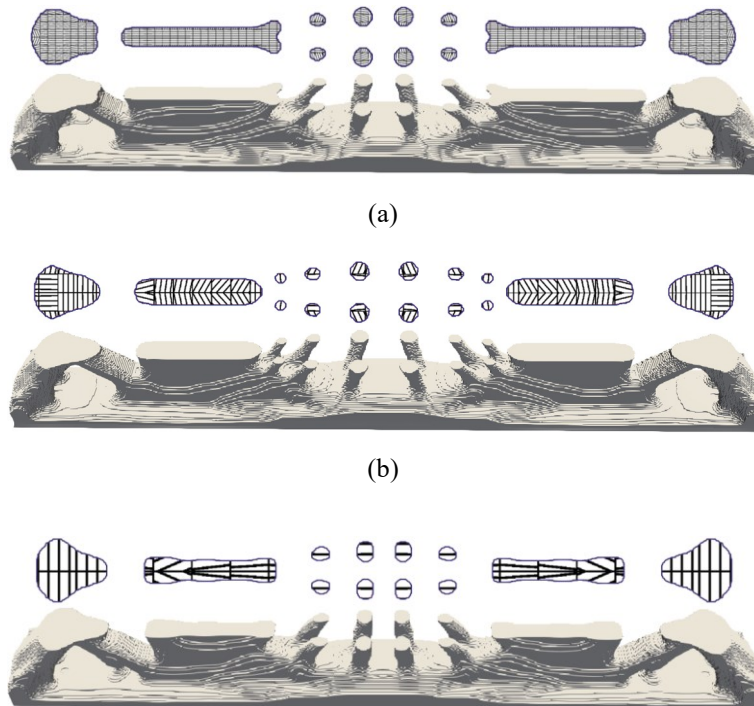
Figure 100. The corresponding part geometry, and island scanning pattern for different cases (z = 15mm).

## 7.4.2. The Cantilever structure design



(a)                                    (b)
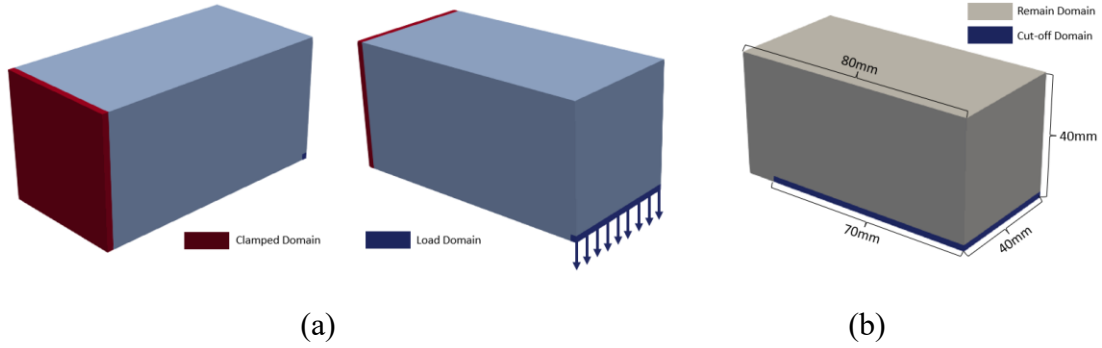
Figure 101. Fixed design domain and boundary conditions for the Cantilever beam.

The second numerical example is to design the Cantilever beam shown in Figure 101, whose structural sizes are defined with L = 80 mm, H = 40 mm, and W = 40 mm, and the build direction is bottom-up (along the positive z-axis). The red surface is fully clamped, and the dark-blue surface is applied of downward tractions. A mesh with 240×120×120 square elements is employed to discretize the design space. The fixed design domain in Figure 101 is divided into m = 40 layers (consisting of 39 printing layers and 1 base removal layer), with a layer thickness of 0.33 mm and lumped with 3 elements along the building direction. For each layer, there are 16×8 islands with dimensions of 5mm×5mm, while other parameters keep the same with the MBB case.
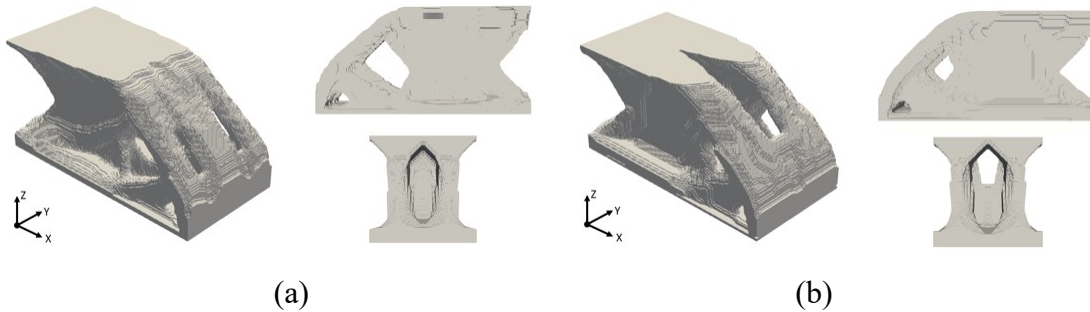


(a)                                    (b)

Similarly, two optimization cases (StiffOnly-PartOnly-OPT and MetalStiff-PartPath-OPT) are provided in this subsection. Figure 102 presents the optimization results for these two cases, and the compliance value for the structure in MetalStiff-PartPath-OPT is 335.7526KJ, while for the design in StiffOnly-PartOnly-OPT, the value is 334.6447KJ. The stiffness performance for these two designs is very close, even though their material distributions are different. The optimized layer-wise island scanning paths at different printing heights along z-axis in MetalStiff-PartPath-OPT design are presented in Figure 103.

The simulation results on total distortion distribution for the two as-constructed structures are given in Figure 104. The result of StiffOnly-PartOnly-OPT exhibits higher distortions, which has the maximum distortion of 1.4470mm. For the design in MetalStiff-PartPath-OPT, the maximum distortion is reduced to 1.1388mm, which achieves a reduction of 23%.



(a)                                  (b)                                  (c)
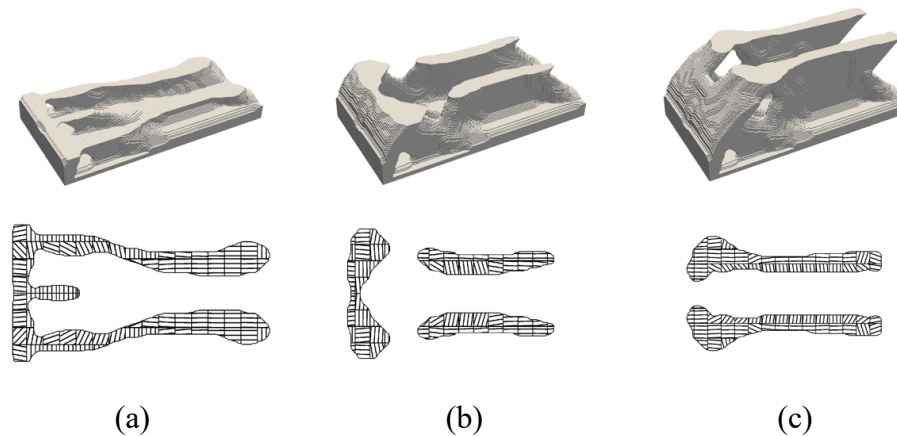
Figure 103. The part geometry and island scanning patterns for the design in (b) at different heights: (a) $z = 5$mm; (b) $z = 10$mm; (c) $z = 15$mm.
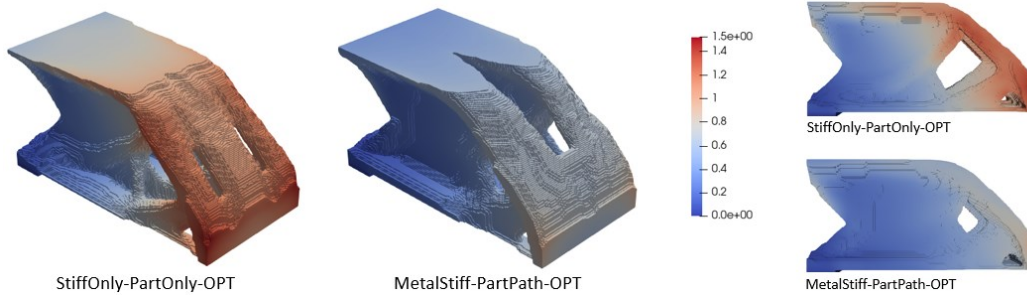
Figure 104. The residual warpage predictions for the MetalStiff-PartPath-OPT design and StiffOnly-PartOnly-OPT design.

### 7.4.3. Computational cost analysis

Firstly, the computational cost analysis for LPBF oriented topology optimization problem is concluded in this subsection. A typical MBB case study is performed with $200 \times 40 \times 20$ square elements and 40 simulation layers. Based on the algorithm shown in Figure 105, the total computing time is consisting of four parts: ($T_1$) the time for solving the state equations by the FEA (the LPBF process FEM solver and Mechanical FEM solver); ($T_2$) the time for conducting the sensitivity analysis (the adjoint solver); ($T_3$) the time for updating the design variables (MMA solver); ($T_4$) the time for other parts, like the pre-process, material interpolation, filter, projection, data saving and so forth.
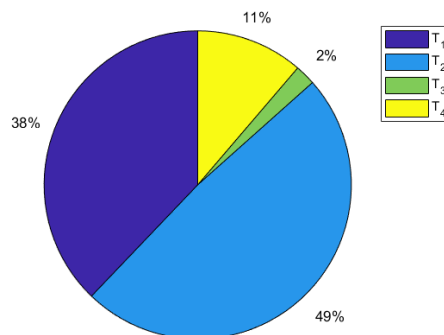


Figure 105. The computational cost for the proposed method.

The ratios of these three parts to the total time for different examples are shown in 0, from which we can see that for all the examples, nearly 90% of the computing time is consumed

164

for solving the state equations and sensitivity analysis. Specifically, the time for solving the state equations by the FEA takes 38.167% the time for conducting the sensitivity analysis takes 49.284%, the time for updating the design variables takes 10.840%, and other parts take 2.080%. From Figure 105, we can see that for all the examples more than 85% of the computing time is consumed for solving the physical state equation and sensitivity adjoint equation. Namely, the most time consuming part in this workflow lies in the solution of the sequence of linear systems of the form $\mathbf{Ax} = \mathbf{b}$.

### 7.4.4. Speedup and efficiency of parallelization

The parallelization speedup and efficiency of this proposed framework have been briefly examined as well. The framework is based on the parallel computing topology optimization program [302]. The 3D cantilever that has been mentioned in the previous section was executed multiple times with different numbers of cores (8, 16, 32, and 64) to study the effectiveness of the proposed framework. The mesh used in the following tests is $200 \times 40 \times 20$ (160000 elements). The filter radius, rmin, used here is 5. All cases were run for a maximum of 100 iterations. The default solver settings in Aage et al. [302] have been used in this section because the default iterative solver is generally more suitable for larger-scale 3D problems than direct solvers (e.g., Cholesky solver). However, further comparisons of the solvers are out of the scope of this paper and will be left for future work. An index, indicating the normalized speedup, is introduced in Eq. (44) to show the parallelization acceleration for the proposed method:

$$S_n = \frac{T_n}{T_8} \tag{45}$$

where $S_n$ and $T_n$ are the normalized speedup and computation time for utilizing n cores, respectively.
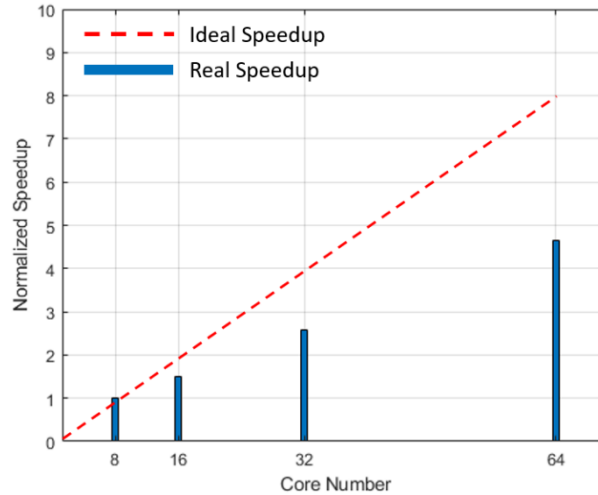
Figure 106. The normalized speedup of the parallel computing program when increasing the number of cores.

The computation time with 8 cores ($T_8$) is regarded as the reference. Figure 106 shows the normalized speedup achieved with the parallelization. It shows that the normalized speedup increases with more cores, but the normalized speedup doesn't increase linearly since the communication cost among the cores has increased at the same time.

## 7.5. Conclusion for this work

In this work, we have presented a concurrent scanning pattern and topology optimization method to design manufacturable structures considering the residual warpage induced in LPBF process. The formulation has been developed as a multi-objective topology optimization problem that considers both a stiffness objective function and a residual warpage objective function. A couple of conclusions can be drawn as follows: (1) when the weighting coefficient $\gamma$ is large, the objective function that represents the part residual warpage in AM increases, and the structural compliance decreases. Besides, it also affects the structural complexity, thus the users can adjust the weighting factor $\gamma$ to control the structural performance and complexity; (2) compared with the sequential method, the concurrent method can more effectively improve the structural stiffness, even though the

166

two achieve similar reductions in residual warpage; (3) the optimized structure obtained from the scanning pattern with higher number of islands lead to better structural performance. A proper scanning pattern selection could facilitate the structural performance while not obviously increase the manufacturing cost.

In the future, we plan to incorporate more AM constraints, including the closed cavity constraint and AM tool non-collision constraint. Furthermore, we will make further modifications to the adopted parallel-based ISM to improve the performance of obtained complex structures and align them more closely with actual experimental results.

# Chapter 8. Conclusions

This research proposed a topology optimization coupled with AM constraints and process simulation system to deal with the challenges and opportunities in the AM-oriented design field. The system mainly includes a topology optimization model for printed plastic parts and an ISM-based topology optimization model to reduce the deformation or residual stress in metal AM parts. In addition, the proposed system also includes several supplementary modules, a new material interpolation for multiple material stress constraint problem, post-processing techniques, performance simulation, and LPBF process simulation. According to the developed system and associated experimental results, this chapter would summarize the contributions in detail and propose the future directions.

## 8.1. Topology optimization for AM framework (Chapter 3)

A robust framework for topology optimization in AM has been developed. This framework possesses the capability to address various challenges encountered in AM, including the minimum feature size control, self-support constraint, and so forth. Moreover, it is compatible with diverse physical problems such as elastic deformations, heat conduction, and others. This versatile framework provides a powerful tool for optimizing designs in the context of AM, addressing a wide range of AM-related issues.

## 8.2. Topology optimization method for advanced AM parts (Chapter 4)

1. A novel solution to the SMMTO problem is proposed in this work based on the ordered SIMP method. To be specific, description of the multi-material elastic model is achieved with the ordered SIMP interpolation. More importantly, a novel ordered SIMP like interpolation function is proposed to realize the relaxed and scaled stress interpolation, so that only a unique set of density variables is required for the SMMTO problem.

2. In the porous infill design, the incorporation of solid interface layers successfully

addresses the connectivity challenge, enhancing the overall robustness of the multiscale structures. Experimental validation confirms the positive impact of adding interface layers, as the designs lacking interior interface layers exhibit noticeably reduced stiffness and strength performance.

## 8.3. Topology optimization framework for LPBF metal AM (Chapter 5)

1. The ISM model, which is based on elastic FEM, is one of the most suitable methods for part-level simulation. This is primarily due to its remarkable ability to significantly reduce computational time, cutting it down from months to mere minutes in comparison to alternative models.

2. The ISM model was also employed in predicting the deflections of the printed part. Results show an average of only 5% error between the commercial software and proposed solver results.

3. For the integration of topology optimization and LPBF metal AM, the formulation has been developed as a multi-objective topology optimization problem considering structural performance and residual distortion objective functions. This kind of formulation could effectively solve the issues in LPBF metal AM oriented design problems.

## 8.4. Quality control topology optimization for LPBF metal AM (Chapter 6)

1. To facilitate the formulation of the topology optimization problem involving the inherent strain load, the concept of ILC is introduced in this study as an inherent property of the material. Using the RAMP interpolation and a corrected aggregation technique for elemental stresses, the proposed method is shown to effectively enforce the maximum residual stress and volume fraction limits on benchmark numerical examples.

2. It is found that the scanning path plays an important role for distortion minimization,

and the part printed by the optimized scanning path exhibits better performances (smaller maximum distortion). In addition, a fast yet stable convergence curve (0) also demonstrates the efficiency of the proposed method. Thus, this method is capable of improving the manufacturability of AM builds.

3. A topology optimization method to design manufacturable support structures considering the residual distortion induced in the LPBF AM process and various AM issues (easy removal support structure, self-support structure, and minimum length control), however these features will more or less sacrifice the structural performance.

**8.5. Concurrent path and structure optimization for LPBF metal AM (Chapter 7)**

1. A comparative design framework for LPBF fabricated part has been proposed. This work cannot only optimize the laser scanning pattern but structure geometry, and can effectively avoid part failures of cracking, delamination, or warpage during the printing process, and therefore the printing cost is reduced.

2. The parallel computing framework for topology optimization considering the metal AM has fully been established. This framework is able to solve the high-resolution problem.

3. Compared with the sequential optimization strategy (methods in Sections 6.2 and 6.3), the proposed concurrent optimization strategy could further reduce the residual distortion and achieve better structural performance.

**8.6. Limitations and future work**

1. Most of the presented works are still limited to the linear physics. This model will greatly restrict the applications of the algorithm to distinct optimization problems. In the future, the nonlinear physics will be taken into account.

2. ISM could be further refined by including the elastic-plastic model, and further

experimental validations are needed.

3. Guidelines for structural optimization for LPBF should be developed. Structural optimization for LPBF needs a variety of different knowledge ranging from structural design to process optimization. It should be significantly beneficial that one can generate guidelines for structural optimization for LPBF via several trial-and-errors based on experiments and simulations.

# Reference

[1] Wong, K. V., & Hernandez, A. (2012). A review of additive manufacturing. *International scholarly research notices*, 2012.

[2] Sigmund, O., & Maute, K. (2013). Topology optimization approaches: A comparative review. *Structural and Multidisciplinary Optimization*, 48(6), 1031-1055.

[3] Brackett, D., Ashcroft, I., & Hague, R. (2011, August). Topology optimization for additive manufacturing. In 2011 International Solid Freeform Fabrication Symposium. University of Texas at Austin.

[4] Zegard, T., & Paulino, G. H. (2016). Bridging topology optimization and additive manufacturing. Structural and Multidisciplinary Optimization, 53(1), 175-192.

[5] Khorasani, A., Gibson, I., Veetil, J. K., & Ghasemi, A. H. (2020). A review of technological improvements in laser-based powder bed fusion of metal printers. *The International Journal of Advanced Manufacturing Technology*, *108*, 191-209.

[6] Svetlizky, D., Das, M., Zheng, B., Vyatskikh, A. L., Bose, S., Bandyopadhyay, A., ... & Eliaz, N. (2021). Directed energy deposition (DED) additive manufacturing: Physical characteristics, defects, challenges and applications. *Materials Today*, *49*, 271-295.

[7] Li, J. Z., Alkahari, M. R., Rosli, N. A. B., Hasan, R., Sudin, M. N., & Ramli, F. R. (2019). Review of wire arc additive manufacturing for 3D metal printing. *International Journal of Automation Technology*, *13*(3), 346-353.

[8] Sigmund, O. (2009). Manufacturing tolerant topology optimization. *Acta Mechanica Sinica*, *25*, 227-239.

[9] Liu, J., Gaynor, A. T., Chen, S., Kang, Z., Suresh, K., Takezawa, A., ... & To, A. (2018). Current and future trends in topology optimization for additive manufacturing. *Structural and multidisciplinary optimization*, *57*(6), 2457-2483.

[10] Jihong, Z. H. U., Han, Z. H. O. U., Chuang, W. A. N. G., Lu, Z. H. O. U., Shangqin, Y. U. A. N., & Zhang, W. (2021). A review of topology optimization for additive manufacturing: Status and challenges. *Chinese Journal of Aeronautics*, *34*(1), 91-110.

[11] Ranjan, R., Samant, R., & Anand, S. (2017). Integration of design for manufacturing methods with topology optimization in additive manufacturing. *Journal of Manufacturing Science and Engineering*, *139*(6), 061007.

[12] Saadlaoui, Y., Milan, J. L., Rossi, J. M., & Chabrand, P. (2017). Topology optimization and additive manufacturing: Comparison of conception methods using industrial codes. *Journal of Manufacturing Systems*, *43*, 178-186.

[13] Gibson, I., Rosen, D. W., Stucker, B., Khorasani, M., Rosen, D., Stucker, B., & Khorasani, M. (2021). Additive manufacturing technologies (Vol. 17). Cham, Switzerland: Springer.

[14] Frazier, W. E. (2014). Metal additive manufacturing: a review. Journal of Materials Engineering and performance, 23(6), 1917-1928.

[15] Sigmund, O. (2022). On benchmarking and good scientific practise in topology optimization. *Structural and Multidisciplinary Optimization*, *65*(11), 315.

[16] Ramani, A. (2011). Multi-material topology optimization with strength constraints. *Structural and Multidisciplinary Optimization*, *43*(5), 597-615.

[17] Wu, J., Sigmund, O., & Groen, J. P. (2021). Topology optimization of multi-scale structures: a review. *Structural and Multidisciplinary Optimization*, *63*, 1455-1480.

[18] Gandhi, Y., & Minak, G. (2022). A Review on Topology Optimization Strategies for Additively Manufactured Continuous Fiber-Reinforced Composite Structures. *Applied Sciences*, *12*(21), 11211.

[19] Ibhadode, O., Zhang, Z., Sixt, J., Nsiempba, K. M., Orakwe, J., Martinez-Marchese, A., ... & Toyserkani, E. (2023). Topology optimization for metal additive manufacturing: current trends, challenges, and future outlook. *Virtual and Physical Prototyping*, *18*(1), e2181192.

[20] Mukherjee, S., Lu, D., Raghavan, B., Breitkopf, P., Dutta, S., Xiao, M., & Zhang, W. (2021). Accelerating large-scale topology optimization: State-of-the-art and challenges. *Archives of Computational Methods in Engineering*, 1-23.

[21] Träff, E. A., Rydahl, A., Karlsson, S., Sigmund, O., & Aage, N. (2023). Simple and efficient GPU accelerated topology optimisation: Codes and applications. *Computer Methods in Applied Mechanics and Engineering*, *410*, 116043.

[22] Aage, N., Andreassen, E., & Lazarov, B. S. (2015). Topology optimization using PETSc: An easy-to-use, fully parallel, open source topology optimization framework. *Structural and Multidisciplinary Optimization*, *51*, 565-572.

[23] Smit, T., Aage, N., Ferguson, S. J., & Helgason, B. (2021). Topology optimization using PETSc: a Python wrapper and extended functionality. *Structural and Multidisciplinary Optimization*, *64*, 4343-4353.

[24] Kristiansen, H., & Aage, N. (2022). An open-source framework for large-scale transient topology optimization using PETSc. *Structural and Multidisciplinary Optimization*, *65*(10), 295.

[25] Li, H., Yamada, T., Jolivet, P., Furuta, K., Kondoh, T., Izui, K., & Nishiwaki, S. (2021). Full-scale 3D structural topology optimization using adaptive mesh refinement based on the level-set method. *Finite Elements in Analysis and Design*, *194*, 103561.

[26] Zhang, Z. D., Ibhadode, O., Ali, U., Dibia, C. F., Rahnama, P., Bonakdar, A., & Toyserkani, E. (2020). Topology optimization parallel-computing framework based on the inherent strain method for support structure design in laser powder-bed fusion additive manufacturing. *International Journal of Mechanics and Materials in*

*Design*, 16, 897-923.

[27] Bendsoe, M. P., & Sigmund, O. (2003). *Topology optimization: theory, methods, and applications*. Springer Science & Business Media.

[28] Borrvall, T., & Petersson, J. (2003). Topology optimization of fluids in Stokes flow. International journal for numerical methods in fluids, 41(1), 77-107.

[29] Dühring, M. B., Jensen, J. S., & Sigmund, O. (2008). Acoustic design by topology optimization. Journal of sound and vibration, 317(3-5), 557-575.

[30] Zhou, S., Li, W., & Li, Q. (2010). Level-set based topology optimization for electromagnetic dipole antenna design. Journal of Computational Physics, 229(19), 6915-6930.

[31] Andkjær, J., & Sigmund, O. (2011). Topology optimized low-contrast all-dielectric optical cloak. Applied Physics Letters, 98(2), 021112.

[32] Sigmund, O. (2001). Design of multiphysics actuators using topology optimization– Part I: One-material structures. Computer methods in applied mechanics and engineering, 190(49-50), 6577-6604.

[33] Bendsøe, M. P., & Kikuchi, N. (1988). Generating optimal topologies in structural design using a homogenization method. Computer methods in applied mechanics and engineering, 71(2), 197-224.

[34] Bendsøe, M. P. (1989). Optimal shape design as a material distribution problem. Structural optimization, 1(4), 193-202.

[35] Zhou, M., & Rozvany, G. I. N. (1991). The COC algorithm, Part II: Topological, geometrical and generalized shape optimization. Computer methods in applied mechanics and engineering, 89(1-3), 309-336.

[36] Mlejnek, H. P. (1992). Some aspects of the genesis of structures. Structural optimization, 5(1), 64-69.

[37] Allaire, G., Jouve, F., & Toader, A. M. (2002). A level-set method for shape optimization. Comptes Rendus Mathematique, 334(12), 1125-1130.

[38] Allaire, G., Jouve, F., & Toader, A. M. (2004). Structural optimization using sensitivity analysis and a level-set method. Journal of computational physics, 194(1), 363-393.

[39] Wang, M. Y., Wang, X., & Guo, D. (2003). A level set method for structural topology optimization. Computer methods in applied mechanics and engineering, 192(1-2), 227-246.

[40] Yamada, T., Izui, K., & Nishiwaki, S. (2011). A level set-based topology optimization method for maximizing thermal diffusivity in problems including design-dependent effects.

[41] Sokolowski, J., & Zochowski, A. (1999). On the topological derivative in shape optimization. SIAM journal on control and optimization, 37(4), 1251-1272.

[42] Bourdin, B., & Chambolle, A. (2003). Design-dependent loads in topology optimization. ESAIM: Control, Optimisation and Calculus of Variations, 9, 19-48.

[43] Xie, Y. M., & Steven, G. P. (1993). A simple evolutionary procedure for structural optimization. Computers & structures, 49(5), 885-896.

[44] Guo, X., Zhang, W., & Zhong, W. (2014). Doing topology optimization explicitly and geometrically—a new moving morphable components based framework. *Journal of Applied Mechanics*, *81*(8), 081009.

[45] van Dijk, N. P., Maute, K., Langelaar, M., & Van Keulen, F. (2013). Level-set methods for structural topology optimization: a review. Structural and Multidisciplinary Optimization, 48(3), 437-472.

[46] Rozvany, G. I. (2009). A critical review of established methods of structural topology optimization. Structural and multidisciplinary optimization, 37(3), 217-237.

[47] Huang, X., & Xie, Y. M. (2010). A further review of ESO type methods for topology optimization. Structural and Multidisciplinary Optimization, 41(5), 671-683.

[48] Hassani, B., & Hinton, E. (1998). A review of homogenization and topology optimization I—homogenization theory for media with periodic structure. Computers & Structures, 69(6), 707-717.

[49] Sigmund, O., & Maute, K. (2013). Topology optimization approaches. Structural and Multidisciplinary Optimization, 48(6), 1031-1055.

[50] Bendsoe, Martin Philip, and Ole Sigmund. Topology optimization: theory, methods, and applications. Springer Science & Business Media, 2013.

[51] Yin, L., and G. K. Ananthasuresh. " Topology optimization of compliant mechanisms with multiple materials using a peak function material interpolation scheme." Structural and Multidisciplinary Optimization 23.1 (2001): 49-62.

[52] Tavakoli, Rouhollah. "Multimaterial Topology optimization by volume constrained Allen–Cahn system and regularized projected steepest descent method." Computer Methods in Applied Mechanics and Engineering 276 (2014): 534-565.

[53] Wang, Michael Yu, and Xiaoming Wang. ""Color" level sets: a multi-phase method for structural topology optimization with multiple materials." Computer Methods in Applied Mechanics and Engineering 193.6-8 (2004): 469-496.

[54] Li, Hao, Zhen Luo, Mi Xiao, Liang Gao, and Jie Gao. "A new multiscale TO method for multiphase composite structures of frequency response with level sets." Computer Methods in Applied Mechanics and Engineering 356 (2019): 116-144.

[55] Wang, M. Y., & Wang, X. (2004). "Color" level sets: a multi-phase method for structural TO with multiple materials. Computer Methods in Applied Mechanics and Engineering, 193(6-8), 469-496.

[56] Wang, Y., Luo, Z., Kang, Z., & Zhang, N. (2015). A multi-material level set-based

topology and shape optimization method. Computer Methods in Applied Mechanics and Engineering, 283, 1570-1586.

[57] Zuo, Wenjie, and Kazuhiro Saitou. "Multi-material TO using ordered SIMP interpolation." Structural and Multidisciplinary Optimization 55.2 (2017): 477-491.

[58] Rodrigues, H., Jose M. Guedes, and M. P. Bendsoe. "Hierarchical optimization of material and structure." Structural and Multidisciplinary Optimization 24.1 (2002): 1-10.

[59] Coelho, P. G., et al. "A hierarchical model for concurrent material and topology optimisation of three-dimensional structures." Structural and Multidisciplinary Optimization 35.2 (2008): 107-115.

[60] Xia, Liang, and Piotr Breitkopf. "Recent advances on TO of multiscale nonlinear structures." Archives of Computational Methods in Engineering 24.2 (2017): 227-249.

[61] Zhang, Weihong, and Shiping Sun. "Scale-related TO of cellular materials and structures." International Journal for numerical methods in Engineering 68.9 (2006): 993-1011.

[62] Alexandersen, Joe, and Boyan S. Lazarov. "Topology optimisation of manufacturable microstructural details without length scale separation using a spectral coarse basis preconditioner." Computer Methods in Applied Mechanics and Engineering 290 (2015): 156-182.

[63] Li, Hao, et al. "Integrated design of cellular composites using a level-set TO method." Computer Methods in Applied Mechanics and Engineering 309 (2016): 453-475.

[64] Zhang, Yan, et al. "Multiscale concurrent TO for cellular structures with multiple microstructures based on ordered SIMP interpolation." Computational Materials Science 155 (2018): 74-91.

[65] Li, Hao, et al. "TO for functionally graded cellular composites with metamaterials by level sets." Computer Methods in Applied Mechanics and Engineering 328 (2018): 340-364.

[66] Xia, Liang, and Piotr Breitkopf. "Concurrent TO design of material and structure within FE2 nonlinear multiscale analysis framework." Computer Methods in Applied Mechanics and Engineering 278 (2014): 524-542.

[67] Xia, Liang, and Piotr Breitkopf. "Multiscale structural TO with an approximate constitutive model for local material microstructure." Computer Methods in Applied Mechanics and Engineering 286 (2015): 147-167.

[68] Liu, Ling, Jun Yan, and Gengdong Cheng. "Optimum structure with homogeneous optimum truss-like material." Computers & Structures 86.13-14 (2008): 1417-1425.

[69] Yan, Jun, et al. "Concurrent multi-scale design optimization of composite frames with

manufacturing constraints." Structural and Multidisciplinary Optimization 56.3 (2017): 519-533.

[70] Kato, Junji, et al. "TO of micro-structure for composites applying a decoupling multi-scale analysis." Structural and Multidisciplinary Optimization 49.4 (2014): 595-608.

[71] Huang, X., et al. "TO of microstructures of cellular materials and composites for macrostructures." Computational Materials Science 67 (2013): 397-407.

[72] Niu, Bin, Jun Yan, and Gengdong Cheng. "Optimum structure with homogeneous optimum cellular material for maximum fundamental frequency." Structural and Multidisciplinary Optimization 39.2 (2009): 115.

[73] Gao, Jie, et al. "Dynamic multiscale TO for multi-regional micro-structured cellular composites." Composite Structures 211 (2019): 401-417.

[74] Wang, Yiqiang, Feifei Chen, and Michael Yu Wang. "Concurrent design with connectable graded microstructures." Computer Methods in Applied Mechanics and Engineering 317 (2017): 84-101.

[75] Zhang, Yan, et al. "Multiscale TO for minimizing frequency responses of cellular composites with connectable graded microstructures." Mechanical Systems and Signal Processing 135 (2020): 106369.

[76] Du, Zongliang, et al. "Connecting microstructures for multiscale TO with connectivity index constraints." Journal of Mechanical Design 140.11 (2018): 111417.

[77] Groen, Jeroen P., and Ole Sigmund. "Homogenization-based TO for high-resolution manufacturable microstructures." International Journal for Numerical Methods in Engineering 113.8 (2018): 1148-1163.

[78] Deng, Jiadong, Claus BW Pedersen, and Wei Chen. "Connected morphable components-based multiscale TO." Frontiers of Mechanical Engineering 14.2 (2019): 129-140.

[79] Zhao, Junpeng, Heonjun Yoon, and Byeng D. Youn. "An efficient concurrent TO approach for frequency response problems." Computer Methods in Applied Mechanics and Engineering 347 (2019): 700-734.

[80] Kato, Junji, et al. "Micro-macro concurrent TO for nonlinear solids with a decoupling multiscale analysis." International Journal for Numerical Methods in Engineering 113.8 (2018): 1189-1213.

[81] Sivapuram, Raghavendra, Peter D. Dunning, and H. Alicia Kim. "Simultaneous material and structural optimization by multiscale TO." Structural and multidisciplinary optimization 54.5 (2016): 1267-1281.

[82] Xu, Liang, and Gengdong Cheng. "Two-scale concurrent TO with multiple micro materials based on principal stress orientation." Structural and Multidisciplinary Optimization 57.5 (2018): 2093-2107.

[83] Gao, Jie, et al. "TO for multiscale design of porous composites with multi-domain microstructures." Computer Methods in Applied Mechanics and Engineering344 (2019): 451-476.

[84] Le, C., Norato, J., Bruns, T., Ha, C., & Tortorelli, D. (2010). Stress-based TO for continua. Structural and Multidisciplinary Optimization, 41(4), 605-620.

[85] Kirsch, Uri. "On singular topologies in optimum structural design." Structural optimization 2.3 (1990): 133-142.

[86] Cheng, Gengdong, and Zheng Jiang. "Study on TO with stress constraints." Engineering Optimization20.2 (1992): 129-148.

[87] Duysinx, Pierre, and Martin P. Bendsøe. "TO of continuum structures with local stress constraints." International journal for numerical methods in engineering 43.8 (1998): 1453-1478.

[88] Yu, Huangchao, Jiaqi Huang, Bin Zou, Wen Shao, and Jikai Liu. "Stress-constrained shell-lattice infill structural optimization for additive manufacturing." Virtual and Physical Prototyping 15, no. 1 (2020): 35-48.

[89] Cheng, G. D., and Xiao Guo. "ε-relaxed approach in structural TO." Structural optimization 13.4 (1997): 258-266.

[90] Duysinx, Pierre, and Ole Sigmund. "New developments in handling stress constraints in optimal material distribution." 7th AIAA/USAF/NASA/ISSMO symposium on multidisciplinary analysis and optimization. 1998.

[91] Bruggi, Matteo. "On an alternative approach to stress constraints relaxation in TO." Structural and multidisciplinary optimization 36.2 (2008): 125-141.

[92] Bruggi, Matteo, and Pierre Duysinx. "TO for minimum weight with compliance and stress constraints." Structural and Multidisciplinary Optimization 46.3 (2012): 369-384.

[93] Bruggi, Matteo. "On an alternative approach to stress constraints relaxation in TO." Structural and multidisciplinary optimization 36.2 (2008): 125-141.

[94] Luo, Yangjun, Michael Yu Wang, and Zhan Kang. "An enhanced aggregation method for TO with local stress constraints." Computer Methods in Applied Mechanics and Engineering 254 (2013): 31-41.

[95] Kiyono, C. Y., S. L. Vatanabe, E. C. N. Silva, and J. N. Reddy. "A new multi-p-norm formulation approach for stress-based TO design." Composite Structures 156 (2016): 10-19.

[96] Holmberg, Erik, Bo Torstenfelt, and Anders Klarbring. "Stress constrained TO." Structural and Multidisciplinary Optimization 48.1 (2013): 33-47.

[97] París, 26 J., F. Navarrina, I. Colominas, and M. Casteleiro. "TO of continuum structures with local and global stress constraints." Structural and Multidisciplinary

Optimization 39, no. 4 (2009): 419-437.

[98] Yang, R. J., and C. J. Chen. "Stress-based TO." Structural optimization 12.2-3 (1996): 98-105.

[99] Jeong, Seung Hyun, Seon Ho Park, Dong-Hoon Choi, and Gil Ho Yoon. "TO considering static failure theories for ductile and brittle materials." Computers & structures 110 (2012): 116-132.

[100] Luo, Yangjun, and Zhan Kang. "TO of continuum structures with Drucker–Prager yield stress constraints." Computers Structures 90 (2012): 65-75.

[101] Giraldo-Londoño, Oliver, and Glaucio H. Paulino. "A unified approach for TO with local stress constraints considering various failure criteria: von Mises, Drucker–Prager, Tresca, Mohr–Coulomb, Bresler–Pister and Willam–Warnke." Proceedings of the Royal Society A476.2238 (2020): 20190861.

[102] Moon, Seung Jae, and Gil Ho Yoon. "A newly developed qp-relaxation method for element connectivity parameterization to achieve stress-based TO for geometrically nonlinear structures." Computer Methods in Applied Mechanics and Engineering 265 (2013): 226-241.

[103] Takezawa, Akihiro, Gil Ho Yoon, Seung Hyun Jeong, Makoto Kobashi, and Mitsuru Kitamura. "Structural TO with strength and heat conduction constraints." Computer Methods in Applied Mechanics and Engineering 276 (2014): 341-361.

[104] Frazier, W. E. (2014). Metal additive manufacturing: a review. *Journal of Materials Engineering and performance*, *23*, 1917-1928.

[105] Dilberoglu, U. M., Gharehpapagh, B., Yaman, U., & Dolen, M. (2017). The role of additive manufacturing in the era of industry 4.0. *Procedia manufacturing*, *11*, 545-554.

[106] Bandyopadhyay, A., & Bose, S. (Eds.). (2019). *Additive manufacturing*. CRC press.

[107] Singh, P., Singari, R. M., & Mishra, R. S. (2022). A review of study on modeling and simulation of additive manufacturing processes. *Materials Today: Proceedings*, *56*, 3594-3603.

[108] Gusarov, A. V., Yadroitsev, I., Bertrand, P., & Smurov, I. (2009). Model of radiation and heat transfer in laser-powder interaction zone at selective laser melting.

[109] Zhao, C., Fezzaa, K., Cunningham, R. W., Wen, H., De Carlo, F., Chen, L., ... & Sun, T. (2017). Real-time monitoring of laser powder bed fusion process using high-speed X-ray imaging and diffraction. *Scientific reports*, 7(1), 3602.

[110] Matthews, M. J., Guss, G., Khairallah, S. A., Rubenchik, A. M., Depond, P. J., & King, W. E. (2016). Denudation of metal powder layers in laser powder bed fusion

processes. *Acta Materialia*, 114, 33-42.

[111]    Bidare, P., Bitharas, I., Ward, R. M., Attallah, M. M., & Moore, A. J. (2018). Fluid and particle dynamics in laser powder bed fusion. *Acta Materialia*, 142, 107-120.

[112]    Panwisawas, C., Qiu, C., Anderson, M. J., Sovani, Y., Turner, R. P., Attallah, M. M., ... & Basoalto, H. C. (2017). Mesoscale modelling of selective laser melting: Thermal fluid dynamics and microstructural evolution. *Computational Materials Science*, 126, 479-490.

[113]    Bayat, M., Mohanty, S., & Hattel, J. H. (2019). A systematic investigation of the effects of process parameters on heat and fluid flow and metallurgical conditions during laser-based powder bed fusion of Ti6Al4V alloy. *International Journal of Heat and Mass Transfer*, 139, 213-230.

[114]    Bayat, M., Mohanty, S., & Hattel, J. H. (2019). Multiphysics modelling of lack-of-fusion voids formation and evolution in IN718 made by multi-track/multi-layer L-PBF. *International Journal of Heat and Mass Transfer*, 139, 95-114.

[115]    Yan, W., Ge, W., Qian, Y., Lin, S., Zhou, B., Liu, W. K., ... & Wagner, G. J. (2017). Multi-physics modeling of single/multiple-track defect mechanisms in electron beam selective melting. *Acta Materialia*, 134, 324-333.

[116]    Khairallah, S. A., Anderson, A. T., Rubenchik, A., & King, W. E. (2016). Laser powder-bed fusion additive manufacturing: Physics of complex melt flow and formation mechanisms of pores, spatter, and denudation zones. *Acta Materialia*, 108, 36-45.

[117]    Körner, C., Attar, E., & Heinl, P. (2011). Mesoscopic simulation of selective beam melting processes. *Journal of Materials Processing Technology*, 211(6), 978-987.

[118]    Körner, C., Bauereiß, A., & Attar, E. (2013). Fundamental consolidation mechanisms during selective beam melting of powders. *Modelling and Simulation in Materials Science and Engineering*, 21(8), 085011.

[119]    Khairallah, S. A., & Anderson, A. (2014). Mesoscopic simulation model of selective laser melting of stainless steel powder. *Journal of Materials Processing Technology*, 214(11), 2627-2636.

[120]    Xia, M., Gu, D., Yu, G., Dai, D., Chen, H., & Shi, Q. (2017). Porosity evolution and its thermodynamic mechanism of randomly packed powder-bed during selective laser melting of Inconel 718 alloy. *International Journal of Machine Tools and Manufacture*, 116, 96-106.

[121]    Masoomi, M., Pegues, J. W., Thompson, S. M., & Shamsaei, N. (2018). A numerical and experimental investigation of convective heat transfer during laser-powder bed fusion. *Additive Manufacturing*, 22, 729-745.

[122]    Boley, C. D., Khairallah, S. A., & Rubenchik, A. M. (2015). Calculation of laser

absorption by metal powders in additive manufacturing. *Applied optics*, 54(9), 2477-2482.

[123]   Bandyopadhyay, A., & Traxel, K. D. (2018). Invited review article: Metal-additive manufacturing—Modeling strategies for application-optimized designs. *Additive manufacturing*, 22, 758-774.

[124]   Zinovieva, O., Zinoviev, A., & Ploshikhin, V. (2018). Three-dimensional modeling of the microstructure evolution during metal additive manufacturing. *Computational Materials Science*, 141, 207-220.

[125]   Koepf, J. A., Gotterbarm, M. R., Markl, M., & Körner, C. (2018). 3D multi-layer grain structure simulation of powder bed fusion additive manufacturing. *Acta Materialia*, 152, 119-126.

[126]   Wu, J., Wang, L., & An, X. (2017). Numerical analysis of residual stress evolution of AlSi10Mg manufactured by selective laser melting. *Optik*, 137, 65-78.

[127]   Li, Y., Zhou, K., Tan, P., Tor, S. B., Chua, C. K., & Leong, K. F. (2018). Modeling temperature and residual stress fields in selective laser melting. *International Journal of Mechanical Sciences*, 136, 24-35.

[128]   Tan, P., Shen, F., Li, B., & Zhou, K. (2019). A thermo-metallurgical-mechanical model for selective laser melting of Ti6Al4V. *Materials & Design*, 168, 107642.

[129]   Wang, D., Wu, S., Yang, Y., Dou, W., Deng, S., Wang, Z., & Li, S. (2018). The effect of a scanning strategy on the residual stress of 316L steel parts fabricated by selective laser melting (SLM). *Materials*, 11(10), 1821.

[130]   Song, J., Wu, W., Zhang, L., He, B., Lu, L., Ni, X., ... & Zhu, G. (2018). Role of scanning strategy on residual stress distribution in Ti-6Al-4V alloy prepared by selective laser melting. *Optik*, 170, 342-352.

[131]   Mugwagwa, L., Dimitrov, D., Matope, S., & Yadroitsev, I. (2019). Evaluation of the impact of scanning strategies on residual stresses in selective laser melting. *The International Journal of Advanced Manufacturing Technology*, 102, 2441-2450.

[132]   Bhardwaj, T., & Shukla, M. (2018). Effect of laser scanning strategies on texture, physical and mechanical properties of laser sintered maraging steel. *Materials Science and Engineering: A*, 734, 102-109.

[133]   Ramos, D., Belblidia, F., & Sienz, J. (2019). New scanning strategy to reduce warpage in additive manufacturing. *Additive Manufacturing*, 28, 554-564.

[134]   Denlinger, E. R., Gouge, M., Irwin, J., & Michaleris, P. (2017). Thermomechanical model development and in situ experimental validation of the Laser Powder-Bed Fusion process. *Additive Manufacturing*, 16, 73-80.

[135]   Neiva, E., Badia, S., Martín, A. F., & Chiumenti, M. (2019). A scalable parallel finite element framework for growing geometries. Application to metal additive

manufacturing. *International Journal for Numerical Methods in Engineering*, 119(11), 1098-1125.

[136]    Mercelis, P., & Kruth, J. P. (2006). Residual stresses in selective laser sintering and selective laser melting. *Rapid prototyping journal*, 12(5), 254-265.

[137]    Matsumoto, M., Shiomi, M., Osakada, K., & Abe, F. (2002). Finite element analysis of single layer forming on metallic powder bed in rapid prototyping by selective laser processing. *International Journal of Machine Tools and Manufacture*, 42(1), 61-67.

[138]    Shiomi, M., Osakada, K., Nakamura, K., Yamashita, T., & Abe, F. (2004). Residual stress within metallic model made by selective laser melting process. *Cirp Annals*, 53(1), 195-198.

[139]    Roberts, I. A., Wang, C. J., Esterlein, R., Stanford, M., & Mynors, D. J. (2009). A three-dimensional finite element analysis of the temperature field during laser melting of metal powders in additive layer manufacturing. *International Journal of Machine Tools and Manufacture*, 49(12-13), 916-923.

[140]    Lei, Y., Sun, R., Tang, Y., & Niu, W. (2012). Numerical simulation of temperature distribution and TiC growth kinetics for high power laser clad TiC/NiCrBSiC composite coatings. *Optics & Laser Technology*, 44(4), 1141-1147.

[141]    Zhao, H., Zhang, G., Yin, Z., & Wu, L. (2011). A 3D dynamic analysis of thermal behavior during single-pass multi-layer weld-based rapid prototyping. *Journal of Materials Processing Technology*, 211(3), 488-495.

[142]    Kolossov, S., Boillat, E., Glardon, R., Fischer, P., & Locher, M. (2004). 3D FE simulation for temperature evolution in the selective laser sintering process. *International Journal of Machine Tools and Manufacture*, 44(2-3), 117-123.

[143]    Zhang, W., Tong, M., & Harrison, N. M. (2019). Resolution, energy and time dependency on layer scaling in finite element modelling of laser beam powder bed fusion additive manufacturing. *Additive Manufacturing*, 28, 610-620.

[144]    Keller, N., Neugebauer, F., Xu, H., & Ploshikhin, V. (2013, September). Thermo-mechanical simulation of additive layer manufacturing of titanium aerospace structures. *In Proceedings of the Light MAT Conference* (Vol. 3).

[145]    Seidel, C., Zaeh, M. F., Wunderer, M., Weirather, J., Krol, T. A., & Ott, M. (2014). Simulation of the laser beam melting process–approaches for an efficient modelling of the beam-material interaction. *Procedia Cirp*, 25, 146-153.

[146]    Chiumenti, M., Neiva, E., Salsi, E., Cervera, M., Badia, S., Moya, J., ... & Davies, C. (2017). Numerical modelling and experimental validation in Selective Laser Melting. *Additive Manufacturing*, 18, 171-185.

[147]    Li, C., Fu, C. H., Guo, Y. B., & Fang, F. Z. (2016). A multiscale modeling

approach for fast prediction of part distortion in selective laser melting. *Journal of materials processing technology*, 229, 703-712.

[148]   Keller, N., & Ploshikhin, V. (2014). New method for fast predictions on residual stress and distortion of AM parts. *In 2014 International Solid Freeform Fabrication Symposium*. University of Texas at Austin.

[149]   Siewert, M., Neugebauer, F., Epp, J., & Ploshikhin, V. (2019). Validation of Mechanical Layer Equivalent Method for simulation of residual stresses in additive manufactured components. *Computers & Mathematics with Applications*, 78(7), 2407-2416.

[150]   Wong, K. V., & Hernandez, A. (2012). A review of additive manufacturing. International scholarly research notices, 2012.

[151]   Liu, J., Gaynor, A. T., Chen, S., Kang, Z., Suresh, K., Takezawa, A., ... & To, A. C. (2018). Current and future trends in TO for additive manufacturing. Structural and Multidisciplinary Optimization, 57(6), 2457-2483.

[152]   Ahn, S. H. (2002). SR; Wright, PK; Montero, M.; Odell, D.; Roundy, S. Anisotropic material properties of fused deposition modeling ABS. Rapid Prototyp. J, 8, 248-257.

[153]   Bellini, A., & Güçeri, S. (2003). Mechanical characterization of parts fabricated using fused deposition modeling. Rapid Prototyping Journal.

[154]   Clausen, A. (2016). TO for additive manufacturing. DTU Mechanical Engineering.

[155]   Zhang, S. N., Abdel-Wahab, M. A., & Jones, E. B. G. (2015). 2019. Additions to the genus Savoryella( Savoryellaceae), with the asexual morphs Savoryella nypae comb. nov. and S. sarushimana sp. nov. Phytotaxa, 408, 195-207.

[156]   Mirzendehdel, A. M., Rankouhi, B., & Suresh, K. (2018). Strength-based TO for anisotropic parts. Additive Manufacturing, 19, 104-113.

[157]   Suresh, K., & Takalloozadeh, M. (2013). Stress-constrained TO: a topological level-set approach. Structural and Multidisciplinary Optimization, 48(2), 295-309.

[158]   Ulu, E., Korkmaz, E., Yay, K., Burak Ozdoganlar, O., & Burak Kara, L. (2015). Enhancing the structural performance of additively manufactured objects through build orientation optimization. Journal of Mechanical Design, 137(11).

[159]   Umetani, N., & Schmidt, R. M. (2013, November). Cross-sectional structural analysis for 3D printing optimization. In SIGGRAPH Asia Technical Briefs (pp. 5-1).

[160]   Liu, J. (2016). Guidelines for AM part consolidation. Virtual and Physical Prototyping, 11(2), 133-141.

[161]   Bruyneel, M., & Fleury, C. (2002). Composite structures optimization using sequential convex programming. Advances in Engineering Software, 33(7-10), 697-

711.

[162]  Liu, J., Ma, Y., Fu, J., & Duke, K. (2015). A novel CACD/CAD/CAE integrated design framework for fiber-reinforced plastic parts. Advances in Engineering Software, 87, 13-29.

[163]  Song, X., Pan, Y., & Chen, Y. (2015). Development of a low-cost parallel kinematic machine for multidirectional additive manufacturing. Journal of Manufacturing Science and Engineering, 137(2).

[164]  Singh, P., & Dutta, D. (2008). Offset slices for multidirection layered deposition. Journal of manufacturing science and engineering, 130(1).

[165]  Wu, C., Dai, C., Fang, G., Liu, Y. J., & Wang, C. C. (2017, May). RoboFDM: A robotic system for support-free fabrication using FDM. In 2017 IEEE International Conference on Robotics and Automation (ICRA) (pp. 1175-1180). IEEE.

[166]  Zhao, X., Pan, Y., Zhou, C., Chen, Y., & Wang, C. C. (2013). An integrated CNC accumulation system for automatic building-around-inserts. Journal of Manufacturing Processes, 15(4), 432-443.

[167]  Hoglund, R., & Smith, D. E. (2016, August). Continuous fiber angle TO for polymer fused filament fabrication. In Solid Freeform Fabrication Symposium (pp. 1078-1090).

[168]  Liu, J., & Yu, H. (2017). Concurrent deposition path planning and structural TO for additive manufacturing. Rapid Prototyping Journal.

[169]  Dapogny, C., Estevez, R., Faure, A., & Michailidis, G. (2019). Shape and TO considering anisotropic features induced by additive manufacturing processes. Computer Methods in Applied Mechanics and Engineering, 344, 626-665.

[170]  Ding, D., Pan, Z., Cuiuri, D., & Li, H. (2015). A practical path planning methodology for wire and arc additive manufacturing of thin-walled structures. Robotics and Computer-Integrated Manufacturing, 34, 8-19.

[171]  Lazarov, B. S., Wang, F., & Sigmund, O. (2016). Length scale and manufacturability in density-based TO. Archive of Applied Mechanics, 86(1-2), 189-218.

[172]  Lazarov, B. S., & Wang, F. (2017). Maximum length scale in density based TO. Computer Methods in Applied Mechanics and Engineering, 318, 826-844.

[173]  Poulsen, T. A. (2002). TO in wavelet space. International Journal for Numerical Methods in Engineering, 53(3), 567-582.

[174]  Guest, J. K., Prévost, J. H., & Belytschko, T. (2004). Achieving minimum length scale in TO using nodal design variables and projection functions. International journal for numerical methods in engineering, 61(2), 238-254.

[175]  Guest, J. K. (2009). TO with multiple phase projection. Computer Methods in

Applied Mechanics and Engineering, 199(1-4), 123-135.

[176]    Sigmund, O., & Torquato, S. (1997). Design of materials with extreme thermal expansion using a three-phase TO method. Journal of the Mechanics and Physics of Solids, 45(6), 1037-1067.

[177]    Schevenels, M., Lazarov, B. S., & Sigmund, O. (2011). Robust TO accounting for spatially varying manufacturing errors. Computer Methods in Applied Mechanics and Engineering, 200(49-52), 3613-3627.

[178]    Sigmund, O. (2009). Manufacturing tolerant TO. Acta Mechanica Sinica, 25(2), 227-239.

[179]    Wang, F., Lazarov, B. S., & Sigmund, O. (2011). On projection methods, convergence and robust formulations in TO. Structural and Multidisciplinary Optimization, 43(6), 767-784.

[180]    Zhou, M., Lazarov, B. S., Wang, F., & Sigmund, O. (2015). Minimum length scale in TO by geometric constraints. Computer Methods in Applied Mechanics and Engineering, 293, 266-282.

[181]    Guest, J. K. (2009). Imposing maximum length scale in TO. Structural and Multidisciplinary Optimization, 37(5), 463-473.

[182]    Zhang, W., Zhong, W., & Guo, X. (2014). An explicit length scale control approach in SIMP-based TO. Computer Methods in Applied Mechanics and Engineering, 282, 71-86.

[183]    Amir, O., & Lazarov, B. S. (2018). Achieving stress-constrained topological design via length scale control. Structural and Multidisciplinary Optimization, 58(5), 2053-2071.

[184]    Albakri, M., Sturm, L., Williams, C. B., & Tarazaga, P. (2015, August). Non-destructive evaluation of additively manufactured parts via impedance-based monitoring. In Solid Freeform Fabrication Symposium (Vol. 26, pp. 1475-1490).

[185]    Chua, C. K., & Leong, K. F. (2014). 3D Printing and additive manufacturing: Principles and applications (with companion media pack)-of rapid prototyping. World Scientific Publishing Company.

[186]    Diegel, O., Singamneni, S., Reay, S., & Withell, A. (2010). Tools for sustainable product design: additive manufacturing.

[187]    Hu, R., Chen, W., Li, Q., Liu, S., Zhou, P., Dong, Z., & Kang, R. (2017). Design optimization method for additive manufacturing of the primary mirror of a large-aperture space telescope. Journal of Aerospace Engineering, 30(3), 04016093.

[188]    Liu, J., & Ma, Y. (2016). A survey of manufacturing oriented TO methods. Advances in Engineering Software, 100, 161-175.

[189]    Meisel, N., & Williams, C. (2015). An investigation of key design for additive

manufacturing constraints in multimaterial three-dimensional printing. Journal of Mechanical Design, 137(11).

[190]     Zhou, Y., Nomura, T., & Saitou, K. (2018, August). Multi-component TO for powder bed additive manufacturing (MTO-A). In international design engineering technical conferences and computers and information in engineering conference (Vol. 51722, p. V01AT02A051). American Society of Mechanical Engineers.

[191]     Qattawi, A., & Ablat, M. A. (2017). Design consideration for additive manufacturing: fused deposition modelling. Open Journal of Applied Sciences, 7(6), 291-318.

[192]     Liu, S., Li, Q., Chen, W., Tong, L., & Cheng, G. (2015). An identification method for enclosed voids restriction in manufacturability design for additive manufacturing structures. Frontiers of Mechanical Engineering, 10(2), 126-137.

[193]     Li, Q., Chen, W., Liu, S., & Tong, L. (2016). Structural TO considering connectivity constraint. Structural and Multidisciplinary Optimization, 54(4), 971-984.

[194]     Xia, Q., Shi, T., Wang, M. Y., & Liu, S. (2010). A level set based method for the optimization of cast part. Structural and Multidisciplinary Optimization, 41(5), 735-747.

[195]     Gersborg, A. R., & Andreasen, C. S. (2011). An explicit parameterization for casting constraints in gradient driven TO. Structural and Multidisciplinary Optimization, 44(6), 875-881.

[196]     Wu, J., Wang, C. C., Zhang, X., & Westermann, R. (2016). Self-supporting rhombic infill structures for additive manufacturing. Computer-Aided Design, 80, 32-42.

[197]     Huang, X., Ye, C., Wu, S., Guo, K., & Mo, J. (2009). Sloping wall structure support generation for fused deposition modeling. The International Journal of Advanced Manufacturing Technology, 42(11), 1074-1081.

[198]     Vanek, J., Galicia, J. A. G., & Benes, B. (2014, August). Clever support: Efficient support structure generation for digital fabrication. In Computer graphics forum (Vol. 33, No. 5, pp. 117-125).

[199]     Gan, M. X., & Wong, C. H. (2016). Practical support structures for selective laser melting. *Journal of Materials Processing Technology*, 238, 474-484.

[200]     Dumas, J., Hergel, J., & Lefebvre, S. (2014). Bridging the gap: Automated steady scaffoldings for 3d printing. *ACM Transactions on Graphics (TOG)*, 33(4), 1-10.

[201]     Strano, G., Hao, L., Everson, R. M., & Evans, K. E. (2013). A new approach to the design and optimisation of support structures in additive manufacturing. *The International Journal of Advanced Manufacturing Technology*, 66(9-12), 1247-1254.

[202] Hussein, A., Hao, L., Yan, C., Everson, R., & Young, P. (2013). Advanced lattice support structures for metal additive manufacturing. *Journal of Materials Processing Technology*, 213(7), 1019-1026.

[203] Zhou, M., Liu, Y., & Wei, C. (2020). TO of easy-removal support structures for additive manufacturing. *Structural and Multidisciplinary Optimization*, 61(6), 2423-2435.

[204] Mirzendehdel, A. M., & Suresh, K. (2016). Support structure constrained TO for additive manufacturing. *Computer-Aided Design*, 81, 1-13.

[205] Kuo, Y. H., Cheng, C. C., Lin, Y. S., & San, C. H. (2018). Support structure design in additive manufacturing based on topology optimization. *Structural and Multidisciplinary Optimization*, 57(1), 183-195.

[206] Hu, K., Jin, S., & Wang, C. C. (2015). Support slimming for single material based additive manufacturing. *Computer-Aided Design*, 65, 1-10.

[207] Morgan, H. D., Cherry, J. A., Jonnalagadda, S., Ewing, D., & Sienz, J. (2016). Part orientation optimisation for the additive layer manufacture of metal components. *The International Journal of Advanced Manufacturing Technology*, 86(5), 1679-1687.

[208] Muir, M. J., Querin, O. M., & Toropov, V. (2014). Rules, Precursors and Parameterisation Methodologies for Topology Optimised Structural Designs Realised Through Additive Manufacturing. In 10th AIAA Multidisciplinary Design Optimization Conference (p. 0635).

[209] Zhang, X., Le, X., Panotopoulou, A., Whiting, E., & Wang, C. C. (2015). Perceptual models of preference in 3D printing direction. *ACM Transactions on Graphics (TOG)*, 34(6), 1-12.

[210] Ueda, Y., Murakawa, H., & Ma, N. (2012). Welding deformation and residual stress prevention. Elsevier.

[211] DebRoy, T., Wei, H. L., Zuback, J. S., Mukherjee, T., Elmer, J. W., Milewski, J. O., ... & Zhang, W. (2018). Additive manufacturing of metallic components–process, structure and properties. *Progress in Materials Science*, 92, 112-224.

[212] Di Angelo, L., Di Stefano, P., & Guardiani, E. (2020). Search for the optimal build direction in additive manufacturing technologies: A review. *Journal of Manufacturing and Materials Processing*, 4(3), 71.

[213] Sun, W., Ma, Y. E., Zhang, W., Qian, X., Huang, W., & Wang, Z. (2021). Effects of the build direction on mechanical performance of laser powder bed fusion additively manufactured Ti6Al4V under different loadings. *Advanced Engineering Materials*, 23(12), 2100611.

[214] Zhang, P., Toman, J., Yu, Y., Biyikli, E., Kirca, M., Chmielus, M., & To, A. C.

(2015). Efficient design-optimization of variable-density hexagonal cellular structure by additive manufacturing: theory and validation. *Journal of Manufacturing Science and Engineering*, 137(2), 021004.

[215]   Hu, K., Jin, S., & Wang, C. C. (2015). Support slimming for single material based additive manufacturing. *Computer-Aided Design*, 65, 1-10.

[216]   Zhang, Y., Bernard, A., Harik, R., & Karunakaran, K. P. (2017). Build orientation optimization for multi-part production in additive manufacturing. *Journal of Intelligent Manufacturing*, 28, 1393-1407.

[217]   Dunbar, A. J. (2016). Analysis of the laser powder bed fusion additive manufacturing process through experimental measurement and finite element modeling. The Pennsylvania State University.

[218]   Cheng, L., & To, A. (2019). Part-scale build orientation optimization for minimizing residual stress and support volume for metal additive manufacturing: Theory and experimental validation. *Computer-Aided Design*, 113, 1-23.

[219]   Liu, J., & Yu, H. (2020). Self-support topology optimization with horizontal overhangs for additive manufacturing. *Journal of Manufacturing Science and Engineering*, 142(9), 091003.

[220]   Liu, J., & To, A. C. (2017). Deposition path planning-integrated structural topology optimization for 3D additive manufacturing subject to self-support constraint. *Computer-Aided Design*, 91, 27-45.

[221]   Liu, J., & Yu, H. (2017). Concurrent deposition path planning and structural topology optimization for additive manufacturing. *Rapid Prototyping Journal*.

[222]   Luo, Y., Sigmund, O., Li, Q., & Liu, S. (2020). Additive manufacturing oriented topology optimization of structures with self-supported enclosed voids. *Computer Methods in Applied Mechanics and Engineering*, 372, 113385.

[223]   Langelaar, M. (2016). Topology optimization of 3D self-supporting structures for additive manufacturing. Additive Manufacturing, 12, 60-70.

[224]   Langelaar, M. (2017). An additive manufacturing filter for topology optimization of print-ready designs. *Structural and multidisciplinary optimization*, 55(3), 871-883.

[225]   van de Ven, E., Maas, R., Ayas, C., Langelaar, M., & van Keulen, F. (2018). Continuous front propagation-based overhang control for topology optimization with additive manufacturing. *Structural and Multidisciplinary Optimization*, 57(5), 2075-2091.

[226]   Johnson, T. E., & Gaynor, A. T. (2018). Three-dimensional projection-based topology optimization for prescribed-angle self-supporting additively manufactured structures. *Additive Manufacturing*, 24, 667-686.

[227]   Gaynor, A. T., & Guest, J. K. (2016). Topology optimization considering

overhang constraints: Eliminating sacrificial support material in additive manufacturing through design. *Structural and Multidisciplinary Optimization*, 54(5), 1157-1172.

[228]   Qian, X. (2017). Undercut and overhang angle control in topology optimization: a density gradient based integral approach. *International Journal for Numerical Methods in Engineering*, 111(3), 247-272.

[229]   Wu, J., Wang, C. C., Zhang, X., & Westermann, R. (2016). Self-supporting rhombic infill structures for additive manufacturing. *Computer-Aided Design*, 80, 32-42.

[230]   Liu, Y., Zhou, M., Wei, C., & Lin, Z. (2021). Topology optimization of self-supporting infill structures. *Structural and Multidisciplinary Optimization*, 63(5), 2289-2304.

[231]   Leary, M., Merli, L., Torti, F., Mazur, M., & Brandt, M. (2014). Optimal topology for additive manufacture: A method for enabling additive manufacture of support-free optimal structures. *Materials & Design*, 63, 678-690.

[232]   Frazier, William E. "Metal additive manufacturing: a review." *Journal of Materials Engineering and performance* 23.6 (2014): 1917-1928.

[233]   Megahed, Mustafa, et al. "Metal additive-manufacturing process and residual stress modeling." Integrating Materials and Manufacturing Innovation 5.1 (2016): 61-93.

[234]   Wildman, Raymond A., and Andrew T. Gaynor. Topology optimization for Reducing Additive Manufacturing Processing Distortions. No. ARL-TR-8242. Weapons and Materials Research Directorate, US Army Research Laboratory Aberdeen Proving Ground United States, 2017.

[235]   Allaire, Grégoire, and Lukas Jakabčin. "Taking into account thermal residual stresses in TO of structures built by additive manufacturing." *Mathematical Models and Methods in Applied Sciences* 28.12 (2018): 2313-2366.

[236]   Yasin, S. B. M., Mohd, N. F., Mahmud, J., Whashilah, N. S., & Razak, Z. (2018). A reduction of protector cover warpage via topology optimization. *The International Journal of Advanced Manufacturing Technology*, 98, 2531-2537.

[237]   Miki, T., & Yamada, T. (2021). Topology optimization considering the distortion in additive manufacturing. *Finite Elements in Analysis and Design*, 193, 103558.

[238]   Takezawa, A., To, A. C., Chen, Q., Liang, X., Dugast, F., Zhang, X., & Kitamura, M. (2020). Sensitivity analysis and lattice density optimization for sequential inherent strain method used in additive manufacturing process. *Computer Methods in Applied Mechanics and Engineering*, 370, 113231.

[239]   Takezawa, A., Chen, Q., & To, A. C. (2021). Optimally variable density lattice to

reduce warping thermal distortion of laser powder bed fusion. *Additive Manufacturing*, 48, 102422.

[240]   Cheng, L., Liang, X., Bai, J., Chen, Q., Lemon, J., & To, A. (2019). On utilizing topology optimization to design support structure to prevent residual stress induced build failure in laser powder bed metal additive manufacturing. *Additive Manufacturing*, *27*, 290-304.

[241]   Pellens, J., Lombaert, G., Michiels, M., Craeghs, T., & Schevenels, M. (2020). Topology optimization of support structure layout in metal-based additive manufacturing accounting for thermal deformations. *Structural and Multidisciplinary Optimization*, 61, 2291-2303.

[242]   Xu, S., Liu, J., & Ma, Y. (2022). Residual stress constrained self-support topology optimization for metal additive manufacturing. *Computer Methods in Applied Mechanics and Engineering*, 389, 114380.

[243]   Misiun, G., van de Ven, E., Langelaar, M., Geijselaers, H., van Keulen, F., van den Boogaard, T., & Ayas, C. (2021). Topology optimization for additive manufacturing with distortion constraints. *Computer methods in applied mechanics and engineering*, 386, 114095.

[244]   Kruth, J. P., Deckers, J., Yasa, E., & Wauthlé, R. (2012). Assessing and comparing influencing factors of residual stresses in selective laser melting using a novel analysis method. *Proceedings of the institution of mechanical engineers, Part B: Journal of Engineering Manufacture*, 226(6), 980-991.

[245]   Lu, Y., Wu, S., Gan, Y., Huang, T., Yang, C., Junjie, L., & Lin, J. (2015). Study on the microstructure, mechanical property and residual stress of SLM Inconel-718 alloy manufactured by differing island scanning strategy. *Optics & Laser Technology*, *75*, 197-206.

[246]   Cheng, B., Shrestha, S., & Chou, K. (2016). Stress and deformation evaluations of scanning strategy effect in selective laser melting. *Additive Manufacturing*, *12*, 240-251.

[247]   Foteinopoulos, P., Papacharalampopoulos, A., Angelopoulos, K., & Stavropoulos, P. (2020). Development of a simulation approach for laser powder bed fusion based on scanning strategy selection. *The International Journal of Advanced Manufacturing Technology*, *108*(9), 3085-3100.

[248]   Sun, S. H., Koizumi, Y., Kurosu, S., Li, Y. P., Matsumoto, H., & Chiba, A. (2014). Build direction dependence of microstructure and high-temperature tensile property of Co–Cr–Mo alloy fabricated by electron beam melting. *Acta Materialia*, *64*, 154-168.

[249]    Liang, X., Dong, W., Chen, Q., & To, A. C. (2021). On incorporating scanning strategy effects into the modified inherent strain modeling framework for laser powder bed fusion. *Additive Manufacturing*, *37*, 101648.

[250]    Chen, Q., Taylor, H., Takezawa, A., Liang, X., Jimenez, X., Wicker, R., & To, A. C. (2021). Island scanning pattern optimization for residual deformation mitigation in laser powder bed fusion via sequential inherent strain method and sensitivity analysis. *Additive Manufacturing*, 46, 102116.

[251]    Xu, S., Huang, J., Liu, J., Ma, Y., & Liu, J. (2022). An island scanning path-patten optimization for metal additive manufacturing based on inherent strain method. *Comput-Aided Des Appl*.

[252]    Takezawa, A., Guo, H., Kobayashi, R., Chen, Q., & To, A. C. (2022). Simultaneous optimization of hatching orientations and lattice density distribution for residual warpage reduction in laser powder bed fusion considering layerwise residual stress stacking. *Additive Manufacturing*, 60, 103194.

[253]    Beckers, M., & Fleury, C. (1997). Topology optimization involving discrete variables. In *Second World Congress of Structural and Multidisciplinary Optimization-WCSMO2*. Polish Academy of Sciences. Institute of Fundamental Technological Research, Warsaw, Poland.

[254]    Beckers, M. (1999). Topology optimization using a dual method with discrete variables. *Structural optimization*, *17*, 14-24.

[255]    Yan, X. Y., Liang, Y., & Cheng, G. D. (2021). Discrete variable topology optimization for simplified convective heat transfer via sequential approximate integer programming with trust-region. *International Journal for Numerical Methods in Engineering*, *122*(20), 5844-5872.

[256]    Liang, Y., Sun, K., & Cheng, G. (2020). Discrete variable topology optimization for compliant mechanism design via Sequential Approximate Integer Programming with Trust Region (SAIP-TR). *Structural and Multidisciplinary Optimization*, *62*, 2851-2879.

[257]    Ranjbarzadeh, S., Picelli, R., Gioria, R., & Silva, E. C. N. (2022). Topology optimization of structures subject to non-Newtonian fluid–structure interaction loads using integer linear programming. *Finite Elements in Analysis and Design*, *202*, 103690.

[258]    Bendsøe, M. P. (1989). Optimal shape design as a material distribution problem. *Structural optimization*, *1*, 193-202.

[259]    Rozvany, G. I., Zhou, M., & Birker, T. (1992). Generalized shape optimization without homogenization. *Structural optimization*, *4*, 250-252.

[260]    Bendsøe, M. P., & Sigmund, O. (1999). Material interpolation schemes in

topology optimization. *Archive of applied mechanics*, *69*, 635-654.

[261]    Hashin, Z., & Shtrikman, S. (1963). A variational approach to the theory of the elastic behaviour of multiphase materials. *Journal of the Mechanics and Physics of Solids*, *11*(2), 127-140.

[262]    Duysinx, P., & Bendsøe, M. P. (1998). Topology optimization of continuum structures with local stress constraints. *International journal for numerical methods in engineering*, *43*(8), 1453-1478.

[263]    Lipton, R. (2002). Design of functionally graded composite structures in the presence of stress constraints. *International journal of solids and structures*, *39*(9), 2575-2586.

[264]    Dzierżanowski, G. (2012). On the comparison of material interpolation schemes and optimal composite properties in plane shape optimization. *Structural and Multidisciplinary Optimization*, *46*, 693-710.

[265]    Zargham, S., Ward, T. A., Ramli, R., & Badruddin, I. A. (2016). Topology optimization: a review for structural designs under vibration problems. *Structural and Multidisciplinary Optimization*, *53*, 1157-1177.

[266]    Stolpe, M., & Svanberg, K. (2001). An alternative interpolation scheme for minimum compliance topology optimization. *Structural and Multidisciplinary Optimization*, *22*, 116-124.

[267]    Swan, C. C., & Arora, J. S. (1997). Topology design of material layout in structured composites of high stiffness and strength. *Structural Optimization*, *13*, 45-59.

[268]    Swan, C. C., & Kosaka, I. (1997). Voigt–Reuss topology optimization for structures with linear elastic material behaviours. *International Journal for Numerical Methods in Engineering*, *40*(16), 3033-3057.

[269]    Lurie, K. A. (2013). *Applied optimal control theory of distributed systems* (Vol. 43). Springer Science & Business Media.

[270]    Cheng, K. T., & Olhoff, N. (1981). An investigation concerning optimal design of solid elastic plates. *International Journal of Solids and Structures*, *17*(3), 305-323.

[271]    Keno-Tung, C., & Olhoff, N. (1982). Regularized formulation for optimal design of axisymmetric plates. *International Journal of Solids and Structures*, *18*(2), 153-169.

[272]    Sigmund, O., & Petersson, J. (1998). Numerical instabilities in topology optimization: a survey on procedures dealing with checkerboards, mesh-dependencies and local minima. *Structural optimization*, *16*, 68-75.

[273]    Diaz, A., & Sigmund, O. (1995). Checkerboard patterns in layout optimization. *Structural optimization*, *10*, 40-45.

[274]    Jog, C. S., & Haber, R. B. (1996). Stability of finite element models for

distributed-parameter optimization and topology design. *Computer methods in applied mechanics and engineering*, *130*(3-4), 203-226.

[275]    Rahmatalla, S. F., & Swan, C. C. (2004). A Q4/Q4 continuum structural topology optimization implementation. *Structural and Multidisciplinary Optimization*, *27*, 130-135.

[276]    Paulino, G. H., & Le, C. H. (2009). A modified Q4/Q4 element for topology optimization. *Structural and Multidisciplinary Optimization*, *37*, 255-264.

[277]    Haber, R. B., Jog, C. S., & Bendsøe, M. P. (1994, September). Variable-topology shape optimization with a control on perimeter. In *International Design Engineering Technical Conferences and Computers and Information in Engineering Conference* (Vol. 97683, pp. 261-272). American Society of Mechanical Engineers.

[278]    Haber, R. B., Jog, C. S., & Bendsøe, M. P. (1996). A new approach to variable-topology shape design using a constraint on perimeter. *Structural optimization*, *11*, 1-12.

[279]    Ambrosio, L., & Buttazzo, G. (1993). An optimal design problem with perimeter penalization. *Calculus of variations and partial differential equations*, *1*, 55-69.

[280]    Petersson, J. (1999). Some convergence results in perimeter-controlled topology optimization. *Computer Methods in Applied Mechanics and Engineering*, *171*(1-2), 123-140.

[281]    Petersson, J., & Sigmund, O. (1998). Slope constrained topology optimization. *International Journal for Numerical Methods in Engineering*, *41*(8), 1417-1434.

[282]    Sigmund, O. (1997). On the design of compliant mechanisms using topology optimization. *Journal of Structural Mechanics*, *25*(4), 493-524.

[283]    Sigmund, O., & Maute, K. (2012). Sensitivity filtering from a continuum mechanics perspective. *Structural and Multidisciplinary Optimization*, *46*(4), 471-475.

[284]    Bruns, T. E., & Tortorelli, D. A. (2001). Topology optimization of non-linear elastic structures and compliant mechanisms. *Computer methods in applied mechanics and engineering*, *190*(26-27), 3443-3459.

[285]    Bourdin, B. (2001). Filters in topology optimization. *International journal for numerical methods in engineering*, *50*(9), 2143-2158.

[286]    Lazarov, B. S., & Sigmund, O. (2011). Filters in topology optimization based on Helmholtz-type differential equations. *International Journal for Numerical Methods in Engineering*, *86*(6), 765-781.

[287]    Wallin, M., Ivarsson, N., Amir, O., & Tortorelli, D. (2020). Consistent boundary conditions for PDE filter regularization in topology optimization. *Structural and*

*Multidisciplinary Optimization*, *62*, 1299-1311.

[288]   Guest, J. K., Prévost, J. H., & Belytschko, T. (2004). Achieving minimum length scale in topology optimization using nodal design variables and projection functions. *International journal for numerical methods in engineering*, *61*(2), 238-254.

[289]   Belytschko, T., Xiao, S. P., & Parimi, C. (2003). Topology optimization with implicit functions and regularization. *International Journal for Numerical Methods in Engineering*, *57*(8), 1177-1196.

[290]   Xu, S., Cai, Y., & Cheng, G. (2010). Volume preserving nonlinear density filter based on heaviside functions. *Structural and Multidisciplinary Optimization*, *41*, 495-505.

[291]   Svanberg, K. (1987). The method of moving asymptotes—a new method for structural optimization. International journal for numerical methods in engineering, 24(2), 359-373.

[292]   Clausen, A., Aage, N., & Sigmund, O. (2015). Topology optimization of coated structures and material interface problems. *Computer Methods in Applied Mechanics and Engineering*, 290, 524-541.

[293]   Clausen, A., Andreassen, E., & Sigmund, O. (2017). Topology optimization of 3D shell structures with porous infill. *Acta Mechanica Sinica*, 33, 778-791.

[294]   Wu, J., Clausen, A., & Sigmund, O. (2017). Minimum compliance topology optimization of shell–infill composites for additive manufacturing. *Computer Methods in Applied Mechanics and Engineering*, 326, 358-375.

[295]   Lazarov, B. S., & Sigmund, O. (2011). Filters in topology optimization based on Helmholtz-type differential equations. *International Journal for Numerical Methods in Engineering*, 86(6), 765-781.

[296]   Wang, F., Lazarov, B. S., & Sigmund, O. (2011). On projection methods, convergence and robust formulations in topology optimization. *Structural and multidisciplinary optimization*, 43, 767-784.

[297]   Kalamkarov, A. L., Andrianov, I. V., & Danishevs' kyy, V. V. (2009). Asymptotic homogenization of composite materials and structures.

[298]   Engquist, B., & Souganidis, P. E. (2008). Asymptotic and numerical homogenization. *Acta Numerica*, 17, 147-190.

[299]   Xia, L., & Breitkopf, P. (2015). Design of materials using topology optimization and energy-based homogenization approach in Matlab. *Structural and multidisciplinary optimization*, 52(6), 1229-1241.

[300]   Cheng, G. D., Cai, Y. W., & Xu, L. (2013). Novel implementation of homogenization method to predict effective properties of periodic materials. *Acta*

*Mechanica Sinica*, 29(4), 550-556.

[301]    Rodin, G. J. (1996). Eshelby's inclusion problem for polygons and polyhedra. *Journal of the Mechanics and Physics of Solids*, 44(12), 1977-1995.

[302]    Aage, N., Andreassen, E., & Lazarov, B. S. (2015). Topology optimization using PETSc: An easy-to-use, fully parallel, open source topology optimization framework. *Structural and Multidisciplinary Optimization*, 51, 565-572.

[303]    Balay, S., Abhyankar, S., Adams, M., Brown, J., Brune, P., Buschelman, K., ... & Zhang, H. (2019). PETSc users manual.

[304]    Gropp, W., Lusk, E., & Skjellum, A. (1999). Using MPI: portable parallel programming with the message-passing interface (Vol. 1). MIT press.